MIT Libraries
Document Services

Room 14-0551
77 Massachusetts Avenue
Cambridge, MA 02139
Ph: 617.253.5668 Fax: 617.253.1690
Email: docs@mit.edu
http://libraries.mit.edu/docs

DISCLAIMER OF QUALITY

Due to the condition of the original material, there are unavoidable flaws in this reproduction. We have made every effort possible to provide you with the best copy available. If you are dissatisfied with this product and find it unusable, please contact Document Services as soon as possible.

Thank you.

The author numbered two pages as page 66.

Temperature Measurements in a Flow using Laser Induced Fluorescence of Oxygen

by

Franck Kolczak

Ingénieur des Arts et Métiers, Paris 1986
Diplôme d'Etudes Supérieures Spécialisées en gestion, Sorbonne-Paris I 1987

Submitted to the Department of Aeronautics and Astronautics
in Partial Fulfillment of the Requirements for the Degree of

Master of Science in Aeronautics and Astronautics

at the

Massachusetts Institute of Technology

September 1992

© Massachusetts Institute of Technology, 1992, All Rights Reserved

Signature of Author _____
Department of Aeronautics and Astronautics
August 1992

Certified by _____
Professor Alan H. Epstein
Professor of Aeronautics and Astronautics
Associate Director of the Gas Turbine Laboratory
Thesis Supervisor

Approved by _____
Professor Harold Y. Wachman
Chairman, Department Graduate Committee

MASSACHUSETTS INSTITUTE
OF TECHNOLOGY

SEP 22 1992

LIBRARIES

Temperature Measurements in a Flow using Laser Induced Fluorescence of Oxygen

by

Franck Kolczak

Submitted to the Department of Aeronautics and Astronautics
in Partial Fulfillment of the Requirements for the Degree of
Master of Science in Aeronautics and Astronautics

ABSTRACT

Optical techniques are particularly attractive for non-intrusive flow field measurement. Among the most promising for gas temperature measurement in the 300-500°K, 1-5 atm flow range is Laser Induced Fluorescence (LIF) of oxygen (O_2).The applicability of O_2 LIF for turbomachinery gas temperature measurement is investigated in this thesis. The technique consists of using a ultra-violet laser beam as a source of excitation for the oxygen molecules in the flow studied, and looking at the spectrum resulting from the emission of the excited molecules to infer information about the state variables of the flow. The specific objective of this effort has been directed at a calibration of the technique in a test chamber 330 cm^3 volume with variable and accurately controlled temperature and pressure. The chamber was illuminated with a narrow band pulsed ArF laser tunable in a range of 1 nm centered around 193.4nm, and the resultant gas emission spectra were recorded with an Optical Spectroscopic Multichannel Analyzer (OSMA). The OSMA recorded a set of spectra for every pulse of the laser. The various parameters varied during the experiments were the temperature and pressure of the gas in the testing cell, the intensity of excitation (power of the laser beam), the wavelength and mode of operation (broad/narrow band) of the laser. Various data processing schemes have been examined to maximize the accuracy of the temperature measurement and make it independent, in so far as possible, of the laser power and mode locking efficiency, and of the gas pressure.

Acknowledgments

I am greatly indebted to many people for their assistance and support during the course of this work:

My advisor, Professor Alan H. Epstein, for his helpful guidance and encouragement.

Professor Edward M. Greitzer, for welcoming me in the Gas Turbine Laboratory.

Dr. Gerry Guenette and Dr. Choon S. Tan, for their friendly remarks and for sharing their expertise respectively in heat transfer and numerical analysis.

Alissa Fitzgerald for her calibration of the probes used in this experiment.

Dave Dvore for demystifying the use of FORTRAN for programming.

Victor Dubrowski for understanding, improving and turning my drawings into reality.

Jim Nash, Jim Legendre and Roy Andrews for their every day help in lab.

Diana Park for sharing some of her tricks on the Macintosh.

Holly Rathbun for enlightening GTL with her smile and for helping with all the administrative procedures.

The GTL students for their friendship and for making me feel that we were on the same boat.

On a more personal note, I would like to thank Maria for a skillful editing and most of all for reminding me that I could do it, when I needed it. I would like to dedicate this work to my mother whose love and support have made everything possible.

Financial support for this work was provided by NASA Lewis Research Center. The support of Dr. Anthony Strazisar, technical monitor, was very much appreciated.

Table of Contents

List of figures

List of tables

Chapter 1

Introduction

1.1 Problem Statement

Non intrusive optical techniques have been at the forefront of progress in the field of instrumentation in fluid mechanics in the most recent years. Recent advances in optical and electro-optical technologies have generated a large number of new attractive optical techniques. The use of these techniques is of major importance in a turbomachine development environment where they bring a new insight on complex fluid mechanics problems to scientists and engineers.

Complex engineering problems are stretching the implementation time of optical techniques to turbomachine environment : it took almost twenty years for laser anemometry to come to maturation and to be routinely applied in the turbines research field.

However, the measurement of another state variable is still required to compute the Mach number $\left(M = \frac{V}{\sqrt{\gamma RT}} \right)$, which allows to characterization all the variables in the flow. Therefore, there is a large incentive to find another non intrusive technique which would be able to measure a state variable (pressure, temperature or density). The specific goal of this project is to implement such a new optical technique in a high speed turbomachine.

1.2 Screening Techniques

The first step of this project was to list the potential techniques that could be used and to weight the trade offs among them in order to select the most appropriate one. This preliminary feasibility survey of various non intrusive techniques to measure state variables was performed by Dr. Kurt Annen from Aerodyne Research (see Reference [1]).

This survey included 2 steps:

a) Selecting the most promising technique

b) Carrying proof-of-principle experiments to demonstrate its feasibility.

The candidate techniques considered were:

1) Oxygen (0_2) LIF temperature measurement

2) Nitrogen monoxide N0 LIF

3) Biacetyl ($CH_2CO\ COH_2$) density measurement

4) Carbon Monoxide CO LIF density measurement

5) Formaldehyde (CH_2O) LIF density measurement

6) $O2/N_2$ Raman scattering density measurement

After assessing the potential of each technique and taking into account the engineering severe constraints (refer next section for more details about these constraints), 0_2 LIF was chosen. Therefore the second part of the survey consisted of a proof-of-concept of 0_2 LIF experiment.

The experimental results confirmed the previous choice by proving the feasibility of the scheme. They also helped to select the most appropriate configuration of laser for the future experimental investigation (a narrow band or tunable Excimer Laser—see chapter 3). It is interesting to note that experiments performed by other teams were leading to the same conclusions validating the 02 LIF technique (see ch. 2 for more information about other works.)

1.3 Principle of O_2 LIF temperature measurements

The O_2 LIF technique can be schematically described as follows. The laser beam produced by a narrow band/tunable Argon Fluoride (ArF) excimer laser is used to excite one of the several absorption bands encompassed by the laser gain curve (see Fig. 1.1). The excited molecules release the energy absorbed by fluorescence. The emission spectrum is composed of several lines corresponding to the rotational levels of the O_2 molecules and located in the spectral domain between 210 nm and 400 nm. An advantage of the technique is that the Raman emission is located close to the LIF lines (at 199 nm), so that it can be collected at the same time (see Fig. 1.2). Both the Raman and the LIF lines convey information about the state of the O_2 molecules(temperature and pressure) and the nature of the excitation source (wavelength and intensity of the laser beam). The wavelength position of the laser, chosen when tuning the laser, isn't a source of strong variation for the collected spectra. So the data reduction consists in compensating for the laser power and gas pressure effects to compute the temperature of the gas from the 10 available signals (3 Raman and 7 LIF shown in Fig. 1.2).

1.4 Design goals of the project

The engineering specifications of the project were dictated by turbomachinery geometry such as, illustrated in figure 1.3. This include :

- a spatial resolution of 2% of blade pitch which translates in a measurement volume of less than 1 mm^3
- a temporal resolution of 2% of blade passing
- a temperature resolution between 0.1 and 1 °K

Furthermore, the collection optics must respect the complex geometry of turbomachines. Figure 1.4 illustrates the proposed set up for measurements inside a turbomachine.

Finally, the power variation of the laser beam and the gas pressure effects should be compensated for based only on the collected spectra. The advantage of using only optical information is to eliminate any trouble coming from inaccurate power reading or variations of light transmission due for instance to dirty windows.

1.5 Design goals of this work

- design and build an experimental apparatus
- elucidate experimental difficulties
- calibrate of the spectra collected versus temperature, pressure and intensity
- develop data reduction procedures

1.6 Organization of the thesis

The rest of the thesis is organized as follows:

- Chapter 2 reviews the theoretical background of oxygen fluorescent processes and explains the principles involved. This section also gives theoretical quantification of the phenomenon such as the expected signal strength and precision. and reviews the literature.
- Chapter 3 gives a description of the experimental apparatus and rational for its design.
- Chapter 4 describes the methodology and procedures of the experiments.
- Chapter 5 presents the experimental results and compares them to theoretical expectations and finally lists a series of practical problems encountered.
- Chapter 6 closes the thesis with conclusions and recommendations for future work.

Chapter 2

Theoretical background

This Chapter gives an overview of the physical principles involved in 0_2 LIF experiments before studying the equations quantizing the different variables.

2.1 Principles Involved

An 0_2 LIF experiment can be described very simply as follows : a laser beam is focused on a point providing a source of excitation for the oxygen molecules located at this point at this instant. A key point that made this experiment feasible with a rather simple set up is that a laser emitting light at an appropriate wavelength, near the absorption band of 0_2, happens to exist. The laser is an excimer tunable UV laser and will be further described in chapter 4.1. The technology for this kind of laser has been commercially available only since the mid 80's. This fact explains that although the field of 0_2 LIF is quite attractive since it opens new scientific horizons with various applications it is also brand new. The pioneers of this concept were Massey and Lemon who had to build a home-made laser to carry out their experiments in 1984. [4]

Figure (2.1) clearly shows the overlap between the laser energy output distribution and the absorption band of the molecule of oxygen. For more information about the choice of the laser configuration broad band/narrow band–see chapter 4.1.

The molecules of oxygen are excited from the ground state $X^3\Sigma_g^- \ (v=0)$ to the excited state $B^3\Sigma_u^- \ (v=4)$ by a single photon absorption process; the photons coming from the laser at 193.5nm or 51 680cm $^{-1}$ (see figure (2.2)).

The transitions between the X and B status for 0_2 are referred in the literature as the Schumann–Runge band. As the excited state B is unstable most of the molecules in that state are bound to be further transformed and release the acquired energy. This relaxation phenomenon may take different forms:

1) the molecules may decay back to the initial state releasing the acquired energy as fluorescence : see spontaneous emission rate W_{21} in figure (2.3).
2) the molecules may decay back to the ground state but in other accessible levels than the initial rotational electronic one : see relaxation rate W_f in figure (2.3).
3) the dominant transfer process in this case is predissociation consisting of the dissociation of the 0_2 molecule into two oxygen atoms : see relaxation rate W_D in figure (2.3).
4) the laser pump is also pumping back some excited molecules to the initial level generating most of the observed fluorescence: see stimulated emission rate W_L in figure (2.3).

The predissociation is the preponderant phenomenon for molecules in the B state since: $W_D \approx 10^{11}$sec-1 whereas $W_{12} \approx 10^5 sec^{-1}$, $W_f \approx 10^5 sec^{-1}$ and even the laser pump $W_L \approx 10^9 sec^{-1}$ is several orders of magnitude lower.

Due to this strong predissociation, the fluorescence yield—the ratio of excited molecules decaying to the initial state to the total number of excited molecules—is of the order of 10^{-5} to 10^{-4}. [2] [3]

The advantage of the very short life time (few pico seconds) due to the predissociation is that at atmospheric pressure, all the problems associated with collisional quenching are avoided. Knowing the fluorescence yield, one can infer the rotational population profile of the original molecule population [4] (see equations in the following section for more details). This population distribution is in turn sensitive to both gas temperature and density. Therefore, in order to know the temperature level, a density measurement should be performed.

A crucial advantage of the 0_2 LIF technique is that this density measurement can be done optically at the same time as the scanning is performed to measure the fluorescence signal. Hence, the Raman scattering (of oxygen and nitrogen) that sits next to the fluorescence in the spectral domain can be used to measure density. Raman scattering has 3 major advantages:

1) it is very close to LIF signal in wavelength hence easily accessible
2) it is linearly dependent on density and rather insensitive to temperature (see experimental data)
3) Raman cross section of oxygen is exceptionally high in this case due to the near-resonance of laser wavelength with dipole transitions in the oxygen.Raman intensity coming from an excimer laser source (193 mm) is supposed to be 72 times greater than the ones coming from a frequency-double Nd:YaG laser (532nm)

In conclusion, to measure temperature, only one optical data acquisition is required. From the medium collected, it is easy to take out the effect of density on the LIF fluorescence by scaling it with the Raman signal. This way of proceeding is not only the simplest but it should also take

out many perturbation sources for the measure such as: power variation, variation in efficiency collection (dirty optics etc...).

2.2 Spectral Model

A more mathematical approach leading to a deeper insight has been proposed by various teams that have worked on this subject. [3] [4] [6]

The following nomenclature is used in the next sections:

- N_1, N_1^*, N_2, N_2^* populations densities 1: initial state, 2: upper state and *: at thermal equilibrium
- g_1, g_2 respective degenerencies
- W_{12}, W_L, W_D, W_f as defined in previous section
- $W_C, W_{C'}$ redistribution rates among rotational levels

The energy transfer path represented in figure (2.3) leads to the following equation rate :

for the level 1 :

$$\frac{d}{dt}\left(\frac{N_1}{g_1}\right) = W_{12}\left(\frac{N_2}{g_2}\right) - W_L\left(\frac{N_1}{g_1} - \frac{N_2}{g_2}\right) - W_C\left(\frac{N_1}{g_1} - \frac{N_1^*}{g_1}\right) \qquad (2\text{-}1)$$

for the level 2 :

$$\frac{d}{dt}\left(\frac{N_2}{g_2}\right) = -\left(W_D + W_f + W_{21}\right)\frac{N_2}{g_2} + W_L\left(\frac{N_1}{g_1} - \frac{N_2}{g_2}\right) - W_C'\left(\frac{N_2}{g_2} - \frac{N_2^*}{g_2}\right) \qquad (2\text{-}2)$$

Furthermore, as pointed out in the previous section, the following is seen:

$W_f << W_D$

$W_{21} << W_D$

$W_L << W_D$

So, according to equation (2.2), N_2 is always much lower than N_1: $N_2 << N_1$

Hence, the equations can be simplified to:

$$\frac{dN_1}{dt} = W_C N_1^* - (W_L + W_C) N_1 \qquad (2\text{-}3)$$

$$\frac{dN_2}{dt} = -W_D N_2 + W_L \frac{g_2}{g_1} N_1 - W_C'\left(N_2 - N_2^*\right) \tag{2-4}$$

As we are interested in the fluorescence from all the rotational levels of the upper state, it is advantageous to consider the total population density in the upper electronic state N_u in terms of N_u, equation (2.4) simplifies to:

$$\frac{dN_u}{dt} = -W_D N_u + W_L \frac{g_2}{g_1} N_1 \tag{2-5}$$

The total fluorescence signal, is the total number of photons emitted. If the observation time is T and the imaged volume is V, then :

$$S_f = VW_f \int_0^T N_u(t)dt$$

According to (2.5) :

$$\int_0^T N_u(t)dt = \int_0^T \frac{W_L}{W_D}\frac{g_2}{g_1} N_1(t)dt - \int_0^T \frac{1}{W_D}\frac{dN_u}{dt}dt$$

$$\int_0^T N_u(t)dt = \frac{W_L}{W_D}\frac{g_2}{g_1}\int_0^T N_1(t)dt - \frac{1}{W_d}\left[N_u(T) - N_u(0)\right] \tag{2-6}$$

As pointed out previously W_D is large and $N_u(0)\approx 0$ and if T is equal or larger to the laser pulse duration, then again $N_{u(T)}\approx 0$, so the last term of the equation can be neglected.

According to (2.3) :

$$\int_0^T N_1(t)dt = \int_0^T \frac{W_C}{W_L + W_C} N_1^* dt - \int_0^T \frac{1}{W_L + W_C}\frac{dN_1}{dt}dt$$

so :

$$\int_0^T N_1(t)dt = \frac{W_C N_1^*}{W_L + W_C} T - \frac{1}{W_L + W_C}\left(N_1(T) - N_1(0)\right)$$

and :

$$S_f = VW_f \frac{W_L}{W_D}\frac{g_2}{g_1}\left[\frac{W_C N_1^*}{W_L + W_C} T - \frac{1}{W_L + W_C}\left(N_1(T) - N_1(0)\right)\right]$$

conclusion :

$$S_f = \frac{VW_f}{W_L + W_C}\frac{W_L}{W_D}\frac{g_2}{g_1}\left[W_C N_1^* T + \left(N_1(0) - N_1(T)\right)\right] \qquad (2.7)$$

2.3 Theoretical Expectations

2.3.1 Expected signal

The O_2 LIF signal collected during the experiments may be written as:

$$S_f = \frac{IT_p}{E} n_{O_2} V\eta \prod_k (T_k)\Omega L \frac{d\sigma}{d\Omega} \qquad (2.8)$$

I = power of laser beam (within absorption line width)

Tp = length of pulse (in second)

E = energy per photon (in Joule)

n_{O_2} = 0_2 density in cm^{-3}

V = volume imaged

η = efficiency of spectrometer

T_k = transmission of various optical components

Ω = collection solid angle (sr)

L = length of interaction imaged (in m)

$\frac{d\sigma}{d\Omega}$=0_2 LIF differential cross section

2.3.2 Molecular Spectroscopy Considerations.

Before trying to estimate what should be the sensitivity of the 0_2 LIF technique to measure the temperature, it is helpful to step back to some more general concepts of molecular spectroscopy. More specifically, the rotational energy of linear molecules is of prime interest here:

2.3.2.1 Simplest approach for a classical system

For a particule moving with a linear velocity V at a distance from the center of gravity, the angular velocity and the moment of inertia are:

$$\omega = \frac{V}{r}$$

and $I=mr^2$

For a system of particles, the angular momentum is defined by:

$$I = \sum_i m_i V_i r_i = \sum_i m_i r_i^2 \left(\frac{V_i}{r_i} \right) = I\omega$$

the rotational energy is : $\varepsilon_J = \frac{1}{2} I\omega^2$

The Bohr theory and its principle of quantized angular momentum requires that :

$$I\omega = J\frac{h}{2\pi}$$

hence :

$$\varepsilon_J = \frac{1}{2}(I\omega)^2 . \frac{1}{I} = \frac{h^2 J^2}{8\pi^2 I} \qquad (2.9)$$

2.3.2.2 Quantum Mechanical Treatment

To go a step further towards creating a model that better describes the complexity of reality, we should consider the equation established by Erwin Schrodinger in 1925. The equation is written here in its time–dependent, one dimensional form :

$$-\frac{h^2}{8\pi^2 m} . \frac{\partial \psi(x,t)}{\partial x^2} + U(x)\psi(x,t) = -\frac{h}{2\pi i} . \frac{\partial \psi}{\partial t}(x,t) \qquad (2.10)$$

This equation gives a greater insight about the wave mechanic aspect of a particle of mass subject to a potential function U(x). $\psi^2(x,t)$ gives the probability for particle to be found at a point at a given instant.

To draw an analogy with a classical model, the first term of the equation can be associated with kinetic energy, the second term is linked to potential energy (spring effect or gravitational effect.) Hence the total equation expresses the conservation of energy. This fact indicates clearly why the equation is brings some information about the energy level of molecules. Solving Schrodinger's equation gives a slightly different and more exact expression for the rotational energy of a molecule:

$$\varepsilon_J = \frac{h^2}{8\pi^2 I} J(J+1) \tag{2.11}$$

The energy can also be expressed in wave number units :

$$\overline{\varepsilon_J} = \frac{\varepsilon_J}{c} = \frac{h^2}{8\pi^2 Ic} J(J+1) \tag{2.12}$$

Respecting spectroscopists notations: $\overline{B} = \frac{h}{8\pi^2 Ic}$

$$\overline{\varepsilon_J} = \overline{B} J(J+1) \tag{2.13}$$

2.3.2.3 Rotational Energy Level Populations

The Boltzmann distribution is a relation linking the population level of particles in some given states to the energy levels of these states:

$$\frac{N_i}{N_j} = e^{\frac{(\varepsilon_i - \varepsilon_j)}{kT}} \tag{2.14}$$

Before applying the Boltzmann distribution to the rotational energy level, it is important to take into account the various degeneracies for each rotational level which is illustrated in figure 2.3.

For a given value of J or level of energy $\overline{\varepsilon_J} = \overline{B} J(J+1)$ there are 2J+1 states corresponding to angular momentum components ranging from $+J\frac{h}{2\pi}$ to $-J\frac{h}{2\pi}$ Hence, the population of the J^{th} energy level is :

$$N_J = (2J+1) N_0 e^{-\frac{\varepsilon_J}{kT}} \tag{2.15}$$

N_0 being the population of the ground state(see Figure (2.4)). So :

$$N_J = (2J+1) N_0 e^{-J(J+1)\frac{h^2}{8\pi^2 IkT}} \tag{2.16}$$

[7] [8]

2.3.3 Expected Sensitivity of 0_2 LIF to Temperature

In the following analysis we make the simplifying assumption: $N_0 = N_T$. N_T being the total number of molecules. (This assumption is realistic since at room temperature typically for a diatomic molecule : $\frac{N_0}{N_T} \geq 0.99$)

Then : $N_0 = \frac{P_{O_2} V}{RT}$

with : P_{O2} = partial pressure of $O2$

V = volume of interaction imaged

R = 8.32 J/mol

T = temperature in K

Therefore :

$$n_J = \frac{P_{O_2} V}{RT}(2J+1)e^{-J(J+1)\frac{h^2}{8\pi^2 IkT}} \tag{2.17}$$

An error estimation leads to :

$$\Delta n_J = \frac{\partial n_J}{\partial T}\Delta T + \frac{\partial n_J}{\partial P_{O_2}}\Delta O_2 \tag{2.18}$$

or :

$$\frac{\Delta n_J}{n_J} = \frac{\partial n_J}{\partial T}\frac{T}{n_J}\frac{\Delta T}{T} + \frac{\partial n_J}{\partial P_{O_2}}\frac{P_{O_2}}{n_J}\frac{\Delta P_{O_2}}{P_{O_2}} \tag{2.19}$$

$$\frac{\partial n_J}{\partial P_{O_2}}\frac{P_{O_2}}{n_J} = 1$$

$$\frac{\partial n_J}{\partial T}\frac{T}{n_J} = -1 + J(J+1)\frac{h^2}{8\pi^2 IkT}$$

Hence :

$$\frac{\Delta n_J}{n_J} = \frac{\Delta P_{O_2}}{P_{O_2}} + \left[J(J+1)\frac{h^2}{8\pi^2 IkT} - 1\right]\frac{\Delta T}{T} \tag{2.20}$$

Furthermore the fluorescence signal is the sum of the contribution from the different absorption bands overlapping the energy distribution shape of the laser beam $S = K\left(\sum_J n_J\right)$

K: Fluorescence yield.

Even if the laser is in a narrow band configuration (case that we study in the following part), the absorption spectrum of O_2 is such that there is always a pair of transitions excited together [see figure 2.1]

An R branch corresponds to a transition where the quantum number J is raised by one unit.

A P branch corresponds to a transition where the quantum number J is diminished by one unit.

So a narrow band laser: $S = K\left(n_{J_R} + n_{J_P}\right)$

so :

$$\frac{\Delta S}{S} = \left(\frac{\Delta n_{j_R}}{n_{j_R}} + \frac{\Delta n_{j_P}}{n_{j_P}}\right)$$

Therefore:

$$\frac{\Delta S}{S} = \frac{\Delta P_{O_2}}{P_{O_2}} + \left[\left[J_R(J_R+1) + J_P(J_P+1)\right]\frac{h^2}{8\pi^2 IkT} - 2\right]\frac{\Delta T}{T} \qquad (2.21)$$

$$\frac{h^2}{8\pi^2 IkT} = \frac{hc\overline{B}}{kT} = \frac{2.0686}{T}$$

or :

$$\frac{\Delta T}{T} \approx \left(\frac{1}{\left(J_R(J_R+1) + J_P(J_P+1)\right)\frac{2.0686}{T} - 2}\right)\left[\frac{\Delta S}{S} + 2\frac{\Delta P_{O_2}}{P_{O_2}}\right]$$

Example: For the transitions R17 & P15 at 293K

$$\frac{\Delta T}{T} \approx \left(\frac{1}{(17\times 18 + 15\times 16)\frac{2.0686}{293} - 2}\right)\left[\frac{\Delta S}{S} + 2\frac{\Delta P_{O_2}}{P_{O_2}}\right]$$

$$\frac{\Delta T}{T} \approx 0.53914\left[\frac{\Delta S}{S} + 2\frac{\Delta P_{O_2}}{P_{O_2}}\right] \qquad (2.22)$$

Table 2.1 : Variations of Coefficient $K = 1\Big/\left[\left[J_R(J_R+1) + J_P(J_P+1)\right]\frac{h^2}{8\pi^2 IkT} - 2\right]$

Temperature (K)	293	400	500
Coefficient	0.53914	1.2141	3.8623

However when T increases, the total fluorescence increases sharply and $\frac{\Delta S}{S}$ decreases. So the precision of the temperature measurement may actually improve when the temperature increases.

The closing section of this chapter about theoretical background lists previous works on related topics. Although it may not be exhaustive, it will help to get a feel of what has been the progress of research in that field.

2.4 Description of the 02 LIF spectrum

The LIF spectrum was briefly described in the introduction. The goal of this section is to go further in the details of the spectra observed, and to establish some links between the experimental spectra and the spectroscopy theory. The general illustration for this section is Figure 2.4.

- *Fluence level*

It is clear when looking at Figure 2.4 and at the first spectrum presented Figure 1.2, that the same features are present in both of them. However, a closer look shows that the ratio between the corresponding peaks is roughly 3.7. As both spectra correspond to the accumulation for the same number of pulses of the laser, the preceding observation indicates a much higher fluence level in the spectrum V72B#3 than in V72A#3. This increase of energy level results in a dramatic increase of the general baseline and in the apparition of new features between the LIF and Raman peaks. These additional peaks are attributed to the fluorescence of O_2^+. The literature refers to O_2^+ fluorescence as a multiphoton excitation process generating non linearities.

• *Raman peaks*

The Raman peaks are just a shift in the incident light. Many chemistry or physics books are listing the value of the shift according to the nature of the molecule. Traditionally, wave numbers are in use in spectroscopy, therefore the Raman constants are given in wave number or cm^{-1}. For O_2, the value of the Raman constant is 1554.7 cm^{-1}, and N_2 it is 2330.7 cm^{-1}. Conclusion : for an excitation light close to 193.18 nm (near the P17 O_2 absorption band), the positions of the Raman peaks should be :

O2 first order : $\lambda_{O_2Raman} = \left(193.18^{-1} - 1\times 1554.7\times 10^{-7}\right)^{-1} = 199.16nm$

O2 second order : $\lambda_{O_2Raman2^{nd}} = \left(193.18^{-1} - 2\times 1554.7\times 10^{-7}\right)^{-1} = 205.53nm$

N2 first order : $\lambda_{N_2Raman} = \left(193.18^{-1} - 1\times 2330.7\times 10^{-7}\right)^{-1} = 202.29nm$

In the same manner, the third order of Raman O_2 and the second order of Raman N_2 should be respectively at 212.31 nm and 212.30 nm which very close to the 4,3 LIF line. So it is not clear weather these superior order are too weak to be observed, or if they are just hidden by the LIF peaks. In theory, the Raman peaks are supposed to be proportional to the intensity of the excitation, the density of the species molecules; they are also supposed to be insensitive or at least less sensitive than O_2 LIF to temperature variations. This behavior has been experimentally checked : the Raman peaks are increasing when the pressure (or density) is increasing, and they are reduced when the temperature is increasing at constant pressure because of the resulting drop of density.

• *O_2 LIF peaks*

In Figure 2.4, the numbers written close to each LIF peak refer to rotational numbers for the molecules that contributed to the emission of a given LIF peak. For instance, 4.7 would correspond to v'=4 and v'=7. The spectroscopic theory can give the location of each peak according to the rotational numbers related to it. The location of the head of each excitation band was found in Reference [23] and used for linear regression at the beginning of the procedure converting the diode number in wavelength. However, the location of the LIF peaks also depend slightly on the source of the excitation (P13, P15 or P17...). So more accurate information

can be found by a deeper spectroscopic analysis of the oxygen molecule. The results of this kind of analysis are listed in table (2.2). (Source : Reference [24])

•*Finer details*

The spectroscopic study mentioned before allows to better understand the features of the experimental spectrum. The LIF peaks show 2 strong narrow peaks with the beginning of one or two smaller peaks next to them. The presence of four peaks is explained by spectroscopic theory. The selection rules governing allowed transitions for atoms stipulate that $\Delta J = \pm 1$ in the case of an emission spectrum. Therefore, the narrow band beam of the laser can excite mainly one transition, for example P17, but it will also excite slightly the other closest absorption band here : R19 (see Fig. 1.1). Then the contributions of both lines split again in two other lines due to the J=+1 or J=-1 cases. The following table is the result from a software performing spectroscopic analysis for the oxygen molecule. It gives the expected location of the four expected peaks for each LIF line. [24]

Table 2.2 : Expected location of the peaks in the case of an excitation close to the P17 position

	P17 peak #1	P17 peak 2	R19 peak #1	R 19 peak #2
4.3	211.68	212.13	212.05	212.56
4.4	218.53	218.97	218.92	219.46
4.5	225.73	226.19	226.13	226.71
4.6	233.3	233.78	233.72	234.32
4.7	241.26	241.77	241.7	242.33
4.8	249.64	250.18	250.09	250.76
4.9	258.47	259.04	258.93	259.65

The presence of these strong double (or multiple) peak is a proof of the narrow band nature of the excitation source light. An example of experimental spectrum taken with a broad band laser is illustrated in Figure 5.16. No multiple peaks appear there, and the width of the LIF lines is much larger than in the narrow band case. This broadening is coming from the interaction of the contribution of all the absorption peaks under the gain curve of the laser.

Another interesting insight from the theory is that the nature of the peak (shape) can be known. In the context of this experiment, all the peaks (Raman and each of the four peaks for

each LIF line) should have a Lorentzian shape (see appendix H) or in the case of a larger broadening, they should have a Voigt distribution. For more detail about modeling, see the section on data reduction in chapter 5.

2.5 Other research works related to 02 LIF

- in 1979, McKenzie, Manson and Gyberger used biacetyl LIF to measure time dependent density fluctuation in turbulent flows. [9]
- in 1984, as mentioned previously Massey and Lemon pioneered 02 LIF experiments to measure temperature and density with a home-made laser. They were using the information from 2 fluorescence spectra from 0_2 excited by 2 pulses of the laser tuned at different rotational transitions (P15/R17 and P21/R23) [4]
- in 1986 Leen and Hanson performed calculation for absorption and fluorescence yield at high temperature [10]
- in 1987 Gross, McKenzie and Logan implemented NO LIF to measure temperature, density, pressure in a supersonic flow. [11]
- in 1988 Laufer, McKenzie and Logan investigated experimentally and theoretically the emission spectrum of air excited by an ArF laser [12]
- Miles et al proposed a method LIF and Raleigh scattering to get a two–dimensional temperature and density measurements of oxygen or air [6]
- Laufer and McKenzie investigated 0_2 LIF to measure the fluctuations of temperature of air in a hypersonic wind tunnel [14]
- Lanrendeau reviewed various temperature measurements by light scattering methods including Raman scattering, Raleigh Scattering and LIF in different combinations [13]
- in 1989 Milton, Lee, Paul and Hanson implemented planar LIF of NO in flows with one and two dimensional shock wave [15]

- in 1990 Laufer, Fletcher and McKenzie developed their model of O_2 LIF showing the feasibility of measuring temperature and densities with Raman scattering and LIF signal. They also performed an experimental check with a tunable ArF laser [3]
- in 1991 McKenzie wrote an overview of the progress in laser spectroscopic techniques for instrumentation, including laser absorption, LIF, Raleigh and Raman spontaneous and coherent processes [5]
- in the same year, Fletcher and McKenzie investigated in more details (than in reference [12]) the experimental measurement of temperature and density using O_2 LIF. [16]
- Finally in 1992 Smith, Price and Williams investigated an O_2 LIF method to measure oxygen temperature and density but using the excitation of two fluorescence transitions rather than using 0_2 LIF and 0_2 Raman as Laufer, Fletcher and McKenzie or as in the present thesis. [17]

Chapter 3

Experimental design

The goal of this chapter is to describe the equipment used for this experiment. For the major items, some background theory is presented, then the physics and engineering principles involved are explained in appendices, in order to provide a deeper understanding of the behavior of each component. Lastly, the major equipment characteristics and specifications are listed.

The principal components of the experimental apparatus described in the following sections are :

- *the illumination system* composed of :
  - the laser providing the excitation source
  - optics used to direct and focus the laser beam (turning mirrors, spherical lens)
- *the sensor system* composed of :
  - the spectrometer (monochromator & OSMA)
  - the collection optics (two reflective mirrors in a Cassegrain configuration)

- *the test chamber* composed of :
  - a 6 arm cell externally heated with hot heat transfer fluid
  - a series of thermal probes (type K thermocouples and RTD's)
- *the data recording and analysis equipment* composed of :
  - a IBM PC compatible connected to the monochromator and running the OSMA software
  - a front end computer Helios system to monitor the acquisition of thermocouple and RTD data
  - a second PC running the software Labtech Notebook to interface with the Helios

Finally, the section closing this chapter analyzes the errors and uncertainties sources in this experiment.

3.1 Illumination system

3.1.1 Laser

The laser is by far, the most expensive part of the equipment used in the experiment. As mentioned in chapter two the first commercially available excimer lasers appeared in the mid 80's opening the door for a new range of applications involving UV spectroscopic processes (one of them being O_2 LIF).

The first part of this section reviews the specifications of the laser. The second part describes the cryogenic gas recirculation system which was added to improves the behavior of the laser. The most important aspect of the laser for the user : the beam characteristics, is treated in the third section. Some experimental considerations are noted in the fourth section.

3.1.1.1 Description of the laser used

The laser chosen for this experiment was a Lambda Physik: EMG 160 MSG with ArF configuration. The advantage of the ArF laser is to offer a gain curve overlapping several

absorption peaks of oxygen as mentioned in chapter 2 (see Fig. 1.1). Furthermore, the EMG 160 could be used in a broad band, or a narrow band and tunable, configuration the only narrow band laser commercially available at that time. To convert the standard EMG 160 from narrow band to broad band, one need just to replace the set of dispersing prisms in front of the oscillator cavity with a plain mirror.

Table 3.1 lists the major characteristics given by the manufacturer in both configurations.

Table 31 Laser EMG 160 characteristics:

Configuration	Wavelength	Max pulse energy	Power maxi.	divergence
Broad band	~193 nm	240 mJ	40 W	0.2 mrad
Tunable	192.8 - 193.8 nm	100 mJ	15 W	< 0.2 mrad

For both configurations :

Max Rep. rate	beam shape	pulse duration
250 Hz	21x4 mm	13 ns

For the tunable version:

Bandwidth	tuning range	locking efficiency
0.005 nm	1 nm	50%

The EMG 160 consists of two separate laser heads (or cavities), a common thyraton, an MSC switch and a switch mode power supply (see Fig 3.1)

The advantage of the two cavity design, is that it can be operated in different modes:

1) a narrow bandwidth–tuning mode for increased beam quality

2) an oscillator /power amplifier mode for increased power

3) a two color mode giving two beams at different wavelengths by using different gas mixtures in each cavity.

The manufacturer has limited the divergence of the output beam by using an unstable resonator in the amplifier cavity. The quality of the beam is further improved in the tunable configuration by injecting a beam into the amplifier that is already diffraction limited yielding the very low 0.2 mrad divergence.

One constraint of the ArF laser is that after a number of pulses, the gas is contaminated by impurities or secondary products generated by the reaction inside the cavity, resulting in a decrease in the performances or in an irregular behavior. To overcome the problem, a gas treatment unit has been built. It is described in the next section.

3.1.1.2 Cryogenic Gas Processing Unit

In order to avoid the degradation of the performances of the laser, the manufacturer recommended that a gas treatment unit be used.

This unit is based on the fact that the gas impurities degrading the laser behavior can be trapped at very temperature, near $77^{O}K$ the temperature of liquid nitrogen. The principle of the processing is then simply to use a cryogenic trap, filling a dewar with liquid nitrogen, and then to circulate the content of the cavities inside copper tubing going through the dewar. The set-up used is illustrated in figure 3.2. The gas processing system consists of 2 independent loops including filter and circulation pumps to circulate the content of the oscillator and amplifier cavities through the tubing emerged in liquid nitrogen. Additional connections to the exhaust line (going to the vacuum pump) were required for maintenance.

3.1.1.3 Output Beam Quality

As mentioned in section 3.1.1, the laser beam divergence was reduced by the manufacturer by using unstable optics and injecting a diffraction limited beam in the second cavity. The divergence specification of table 4.1 means that the manufacturer guaranties that at least 50% of the energy goes within a cone with a full angle of 0.2 mrad or less when the beam is focused with a lens.

Focused beam size

It is interesting from many points of view to be able to estimate the size of the focal point of the laser beam when using a given lens. With a 750 mm spherical fused silica lens at 589.3 mm, according to appendix B :

$$f_{193} = 0.8170 f_{base} = 612.75mm$$

so the working focal length is : 612.75 mm.

1) If the beam had a diffraction limited TEMoo profile, the size of the waist would be given by:

$$2w_0 = \frac{4\lambda}{\pi}\frac{F}{D} \qquad (4.5)$$

Hence the original beam of 21x4 mm would be focused to : 7.21x37.87 µm

Remark : At the focal point the initial larger dimension is shrunk to a smaller size than the initially smaller one.

2) However the beam is not gaussian and an approximation of the size of the focal spot can be obtained with the divergence specification of the beam: the size of the waist is given by : $2w_0 \approx F\theta$

For the laser used, the manufacturer guaranties that more than half of the energy goes through an angle of 0.2 mrad or less, which would lead to a waist of 612.72x0.2 = 122.5 µm.

3) According to the manufacturer, the divergence is not uniform but would correspond to roughly 0.1 mradx0.3mrad (again the higher divergence corresponding to the smaller beam dimension) According to this information, the beam should be : $0.1 \times 612.72 = 61.2 \mu m$ $0.3 \times 612.72 = 183.8 \mu m$

More practical remarks about the laser beam quality can be found in the next section and in the section 3.6.

3.1.1.4 Experimental considerations

a) Beam variability

The power of the laser beam showed a lot of variability. The shot to shot variations were not easy to characterize due to slow time response of the power meter used. The shot to shot variability could be measured relatively by imaging the second order of the laser light from the grating of highest resolution (3600 g./mm) mounted in the spectrometer. Examples of the spectra obtained are illustrated in Figures 3.3 and 3.4.

b) Gain curve

The imaging of the spectral shape of the beam points out a potential experimental difficulty. The gain curve of the laser which corresponds to the broad band emission of the laser isn't an ideal bell shaped curve. Dips are present where the oxygen absorption bands are located. Figure 3.5 shows nicely this correlation by superposing one experimental spectrum of the gain curve of the laser with a graph from Figure 1.1 illustrating the theoretical absorption peaks of oxygen, These dips simply represent O_2 absorption within the laser beam path.

This irregular gain curve is troublesome in that the dips reduce the locking efficiency (i.e. proportion of the energy contained in the narrow band emission compared to the total emission) at the tuning locations that are the most interesting for this experiment, the O_2 absorption peaks. The reduction was such that in the case of the P15 peak, the laser couldn't be operated narrow band when tuned at the central position of this peak. The laser could still be operated narrow band when tuned at the center of the P17 peak since this peak is located almost at the

center of the gain curve, and the absorption of oxygen is weaker. This tuning position gave the strongest LIF spectra, therefore it was the wavelength selected for most of the experiments.

This irregular gain curve is due to a poor design of the laser. The laser beam path, is exposed to air and therefore to oxygen outside of the gas cavities. So oxygen absorption occurs between the diffracting prism set to the oscillator cavity ,and from the oscillator cavity to the amplifier cavity (see Fig 3.1), resulting in a weakened oscillator beam insufficient for narrow band operation. A quick attempt to improve this behavior by building an external purge system had little success because of the internal laser ventilation system continuously removed the N_2 purge gas A more serious re engineering of the laser should probably get better results.

3.1.2 Illumination optics

3.1.2.1 Laser Beam Focusing Lens

The calibration tests were to be run at conditions similar to those in a turbomachine (Appendix D), so a rather long focal length was required. A symmetric convex synthetic fused silica lens was used in preliminary experiments with a diameter ϕ = 25 mm and a nominal focal length of 500 mm

However, reduced aberrations are obtained when using a plano-convex lens and by using a restricted area around its center. Therefore a 3" = 76.2 mm diameter plano-convex fused silica lens with a nominal focal length =750mm was used the rest of the time.

$(f_{no\,min\,al} = 750mm \Rightarrow f_{193} = 612.75mm)$

3.1.2.2 Laser Beam Tuning Mirrors

To add some flexibility in the experimental set -up illustrated in figure 3.6, two high power Excimer laser beam—tuning mirrors (from Acton Research Corporation) were used and mounted on a beam steering instrument. The specified reflectance at 193 nm was between 94% and 98%. However, the damage energy level threshold was : 1 to 2 J/cm^2, and during some experiments, the first mirror was burnt so that, the losses level for the two mirrors unit went up to 25-30%

(see more about burning problems in the section of chapter 5 concerning experimental problems encountered) Total beam path length from laser output mirror to the cell window was about 140 cm.

3.2 Sensor system

3.2.1 Spectrometer

3.2.1.1 Description

The spectrometer spectrally disperses the collected light in order to get the spatial dispersion of spectrum. The model used included two spherical minors and a reflection grating in an arrangement known as the Czerny–Turner mount. (see figure 3.7)

The two spherical mirrors are used as focusing lenses as illustrated in the model of the spectrometer illustrated with figure F1. The advantage of using reflection mirrors instead of the classical lens, as previously explained in section 3.1.4, is that it avoids chromatic aberrations.

As shown in figure 3.7 (spectrometer interior), the spectrometer used has a triple indexable grating turret allowing it to select a grating among the set of the three mounted gratings. The spectrometer also included a microprocessor controlling the motor moving the grating turret. This last feature allows the operator easy changes of the working point (wavelength), or scans over a spectral range at a given speed (among other things). Finally the spectrometer offers compatibility with plane focal detectors making it easy to use an external detection system (provided by another company).

3.2.1.2 Specifications

The spectrometer used was composed of:

- a 0.275m digital scanning monochromator from Acton Research Corporation—a Model Spectra Pro 275

• an Optical Spectroscopic Multichannel Analyzer (OSMA) system from Princeton Instruments including:

- an Intensified Photo diode Array of 1024 diodes, IPDA 1024 S/B
- a detector head
- a detector controller ST 1000 connected to a personal computer IBM compatible

The major specifications of the monochromator were:

focal length : 0.275 m

aperture ratio : f/3.8

entrance slit of variable width from 10 µm to 3.0 mm via a micrometer

resolution: 0.1 nm with 10µm slit at 435.8 nm (*)

reciprocal linear dispersion: nominal 3nm/mm (*)

wavelength operating range: 185 nm to 1.4µm (*)

wavelength accuracy : ± 0.2 nm / 500 nm (*)

wavelength reproducibility : ± 0.05 nm (*)

focal plane width : 25 mm

nominal coverage: 64 nm (*)

the specifications followed by (*) are valid for a grating of 1200g/nm

Table 3.2 : Gratings mounted in the spectrometer

number of lines per mm	Blaze wavelength (in nm)	optimum range (in nm)
300	300	200 - 400
1200	holographic	190 - 800
3600	240	160 - 320

Specifications of the ST 1000 :

ADC range: 16 bits or 65536 counts maximum

electric noise=1300e^-/diode/scan rms (1500c e^- rms maxi)

exposure time : from 1ns to hours

diode readout /storage rate : 4 μs / diode

Specification of the detector head :

read out noise (cts rms) : 0.88

sensitivity (cts/pe$^-$) : 1.22

EBI (cts/sec) : 0.43

dark charge (-23°C) : (cts/sec) : 18.19

quantum efficiency: 10 to 12%

typical noise from diode to diode=2.3 counts

3.2.2 Collection optics

A commercially available lens having characteristics not very far from the specifications listed in appendix D was bought in order to image the LIF fluorescence. It was a model : Lyman Alpha I lens 200 mm f/2.8 from NYE Optical Company.

Figure 3.8 shows a schematic of this lens, and table 4.5 briefly lists its quoted specifications.

Table 3.3 Characteristics of the Lyman-alpha I lens:

Spectral range	Type	Focusing range	Angular field	Length
100 nm to I.R.	reflective	12" to ∞	12° or f/2.35	5"

Resolution	back focus
@ 12" : 60 l/mm @ ∞ : 25 l/mm	0 to 2" adjustable

Between 190 mm and 400 mm, the reflectance is between 85% and 88%. As shown in figure 3.8, the design of this lens included a spider mount of the secondary mirror that allow to change the configuration of the lens by moving one mirror with respect to the other. When using the lens in the classic configuration (object on the spider side), the magnification could be varied from ≈ 0

to 1.0. When using the lens in the reverse conjugate configuration (lens turned around), the magnification could be varied from 0.5 to 7.0. For the experiments, the lens was always used with the spider at the extremity of the "cylinder frame." At this position, the characteristics of the lens were :

- Object distance BBL = 10.25"
- Back Focal length = 1.8"
- Magnification ratio = 1.0.

3.3 Test chamber

3.3.1 Design Goal

The calibration phase of this project required building a testing environment subject to many constraints. To perform the temperature calibration, the temperature of the testing volume had to be controlled very well. The goal of the project which was to measures temperature with an accuracy of 0.1°K from room temperature to 500°F (533°K) at pressures ranging from 1.0 to 3.0 bar. This implies that the temperature of the measurement volume must be kept within 0.1°K during the measurement time (typically one second) and over the stated range of temperature. Furthermore a measurement of temperature as precise as 0.1°K had to be performed during the experiments. Also, since the laser light destroys the oxygen and generates unwanted by products such as O_2^+, the gas in the chamber could not be stagnant. Flushing at a rate commensurate with the fastest laser repetition rate (250 Hz) was required. Building such a testing environment was a challenge.

3.3.2 Design

The general design concept chosen was an oil heated test chamber supplied with compressed air preheated in an oil-air heat exchanger. The next section describes the design

method for the hardware meeting the specifications described above. Then the general set up of the testing chamber is reviewed. Finally, the specifications of the hardware parts are listed. The design calculations have been included in appendices.

3.3.2.1 Method

First a general set-up for the testing environment was chosen. Then heat transfer calculations were performed to find the conditions for which the measurement volume would be thermally stable. The next step was to take the previous conditions and to compute the pressure drop for the heat transfer fluid in the circuit. All these preliminary calculation steps resulted in engineering specifications for the various hardware parts which could then be selected. The next sections follow the order described above.

3.3.2.2. General Set-up for Testing

A commercially available 330 cm^3 inside chamber six-arm cell was used to house the test volume. This cell is illustrated in Figure 3.9 and can also be seen in the general set-up Fig. 3.6

- the vertical axis was the axis of the gas flow
- one horizontal axis was the axis of the laser beam
- the second axis was the optical viewing axis, it was also the axis for the direction of probe movement.

Flanges or windows were installed at the extremity of each arm. In order to get an homogeneous flow inside the cell, two nipples were added on the vertical axis to straighten the flow with flow breakers, screens and honeycomb.

Pressure Control

On the air circuit connected to the cell, a variable pressure regulator and a globe valve controlled the flow rate and its pressure.

Temperature control

A 1/4 inch copper tubing was wrapped tightly around the two nipples and all the arms of the cell. A commercial heat transfer fluid "Dowtherm G" (whose characteristics are listed in table 3.4) was circulated inside this tubing.

Table 3.4 Characteristics of the Dowtherm G heat transfer fluid

Temperature	75 °F	550 °F
Specific gravity	69 lb/ft^3 1105.2 kg/m^3	56 lb/ft^3 897.0 kg/m^3
Specific heat	0.388 BTU/lb.°F 1623.4 J/kg.°K	0.52 BTU/lb.°F 2175.7 J/kg.°K
Viscosity	125 cst	@ 210 °F 20 cst

The Dowtherm G fluid was circulated with a pumping system through a circuit including a tank, an expansion tank, a circulating pump and an electrical heater (providing the source of heat). The heat losses were diminished by insulating the whole circuit (about 2" thick of fiber glass) (see fig 3.9 for testing cell insulation).

The heat transfer coefficient between the cell arms and the copper was enhanced by adding a thermal conductive paste : the Omegatherm 201 High temperature-high thermally conductive paste

Table 3.5 Characteristics of the thermal conductive paste Omergatherm 201

Material	Max continuous temperature	thermal conductivity	Resistivity
silicone grease	400 °F	k = 16 BTU.in/hr.ft^2.F	10^{14} Ω.cm

Another solution to improve the thermal conductivity between the cell and the copper tubing was to braze the tubing on the cell. However, in spite of many trials, furnace brazing the copper tubing on the stainless steel with a silver alloy failed. Therefore, the easier use of the Omegatherm paste was used.

Air Displacement

Once the laser pulse has been focused on a given volume of air, many molecules of air in this volume are degraded into 0_2^+, oxygen atoms, ozone or other products. Therefore, it is important to insure that the products generated by the laser energy. are flushed from the measurement volume and that "fresh" oxygen molecules are brought in. Hence, the need for air flow. The minimum flow rate is such that the displacement of air inside the cell between two pulses is larger than the measurement volume size.

Displacement minimum = spatial resolution = 1 mm

Maximum repetition rate = 250HZ

Cell inside diameter 1 3/8" (35 mm)

If we want a displacement of X mm between two shots:

Flow rate : $X * 250 * [\pi 35^2/4] = 240\,538 * X\ mm^3/s$

$= 0.241 * X\ l/s$

Note : $1\ l/s = 0.035315 * 3600 = 127.13$ scfh (standard cubic feet per hour)

So : Flow rate = $30.51 * X$ scfh

Typical flow rates for the tests used were 20 to 50 scfh. Most of the later data was taken with a flow rate of about 32 scfh corresponding to a local pressure in the cell of 1.3 bar with the valves fully open.

3.3.2.3 Choice for the Equipment

•*Pump*

A high temperature (able to pump at up to 500°F) pump was selected. It was a Tri Rotor 20D model: with a 1/4 stroke solid head to reduce the flow rate from 20 to 5 GPM. The electric motor coupled to this pump was a 1/2 HP rotating at 1140 RPM. The characteristic curve of the pump was flat at 5 GPM from 0 to 100 psi. Hence according to equation G.13, this pump was able to

move a flow of 2.54 GPM in the circuit. Note: the choice of pumps available to work with a high temperature and a small flow rate was rather limited.

•*Heater*

The model chosen was a circulation heater from Chromalox NWHMTO 3305 (3 kW) with a temperature range: 200-550°F and a watt density corresponding to light oil 23w/in^2. Raising the temperature of the system form 293°K to 560°K according to equation G.11 should take about 2.5 hours. It is interesting to note that this choice of the heater roughly follows the rule of thumb given by the manufacturer of having a flow rate ranging form 1 to 1.6 GPM per KW of heater. In this case, the 3 kW heater would imply a flow rate from 3 to 4.8GPM

3.3.2.4 Instrumentation

Table 3.6 lists the probes used to measure temperature in this experiment.

Table 3.6 Temperature probes

Name	Type	Location
Th3	thermocouple K very thin junction (10μm)	inside cell - on central axis
Th4	thermocouple K 1/16" with sheath 304SS	inside cell - in horizontal plane 0.6" upstream Th3
Th6	thermocouple K 1/16" with sheath 304SS	immersed in oil - before the cell
Th5	thermocouple K 1/16" with sheath 304SS	immersed in oil - after the cell
RTD11	platinum RTD 1mm thick	inside the cell - in vertical plane 0.6" above Th3
RTD14	platinum RTD 1mm thick	skin contact of the cell

All these thermocouples and RTD were calibrated against reference RTD and glass thermometers. However, a secondary standard platinium RTD was purchased and further calibration was planned. Therefore, the temperature data consists of a simple reading and can be corrected when the calibration using the new high precision thermometer is performed.

3.3.2.5 Experimental considerations

The oil system generated cavitation resulting in severe destruction of the inside of the pump during the first heating tests. In order to avoid this cavitation, the remaining heat tests were run at temperature below 140 °C (or about 285°F). In future calibration runs, one way to go around this problem would be pressurize the heat transfer system. However, the expansion of the Dowtherm G fluid should be carefully accounted for when doing that.

3.4 Data recording

3.4..1 Optical data

The software controlling the acquisition of spectra and running on an IBM PC compatible was provided by Princeton Instrument, was the ST–1000 software version 2.0. This software had some capabilities to:

1) Present data on screen

2) Manipulate data

3) Store new experimental data

Presentation of data :

The software was able to display one or several spectra on the computer monitor. It had various scaling and zooming options. It could also display a series of spectra contained in one file as a movie—slowing sequentially all the spectra in an infinite loop.

Manipulation of data:

A built in macro calculator included macro instructions to process spectra. This allowed one to add, subtract, multiply, different spectra or to operate a simple transformation such as taking the logarithm, the exponential or the square not of a spectrum. However, to have more

flexibility, the data manipulation was performed with other software after exporting the data file in an ASCII format.

Acquisition of Data

The ST-1000 software was mainly used in this experiment to monitor the data acquisition process for which a wide range of options was available.

• the exposure time (variable from 30ms to hours) controlled the number of laser pulses recorded before reading the signal from the diode array.

• More than one spectrum could be stored in one experimental file, therefore the desired number of spectra had to be input.

• The storage mode determined when data storage should begin as soon as the experiment starts or when activated manually.

• Background subtraction could be done from individual spectra (an option used to account for the dark noise or to using a recorded experimental file) The calibration of spectra i.e. conversion from diode number to wavelength was done with other software to increase flexibility (see appendix F for more details about this calculation).

• The experiment mode selected the scanning procedure.

Free Run : continuous scanning

External synchronization or External Trigger : begin scanning upon receipt of TTL pulse.

Line Synchronization : synchronize the scanning with an internal reference (60 Hz from AC Current)

3.4.2 Temperature Data

3.4.2.1 Helios Computer Front End

The acquisition of the temperature measurement was monitored by data acquisition and control subsystem : the Fluke Helios computer front end. The Helios provided a smart intermediary between the IBM PC compatible and the probe measurements. The addition of two

optional cards made it possible to read directly the voltage from the thermocouples and RTD used. With its additional cards, the Helios could manage simultaneously the reading of 20 thermocouples, 20 RTDs at a maximum sampling rate of 0.25 Hz (one measurement every 4 second) The second interface between the temperature measurements and the data file was the software running the IBM PC described in the next section.

3.4.2.2 The Software: Labtech Notebook

Labtech Notebook /XE version 6.2.1 was the software interface which allowed to:

1) operate the Helios

2) organize data easily

3) monitor the experiments through a user friendly interface. Among the handy features of Labtech Notebook used in this experiment were:

- it's capability to convert the voltage reaching from the Helios in temperature according to the nature of the probe used.
- the possibility to include a variable keeping track of time during the data acquisition
- the easy manipulation of data files (including the choice of the units of the various variables).

3.5 Errors and uncertainties

a) Laser

The variability of the laser on Figure 3.3, for a series of 10 spectra of 1 shot each is about ± 22 % compared to the average level of the narrow band height peak. For the series of 10 spectra including 20 shots each, the variability fell to ± 5.7 %. . According to statistics laws, the standard deviation of a variable equal to the sum of N identical, independent variables X_I, is equal to the standard deviation of the variable X divided by square root of N. The application

of this rule in this case give a ratio in the standard deviations of $\sqrt{20} = 4.47$. The observed ratio of variability is : 22/5.7 = 3.85 not far from the theoretical prediction. However, this variation doesn't account for any variation of the LIF peak relatively to one another.

b) Spectrometer

The noise level for any diode is of the order of 4 to 5 counts. Assuming that the width of the observed peaks is about 30 diodes, the total maximum variation per peak due to this noise is of the order of 150 counts.

c) initial procedure

The major source of difference between the empirical peak identification and the Lorentzian curve fitting, is due to the presence of a baseline. For a high baseline of about 1000 counts for the first LIF peak as in test V72B, the disparities between the two procedures already amount to 30*1000 = 30000 count per peak. Therefore, the magnitude of the error induced in the results by the data reduction method is much larger than the one induced by the noise level in the spectrometer. But in this case again, this problem of data analysis doesn't generate fluctuations as large as those observed in the data.

Chapter 4

Experimental procedures

This chapter describes the procedures and parameters settings used during the experiments.

4.1 General settings

4.1.1 Spectrometer

a) LIF Spectra

As 70 % of the total fluorescence occurs between 200 and 250 nm, the grating used in the spectrometer had to be able to cover all this area in details. The 1200 g/mm was used to take the LIF spectra since it had a nominal dispersion of 3nm/mm resulting in the coverage of an interval of more than 70 nm wide.

Since the straight light from the laser was several orders of magnitude higher than the signal imaged, it was rejected by positioning the spectrometer at 234 nm. This position allowed to reject the light from the laser beam at 193 nm and to image the O_2 Raman line close to 199 nm.

b) Spectral shape of the beam

As the spectral shape of the beam is only 1 nm wide, the 3600 g/mm grating offering the maximum dispersion was used. To avoid that the high intensity of the laser light saturates the detector array, the second order of the laser light was imaged by positioning the spectrometer at 386 nm. It was not possible to image a higher order of the laser light since this grating couldn't be set at a spectral position above 500 nm (see table 3.2).

The gain of the spectrometer was constantly kept close to its maximum value : 9.90. For most of the experiments, the slit size was set to 50 μm. This offered a good compromise between a reasonable signal strength and a sufficient resolution (see appendix F for more information about the achievable resolution).

4.1.2 Chamber air flow conditions

The flow rate was kept constant at about 32 scfh, which results in an air displacement of 5.2 mm between each pulse when the laser was operating at 50 Hz. The pressure in the cell corresponding to the previous flow rate with the valve fully open was 1300 mb. When the temperature was not varied, the cell was at room temperature between 23 and 27 °C.

4.1.3 Laser operation

The laser was typically operated with a high voltage between 20.0 and 21.0 kV (the potentia range was : 19.0 to 26.3 kV). For all the experiments, the repetition rate was 10 or 50 Hz.

The laser emission proved to be quite sensitive to the temperature of the cavities, a lower temperature resulting in a reduced power. On the other hand, after using the laser for a while, the gas mixture began to be contaminated by impurities making it necessary to run the home built cryogenic system to recover normal operation conditions. A secondary effect of running the cryogenic recirculation was to cool the cavities which could result in a power loss if the cavities

were not warm enough. Conclusion, using the cryogenic recirculation was the result of a trade off between the contamination level of the gas and the temperature of the cavities.

4.2 Temperature data acquisition

4.2.1 Temperature variation

Two different procedures were used to vary the temperature. The first consisted in heating the experimental set up to the maximum temperature and to let it cool down when performing the experiments. The circulation of the hot oil inside the tubings would insure a reduced cooling rate. This procedure is illustrated in Figure 4.1 where the reading of the various probes used are plotted in function of the time, the initial time was chosen after the beginning of the cooling down of the system.

The second procedure consisted in turning on and off the heater for temperature stage. The experiments were not performed when the heater was not since the rate of variation of temperature is then greater than the rate of variation when the system is cooling down with the oil circulated in the tubings. The general temperature variations corresponding to this procedure is illustrated in Figure 4.4. Figure 4.5 shows that the system take some time to begin to cool down after the heater is turned off; the measurements were performed only at the beginning of the cooling phase.

4.2.2 Temperature reading

A thermocouple with a 10 μm junction(Th3) was reading the temperature of the air flow at the measurement volume. It was removed just when the laser was firing. The reading of Th3 was compared to the one of a second thermocouple (Th4) that was standing still on the side of the testing cell. Figure 4.2 illustrates the difference of reading between Th3 and Th4. Each spike corresponds to a movement of Th3. Figure 4.3 represents the same curve after a smoothing using a 10 points interval. The smoothing clear out much of the noise from the preceding curve, making

it easier to interpolate the value of the reading of Th3 at the measurement volume when the experiments were performed.

Chapter 5

Experimental measurements and discussion

This chapter presents the data reduction procedures. It reviews the tests which were run, and presents the experimental data.

5.1 Data reduction

As seen in chapter 2, the total energy in each line should be the spectral feature most sensitive to temperature change. Therefore, the data reduction procedure must estimate this energy in the most accurate way. As the energy is represented by the area under the peaks, the main task of the procedure computing the energy is to identify the peaks and to compute the area under them.

5.1.1 Empirical reduction procedure

Initially, no assumptions were made on the nature or shape of the peaks. So the goal was to establish empirical procedures able to identify the LIF and Raman peaks and calculate the energy in them.

Finding the peaks location

Finding the peaks was a relatively easy thing since :

1) even for a low power spectrum, the signal to noise ratio is typically above 6,

2) for a fixed spectrometer setting, the LIF and Raman peaks position vary by no more than 5 diodes (Figures 5.53 to 5.61 illustrating the variations of individual peaks with pressure and temperature show a shift for the peak positions of 5 diodes or less and the experimental settings for the spectrometer were the same for the pressure test W72P and the temperature test V72H).

In the experiments, the grating and the position of the spectrometer were fixed making the problem simpler. Since the respective position of the peaks didn't change (as long as the same grating is used), it was convenient to reference the position of all the peaks to that of the O_2 Raman peak position. This procedure has the advantage that it is robust to alignment changes in the spectrometer (which proved not to be a problem in any case).

The procedure starts by locating the O_2 Raman peak by identifying the location of the maximum count over a 10 diodes interval centered on the expected location of the O_2 Raman peak. The spectral shift to each of the other lines of interest is known from theory and experiment. Once the O_2 Raman is known, the location of the maximum of each peak can be found in a similar way (scanning an interval centered on the expected location).

• *Finding the peaks width*

Determining the width of each spectral line is more difficult than establishing the peak height. The rule adopted here is to move away from the peak maximum until a minimum is found with at least 3 diodes in a row with an increasing slope (the sign of the slope is computed with regard to the direction of the movement). This rule seems to work well for a moderately noisy spectrum with strong slopes near the peaks maximum. This approach, however, can not find the limit of a peak which has a smooth exponential decay. Here, an alternate rule set is to stop the peak when a point where the slope is less than one tenth of the slope between the maximum of the peak and the point at mid height of the peak. In

conclusion, in order to find the extremity of the peak, the empirical procedure is moving away from the center of the peak and looking for a point meeting one or the other of the two previous criteria. Although quite simple, this approach works reasonably well for the data collected.

5.1.2 Lorentzian and Voigt curve fitting

The spectroscopic theory predicts that the nature of the peaks observed should be a Lorentzian curve or, if enough broadening is generated by the instruments used, a Voigt curve. Appendix H describes these functions and their modeling in the context of this curve fitting analysis.

A second data reduction procedure based on this information was implemented. However, due to limitations in the features of the software used to plot and analyze the data and to time constraints, the curve fitting could be performed on only two peaks at a time. The fact that the curve fitting module had to be run manually for each group of peaks explains why only a limited number of spectra were thus analyzed in the limited time available.

Figures 5.1 to 5.8 illustrate the quality of the curve fitting on some peaks of the spectra corresponding to the tests V72A #3 (low fluence and reduced baseline) and V72B #3 (high fluence and higher baseline). The global spectrum V72A #3 is illustrated in Figure 1.2 and the spectrum V72B #3 is illustrated in Figure 2.4. Modeling a single Lorentzian peak with a straight baseline requires 5 parameters; these parameters represented in Figures 5.1 to 5.4 are :

m1 = position of the maximum of the peak

m2 = half width of the peak

m3 = scaling coefficient for the peak

m4 = slope of the baseline

m5 = height of the baseline at the origin (since this equation is used only in an interval which doesn't include the origin, this coefficient can have a negative value while the value of the baseline on the interval considered remains positive).

When modeling two Lorentzian curves as in Figures 5.5 to 5.8, the parameters are defined as follows:

m1 = position of the maximum of the first peak

m2 = half width of the first peak

m3 = scaling coefficient for the first peak

m4 = position of the maximum of the second peak

m5 = half width of the second peak

m6 = scaling coefficient for the second peak

m7 = slope of the baseline

m8 = height of the baseline at the origin

The curve fitting module of Kaleidagraph, the software used for data reduction, was restricted to 10 different variables which made it impossible to model the 4 different peaks that were predicted by spectroscopic theory (see Section 2.4). In spite of this limitation, the results still show a very good agreement when modeling the 2 major peaks as illustrated for the O_2 LIF 4.4 and 4.7 lines in Figures 5.5 to 5.8.

As mentioned previously, if the instruments induce a large enough broadening, the modeling function to use is a Voigt function. Mathematically, the Voigt function is just the convolution product of a Lorentzian function with a normal distribution (see appendix H for more details about the numerical modeling). In Figure 5.9, m1 represents the peak location and m2 the scaling factor, the width factor having been fixed arbitrarily. In Figure 5.10, m1 represents the peak location, m2 the width factor, m3 the scaling factor. In both cases, the quality of the fit is much poorer than in the Lorentzian case.

As explained in appendix H, in the Lorentzian case the area under the curve is characterized only by the scaling factor. Therefore, when using the curve fitting analysis, the variations of the scaling factor (or sum of the scaling factor in the case of a double peak) were plotted in Figures 5.11 and 5.13. Figures 5.12 and 5.14 show the corresponding empirical analysis in order to compare the data reduction procedures. The results differ more in the case of high fluence level. This difference may be explained by the fact that the empirical

procedure doesn't subtract any baseline, therefore the higher the baseline the more the procedures will differ. In spite of these differences, the empirical procedure is still tracking the Lorentzian curve fitting procedure and is able to catch the trend for the variations of the data.

5.2 Experiments

All the information concerning the experiments has been collected in table I in appendix I.

5.2.1 Wavelength variation

The goal of the first set of experiments was to identify the most appropriate tuning positions of the laser to generate LIF spectra. This was done in two different ways.

a) Gain curve method

A spectrum corresponding to the spectral shape of the laser beam operating in the broad band mode was taken with the highest resolution grating (3600 groove/mm) (as explained in chapter 4). The positions of the O_2 absorption peaks were defined with the diodes corresponding to the minimum of each dip in the broad band curve (see Figure 5.15). Then, the laser was tuned in order to get a narrow band peak as close as possible to the previous diodes. For the P15 and P13 bands, the laser wasn't able to operate narrow band at the central position. The alternative solution adopted was to go a little further on either side to get a narrow band peak close to the center of the absorption peak. Some tests (W72Q and W72G) were run with the laser tuned next to the P15 peak. For almost all the rest of the data, the experiments were run with the laser tuned at the center of the P17 peak, where the laser had the best narrow band behavior.

b) LIF spectra observation

The second method used in complement to the previous one is simply based on looking at the spectra and deciding where the "best" LIF spectrum is. Criteria to judge the quality of the LIF spectra were: the height of the peaks, the height of the baseline, the respective strength

(or height) among the LIF lines. This approach showed that the P17 and the P15 peaks were generating LIF spectra of a higher quality, confirming the results from the previous method.

In the rest of this section, various spectra are described to show the changes in the spectral features when the laser wavelength changes. Figure 5.16 illustrates an example of a spectrum generated with a broad band laser beam which can be contrasted for instance with Figures 1.2 and 2.4. In the "broad band" spectrum case, there are no multiple peaks for any LIF line. The LIF peaks observed are the sum of the contribution of all the O_2 absorption lines encompassed by the gain curve of the laser. Therefore, each peak is composed of many narrow lines that are too close to be distinguished and that result in a broader peak. As mentioned in section 2.4, the presence of double or multiple peaks for each LIF line is a good indication of the nature of the operating mode of the laser. Figures 5.19 and 5.20 provide a good illustration of this point. Figure 5.19 shows an LIF spectrum taken with the laser tuned at 0.009 mm for the tuning knob of the center of the P15 absorption line, whereas Figure 5.20 shows the equivalent spectrum taken with the laser tuned at the center of the P15 line. Instead of improving the "quality" of the spectrum, tuning the laser right in the center of the absorption band has made the second spectrum look much more like a broad band LIF spectrum. The second spectrum is actually broad band due to the problem the laser has in operating narrow band exactly in the center of the P15 area (refer to section 3.1.1 for more details).

Figures 5.21a to 5.21h illustrate a series of 16 spectra. The tuning knob of the laser was moved by 0.001 mm among each spectrum. The object of this series is to show: 1) how quickly the spectral features are varying, and 2) how accurate the estimation can be of the excitation wavelength by looking only at the LIF spectra. The tuning positions of the laser were varied symmetrically with respect to the center of the absorption line P17 (which corresponds to a tuning position of 0.9245 mm). The tuning position is shown in the higher right hand side corner for each plot. The spectra at 0.925, 0.924 and 0.923 clearly show a "more classical" O_2 LIF

spectrum at room temperature. Figures 5.23 and 5.24 describe different areas of the tuning range than the one close to the O_2 absorption peak.

Figure 5.23 shows that, for some tuning positions, the four peaks predicted by the spectroscopic theory are more separated than when the laser is tuned on the P17 line. Figure 5.24 shows another interesting spectrum which is probably the emission spectrum of O_2^+. Figure 5.22 illustrates the small advantage of purging the laser beam path around the two cavities of the laser (operation referred to as internal purge in appendix I).

5.2.2 Stability- reproducibility of the LIF measurements

The object of these tests is to quantify the stability of the LIF measurements in order to validate the reproducibility of this technique. In order to do that, the experimental parameters (temperature, pressure, flow rate in the chamber and laser settings) were held as constant as possible. The major source of variation not controlled was the power of the laser (see Figures 3.3 and 3.4, the laser pulse to pulse energy fluctuations). The test files V72A, V72B, ...V72F each contain a series of 10 spectra, each spectrum resulting from the accumulation of 100 shots over 2 seconds. Each test was performed 10 minutes after its previous one. The file V72Sample, which is analyzed in Figures 5.11 and 5.12, is a sample of 10 spectra taken from one of the series B to F.

Figure 5.33 illustrates the analysis of the tests B, C, D, E and F with the empirical procedure. The test V72A was run with the beam path not purged with nitrogen (as it was for the other series), resulting in power and fluence levels lower by at least a factor of 3 compared to the tests B to F. It was expected that a power variation should result in an equivalent variation in percentage for all the peaks of the spectrum, thus scaling the spectra up or down. In practice, the signals appear to be correlated, but the correlation is not absolute in the sense that no simple scheme was found to be able to remove the power variation effect. This fact has a dramatic implication for the precision of the foreseen measurement using O_2 LIF.

The use of the Lorentzian curve fitting in place of the empirical procedures attenuates the variations observed with the empirical procedures. However, the computed values of the peak keep on changing by as much as 20% (see Figure 5.11), and again no simple scheme of data processing was found to reduce the amplitude of the variations.

The two following sections describe tests which explore the variability in the signal received, and the two last sections evaluate the impact of other factors on the signal.

5.2.3 Gas flow rate variation

This test establishes whether some depletion occurs in the test chamber. Any depletion of the oxygen molecules in the test chamber would affect the LIF spectra in a visible way. Increasing the air flow rate in the chamber increases the air displacement among two pulses of the laser, which reduces any potential depletion effect.

For this test, all the controllable experimental variables but the flow rate of the air inside the test chamber were held constant. The flow rate was varied from 0 to 40 scfh. The resulting spectra are presented in Figures 5.25, 5.26a and 5.26b. All these spectra look very similar, revealing no sign of a depletion problem, even with no flow inside the cell.

5.2.4 Power variation

The object of this test was to document the effect of a power variation in the laser beam. A change in the high voltage settings may result in a change in the locking efficiency of the laser (i.e. the proportion of the output power which is contained in the narrow peak). In order to avoid this spectral variation, two power variation schemes external to the laser were investigated.

a) Window insertion

The first solution to vary the power of the laser beam was to insert uncoated quartz windows on the path of the beam. Four windows of fused silica were used. They each decreased the output power by 9 to 10%. However, during the experiment they were

improperly placed after the cylindrical lens (instead of before). So the windows not only decreased the power by 10% but also shifted the focal point inside the chamber, which might have had a larger effect than the 10% decrease expected. Figure 5.27 shows the variation of the spectral shape of the laser taken with the 3600 g/mm grating positioned at the second order. The corresponding LIF spectra are shown in Figures 5.28a to 5.28d. They all look scaled down from one another. The decrease in the baseline level, when the power is lower, is proportionally larger than the decrease in the LIF lines.

For the test V75E7, all the windows were removed and the beam path was purged with nitrogen, resulting in a higher power beam. This spectrum represented in Figure 5.28e has a baseline almost twice as large as the spectrum with 0 window, with only a 30 % increase in the LIF peaks. Moreover, the shape of the spectrum (respective height among all the peaks) is altered: the 4.3, 4.4 and 4.5 LIF lines are increasing faster than the other lines.

Figure 5.29 shows the signals computed with the empirical procedures and Figure 5.30 shows the same signal scaled with themselves in the lower fluence level case. This representation shows which lines are most sensitive to power variation. Again the 4.3, 4.4 LIF and second order of O_2 Raman are increasing faster than the other lines.

b) Purge variation

The second scheme investigated consisted of taking a series of spectra and beginning to purge the path of the beam with nitrogen during the data acquisition. The nitrogen progressively flushes the air on the beam path, therefore reducing the absorption and resulting in an increase of power at the point imaged inside the chamber. Figure 5.31 illustrates the analysis of the spectra with the empirical procedures. Figure 5.32 represents the same parameters scaled by themselves. The results are consistent with those of the previous experiment.

The conclusion of these tests is that, after a given fluence level, some lines are more sensitive to the power variations than the others. The last two tests look at the impact of pressure and temperature on the LIF spectra.

5.2.5 Pressure variation

In this experiment, a series of 18 spectra was taken. The only externally controlled parameter varied was the pressure, which was increased by 0.1 b from 1.3 b to 3.0 b. The flow rate was readjusted to about 30 scfh for all the spectra. The pressure and flow rate were tuned by simultaneously adjusting the chamber air supply rate and discharge valve..

The accumulation of 18 spectra is represented in Figure 5.36. For more details, some individual spectra are represented in Figures 5.37a and 5.37b. The signal obtained from the spectra with the empirical data reduction is represented in Figures 5.38 and 5.39 (for the relative variations).

The same test was run with the laser tuned close to the P15 absorption line. Again, plots of the empirical analysis can be found in Figures 5.40 and 5.41. In the P15 and P17 cases, the results suggest that all the peaks present in the observed spectra are moving proportionally to one another.

5.2.6 Temperature variation

The objective of the last test was to establish the influence of temperature on the experimental spectra. The temperature was the only controllable parameter varied. The results of three heat tests are presented, spanning the temperature range from 28°C (82°F) to 128°C (263°F). Severe cavitation in the oil pump prevented running at higher temperatures. For the first test, V72H, Figure 5.42 presents the spectra at room temperature and at the highest temperature. Figure 5.43 shows the superposition of the 18 spectra taken during this run. The data obtained from the spectra with the empirical procedures are plotted in absolute variations, Figure 5.44, and relative variations, Figure 5.45. The relative variations plot shows that the three Raman peaks are decreasing, whereas the 4.3 and 4.4 LIF lines are slightly increasing and the other LIF lines are decreasing but more slowly than the Raman peaks.

W72F and W72G are two tests that were run the same day, and for which the laser was tuned at a wavelength corresponding respectively to the P17 and the P15 absorption peaks.

Unfortunately, the behavior of the laser wasn't stable and some problem with the cryogenic recirculation system provoked the large fluctuations observed in Figures 5.47 to 5.51. Figures 5.48 and 5.51, illustrating the proportional variations of the various lines, show results consistent with the previous test: the Raman peak tends to decrease and the LIF lines are either stable or slightly increasing.

Figure 5.52 represents the same data as Figure 5.44 corrected for the density fluctuations. The height of the peaks coming from all the spectra other than the first one were adjusted to the values they would have had if the density was the same density as for the first spectrum. For example, the values of all the peaks from the spectrum taken at 59°C were scaled by $\frac{273.15+59}{273.15+27}$, the ratio of the absolute temperature for this spectrum and for the reference spectrum taken at 27°C, in order to readjust them to the values they would have had if the densities had been the same for both spectra.

In Figure 5.52, the Raman peaks are relatively insensitive to temperature variation and the LIF peaks are all slightly increasing on average.

Figures 5.53 to 5.61 show the variations of the individual Raman and LIF lines with pressure and temperature in more detail. All the peaks respond almost linearly to a pressure variation. The O_2 and N_2 Raman peaks are decreasing when the temperature is increasing, but Figure 5.52 showed that this variation could be accounted for by the variations of density induced by the variations of temperature. The second order of O_2 Raman is corrupted with other signals since several peaks are present close to one another, whereas the spectroscopic theory predicts the presence of a unique peak due to the Raman shift. The additional peaks may be due to non linear processes previously mentioned. Therefore, the information given by the second order of O_2 Raman should only be considered cautiously for analysis.

O_2 LIF peaks 4.3 and 4.4 increase with the temperature up to 103°C and then decrease for higher temperatures. LIF peaks 4.5 and 4.8, illustrated in Figures 5.58 and 5.61, show a slight shift with the temperature variation. In both cases, the two major peaks decrease for an

increase of temperature but a smaller peak close to them has an opposite variation. LIF peaks 4.6 and 4.7 both decrease regularly for a rise in temperature.

Chapter 6

Conclusions and recommendations

6.1 Conclusions

In spite of the high variability in the energy levels, the experiments also showed some good agreement with the theory :

- the data shows a very good fit with the Lorentzian model
- the magnitude of the LIF signal is not very far from the expected one (appendix C)
- the general trends in the experiments are also in agreement with the theory
  - LIF and Raman peaks respond almost linearly to pressure variations
  - the Raman peaks are relatively insensitive to temperature since the observed drop can be accounted for by the density decrease (see Figure 5.52 with densities correction in the temperature sweep)
  - LIF lines were varying much less than the Raman peaks in absolute number for a temperature change. Therefore when the density effect is accounted for, the LIF appear to be sensitive to temperature changes.

However, unexplained variations in the energy levels computed from the experimental data could not be reduced. A shift in the laser wavelength could generate LIF spectra with different spectral shapes (the peaks would not keep the same proportions among themselves), which in turn would result variations in the energy levels. However, although the laser showed had

significant power output variations (± 20 % for shot to shot analysis), it had a stable behavior in terms of operating wavelength.

Other reasons for the variations the signal of the energy levels may be : a non completely adequate data processing and non linear phenomenon due to a too high fluence level. Reference [16] mentions a fluence level of 1.8 J/cm^2 as the limit in order to avoid non linear phenomenons. For most of the experiments, the typical energy per pulse used would be 15 to 20 mJ/pulse; for the focal volume computed in chapter 3, this would result in a fluence level of 135 to 180 J/cm^2. Even when accounting for uncertainties on the measurement volume, the fluence level used for the experiments is certainly above the stated threshold of 1.8 J/cm^2.

6.2 recommendations

• Reproduce the experiments with a lower fluence level. The limitation of the fluence level could be achieved by : - defocusing the laser beam inside the chamber

- imaging a point further away from the focal section
- occulting part of the laser beam
- using a cylindrical lens (review problems of spatial definitions)

• Improve the data reduction procedures in order to be able to fit more than 2 Lorentzian peaks.

• Reengineer the laser in order to avoid to get the dips in the gain curve.

References

[1] Annen K. "State Variable Diagnostic Studies" Feb 90

[2] Diskin G.S., Lengert W.R., Kuman V, Glesk I and Miles R.B. "Imaging of Molecular Hydrogen and Oxygen by Single and Two-Photon Fluorescence Using laser and flash lamp sources." *AIAA 91-0463*

[3] Laufer G., Fletcher D and McKenzie R. "A method for measuring temperatures and densities in hypersanic wind tunnel air flows using laser-induced or fluorescence" *AIAA 90-0626*

[4] Massey G.A. and Lemon C.J. "Feasility of measuring temperature and density fluctuation in air using laser-induced 02 fluorescence" *IEEEJ. Quantum. Electron. E-20454* (1984)

[5] McKenzie R. "Prayers in Laser-Spectroscopic techniques for aerodynamic measurements-an overview" *AIAA 91-0059*

[6] Miles R.B., Connors JJ., Howard P.J., Markovitz C.E. and Roth G.J. "Proposed single pulse two dimensional temperature and density measurements of oxygen and arh" *Opt. Lett 13, 195* (1988)

[7] Barrow G. "Introduction to Molecular Spectroscopy" *McGraw Hill* (1962)

[8] Herzberg G. "Spectra of diatomic molecules" *Van Nostrand Reinhold* (1930)

[9] McKenzie L.H., Nomson D.J. , Exberger R.S. "Time dependant local density measurement in unsteady flows" *NASA techn. Memo. 78555* (1978)

[10] Lee M.P., Hanson R.K. "Calculations of 02 absorbtion and fluorescence at elevated temperatures for a broadband Arf laser source at 193mm. *Opt.Lett. 12 75* (087)

[11] Gross K.P., McKenzie R.l., Logan R. "Measurements of temperature density, pressure and their fluctuations in supersonic turbulance using laser-induced fluorescence." *Experiments in Fluids 5.* (1987)

[12] Laufer G., McKenzie R.L., and Huo W. "Radiative process in an excited by an ArF laser" *Opt. Lett. 13 99* (1988)

[13] Laurendeau N.M. "Temperature measurements by light scattering methods" *Prog. Energy combust. Sci. Vol 1h* (1988)

[14] Laufer G., McKenzie R.L. "Temperature measurements in hypersonic air flows using laser induced O_2 fluorescence" *AIAA 88-4679 CP*

[15] McMillin B.K., Lee M.P.Paul P.H. and Hanson R.K." Planar Laser-induced fluorescence of Nitric oxide in a shock tube" *AIAA 89-4679-CP.*

[16] Fletcher D.G. and McKenzie R.L. "Simultaneous measurements of temperature and density in air flows using UV laser spectroscopy" *AIAA 91-0458*

[17] Smith M.S., Price L.L., Williams W.D. "Laser induced fluorescence diagnostics using a two line excitationmethod" *AIAA 92–0512*

[18] Born M. & Wolf E. "Principles of optics" *Pergamon Press* 1980

[19] Kingslake R. "Optical System Design" *Academic Press* 1983

[20] Möller K.D. "Optics" *University Science Books* 1988

[21] Hutley M.C. "Diffraction Gratings" *Academic Press* 1982

[22] Pitts D.R., Sissom L.P. "Heat transfer" Schaum outline serie *Mc Graw Hill*

[23] Krupenie P. "PThe spectrum of molecular oxygen" J.Phys>Chem.Ref.Data,Vol.1,N_{O2},1972

[24] Annen K. "Private Communications" -1992

[25] Ralston A., Rabinowitz P. "A first course in numerical analysis" *McGraw Hill*

Appendix A

Relation between solid angle and f number

If we consider a cone with a half angle a,

by definition : the solid angle generated by a is equal to the surface centered at O with a radius of 1 intercepted by the cone.

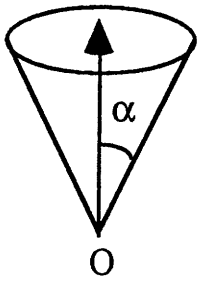

Expression of a solid angle :

the solid angle is given by : $SA = \iint_S dS$

with : $dS = rd\varphi \times r\sin\varphi d\theta$

$r = 1$

and : $\theta \in [0, 2\pi]$

$\varphi \in [0, \alpha]$

$$SA = \int_0^{\alpha} \sin\varphi d\varphi \int_0^{2\pi} d\theta$$

$$SA = [-\cos\varphi]_0^{\alpha} \times 2\pi$$

$$SA = 2\pi[1 - \cos\alpha]$$

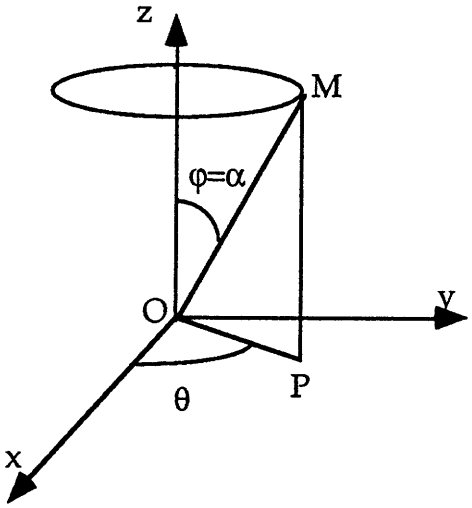

Expression of an f number :

$$\left.\begin{aligned} f_N &= \frac{h}{d} \\ \tan\alpha &= \frac{d/2}{h} \end{aligned}\right\} \Rightarrow \begin{cases} f_N = \dfrac{1}{2\tan\alpha} \\ \alpha = A\tan\left[\dfrac{1}{2f_N}\right] \end{cases}$$

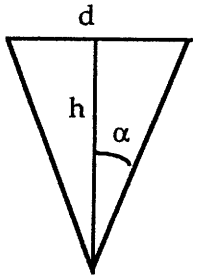

Conclusion :

$$SA = 2\pi\left[1-\cos\left[A\tan\left(\frac{1}{2f_N}\right)\right]\right]$$

$$f_N = \frac{1}{2\tan\left[A\cos\left[1-\frac{SA}{2\pi}\right]\right]}$$

$$\alpha = A\tan\left[\frac{1}{2f_N}\right]$$

Table A1 : Corresponding values of f number and solid angles.

f_N	1.0	3.0	4.0	5.0	6.0	7.0	8.0	10.0
SA (sr)	0.66	0.00854	0.00485	0.00311	0.00217	0.0016	0.00122	0.00078

Appendix B

Correction of the focal length of a lens according to the working wavelength

All the lenses through which light is propagating, are using a physical phenomenon called refraction. Snell's law, illustrated below, shows how refraction is sensitive to the refractive index of the medium involved.

Snell's law :

$$N_i \sin(i) = N_r \sin(r)$$

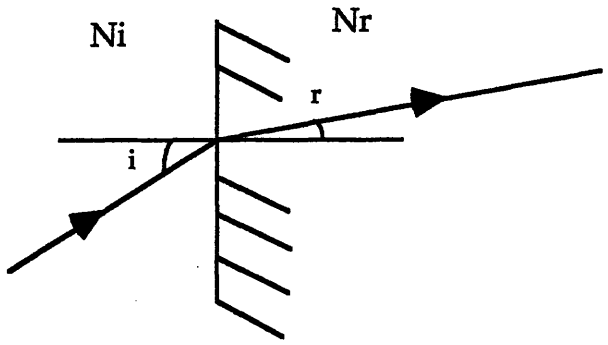

However, the refractive index of a medium varies in function of the wavelength of the light. Hence , the focal lengths tabulated in manufacturers catalogs for a base value of λ, have to be corrected.

The correction formula is : $f_\lambda = f_{base}\dfrac{(n_{base}-1)}{(n_\lambda-1)}$

Usually λ_{base} is close to yellow light (589 nm)

Table B gives the variation of refractive index of fused silica (material of lens used in this experiment).

Table B Refractive index of fused silica

l	185	195	200	220	250	300	400	500	589.3	600	800
n(l)	1.5749	1.5577	1.5505	1.5285	1.5075	1.4878	1.4707	1.4623	1.4584	1.4580	1.4533

Conclusion :

To get the working focal length at 193 nm of a fused silica lens for which the nominal focal length is given at $\lambda_{base} = 589.3nm$, the following correction must be made :

$$f_{193} = f_{base} \times \frac{(1.4584-1)}{(1.5611-1)} = 0.8170 f_{base}$$

Appendix C

Saturation and expected signal calculations

This appendix calculates the saturation conditions for the experimental set up used.

The values of the variuos constants interveening are listed here :

Speed of light : $c = 299742.4580 \pm 0.0012 * 10^3$ m/s
Plank's constant : $h = 6.62620 \pm 0.0005 * 10^{-34}$ J.s
Avogadro's number : $N = 6.02213 * 10^{23}$
Perfect gas constant : $R = 8.314$
Volume of 1 mole at normal conditions : 22.4 l (or dm^3)
Normal % of O2 in air : 21%

For the other variables, the following nomenclature is adopted :

E : energy of a laser pulse
N_P : number of photons per pulse
n : frequency of the laser light
λ : wavelength of the laser light
d_{O2} : density of molecules of oxygen
T : absolute temperature of the gas
P : total pressure of the gas
P_{O2} : partial pressure of oxygen
V : focal measurement volume
N_{O2} : number of molecules of oxygen inside the measurement volume
W : solid angle of light collection system
f_N : f number of light collection system
$\frac{d\sigma}{d\Omega}$: cross section of oxygenfor the P17 peak
h : quantum efficiency of the spectrometer
t : transmission of the optics
L : observed length

Saturation level

Number of photons input per pulse :

and : $$E = N_p h\nu = N_p h\frac{c}{\lambda}$$

therefore : $N_P = \frac{E \cdot \lambda}{h \cdot c}$

the working range for energy per pulse was 15 to 25 mJ
Assuming an energy per pulse of 20 mJ :

$$N_P = \frac{0.02 \times 193.2 \times 10^{-9}}{6.6262 \times 10^{-34} \times 2.9974 \times 10^{8}} = 1.94548 \times 10^{16} \text{Photons}$$

Number of oxygen molecules in the focal volume :

Focal volume : $V = 180 \times 65 \times 50 \mu m^3 = 5.85 \times 10^{-13} m^3$

density of oxygen : $d_{O2} = \frac{P_{O2} \cdot N}{R \cdot T} = \frac{0.21 \times P \cdot N}{R \cdot T}$

$$d_{O2} = \frac{0.21 \times 10^5 \times 6.022 \times 10^{23}}{8.314 \times (273.15 + 20)} = 5.18872 \times 10^{24} \text{atoms } /m^3$$

$N_{O2} = d_{O2} \cdot V$

so : $N_{O2} = 5.188718 \times 10^{24} \times 5.85 \times 10^{-13} = 3.0354 \times 10^{12}$

Solid angle :
the f number is imposed by the entrance f number of the spectrometer : 3.8

according to appendix A : $\Omega = 2\pi\left[1 - \cos\left(a\tan\left(\frac{1}{2 \times 3.8}\right)\right)\right] = 5.3694 \times 10^{-2} sr$

Number of photons absorbed :
For the P17 absorption peak, the absorption coefficient is equal to : $3.5 \times 10^{-2} cm^{-1} \cdot Atm^{-1}$
here assuming a pressure of O_2 of 0.21 bar and an observed length of 50 µm,
the total absortion coefficient is : $3.5 \times 10^{-2} \times 0.21 \times 50 \times 10^{-4} = 3.675 \times 10^{-5}$

therefore, the total number of photons absorbed is :

$$1.94548 \times 10^{16} \times 3.675 \times 10^{-5} = 7.1496 \times 10^{11} \text{photons}$$

Conclusion at the level of fluance used in the experiments, the ratio of number of molecules in the measurement volume to the number of photons emited is equal to : 4.24

Expected signal :

The O_2 LIF and O_2 Raman signals can be calculated using the following expression :

$$S = N_P \cdot d_{O2} \cdot \frac{d\sigma}{d\Omega} \cdot \Omega \cdot \eta \cdot \tau \cdot L$$

and : $$\frac{d\sigma}{d\Omega} = \text{Absorp Coef} \times \frac{1}{N_0} \times \text{efficiency} \times \frac{1}{4\pi}$$

the Absorption coefficient considered is : $3.5 * 10^{-2}$

N_0 is the density of oxygen molecules at normal conditions $N_0 = d_{O2}$ in # molecule / cm^3

$$N_0 = 5.18874 * 10^{18}$$

the quantum efficiency used in the literature is : $3.8 * 10^{-5}$

Hence : $$\frac{d\sigma}{d\Omega} = 0.035 \times \frac{1}{5.18874 \times 10^{18}} \times 3.8 \times 10^{-5} \times \frac{1}{4\pi} = 2.039 \times 10^{-26}$$

considering an optics transmission of 0.7
a quantum efficiency of the spectrometer of 0.1
an observation length of 50 µm

Plugging the numbers in the initial formula : S = 37941.2

S is here the expected signal per pulse

for the experiment done for the flow rate variation L65Y, the fluence level was about 18 mJ/pulse and the resulting count number for all the LIF lines was 38540 for 10 pulses (obtained by the initial procedures)

According to the previous calculation, the theoritical number of count should have been :
37941 * 0.18 / 0.20 * 0.70 * 10 = 239028 counts

conclusion : the observed LIF signal is lower by a ratio of 6 compared to the theoritical calculated level. However, a ratioo of 6 is really acceptable here given the uncertaintities existing on the constant used (absorption coefficient, quantum efficiency ...)

Appendix D

Optical design for turbomachinery temperature measurement

Before selecting and designing the apparatus used for the calibration tests, it is interesting to have a precise idea of the engineering requirement of the test rigs in which this technique will be used. A broad knowledge of the conditions to acquire data in the final configuration, is necessary to reproduce or to model these conditions for the calibration phase. Therefore, this appendix analyzes the setup for measurements in a turbomachine

D1 Specifications

The original specifications of this project based on temperature measurement for MACH number determination were :

- a spatial resolution of about 2% of pitch which translates in $1mm^3$ or less,
- a temporal resolution of 2% of blade passing
- an overall accuracy greater than 5%

Secondary considerations were: practical optical system (f/10 aperture), minimal optical complexity...

Geometry of System

Measurements are to be performed points between the blades of a wheel having a radius of R=10.072 in (R=255.8 mm) and holding 61 blades

the pitch at the base of the blades is given by: $P = 2R\sin\left(\frac{\alpha}{2}\right)$ with : $\alpha = \frac{2\pi}{61}$

Hence : $P = 2 \times 255.8 \sin\left(\frac{2\pi}{2 \times 61}\right) = 26.3mm$

The geometry of the blades is given in figure D.1 which is a planar representation of the base of the blades at scale 5.0. This figure is useful to :

1) show that in the throat area the minimum distance between two blades is about 10.6 mm

2) to be able to estimate the proportion of the fluorescence signal lost due to side reflections if an f number too small is used.

Figure D.2 shows how the height of the blades (45mm) is limiting the f number that can be used. If a smaller f number than the one illustrated in Figure D.2 were used, some rays on the external surface of the solid angle (which represents the light collection system) would intercept the vertical faces of the blades. Therefore, some part of the light in the collecting solid angle would be occulted by the blades. Figure 1.3 shows a three dimensional representation of the geometry of the previous elements in a turbomachinery.

Note : as it is more usual to use f numbers in optical design, most of the calculations will be done in terms of f numbers. However, appendix A establishes the link between f numbers and solid angles that are used to compute the fluorescence signal strength.

Table D.1 provides a more quantitative description of the occulting phenomenon for the throat section described above.

Table D.1 : limitation of the volume imaged in function of the imaging f number

f/ number	f	4.25	5	6	8.5
% of section imaged at mid height	$100\left[1-\frac{H}{2fd}\right]$	50	57.5	65	75
% of section imaged at blade bottom	$100\left[1-\frac{H}{fd}\right]$	0	16	29	50

Conclusion, in order to image a point without loosing part of the light in the collecting solid angle, if a f number of 4.25 is used, only one point (exactly in the middle of the blades) can be imaged at the base of the blades. Similarly, if an f number of 8.5 is used, half of the distance between the blades can be imaged at the base of the blades.

As illustrated in figure D.2, it is possible to improve the performance of the imaging system by slightly tilting the optical axis with regard to the wheel normal direction in order to image the extreme corner points.

Knowing that any decrease in the f number involves a reduction in the fluorescence signal strength due to an occultation of part of the collecting solid angle, one can quickly appreciate the advantage of tilting the optical axis to image any point between the blades. In this configuration :

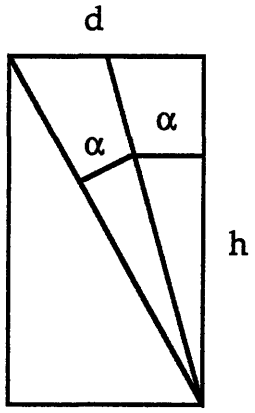

$$\tan 2\alpha = \frac{d}{h} \Leftrightarrow \alpha = \frac{1}{2} A\tan\left(\frac{d}{h}\right)$$

$$\text{and : } f_N = \frac{1}{2\tan\alpha} = \frac{1}{2\tan\left(\frac{1}{2} A\tan\left(\frac{d}{h}\right)\right)}$$

$$\text{Numerically : } f_N = \frac{1}{2\tan\left(\frac{1}{2} A\tan\left(\frac{10.6}{45}\right)\right)} \approx 4.3$$

Conclusion : with an f number equal to 4.4, any point between the blades can be imaged.

D2 Imaging system configurations

Given the severe constraints imposed by the geometry of the blades, only two set-ups were studied.

D2.1 Back scattering set-up

This set-up was used in the preliminary study (see ref [1]). The major problems involved with this set-up were related to the limitations of solid angles or f number that can be used to

image the interaction volume. Figure D.3 illustrates this set–up in the context of the experimentation performed. However, in order to be more clear, it enlarged the angles used. The actual f numbers used was of the order 9.5 and the difference of angle between the laser beam axis and the imaging solid angle axis was about 7 degrees. In this configuration, the rejection of straight light (from the laser beam) in the imaging cone was a serious problem.

D2.2 The coaxial set–up

This set–up is illustrated in figure 1.4. It will be referred as the coaxial set–up because in this configuration the laser beam has the same optical axis as the collecting optics. The fluorescence light can be collected with a much larger solid angle as before. However, the fluorescence close to the optical axis can't be collected because a solid angle around this axis is reserved for the path of the focused small laser beam.

In turbomachinery measurements, the constraints (mainly due to a required large object distance) are much more severe than the experimental case described above; this would lead to:

- the use of a larger f number and so a reduction of collected signal
- the same problems of straight light rejection

For these reasons the coaxial set-up was preferred to the back scattering one.

D3 Optimization of the configuration

The goal of this section is to choose the parameters remaining free in order to optimize the collection of the fluorescence signal. The existing constraints being:

- an object distance of at least 300 mm.(distance between measurement point and the first lens or mirror)
- an image distance (distance between last lens or mirror and image) of at least 50 mm.
- a reasonable working f number to avoid getting too large size optics.

• a spatial resolution of less than 1 mm^3.

D3.1 Optimization of the Imaged Volume at a Given f number

Figure D.4 illustrates the geometry of the imaged volume given the following simplifying assumptions:

a) the rectangular shaped beam is replaced by an equivalent circular shaped beam

b) along the length considered, the laser beam is supposed collimated

Hence for the volume considered the laser beam is equivalent to a cylinder with a spherical section. The volume imaged is then the volume contained between two solid angles of angle a_1 and a_2, and a cylinder of radius R_L. With the notations of figure D.4 :

$$\frac{V}{2} = \int_0^l \pi\left[(\tan\alpha_1 z)^2 - (\tan\alpha_2 z)^2\right]dz - \int_m^l \left[(\tan\alpha_1 z)^2 - R_L^2\right]dz$$

Or, after some algebra :

$$\frac{V}{2} = \frac{2\pi}{3} R_L^3 \left[l - f\frac{R_L}{R} \right] \qquad \text{(D.1)}$$

in terms of f numbers

$$f_N = \frac{f}{2R} \qquad \text{for the external cone}$$

$$f_{N'} = \frac{f}{2R_I} \qquad \text{for the internal cone}$$

$$V = \frac{\pi}{3}\left(\frac{l}{f_N'}\right)^3 \left[f_N' - f_N\right] \qquad \text{(D.2)}$$

and l=0.5 mm to have a spatial resolution of 1 mm.

For a given value of f_N, it is interesting to know whether there is a value of f_N' that maximizes V.

$$\frac{\partial V}{\partial f_{N'}} = \frac{\pi}{3} l^3 \left[-3 f_{N'}^{-4}\right]\left(f_{N'} - f_N\right) + \frac{\pi}{3}\frac{l^3}{f_{N'}^3}$$

$$\frac{\partial V}{\partial f_{N'}} = \frac{\pi}{3}\frac{l^3}{f_{N'}^4}\left(3f_N - 2f_{N'}\right)$$

$$\frac{\partial V}{\partial f_{N'}} = 0 \Rightarrow f_{N'} = \frac{3}{2} f_N \tag{D.3}$$

Furthermore,

$$f_{N'} < \frac{3}{2} f_N \Rightarrow \frac{\partial V}{\partial f_{N'}} > 0$$

$$f_{N'} > \frac{3}{2} f_N \Rightarrow \frac{\partial V}{\partial f_{N'}} < 0$$

Therefore, the value $f_{N'} = \frac{3}{2} f_N$ corresponds to maximum volume V_{Max}

$$V_{Max} = \frac{\pi}{3}\left(\frac{1/2}{3/2 f_N}\right)^3 \left[\frac{3}{2} f_N - f_N\right]$$

Conclusion :

$$V_{Max} = \frac{\pi}{162 f_N^2} mm^3 \tag{D.4}$$

D3.2 Choice for f_N

The expression of V_{Max} (D.4) shows that the smaller f_N, the larger V_{Max}. However, for the values of f_N smaller than 4.25 (= 45/10.6), part of the fluorescence signal is occulted by the top part of the blades and therefore lost. The previous remark applies in the most severe case: for points in the throat section and close to the bottom of the blades. So, in the most limiting conditions the two following phenomena with opposing effects are present:

1) V_{Max} increases when f_N gets smaller (equation(D.4))

2) When f_N gets smaller than 4.25, an increasing part of the fluorescence signal is lost due to the geometry of the blades.

In order to estimate the global effect of decreasing the value of f_N, graphical simulations were performed in which for each value of f_N the hidden or lost part of the fluorescence was estimated. Results of these tests are shown in table D.2

Table D.2 Effect of f_N decreases in the most limiting conditions (point in the throat section near blades bottom):

f number	f_N	4.25	3.0	2.5	2.0	1.5
Theoretical volume imaged	$V_T = \frac{\pi}{162 f_N^2}\left(in10^{-3}mm^3\right)$	1.07	2.15	3.10	4.85	8.62
Transmission efficiency	Eff. = part of V_T observed / V_T	100	75	62.5	54.2	39.5
Signal received	V_T* Eff. $\left(in10^{-3}mm^3\right)$	1.07	1.62	1.94	2.63	3.40

It is clear that when f_N decreases, V_{Max} increases more quickly than the efficiency is dropping. Therefore, the lower f_N, the stronger the fluorescence signal observed.

Note : It is important to be aware at this point that a choice for f_N will also imply a choice for R_L the dimension of the beam in the focal section. Since $f_{N'} = \frac{3}{2} f_N$, setting f_N will also set $f_{N'}$ and since $f_{N'} = \frac{f}{2R_I}$ with l=0.5mm the value R_L is linked to the one of f_N.

$$R_L = \frac{1/2}{2f_{N'}} = \frac{1/2}{2 \times \frac{3}{2} f_N} = \frac{1}{6f_N}$$

On the other hand, the size of the laser beam at the focal point is a function of the lens focal length used. For more details about these relations see section 3.1.1.3. So the choice for f_N is also connected to the choice of the lens used to focus the laser beam.

The previous conclusion is naturally even more true for measurement points not located in the throat section, because the geometrical constraints are then relaxed and the transmission efficiency is higher than the corresponding one in the throat section.

D3.3 Conclusion

The general conclusion of this section is that in order to obtain the maximum fluorescence signal with coaxial configuration, we should have:

1) $f_{N'} = \frac{3}{2} f_N$

2) f_N as large as possible with no limitation appearing from this preliminary calculation. A lower limit will be imposed on f_N by other engineering considerations (such as the size of the collection optics for instance) Too many simplifying assumptions were made to perform these preliminary calculations, to pretend that this conclusion will apply quite exactly to the real life configuration. However, the assumptions made were close enough to reality to think that the previous conclusions can be extended from the simplified case to the real life set-up. The following paragraph reviews the validity of these assumptions.

The first assumption (see section D3.1) referred to the shape of the beam at focal point. This question is the object of section 3.1.1.3. The most precise information from the laser manufacturer lead us to think that the focal section for the beam should have the shape of a rectangle or more realistically of an ellipse were the ratio of the 2 dimensions would be 3:1 . Figure D.5-a should give an idea of the presumed difference between the two cases. (see also figures D.6-a and D.6-b)

The second assumption referred to the shape of the contour lines of the laser beam along the propagation axis. Figures D.5b and D.5c show very schematically the difference of shape between a long and a short focal length lens. Clearly for a longer focal lens, the shape of the beam varies much less quickly than with a shorter one. Furthermore the spatial resolution which was fixed at 1mm in every direction will appear proportionally smaller with a long focal length less than with a short one. The conclusion is that this assumption is more relevant than a long focal length is used.

D4 Constraints of the imaging system

The imaging system is subject to three different sources of constraints:

• *On the object side:*

- the preceding section showed that the f number should be chosen as small as possible
- the requirement for a long object distance imposes the use of a relatively long focal length lens which involves a waist size for the laser beam on the order of 100mm. For example; a 500 mm lens at 193 nm results in a beam waist of 50x150mm. Therefore R_L=100 mm and $f_N = \frac{1}{6R_L} = \frac{1}{6 \times 0.1} \approx 1.67$

• *On the image side*

- the spectrometer chosen has an internal f number of 3.8 thus the image f number should be as close as possible to 3.8.
- The entrance slit of the spectrometer has a variable slit width from 10 μm to 3mm, but the smallest size results in a highest resolution. Hence it is preferable that the size of the image in the plane of the entrance slit would be of the order of 10 μm.

• *Chromatic aberrations considerations*

The last source of constraints for the imaging system comes from the fact that it is supposed to image the various peak of LIF of oxygen. Therefore a bandwidth of wavelength should be imaged from the emission point (focal point of the laser beam) to an image point in the entrance plane of the spectrometer. Appendix B explains how the use of a refractive lens using the refraction phenomenon leads to a spectral aberration (since each wavelength will be imaged at a different point).

The way to go around this problem is to use a two mirror system in a Cassegrain telescope configuration. Such a system reproduces the behavior of a lens using only reflection of light which is achromatic. (see Ref [18] p246)

D5 Proposed design of imaging system

This selection begins with a review of the constraints listed above and the trade–off necessary to make them compatible. Then a rough geometrical models of the design is proposed. In a third part, the software used for ray tracing the final design is described. Finally a simple design meeting the requirements is proposed.

D5.1 Trade–off considerations for constraints relaxation

It is unfortunately hard to conceive an optical system respecting the constraints described in section 4, because they lead to a magnification of 1/10 with a simultaneous ratio of f number :

$$\frac{f_{obj}}{f_{im}} = \frac{1}{2}.$$

Any traditional system would respect :

$$\frac{Object\_size}{f_{obj}} = \frac{\mathrm{Im}\,age\_size}{f_{im}} \qquad \text{(D.5)}$$

therefore any ratio $\frac{f_{obj}}{f_{im}}$ lower than 1 would lead to a magnification ratio higher than 1. Consequently, it is important to establish what constraints are of prime importance to make relevant trade–off .

The cost of modifying (in either way) the value of the imaging f number imposed by the internal f number of the spectrometer is high. Therefore, we will keep : $f_{im} = f_{spectro} = 3.8$

The object size is given by the specifications for the spatial resolution (of the order of 1mm). So, according to Eq D.5, the choice is now either to have a small image size which leads to a high f number for collecting the signal, or to have a collecting f number as high as possible which will lead to an image much larger than the minimal width (and so to a reduced resolution - see Appendix F)

Again, the choice is not too difficult to make since the cost in signal in raising the collecting f number is much higher than a reduced resolution due to a larger image impressed by a lower collective f number.

A reasonable trade off is to take a magnification ratio of one, associated to a larger size image.

In conclusion, the specifications for the following design are: a configuration of Cassegrain telescope, a magnification ratio of 1 and a collecting and imaging f number equal to 3.8.

D5.2 Geometrical Considerations

Ref [19] p. 258 mentioned a monocentric pair of spherical mirrors forming a Cassegrain telescope. It is this configuration that is modeled in this section. The following analysis is based on figure D.7. The variables involved are: a, D, k, R_1, R_2, e ,w_1, w_2

D and k are the fixed external working distances

a is the angle corresponding to an f number of 3.8

Assuming an monocentric configuration: $e = R_1 - R_2$

so the remaining unknowns are: R_1, R_2, w_1, w_2

looking at the triangle CM_2M_1: $\omega_1 - \omega_2 + \langle CM_1M_2 \rangle + \delta_1 = \pi$

looking at the triangle CM_2I : $\omega_2 + \langle CM_2I \rangle + \alpha = \pi$

furthermore, as : $\langle CM_1M_2 \rangle = \langle CM_2I \rangle$ so :

$$\omega_2 = \omega_1 - \alpha \tag{D.6}$$

Expressing a with the left triangle (light collecting cone) :

$$\tan\alpha = \frac{R_1 \sin\omega_1}{D + e - R_1(1 - \cos\omega_1)} \tag{D.7}$$

Expressing a with the right triangle (imaging cone inside spectrometer) :

$$\tan\alpha = \frac{R_2 \sin\omega_2}{k + e + R_2(1-\cos\omega_2)} \qquad \text{(D.8)}$$

Expressing that the point M_2 belongs to the mirror M_2 and the line M_1M_2 :

$$(R_2\cos\omega_2)^2 + \left[(R_2\cos\omega_2 - R_1\cos\omega_1)\tan(\omega_1+\delta_1) + R_1\sin\omega_1\right]^2 = R_2^2 \qquad \text{(D.9)}$$

Hence we have a system of four non linear independent equations which when solved numerically gives the value of all the variables. The conclusion is that: for a = 3.8, setting the value of two other variables (D and k, or D and w_1) allows us to get the dimension of the corresponding monocentric Cassegrain configuration. The next step in the optical design is to tune the geometrical dimensions to minimize the aberrations with a ray tracing program.

D5.3 Ray Tracing & Design

a) The software

The software used for the ray tracing part of this design was Oslo 3.0 from Sinclair Optics. This optical program includes standard commands and tools that can be used to solve a wide range of optical design problems. The description system of Oslo is based on a description of the various surfaces (geometric, and refractive index) that a beam of light is passing along its path. The input system can be rescaled in order to adjust values of the effective focal length or of the f number. For a given optical set-up, the program computes all the major variables and aberrations; among the parameters relevant for the system are:

- the focal length
- the working f number
- the gaussian image height
- the paraxial of Lagrange invariant
- the Petzval radius
- the transverse magnification of the system

Concerning the aberrations:

• the primary and secondary, axial and lateral chromatic aberrations are computed for all the surfaces

• the Seidel aberration given includes :

- the 3rd order spherical
- the coma
- the astigmatism
- the Pelzval blur
- the distortion
- the spherical aberration of the pupil

b) Proposed Design

The method used consisted basically in varying some design parameters in order to minimize the aberration generated. The starting analysis geometry was given by the previous geometrical analysis.

The specifications for this analysis were:

• to have a corresponding to an f number of 3.8

• to take D=400mm

• to take an existing shape of lens for the mirror M_2. The shape chosen was a plano-convex lens KPX208 from Newport radius R_2-206.09.

The parameters tuned from that configuration were:

1) e, the distance between M_1 and M_2, no more equal to R_1-R_2 as in the previous monocentric case

2) R_1, the radius of Mirror M_1

The result obtained and hereby proposed as the basis of a preliminary design is illustrated in Fig. (3.9-a) and (3.9-b). The calculated performance of this system were found to be very good:

collecting f number : 3.93

imaging f number : 3.8

obscure angle due to M_2 : f number of 6.59

The computed aberrations were :

spherical 3rd order =0.0 mm

coma : 0.8 mm

other aberrations : 0.0 mm

To give a comparison basis, the other configurations modeled had aberrations ranging from few micrometers to several hundred of micrometers!!

Appendix E

Generalities on Excimer lasers

Principle

Excimer lasers are lasers which are pulsed. (they generate beams of light only in pulses of short duration) and in which the light amplifying medium is a mixture of gas. The word excimer comes from a contraction of excited dimmer. If we consider a species A, the dimmer form of A is A_2 and the excited dimmer represents molecules of the dimmer of A in the excited state: A_2^*. The basic idea beyond the principle of excimer laser is to use excimer molecules having potential energy curve with no minimum for the ground level so that the ground state has a repulsive behavior allowing no stable ground state. By generalization, the excimer name has been given to any laser using molecules with no stable ground state (the molecules can be composed of different atoms as in the gas oxides or in monoholides cases, or they may not be diatomic). So excimer laser are a special case of vibronic lasers since they use transitions between vibrational levels of different electronic states. The most important properties of excimer lasers follow immediately from the principle exposed above.

Properties:

1) Since population inversion is easy to get (no ground state), excimer lasers can have high gain and be very powerful (pulses of 350J have been achieved with KrF)

2) Since no well defined rotational transitions exist, the emission of light is likely to be broader than in other lasers. This broad band characteristic along with the high gain allows for a tunable laser to be built.

3) Although excimer lasers are spanning the spectrum from green to UV, many of them are in the UV region providing new sources in the UV.

Major categories of existing excimer lasers

Many different categories of excimer lasers are existing now:

- Rare gas ex: Ar_2 —126 nm, Kr_2—146mm
- Rare gas oxides
- Rare gas monohalides ex: ArF-193 nm, KrF-248 nm, XeCl-308 nm

This class is the most popular one, providing high efficiency and high energy pulse commercially available lasers.

- triatomic gas
- metal vapor halide ex: HgI-443 nm

Excitation mechanisms for rare gas monoholides

The following description is a very simple one, which gives a feel for the mechanisms involved without getting into the complexity of reality. Rare gases are excited in order to form ions or excited atoms. These former categories interact with halogen molecules as follows:

$$Ar^* + F_2 \longrightarrow ArF^* + F \qquad \text{(E.1)}$$

$$M + Ar^+ + F^- \longrightarrow ArF^* + M \qquad \text{(E.2)}$$

It is interesting to note that the second reaction required an inert atom since the combination occurs via a three body collision process. This fact explains partly the actual mixture of gas used (see following chapter).

These reactions are easy and fast since the excited rare gas reacts as an alkali atom (reacting strongly with halogen). The resulting laser transitions are favored by a lifetime of the order of 10ns and a gain cross-section as large as $10^{-16} cm^2$. Very rapid quenching processes exist as well:

$$ArF^* + F_2 \longrightarrow Ar + 3F \quad \text{(E.3)}$$

$$ArF^* + Ar + Kr \longrightarrow Ar_2F^* + Kr \quad \text{(E.4)}$$

*Note that as the major property used of these lasers is their power, manufacturers include many modes, and as much as thousands of different modes may be included in the output beam. In these conditions, the shape of the beam is controlled by the geometry of the electrodes (more about the beam characteristics in section 4.1.3).

Appendix F

Spectrometer analysis

F1 Model

A model of the spectrometer is useful to have a better understanding of its behavior. Such a knowledge is useful to be able to optimize its performances by operating it more properly. The model of the spectrometer is quite simple and nevertheless it helps to explain the behavior of the spectrometer quite well.

As illustrated in figure F.1, the simple model includes an entrance slit, an imaging lens of focal lens f, a transmission grating of 1200 grooves/mm, a second imaging lens of focal lens x (the set-up of the SpectraPro being symmetrical, the two focal length are equal) and an imaging focal plane. Modeling the existing reflection grating, with a transmission grating doesn't generate any difference of behavior between the experimental monochromator and this model.

Application of the model on the analysis of the resolution

The following section analyzes the theoretical best resolution that can be obtained with a spectrometer corresponding to the model from figure F.1 and the impact of the entrance slit size on the spectrometer resolution.

Definition : The most commonly used criterion used for the resolution of spectrum lines is the Raleigh criterion. This criterion states that two lines are considered resolved if the main maximum of one line is positioned at the first minimum of the other line.

• Case of an ideal point source

According to reference [20] page 312, the diffraction pattern for a point source and a diffraction grating including N slits is given by :

$$u^2 = u_0^2 \frac{\sin^2\left[k\frac{d}{2}\sin\theta\right]\sin^2\left[Nk\frac{a}{2}\sin\theta\right]}{\left(k\frac{d}{2}\sin\theta\right)^2 \sin^2\left[k\frac{a}{2}\sin\theta\right]} \qquad \text{(F.1)}$$

where : $k = \frac{2\pi}{\lambda}$ is the wave or propagation vector

u_0 : amplitude wave

N : number of slits

d : width of slits

a : distance between two slits, also called periodicity constant

q : angle of diffraction

L = Na : grating width

In the small angle approximation represented figure (F.2b) : $\frac{Y}{X} = \sin\theta$

For the function described in equation (F.1), the main maximum and its closest minima are separated by : $\frac{Y}{X} = \pm\frac{2\pi}{kNa} = \pm\frac{\lambda}{Na}$

Hence, applying the Raleigh criterion in this case , the resolution limit is equal to: $Y = \frac{\lambda X}{Na}$

If the dispersion at the output is a nm/nm, then the resolution limit in terms of wavelength is :

$$resolution = \alpha\frac{\lambda X}{Na} = \alpha\frac{\lambda X}{L} \qquad \text{(F.2)}$$

• Case of a slit source

We consider a size h at focal distance from the imaging lens before the grating . Then the angles introduced by the size of the slit on both sides of the optical axis are equal to θ. (see figure.F.2) The resulting deviation angles after the grating are again equal to θ. on both sides of the optical axis.

According to Möller Ref [20], in the small angle approximation:

$$\frac{Y}{X} = \sin\theta = \theta$$

Therefore, the spread due to the slit size is : $Y = 2\theta X$

and as : $\theta = \frac{h/2}{f}$

$$H = \Delta Y = \frac{hX}{f} \qquad \text{(F.3)}$$

However as seen before the resulting diffraction pattern from a point source through a grating is given by equation (F.1) So the resulting pattern from the diffraction of an illuminated slit of size h is given by the convolution of the 2 following functions :

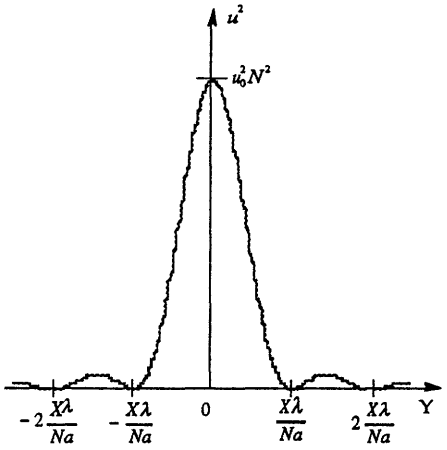

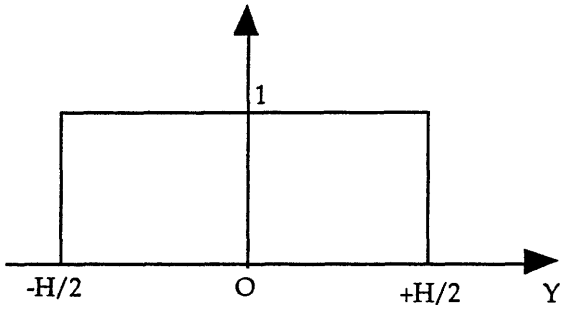

For simplification, the first function has been approximated as follows :

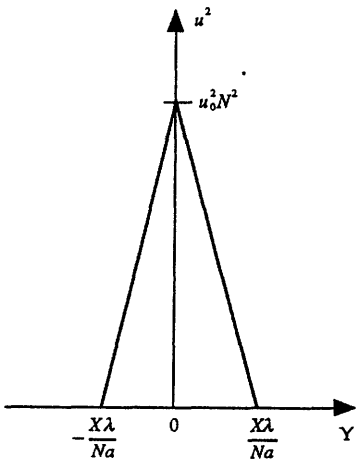

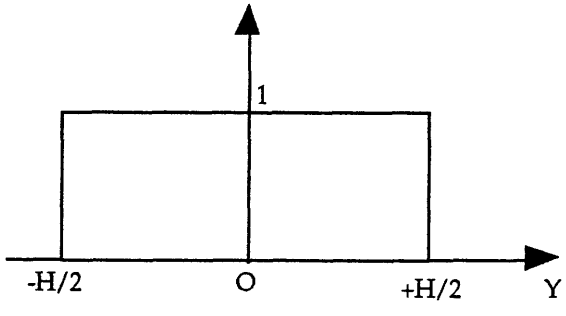

Mathematically :

$$f(Y)=\begin{cases}1-Y\Big/\dfrac{\lambda X}{Na} & 0\le Y\le\dfrac{\lambda X}{Na}\\ 0 & \dfrac{\lambda X}{Na}<Y\end{cases}\qquad g(Y)=\begin{cases}1 & -\dfrac{H}{2}\le Y\le\dfrac{H}{2}\\ 0 & elsewhere\end{cases}$$

and f even

the convolution product is then: h = f * g.

$$\text{or : } h(x)=\int_{-\infty}^{+\infty}f(x-y)g(y)dy$$

After integration : $\begin{cases} h(x)=C & 0<x<\dfrac{H}{2}-C \\ h(x)=\left(\dfrac{H}{2}-x\right)\left(1-\dfrac{x-H/2}{2C}\right) & \dfrac{H}{2}-C<x<\dfrac{H}{2}\end{cases}$ and h is even

with : $C=\dfrac{\lambda X}{Na}$

hence the shape of the convolution function is

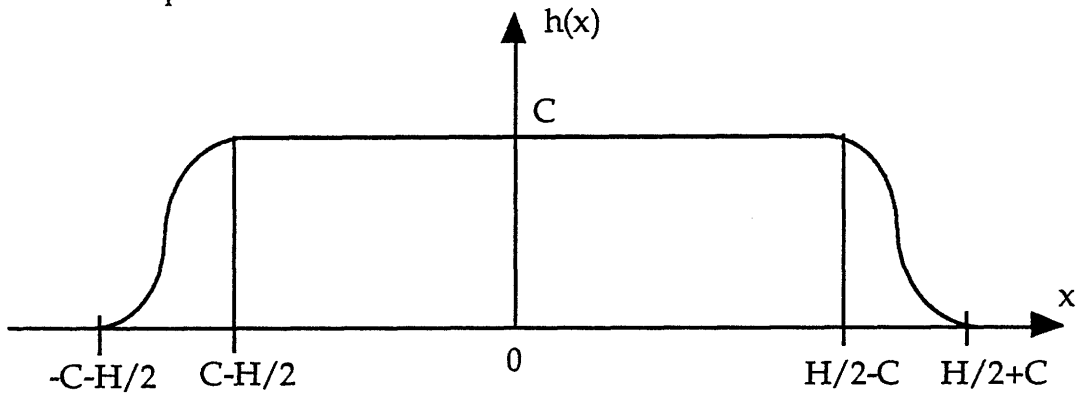

Applying the Raleigh criterion in this case gives a limit of resolution of H, hence for a dispersion of : $\alpha^{nm}/_{mm}$, the spectral resolution is:

$$\text{Spectral resolution} = \alpha H = \alpha\frac{Xh}{f} \qquad \text{(F.4)}$$

For a configuration where x =f , then the spectral resolution for a slit of size h is simply αh.

Remark : Due to the symmetrical configuration, the SpectrPro is such that x=f (the two spherical mirrors used are identical.)

Conclusion : the resolution limit that can be obtained from the diffraction pattern of a slit of size h is given by:

$$\text{resolution limit} = \alpha X \frac{\lambda}{L} + \alpha h \qquad \text{(F.5)}$$

Application to SpectraPro with a grating of :

1200g(nm 0)x=3nm/mm

x = f = 0.275 m

L = 25 mm

l = 200 nm

Table F.1: Resolution limit of SpectraPro in function of the slit size

(Resolution limit for point source $\alpha X \frac{\lambda}{L}$ = 0.0066 nm)

Slit size	Slit size impact on resolution	Total resolution limit
10 mm	0.03 nm	0.10 nm
100 mm	0.3 nm	0.37 nm

The previous results are in good agreement with specifications listed by Acton Research.

F2 Relation between resolution and Signal/Noise Ratio

Having established the relation between the entrance slit size and the resolution, it is now interesting to look at the influence of the resolution on the signal to noise ratio. In order to estimate the amplitude of the signal and its variations we computed the proportion of the signal that goes on the diode is the central diffraction line. Two extreme configurations have been studied:

1) the central diffraction line falls right in the middle of one diode

2) the central diffraction line falls between two diodes.

As illustrated in figure F.3a, the general diffraction pattern is proportional to a function of the following form: $f(\theta) = K\left[\frac{\sin\theta}{\theta}\right]^2$. Figure F.3b illustrates the two cases described above.

If Y represents a physical length in the focal plane, then: $Y = \frac{\delta\theta}{\pi\alpha}$ (F.6)

where : α is the resolution limit (in nm)

θ is the angular argument

α is the nominal dispersion(in nm/mm)

The energy received by a given diode can be computed by adjusting the integration limits

the width of a diode is : d = L/N

where L is the focal plane width

N is the total number of diodes.

Then in the configuration #1 the light signal S_1 received by the central diode is given by:

$$S_1 = \int_{-\frac{d}{2}}^{\frac{d}{2}} K\left(\frac{\sin\left(\frac{\pi\alpha Y}{\delta}\right)}{\frac{\pi\alpha Y}{\delta}}\right)^2 \cdot \frac{\pi\alpha}{\delta} dY$$

$$S_1 = 2\int_0^{\frac{d}{2}} K\left(\frac{\sin\left(\frac{\pi\alpha Y}{\delta}\right)}{\frac{\pi\alpha Y}{\delta}}\right) \cdot \frac{\pi\alpha}{\delta} dY$$

$$S_1 = 2K\int_0^{\frac{\pi\alpha d}{2\delta}} \left(\frac{\sin\theta}{\theta}\right)^2 d\theta$$

in configuration #2, the integration limits are moved to 0 and d, so :

$$S_2 = \int_0^d K \left(\frac{\sin\left(\frac{\pi\alpha Y}{\delta}\right)}{\frac{\pi\alpha Y}{\delta}} \right)^2 \cdot \frac{\pi\alpha}{\delta} dY$$

$$S_2 = 2\int_0^{\frac{\pi\alpha d}{\delta}} \left(\frac{\sin\theta}{\theta} \right)^2 d\theta$$

in both configurations, various slit sizes will be considered and the results will be expressed in percentage of the base case in which the slit size is minimum=10 μm and the resolution is 0.1 nm. Figure F.3c illustrates how varying the resolution affects the integration limit and therefore, the quantity of light received by the central diode.

Tables F.2a and F.2.b give the results of the calculation and figures F.4a and F.4b shows the plot of the variation of % of light received by the central diodes (compared to the base case) in both configurations.

The previous calculations assume that the total amount of light collected is the same for various sizes of the entrance slit, which is obviously not the case in this experiment. The theoretical results have therefore been corrected by assuming that the light collected is roughly proportional to the slit size (this fact has been checked experimentally, see figure F.5. So the last columns of tables F.2 a and b compare the total light collected by the central diode in function of the opening of the slit.

Table F.2a Light collected by central diode in configuration #1

slit (mm)	Resolution (nm)	$A = \frac{\pi d}{2\delta}$	S_1/K	% (/base)	S_1/K *Dsize	% (/base)
10	0.1	1.150	1.996	100	1.996	100
20	0.13	.885	1.626	81.4	3.252	163
30	0.16	.719	1.358	68.1	4.074	204
40	0.19	0.606	1.162	58.3	4.648	233
50	0.22	0.523	1.014	50.8	5.07	254
60	0.25	0.460	0.889	45	5.334	267
70	0.28	0.411	0.806	40.4	5.642	283
80	0.31	0.371	0.732	36.6	5.856	293
90	0.33	0.349	0.688	34.4	6.192	310
100	0.37	0.311	0.614	30.8	6.14	307

Table F.2b Light collected by central diode in configuration #2

slit (mm)	Resolution (nm)	$A = \frac{\pi d}{\delta}$	S_2/K	% (/base)	S_2/K *Dsize	% (/base)
10	0.1	2.301	1.391	100	1.391	100
20	0.13	1.770	1.286	92.5	2.572	185
30	0.16	1.438	1.157	83.2	3.471	249
40	0.19	1.211	1.035	74.4	4.14	298
50	0.22	1.045	0.929	66.8	4.645	334
60	0.25	0.920	0.839	60.4	5.034	362
70	0.28	0.822	0.763	54.9	5.341	384
80	0.31	0.742	0.698	50.2	5.584	401
90	0.33	0.677	0.643	46.3	5.787	416
100	0.37	0.622	0.595	42.9	5.95	428

Conclusion : Tables F.2 show that when the size of the slit increases, the signal is spread more and more. Therefore if the intensity of light collected was the same for any opening, the signal received by the central diode would decrease when the slit is opened (see columns #4 and #5 and figure F.4a). However, as the amount of light collected grows with the size of the slit, opening the slit at least from 10 to 100 μm results in an enhancement of the signal collected by the central diodes and therefore an expected improvement in the signal to noise ratio (see columns #6 and #7 and figure F.4b).

F3 Relation between diode number and wavelength

The light dispersed by the grating is collected by the array of intensified detectors. Therefore, the spectra received in the computer are expressed in terms of diode numbers. The most common way to relate diode number to effective wavelength is to recognize characteristic spectral features (for which the wavelength is known) and to use this information to make a linear regression between wavelength and diode number. However, a deeper understanding of the behavior of the spectrometer, allow to establish a more accurate correlation between wavelength and diode numbers than the previous linear relation. The goal of this section is to establish such a correlation.

In the following analysis:

d is the period of the grating

m is the order of diffraction (integer)

λ is the wavelength

α the incident angle

β the diffracted angle

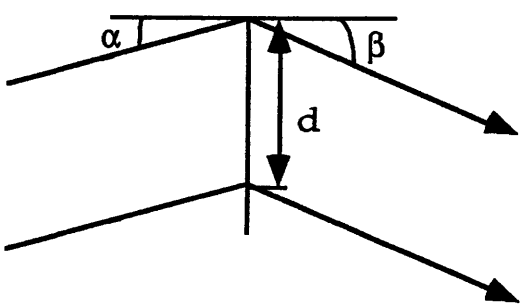

As mentioned previously, reflection and refraction grating have the same behavior and can both be modeled with the present model. The general equation of the grating expresses that the difference for the length of path for light propagating through the slits of the grating is an integer number of wavelength:

$$d(\sin\alpha + \sin\beta) = m\lambda \tag{F.7}$$

When a value for λ is chosen, a position of the spectrometer is set such that the point corresponding to $\beta = 0$ is in the middle of the variation range (see following illustration)

in theory :

$$\beta_{max} = -\beta_{min}$$

$$D_{ref} = \frac{D_{max} + D_{min}}{2}$$

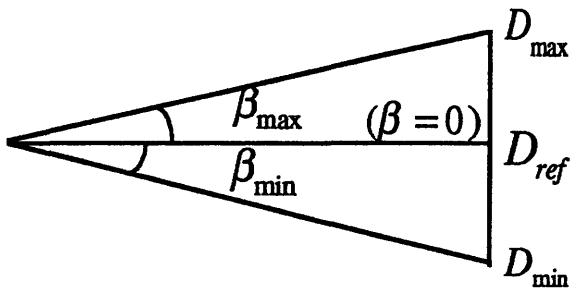

In practice, there might be an offset between the diode corresponding to the position set for the spectrometer D_{ref} and the middle diode of the array. This offset varies with the position set for the spectrometer.; it is illustrated in the following figure :

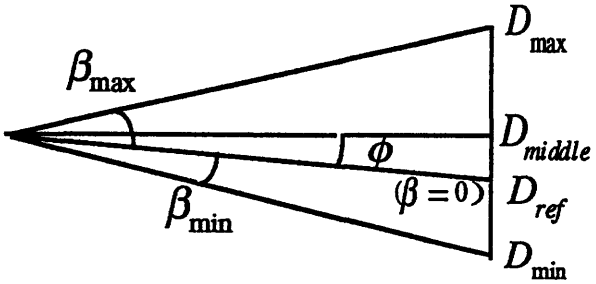

The real diffraction pattern can be deduced from the theoretical one (where D_{ref} is in the middle of the focal plane) by a projection of an angle f.

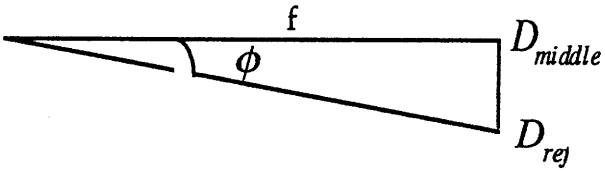

$$\cos\phi = \frac{Y_{th}}{Y_{real}} \qquad \text{(F.8)}$$

$$\tan\phi = \frac{\left(\frac{D_{ref} - N/2}{N}\right)W}{f} \qquad \text{(F.9)}$$

with : N = Number of diodes

W = width of focal plane

f = focal length of spectrometer

For any diode of t he array : $D_{\#} - D_{ref} = Y_{real} = \frac{Y_{th}}{\cos\phi}$

So $$D_{\#} - D_{ref} = \frac{f\tan\beta}{\cos\phi} \qquad \text{(F.10)}$$

And from(F.7) : $$\beta = Arc\sin\left[\frac{m\lambda}{d} - \sin\alpha\right]$$

Hence

$$D_{\#} = D_{ref} + \frac{f}{\cos\phi}\tan\left[Arc\sin\left(\frac{m\lambda}{d} - \sin\alpha\right)\right]\frac{N}{W} \qquad \text{(F.11)}$$

$$\lambda = \frac{d}{m}\left[\sin\alpha + \sin\left(Arc\tan\left(\frac{\left(D_{\#} - D_{ref}\right)\frac{W}{N}\cos\phi}{f}\right)\right)\right] \qquad \text{(F.12)}$$

in (F.12), D_{ref} and f are still unknown. The following steps explain how to find them.

- By definition, when $l = \lambda_{ref}$ then $\beta = 0$.

  So according to Equation (4.12), $$\alpha = Arc\sin\left(\frac{m\lambda_{ref}}{d}\right)$$

- In practice, the angles used are very small, so : $$\sin\theta \approx Arc\tan\theta \approx \theta$$

  Therefore, a close approximation (specially in the middle of the variation range) of λ and D_{ref} can be found by a linear interpolation.

In summary, the following procedure describes the steps to take to know precisely λ :

1) identify the LIF features

2) use a linear interpolation to define D_{ref}

3) compute the value of f from equation (F.9)

4) apply equation (F.12) to find l(D#) with :

   m = 1 (the grating is using the first order of diffraction)

   d = 1/1200 for the grating mostly used of 1200g/mm

   f = 0.275 m specification of spectrometer

   N = 1024 number of diodes in the array

   W = 24 mm width of the focal plane

Notes

1) The specified width of the focal plane from SpectraPro is 25mm. However this value input in (F.12) didn't give a good agreement with the linear regression, whereas the 24mm value showed an excellent agreement with experimental data (see after). It is not clear whether the width of the array of diodes was 24mm or if for some other reason only 24 mm of the diode array could be used.

2) It is assumed that the spectrometer has a good repeatability—setting it to a given wavelength should lead to the same value of D_{ref}, a, f etc... So that the analysis to compute these values has not to be performed for each spectrum.

Example of application of (F.12)

This analysis refers to the file W31R4

Step 1 illustrated on spectrum.of Figure 1.2 (see table 2.2 to know wavelengths of LIF)

Step 2 knowing that the spectrometer was set up at λref = 234 nm

Using LIF 4.6 and 4.7 gives Dref = 549.901

Using LIF 4.5, 4.6, 4.7, 4.8 gives Dref = 549.918 with a correlation coefficient of r=0.99999917 !

so the value taken was : Dref = 550

Step 3

$$\phi = Arc\tan\left(\frac{\frac{550-512}{1024}\times 24}{275}\right) = 0.1933°$$

$$\alpha = Arc\sin\left[\frac{1\times 234.10^{9}}{1/1200\cdot 10^{-3}}\right] = 16.308°$$

Step 4: application of equation (F.12)

$$\lambda = \frac{1}{1200}\left[0.2818 + \sin\left(Arc\tan\left(\frac{(D\#-550)\,24/1024\cos(0.1933)}{275}\right)\right)\right]$$

All the linear regression runs for the different experimental Spectra have shown a correlation coefficient very close to one (typically higher than : 0.999) confirming the specification stating that the deviation from a linear answer is less than 0.1 %.

Conclusion :

An analysis based on the general grating equation gives a formula correlating the diode number to the spectral position which is in very good agreement with the experimental data. Given the high linearity of the detector, a simpler linear regression using the LIF features can be used

without loosing much precision. In the procedures written to process experimental spectra, the more precise equation F.12 was used.

Appendix G

Design of the testing cell

G1 Heat transfer calculations

a) General theory

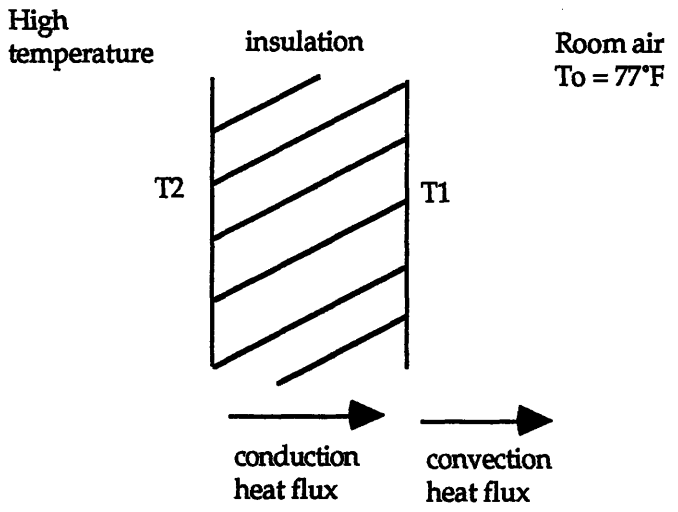

Statement of the problem:

At the steady state, the thermal flux (heat exchanged) is equal to both the conduction and the convection flux.

• Conduction

$$\phi_{cond} = \frac{k_{insul} A (T_2 - T_1)}{thickness} \qquad (G.1)$$

• Convection

$$\phi_{conv} = A\bar{h}(T_1 - T_0) \qquad (G.2)$$

and :

$$\bar{h} = \frac{k}{L}\overline{N_u} = \frac{k}{L}C(G_r P_r)^a \qquad (G.3)$$

according to reference [22] :

in the laminar case, $10^4 \le G_r P_r \le 10^9$ $C = 0.54$ and $a = 1/4$ (G.4)

in the turbulent case, $10^{94} \le G_r P_r \le 10^{12}$ $C = 0.13$ and $a = 1/3$ (G.5)

G_r and P_r being defined as follows :

P_r Prandtl number $$P_r = \frac{\nu \rho c_p}{h} \qquad (G.6)$$

G_r Grashof number $$G_r = \frac{g\beta(T_s - T_\infty)L^3}{\nu^2} \qquad (G.7)$$

with the following nomenclature :

n kinematic viscosity	cst	m^2/s
r specific gravity	kg/m^3	lb/ft^3
c_p specific heat	J/kg.K	BTU/lb.F
k conduction coefficient	W/m.K	BTU/hr.ft.F
T_i absolute temperatures	°K	°F
g acceleration of gravity	m/s^2	ft/s^2
L diameter of tube	m	in

b coefficient of volume expansion, for ideal gas :

$$\beta = \frac{1}{v}\left(\frac{\partial v}{\partial T}\right)_p = \frac{1}{T}$$

The various parameters in the convection equation (G.2) are estimated for air at an average temperature : $T_m = \frac{T_1 + T_0}{2}$

The only unknown in equations (G.1) or (G.2) is T1. The value of T1 is calculated by expressing that $\phi_{cond} = \phi_{conv}$ However, as some parameters in (G.2) are function of the temperature T1 some iterative calculation may be required. After each stage, the assumption laminar or turbulent should be checked by computing the value of the product GrPr

In the laminar case $\phi_{cond} = \phi_{conv}$ leads to :

$$\frac{k_{insul}}{thickness}(T_2 - T_1) = 0.54\left[\frac{g\rho c_p k^3}{\nu L}\frac{T_1 - T_0}{T_1}\right]^{\frac{1}{4}} \qquad (G.8)$$

Initially, a value of Tm is guessed, and the variables corresponding to this values are input in equation (G.8). Solving equation (G.8) (or the corresponding equation for the turbulent case) gives a value of $T_1(1)$ which allows to compute a new value of Tm, and then iterate the previous steps. This iterative procedure can be stopped when its convergence is good enough (in practice after the second or third loop).

Knowing T_1, it is easy to compute the heat flux with (G.1) or (G.2). This analysis will be applied in the rest of this section to main sources of heat losses in the system described in section 3.3 :

- the quartz windows
- the heat to warm up the flowing air
- the lines of oil
- the tank of oil
- the cell and nipples

b) losses analysis

Window losses

hypothesis : fused silica window $k_{wind} = 1W/m.K$

Diameter : 1 1/4", thickness : 1/4"

T_{max} : 550 °K

result : $\phi_{window} = 9.07W$

Heat in Dissipated Air Flow

$$\phi_{air} = mc_p\Delta T = \rho Q_{air} c_p \Delta T$$

resullts in : $\phi_{air} = 0.3026 Q_{air}$ with ϕ_{air} in W, Qair in l/s and X in mm
$\phi_{air} = 0.0726X$

X is the value of the air displacement between two shots defined in section3.3.2.2.

Lines Losses

hypothesis : asbestos used for insulation $k_{asbestos}$ = 0.22 W/m.K @ 400°K

insulation thickness : 1"

lines of 1/2" of diameter - 8 m long

result : $\phi_{lines} = 577W$

Tank Losses

hypothesis : cylindrical tank, diameter = 300 mm, length = 550 mm

insulation : 2" of asbestos

result : $\phi_{tank} = 446W$

Cell & Nipples Losses

hypothesis : the cell and nipples were replaced by an equivalent volume for simplification;

this volume was a straight tube of diameter 2" and of length 11.5"

insulation : 1" of asbestos

result : $\phi_{cell} = 85W$

Total Losses:

The heat losses due to the heat used to warm up the air are very low in comparison to the other sources of losses, so they are neglected for this total. Because of a high level of uncertainty, a "safety" coefficient of 20% has been added to the total looses, therefore the total loss level considered in the following is 1.2* 1117 = 1340 W.

c) Thermal Performances of the System

The most appropriate time to perform the temperature measurement with the laser, was when the temperature of the system was the most steady. The experience from similar experiments showed that for this configuration the best measurement time would be when the electrical heater would be turned off and the thermal fluid would circulate. The thermal fluid would then spread the heat losses over the whole circuit, therefore incorporating the large thermal inertia of the volume of Downtherm G in the tank. Consequently, the cooling rate for the system with circulating oil was of prime interest.

Cooling Rate:

The thermal capacity of 1 gallon of Downtherm G is equal to :

@ 75°F th. cap. 1 = $0.13368\,{}^{ft^3}/_{gal} \times 69\,{}^{lb}/_{ft^3} \times 0.4536\,{}^{kg}/_{lb}\,1623.4\,{}^{J}/_{kg.K} = 6792.3\,{}^{J}/_{K}$

@ 550 °F th. cap. 1 = $7388\,{}^{J}/_{K}$

The thermal capacity of 1 pound of steel is equal to :

th. cap. 2 = $0.4536\,{}^{kg}/_{lb} \times 0.10\,{}^{BTU}/_{lb.F} \times 4184\,\frac{{}^{J}/_{kg.J}}{{}^{BTU}/_{lb.F}} = 189.79\,{}^{J}/_{K}$

For the system, which includes 13 gallons of Dowtherm G and about 60 pounds of steel, the total thermal capacity is : 13 * 7000 + 60 * 190 = 102400 J/K

Equation (G.9) expresses that the energy lost by the system corresponds to the heat flux :

$$P \times t = \Sigma mc_p\,\Delta T \qquad \text{(G.9)}$$

where : P is the total power loss

t is the time

Σmc_p is the total thermal capacity

ΔT is the average temperature difference

So : $$\frac{\Delta T}{t} = \frac{P}{\sum mc_p}$$

Numerically : $\frac{\Delta T}{t} = \frac{1340}{102400} \approx 0.013 °K/s$

Which is a cooling rate of 1°K every 76 second.

Experimentally, a cooling rate of 1°K per two minutes was observed. Various factors may help to explain that the experimental rate was 58% slower than the computed one.

1) the experiments were performed in a lower temperature range than the one considered for the calculations

2) thermal capacity was underestimated

3) heat losses were overestimated and computed in the worse case (highest temperature)

A second interesting performance of the apparatus was a measure of the maximum difference of temperature for the fluid inside the cell (since this system was designed to keep the temperature very stable in the testing cell).

Maximum difference of temperature in the cell:

As : $m_{oil} = \rho_{oil} Q_{oil} t$

Applying equation (4.26) to the cell and neglecting the thermal capacity of the steel mass, gives :

$$P_{cell} = \rho_{oil} Q_{oil} c_{p_{oil}} \Delta T$$

Hence :

$$Q_{oil} = \frac{P_{cell}}{\rho_{oil} c_{p_{oil}} \Delta T} \qquad (G.10)$$

Conclusion : to have a difference of temperature of one °K maximum in the oil flowing inside the cell and nipples, a minimum flow rate of 0.0524 l/s or 0.83 GPM is required.

The last thermal property of the system looked at here is time necessary to raise the temperature of the system.

Warming Time

Neglecting the thermal losses :

$$P_{source} \times t = \sum mc_p \Delta T$$

$$t = \frac{\sum mc_p \Delta T}{P_{source}} \qquad (G.11)$$

Example : if a heater of 1 kW was chosen, then the warming time would be at least :

$$t \geq \frac{102400 \times 250}{1000} = 25600s = 7^h07'$$

G2 Pressure Losses Calculations

The hydraulics system is modeled by 5 m of 1/4" tubing in series with 22 m of 1/2" tubing

Applying the formula form Dancy Weisbach:

$$\Delta h = f\frac{LV^2}{2dg} \qquad (G.12)$$

Results in : $\Delta P = 15.47\, Q^2$ (G.13)

with ΔP in psi

Q in GPM

So for $\Delta P = 50$ psi, $Q = 1.80$ GPM

Appendix H

Lorentzian and Voigt distribution

H1 Lorentzian distribution

The theoretical Lorentzian distribution is characterized by :

$$P_L(x,\mu,\Gamma) = \frac{1}{\pi}\frac{\Gamma/2}{(x-\mu)^2 + (\Gamma/2)^2}$$

where : μ is the location of the maximum

Γ is the band width

As for any probability distribution : $\int_{-\infty}^{+\infty} P_L(x,\mu,\Gamma)dx = 1$

Model used for the curve fitting for the Raman peaks :

$$y = c\frac{b}{(x-a)^2 + b^2} + dx + e$$

where : a is the location of the maximum

b is the half band width

c is a scaling coefficient

d is the slope of the base line

e is the height of the base line at the origin

Some curve fitting procedures require to specify the partial derivatives of the modeling function with respect to the modeling parameters, therefore these derivatives are listed here :

$$\frac{\partial y}{\partial a} = -\frac{2(x-a)cb}{\left[(x-a)^2+b^2\right]^2}$$

$$\frac{\partial y}{\partial b} = \frac{c\left[(x-a)^2-b^2\right]}{\left[(x-a)^2+b^2\right]^2}$$

$$\frac{\partial y}{\partial c} = \frac{b}{(x-a)^2+b^2}$$

$$\frac{\partial y}{\partial d} = x$$

$$\frac{\partial y}{\partial e} = 1$$

The area under the Lorentzian curve (subtracting the baseline) can be computed by analogy with the theoretical model or by direct integration. $\int_{-\infty}^{+\infty} c\frac{b}{(x-a)^2+b^2}dx = \pi c$

For the purpose of this thesis, the scaling coefficient c is clearly the most important one since it is the only coefficient that characterize the energy under a Lorentzian peak. Therefore it is important to estimate the coefficient c as accurately as possible in the curve fitting calculation.

H2 Voigt distribution

The theoretical Voigt distribution is characterized by :

$$U(p,t) = \sqrt{4\pi t}\int_{-\infty}^{+\infty}\frac{e^{-\left[(p-y)^2/4t\right]}}{1+y^2}dy$$

where : U(p,t) is the value of the distribution function which is assumed to be centered at the origin in the previous expression

p is the name the variable

t is a coefficient characterizing the width

The above expression defining the Voigt distribution can be interpreted as the convolution product of the function $f_1(x) = \frac{1}{1+x^2}$ (corresponding to the Lorentzian distribution centered at the origin), and of the function $f_2(x) = e^{-\frac{x^2}{4t}}$ (corresponding to the normal distribution involved in the natural broadening)

By symmetry of the convolution product, the Voigt function can also be written as :

$$U(x,t) = \sqrt{4\pi t}\int_{-\infty}^{+\infty} \frac{e^{-\left[\frac{y^2}{4t}\right]}}{1+(x-y)^2}dy$$

with the following change of variable : $z = \frac{y}{2\sqrt{t}}$

$$U(x,t) = \sqrt{4\pi t}\int_{-\infty}^{+\infty} \frac{e^{-z^2}}{1+\left(x-2\sqrt{t}z\right)^2}2\sqrt{t}dz$$

$$U(x,t) = 4\sqrt{\pi t}\int_{-\infty}^{+\infty} \frac{e^{-z^2}}{1+\left(x-2\sqrt{t}z\right)^2}dz$$

Reference [25] suggests to use the *Gauss-Hermite quadrature formula* to compute such an integral :

$$\int_{-\infty}^{+\infty} e^{-x^2} f(x)dx = \sum_{j=1}^{n} H_j f\left(a_j\right) + E$$

where : H_i is the Hermite polynomial of order i

a_j are the zeros of $H_n(x)$

and the maximum numerical error for this formula is given by :

$E = \frac{n!\sqrt{\pi}}{2^n(2n)!} f^{(2n)}(\eta)$ η being a fixed real number

The zeros of Hermite polynomial and corresponding weights where found in Reference [25].

For n=5

Table H Zeros of H5 th order Hermite polynomial and corresponding weights for the Gauss Hermite quadrature

Abscissas a_j	weights H_j
0	0.945309
±0.958572	0.393619
±2.020183	0.019953

Conclusion : using the preceding formula and table, the Voigt distribution was modeled as follows :

$$U(x,t,\mu) = 4\sqrt{\pi}t\sum_{j=1}^{5} H_j \frac{1}{1+\left(x-\mu-2\sqrt{t}a_j\right)}$$

Appendix I

Experimental conditions

Table I lists all the parameters varied during the experiments. A short description on each item is included here in order to improve the readability of the table.

- *Name* is the name of the test as well as the name of the data file storing the experimental data.
- *Date* is the date of the experiment.
- *Objective* is the topic of interest for the experiment. For *stability* the purpose of the experiment was to quantify the shot to shot variation of the signal, for *broad cur.* it was to study the broad band emission of the laser, for *tuning* it was see the variations of the signal when tuning the laser around to the positions corresponding to the peaks of O_2 absorption, for *explora.* it was to observe the spectra obtained with the laser tuned at other wavelength, for *flow rate* it was to quantify the effect of a flow rate variation of air in the cell, for *power* it was to see the effect of a power variation of the laser beam, for *purge exp* it was to observe the effect of purging the beam path with nitrogen, for *Pressure* it was to see the effect of a pressure variation in the cell and finally for *Temp* it was to see the effect of a temperature variation on the experimental spectra.
- # *shots* is the number of laser pulses fired for one spectrum.
- # *spectra* is the number of spectra stored in the data file.
- *Figure* # refers to the number of the figure presenting the corresponding data.
- *Power is* the power of the laser beam measured in watt with the power meter placed just before the testing cell, or right after it if (1) is following the reading.

- *Rep rate* is the repetition rate of the laser (number of pulses per second).
- *Wv* is the reading of the tuning knob used to vary the wavelength.
- *Peak* is the O_2 absorption peak used for the experiment.
- *HV* is the high voltage of the laser in kV.
- *Recircul* indicates whether the cryogenic recirculation was on or off.
- *Int purge* indicates whether the home built purge system for the laser on the beam path from the diffracting prisms to the reflecting mirror after the amplifier cavity was used or not.
- *Grating* is the number of grooves per millimeter of the grating used.
- *Position* is the wavelength set for the spectrometer in nm.
- *Exposure* is the exposure time in ms set for the spectrometer.
- *Slit* is the size in μm of the entrance slit used.
- *Gain* is the setting for the gain for the intensified diode array.
- *Flow rate* is the flow rate of air inside the testing cell in standard cubic feet per hour (scfh).
- *Pressure* is the pressure in millibar inside the cell.
- *Temp.* is the temperature in degree Celsius at the measurement point inside the cell. (25 C was taken for default temperature at room temperature. The actual temperature was between 23 and 27 C).
- *1/2 Ext p.* indicates whether the beam path from the laser exit to the turning mirrors was purged.
- *2/2 Ext p.* indicates whether the beam path from the focusing lens to the testing cell was purged.
- *note* : *R1* means that the beam at the exit of the oscillator was blocked in order to get a broad band emission, *4 peaks* indicates that 4 distinct peaks are visible for each LIF line for this spectrum, O_2^+ indicates that the corresponding spectrum is characteristic from O_2^+ emission, finally *Windows* indicates that the power level was changed by inserting quartz windows.

Table I : Experiments information (1/3)

Name	V72A Ser.	V72B	V75SG2	V72SEE	D72U10	L73A	D72 P*xx*
date	7/10/92	7/10/92	7/24/92	7/10/92	7/05/92	7/13/92	7/05/92
objective	**Stability**	**Stability**	**Stability**	**Stability**	**broad cur.**	**Stability**	**tuning**
# shots	100	100	1	20	500	100	100
# spectra	10	10	10	10	1	10	20
Figure #	1.2, 5.38, 5.39	2.4, 5.37	3.3	3.4	3.5, 5.15	5.16	5.17-5.21
Power	0.21 (1)	0.40 (1)		0.10 (1)	1.66		0.90
Rep Rate	50	50	1	10	50	50	50
Wv	0.9240	0.9240	0.9240	0.9240	1.00	2.00	**->name**
Peak	P17	P17	P17	P17	NA	NA	**->Series**
HV	20.5	20.5	20.6	20.5	22.0	20.5	19.2
Recircul	on	on	OFF	on	on	on	on
Int purge	on	on	on	on	OFF	on	OFF
Grating	1200	1200	3600	3600	1200	1200	1200
Position	234	234	386	386	234	234	234
Exposure	1995	1995	956	1995	1995	1995	1995
Slit	50	50	10	50	50	50	50
Gain	9.90	9.90	9.90	9.90	9.90	9.90	9.90
Flow rate	32	32	32	32	32	32	32
Pressure	1300	1300	1300	1300	1300	1300	1300
Temp.	25	25	25	25	25	25	25
1/2 Ext p.	OFF	on	on	on	on	on	on
2/2 Ext p.	OFF	on	on	on	on	on	on
note	-	-	-	-	R1		

Experiments information (2/3)

Name	M72K2	M72K3	V71F11	V71F10	L65Y	V75D	V75E
date	7/07/92	7/07/92	7/03/92	7/03/92	6/29/92	7/24/92	7/24/92
objective	**Broad cur**	**Broad cur**	explora.	explora.	flow rate	**Power**	**Power**
# shots	500	500	100	100	10	10	50
# spectra	4	1	1	1	5	5	7
Figure #	5.22	5.22	5.23	5.24	5.25, 5.26	5.27	5.28-5.34
Power			0.21	0.28	0.19	0.22	1.19
Rep Rate	50	50	10	10	10	10	50
Wv	0.9240	0.9240	0.9325	0.7790	old set.	0.926	0.926
Peak	NA	NA	NA	NA	P17 ?	P17	P17
HV			20.1	20.1	20.6	20.6	19.2
Recircul	OFF	OFF	on	on	on	OFF	OFF
Int purge	on	on	on	on	OFF	on	on
Grating	3600	3600	1200	1200	1200	3600	1200
Position	386	386	234	234	234	386	234
Exposure	10000	10000	10000	10000	956	956	994
Slit	50	50	50	50	50	10	50
Gain	9.90	9.90	9.90	9.90	9.90	9.90	9.90
Flow rate	32	32	32	32	see file	32	32
Pressure	1300	1300	1300	1300	2080	1300	1300
Temp.	25	25	25	25	25	25	25
1/2 Ext p.	on	OFF	OFF	OFF	OFF	OFF	OFF
2/2 Ext p.	on	OFF	OFF	OFF	OFF	OFF	OFF
note	R1	-	**4 peaks**	**O2+**		**Windows**	

Experiments information (3/3)

Name	V75H1	W72P	W72Q	V72H	W72F	W72G
date	7/24/92	7/08/92	7/08/92	7/10/92	7/08/92	7/08/92
objective	purge exp	Pressure	Pressure	Temp	Temp	Temp
# shots	100	100	100	100	100	100
# spectra	20	18	18	19	10	10
Figure #	5.35, 5.36	5.40- 5.44	5.45, 5.46	5.49, 5.50	5.51-5.53	5.54-5.56
Power						
Rep Rate	50	50	50	10	50	50
Wv	0.9260	0.9240	1.0530	0.9280	0.924	1.0530
Peak	P17	P17	P15	P17	P17	P15
HV	20.6	20.0	20.0	20.5	20.0	20.0
Recircul	OFF	on	on	on	on	on
Int purge	on	OFF	OFF	on	OFF	OFF
Grating	1200	1200	1200	1200	1200	1200
Position	234	234	234	234	234	234
Exposure	1995	1995	1995	1995	1995	1995
Slit	50	50	50	50	50	50
Gain	9.90	9.90	9.90	9.90	9.90	9.90
Flow rate	32	32	32	32	32	32
Pressure	1300	see file	see file	1300	1300	1300
Temp.	25	25	25	see file	see file	see file
1/2 Ext p.	on	on	on	on	on	on
2/2 Ext p.	on	on	on	on	on	on
note						

Appendix J

Empirical data reduction procedure

This procedure was written to use the programmable functions of the macrocalculator module of Kaleidagraph, the software used to plot and analyze the data.

Spectrum Analysis 2.1

Main : Organizes input, call subroutines

Memories :

R10 - R17 results
R 19 keeps track of selection
R21 counter for peak
R22 Maxi Ad of O2R
R23 Auxiliary variable for relative adressing
R24 store value 0.01
R45 Maxi value for counter Sub #3
R47 Maxi value for counter Sub #5
R48 Width mini of Raman peaks
R49 Width mini of LIF peaks
R50-59 Value/results of peak area
R60 Ratio LIF / Raman
R61 Σ LIF
R62 Σ Raman O2
R70 - R79 referenced peaks
R83 Column # for data
R84 Column # for beginning storage
R85 Row # for storing

Labels :

LBL 01 - 09 : Subroutines
LBL 20, 21, 22, 23, 24

****

Subroutine #1 : Diode # --> Cell Adress

****

Subroutine #2 : (Ad#1,Ad#2) --> Slope

****

Subroutine #3 : (Ad Maxi,sign) --> (Ad alarm,alarm # : 3)

Method : 3 consecutive points with slope of opposite sign

Memories :

R40 Alarm #
R41 point #1

Labels :

LBL 40,41,42,45,46,47,48

```
                R42 point #2
                R43 counter
                R44 Ad alarm
                R45 Maxi counter

************************************************************
Subroutine #4 : (Ad Maxi,sign) --> (Ad alarm,alarm # : 5)
                Method : 5 slope inferior to limit slope
        Memories :                                      Labels :
                R40 Alarm #                                     LBL 50,52,54,56
                R41 point #1
                R42 point #2
                R43 counter
                R44 Ad alarm
                R46 keeps track of sign
                R47 Maxi counter

************************************************************
Subroutine #5 : (Ad1, Ad2) --> Area = integral between Ad1 and Ad2
        Memories :                                      Labels :
                                                                LBL 55

************************************************************
Subroutine #6 : Ad Th Maxi --> (Ad Maxi,Maxi value, Slope limit)
        Memories :                                      Labels :
                R30 Diode # of th maxi          LBL 30,32,34
                R31 Ad maxi
                R32 Ad current cell
                R33 Ad final cell
                R34 Maxi value
                R35 1/2 height value
                R36 Ad 1/2 height
                R37 slope limit

************************************************************
Subroutine #7 : Ad th maxi --> Peak data
        Memories :                                      Labels :
                R10 Ad initial diode                    LBL 35, 36, 37, 38,39,49
                R11 initial diode alarm
                R12 Ad final diode
                R13 final diode alarm
                R14 Ad maxi
                R15 Maxi value
                R16 slope limit
                R17 peak area

************************************************************
Subroutine #8 : Display results on screen
        Memories :                                      Labels :
                R23, 24 auxuliary memories              LBL 60

************************************************************
Subroutine #9 : Store results on data spraedsheet
        Memories :                                      Labels :
                R23, 24 auxuliary memories              LBL 61

************************************************************


CM
alpha   "Spectrum Analysis procedure (check)
STOa 9
alpha   "Version 2.10 - 4/04/92"
alpha   "by Franck Kolczak"
```

```
;
const   5.500000000e+01                    diode of O2 Raman peak @ 234nm
STO 70
const   4.300000000e+01                    delta N2 Raman / O2 Raman
STO 71
const   8.300000000e+01                    delta O2 Raman2 / O2 Raman
STO 72
const   1.710000000e+02                    delta LIF 4.3 / O2 Raman
STO 73
const   2.640000000e+02                    delta LIF 4.4 / O2 Raman
STO 74
const   3.710000000e+02                    delta LIF 4.5 / O2 Raman
STO 75
const   4.760000000e+02                    delta LIF 4.6 / O2 Raman
STO 76
const   5.880000000e+02                    delta LIF 4.7/ O2 Raman
STO 77
const   6.760000000e+02                    delta atom C / O2 Raman
STO 80
const   7.050000000e+02                    delta LIF 4.8 / O2 Raman
STO 78
const   8.300000000e+02                    delta LIF 4.9 / O2 RamanSTO 79
;
;
const   4.000000000e+00
STO 45                                     set Maxi counter for Subr 3
const   1.500000000e+01
STO 47                                     set Maxi counter for Subr 4
const   9.000000000e+00
STO 48                                     set width mini Raman peaks
const   1.100000000e+01
STO 49                                     set width mini LIF peaks


FIX 1
alpha   "Enter data column : "             input of column data
STOa 0
const   1.000000000e+00
STO 00
alpha   "Column # to store (0 to skip)"
STOa 1
const   0.000000000e+00
STO 01
alpha   "Row # to store"
STOa 2
const   0.000000000e+00
STO 02
alpha   "O2R peak position (55 @ 234nm)"
STOa 3
RCL 70
STO 03
RCLa 9
inpt 4
;
RCL 00
STO 83
F
RCL 01
STO 84
;
RCL 02
STO 85
;
;
```

```
FIX 9
const   0.000000000e+00
STO 21                          initiate peak counter to 0
;
LBL 21
RCL 21
const   0.000000000e+00
x != y                          Test counter = 0 to determine O2 Raman peak
GTO 22
RCL 03
STO 01
XEQ 01
RCL 03
STO 01                          Fing th Ad of O2 Raman peak
GTO 23
;
LBL 22
const   7.000000000e+01
RCL 21
 +
STO 23
rclr 23
RCL 22
 +
STO 01                          Find th Ad of other peaks
;
LBL 23
XEQ 07                          compute data about peak chosen
RCL 21
const   5.000000000e+01
 +
STO 23
RCL 17
stor 23
;
RCL 21
const   0.000000000e+00
x != y
GTO 25
RCL 14                          if peak = O2 RAman then store Ad in R22 for other peaks
STO 22
;
LBL 25
RCL 84
const   0.000000000e+00
x = y
GTO 24
;
RCL 84
const   1.000000000e+02
 /
RCL 21
 +
STO 23
;
RCL 21
stor 23
;
const   1.000000000e+00
const   1.000000000e+02
 /
STO 24
ADD 23
RCL 17
```

```
stor 23
RCL 24
ADD 23
RCL 15
stor 23
RCL 24
ADD 23
RCL 10
int
const    1.000000000e+00
 +
stor 23
RCL 24
ADD 23
RCL 11
stor 23
RCL 24
ADD 23
RCL 14
int
const    1.000000000e+00
 +
stor 23
RCL 24
ADD 23
RCL 16
stor 23
RCL 24
ADD 23
RCL 12
int
const    1.000000000e+00
 +
stor 23
RCL 24
ADD 23                          Storing phase in data file
RCL 13
stor 23
;
LBL 24
const    9.000000000e+00
ISG 21                          Loop for all peaks
GTO 21
XEQ 08                          Display results on screen
;
STOP
;
************************************************************

LBL 01
RCL 83                                          Ad od diode = diode -1 + Column#/100
const    1.000000000e+02
/
RCL 01
const    1.000000000e+00
-
 +
STO 03
RTN
;
************************************************************

LBL 02
RCLi 02
```

```
RCLi 01
-
RCL 02                                  Slope = (D2 value - D1 value)/(Ad D2 - Ad  1)
RCL 01
-
/
STO 03
RTN
;
************************************************************


LBL 03
const   0.000000000e+00
STO 40                                  initialize alarm #
STO 43                                  initialize counter
RCL 01
STO 41                                  Ad maxi = point 1
;
;
const   1.000000000e+00
STO 46
RCL 02
const   0.000000000e+00                 Set R46 = value of sign of R02
x < y
GTO 48
const   -1.000000000e+00
MUL 46
LBL 48
RCL 46
RCL 41
+
STO 42                                  point 2 = point 1 + sign
LBL 40
const   1.000000000e+00
ADD 43                                  incremente counter
RCL 46
ADD 41                                  shift point 1
RCL 46
ADD 42                                  shift point 2
RCLi 41
RCLi 42
-
const   0.000000000e+00
x <= y                                  Test value pt2 <= value pt1
GTO 45
RCL 40                                  next loop in search
const   0.000000000e+00
x != y                                  Test alarm # ≠ 0 (first level)
GTO 41
const   1.000000000e+00
STO 40                                  set alarm # = 1
RCL 41
STO 44
GTO 46
LBL 41
RCL 40
const   1.000000000e+00
x != y                                  Test alarm # ≠1 (second level)
GTO 42
const   2.000000000e+00
STO 40                                  set alarm # = 2
GTO 46
LBL 42
```

```
const   3.000000000e+00
STO 40                                  set alarm # = 3
RCL 44
STO 03                                  set R03 = alarm #
GTO 47
LBL 45
const   0.000000000e+00
STO 40                                  reset alarm to 0
LBL 46
RCL 45
RCL 43
x<y                                             Test counter < Max counter
GTO 40
const   0.000000000e+00
STO 40                          reset alarm # to 0
STO 44                          reset Ad alarm to 0
LBL 47
RCL 44
STO 03
RCL 40
STO 04                  return results
RTN
;
*************************************************************

LBL 04
const   0.000000000e+00
STO 43                                  initialize alarm #
;
const   1.000000000e+00
STO 46
RCL 02
const   0.000000000e+00         Set R46 = value of sign of R02
x<y
GTO 56
const   -1.000000000e+00
MUL 46
LBL 56
RCL 01
RCL 02
+
const   1.000000000e+00
-
STO 41                          set Ad of pt1
const   4.000000000e+00
RCL 46
*
+
STO 42                          shift pt1 from 4 diode to get pt2
LBL 50
const   1.000000000e+00
ADD 43                                  increment counter
RCL 46
ADD 41                                  shift pt1
RCL 46
ADD 42                                  shift pt2
RCL 41
STO 01
RCL 42
STO 02
XEQ 02                                  slope (pt1,pt2)
RCL 03
const   -1.000000000e+00
*
```

```
RCL 46
 *
RCL 37
x < y                                   Test slope limit < slope (pt1,pt20
GTO 52
RCL 41
STO 44                                  set Ad alarm = pt1
const   5.000000000e+00
STO 40                                  set alarm # = 5
GTO 54                          exit
LBL 52
RCL 47
RCL 43
x < y                                   Test counter < Maxi counter
GTO 50
const   -1.000000000e+00
STO 40                                  set alarm # = -1 if not found
STO 44                                  set Ad alarm = -1
LBL 54
RCL 44
STO 03
RCL 40                                  retun results
STO 04
RTN
;
************************************************************
;
LBL 05
RCLi 01
const   2.000000000e+00
 /
STO 03
LBL 55
const   1.000000000e+00
ADD 01
RCLi 01
ADD 03                                  ∫ = 1/2(Ad1 + Ad2) + Σ diodes in between
RCL 02
RCL 01
x < y
GTO 55
RCLi 02
const   2.000000000e+00
 /
SUB 03
RTN
;
************************************************************
;
LBL 06
RCL 01
const   6.000000000e+00
 -
STO 31                          initially set Ad maxi & Ad current = Th maxi - 6 diodes
STO 32
const   1.200000000e+01
 +
STO 33                          set Ad final diode = Th maxi + 6 diodes
LBL 30
const   1.000000000e+00
ADD 32                                  increment current diode
RCLi 31
RCLi 32
x < y                                   Test current diode value < Ad maxi
```

```
GTO 32
RCL 32
STO 31                          set Ad maxi = currnt diode
LBL 32
RCL 33
RCL 32
x < y                                   Test Ad current diode < Ad final diode
GTO 30                          next loop
RCLi 31
STO 34                          store R34 = maxi value
const   2.000000000e+00
*
const   3.000000000e+00
/
STO 35
RCL 31
STO 32                  set current diode = maxi diode
LBL 34
const   1.000000000e+00
ADD 32                                  increment current diode
RCLi 32
RCL 35
x < y                                   Test 2/3 maxi value < value current diode
GTO 34                  next loop
RCL 32
STO 02
STO 36
RCL 31                                  return results
STO 01
XEQ 02
RCL 03
const   -1.000000000e+01
/
STO 37
RTN
;
************************************************************

LBL 07
XEQ 06
RCL 34
STO 15                  set R15 = maxi value
RCL 37
STO 16                  set R16 =slope limit
RCL 31
STO 14                  set R14 = Ad maxi
STO 01
;
RCL 48                                  Compute shift for initial diode with width of peak
STO 02
RCL 19
const   3.000000000e+00
x > y                                   Test # > input
GTO 39
RCL 49
STO,02
LBL 39
RCL 02
STO 18
;
XEQ 03                  search for limit + by clear cut (alarm 3)
RCL 04
const   3.000000000e+00
x = y                                           Test alarm # =3
```

```
GTO 35
RCL 31
;
STO 01
RCL 18
STO 02
XEQ 04                          search for limit + by slope method (alarm 5)
RCL 04
const   5.000000000e+00
x != y                                  Test alarm # ≠ 5
GTO 37
LBL 35
RCL 03
STO 12                          set R12 = Ad alarm +
RCL 04
STO 13                          set R13 = Alarm # +
RCL 31
STO 01
;
RCL 48                                  Compute shift for initial diode with width of peak
const   -1.000000000e+00
*
STO 02
RCL 19
const   3.000000000e+00
x > y                                   Test # > input
GTO 49
RCL 49
const   -1.000000000e+00
*
STO,02
LBL 49
RCL 02
STO 18
;

XEQ 03                                  search limit - by clear cur
RCL 04
const   3.000000000e+00
x = y                                           Test alarm # = 3
GTO 36
RCL 14
STO 01
const   -1.000000000e+00
STO 02
XEQ 04                                          search limit - by slope method
RCL 04
const   5.000000000e+00
x != y                                  Test alarm # ≠ 5
GTO 37
LBL 36
RCL 03
STO 01
STO 10
RCL 04
STO 11
RCL 12                                          return results
STO 02
XEQ 05
RCL 03
STO 17
GTO 38
LBL 37
const   -5.000000000e+03
```

```
STO 03                                  return -5000 in case of not found
LBL 38
RTN
;
************************************************************

LBL 08
FIX 7
alpha   "Results spectrum analysis"
STOa 9
;
alpha   "Σ Raman O2 :"
STOa 0
RCL 50
RCL 52
 +
STO 00
STO 62
alpha   "Σ Raman O2 + N2 :"
STOa 1
RCL 00
RCL 51
 +
STO 01
;
alpha   "Σ LIF O2 :"
STOa 2
const   3.000000000e+00
STO 24
const   0.000000000e+00
STO 02
LBL 60
const   5.000000000e+01
RCL 24
 +
STO 23
rclr 23
ADD 02
const   9.000000000e+00
ISG 24
GTO 60
RCL 02
STO 61
;
alpha   "Σ LIF O2 / Σ Raman O2 :"
STOa 3
RCL 02
RCL 00
 /
STO 03
STO 60
;
;
RCLa 9
view 4
;
;
alpha   "LIF 4.3 : "
STOa 0
RCL 53
STO 00
;
alpha   "LIF 4.4 : "
STOa 1
RCL 54
```

```
STO 01
;
alpha    "LIF 4.5 : "
STOa 2
RCL 55
STO 02
;
alpha    "LIF 4.6 : "
STOa 3
RCL 56
STO 03
;
alpha    "LIF 4.7 : "
STOa 4
RCL 57
STO 04
;
alpha    "LIF 4.8 : "
STOa 5
RCL 58
STO 05
;
alpha    "LIF 4.9 :"
STOa 6
RCL 59
STO 06
;
alpha    "Raman O2 : "
STOa 7
RCL 50
STO 07
;
alpha    "Raman O2 2nd : "
STOa 8
RCL 52
STO 08
;
RCLa 9
view 9
RTN

************************************************************

LBL 09
;
;
FIX 7
RCL 84
const    1.000000000e+02
/
RCL 85
+
STO 23                          compute adress of first cell to receive data
;
const    1.000000000e+00
const    1.000000000e+02
/
STO 24                          store 0.01 for use in future increments
;
RCL 60
const    1.000000000e+06
*
STOi 23                         Store Ratio LIF / Raman * 1e6
;
```

```
RCL 24
ADD 23
RCL 61
STOi 23                    Store Σ LIF
;
RCL 24
ADD 23
RCL 62
STOi 23                    Store Σ Raman O2
;
RCL 24
ADD 23
RCL 51
STOi 23                    Store Raman N2
;
RCL 24
ADD 23
RCL 50
STOi 23                    Store Raman O2
;
RCL 24
ADD 23
RCL 52
STOi 23                    Store Raman O2 2nd
;
const   5.300000000e+01
STO 21
LBL 61
RCL 24
ADD 23
rclr 21
STOi 23                    Store LIF peaks
const   5.900000000e+01
ISG 21
GTO 61
;
RTN
```

Figure 1.1 : Absorption Spectrum O_2 and ArF Laser Gain Curve

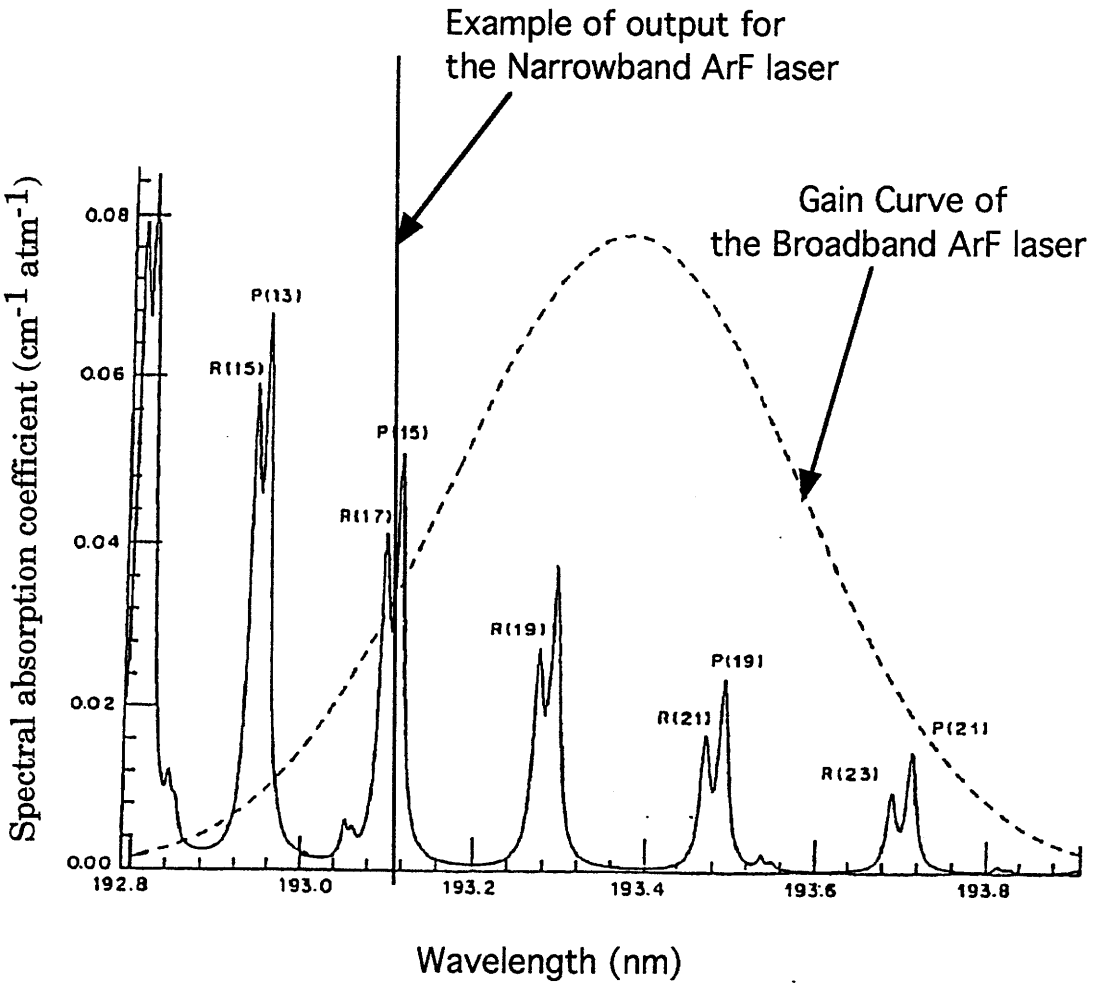

(Absorption at 300°K)

Source : Ref [10]
Lee & Hansen, 1986

Figure 1.2 : Example of O2 LIF spectrum (V72A #3)

Conditions : 100 pulses/spectrum
Exposure : 1995 ms
P ≈ 0.58 W
Grating 1200 g/mm @ 234 nm

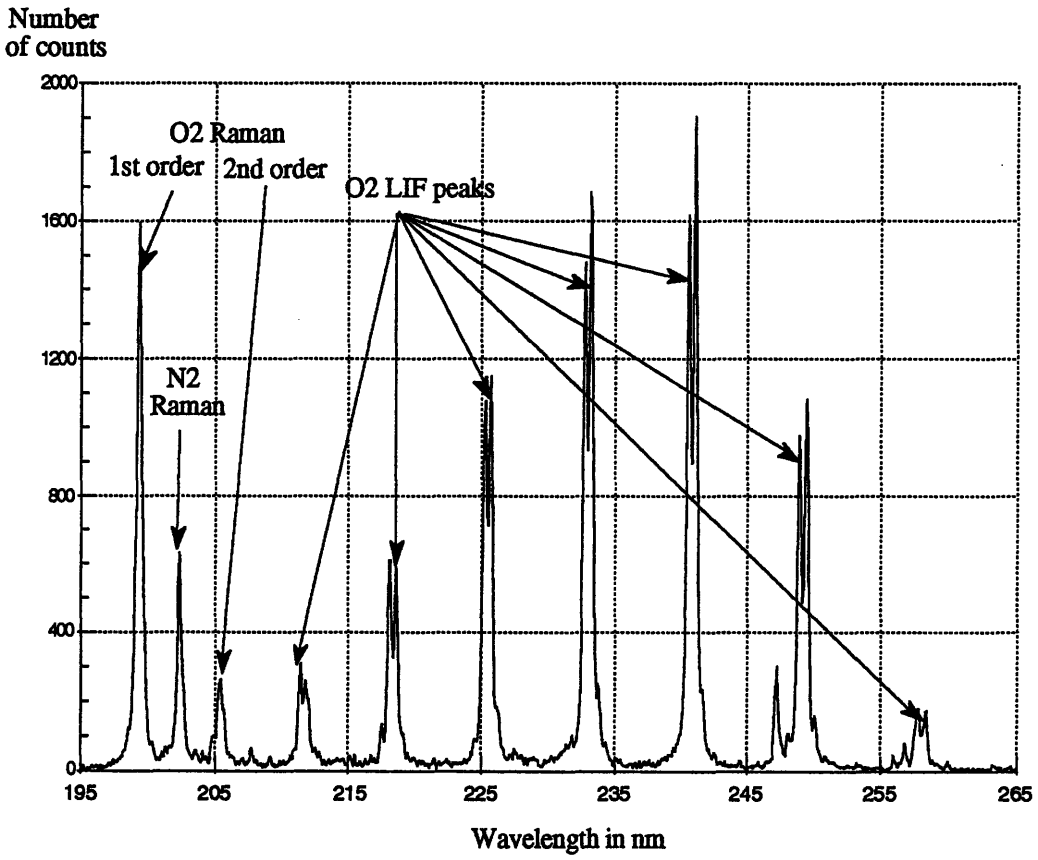

Data File : V72A Spectrum #3

Figure 1.3 : **Turbomachinery geometry in which LIF measurements will be performed**

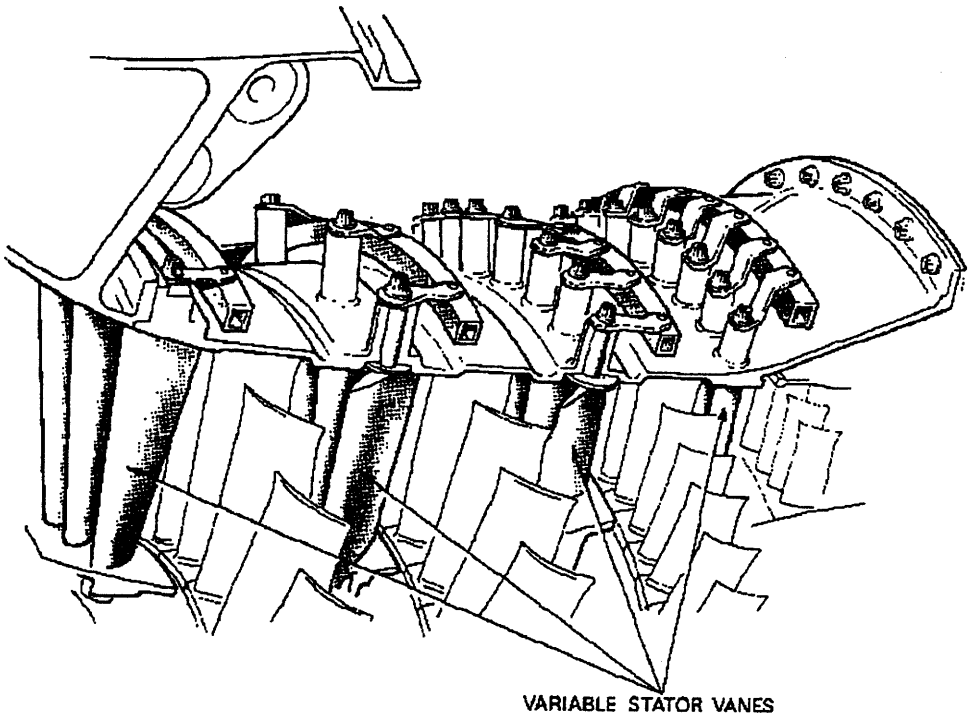

Figure 1.4 : **Coaxial set-up for temperature measurement in turbomachinery**

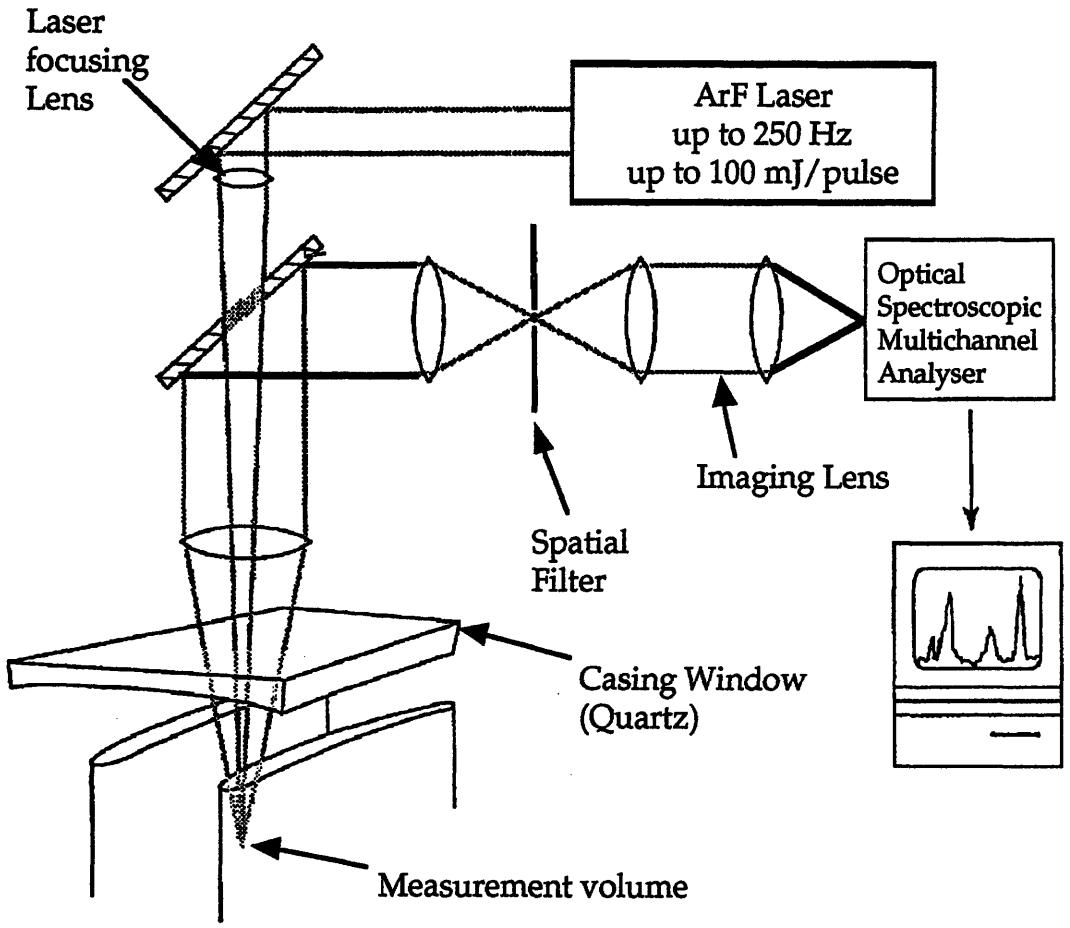

Source : Proposal for a grant GTL - Nov 1988

Figure 2.1 : **Energy Diagram of the O2 Schumann- Runge system**

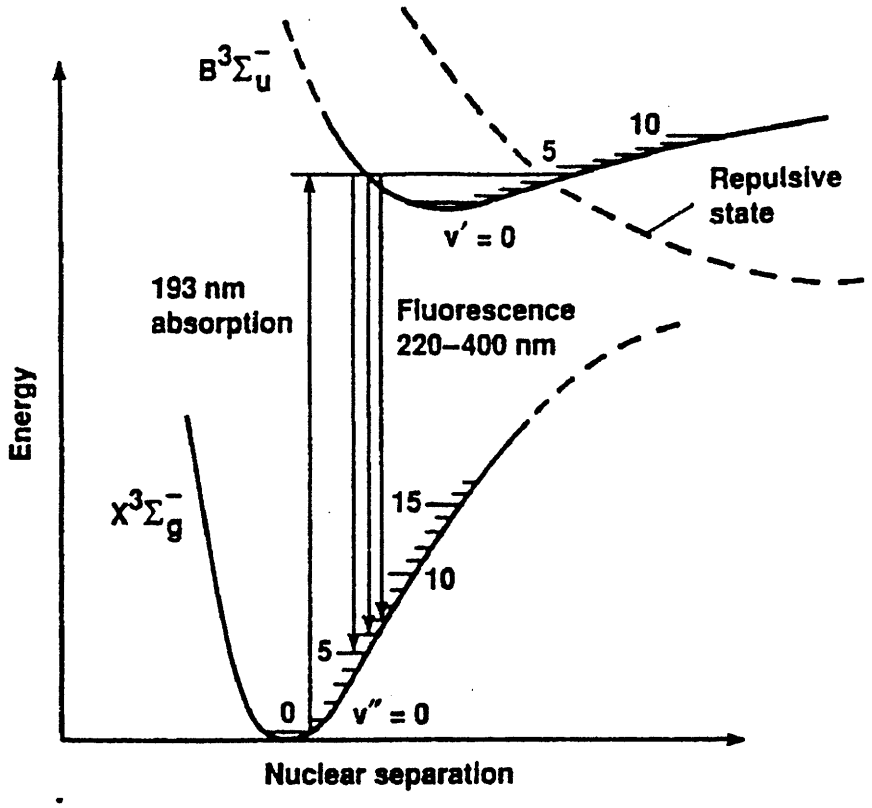

Source : Ref [16]
Fletcher D.G., McKenzie R.L. 1991

Figure 2.2 : **Energy transfer paths for LIF of O2**

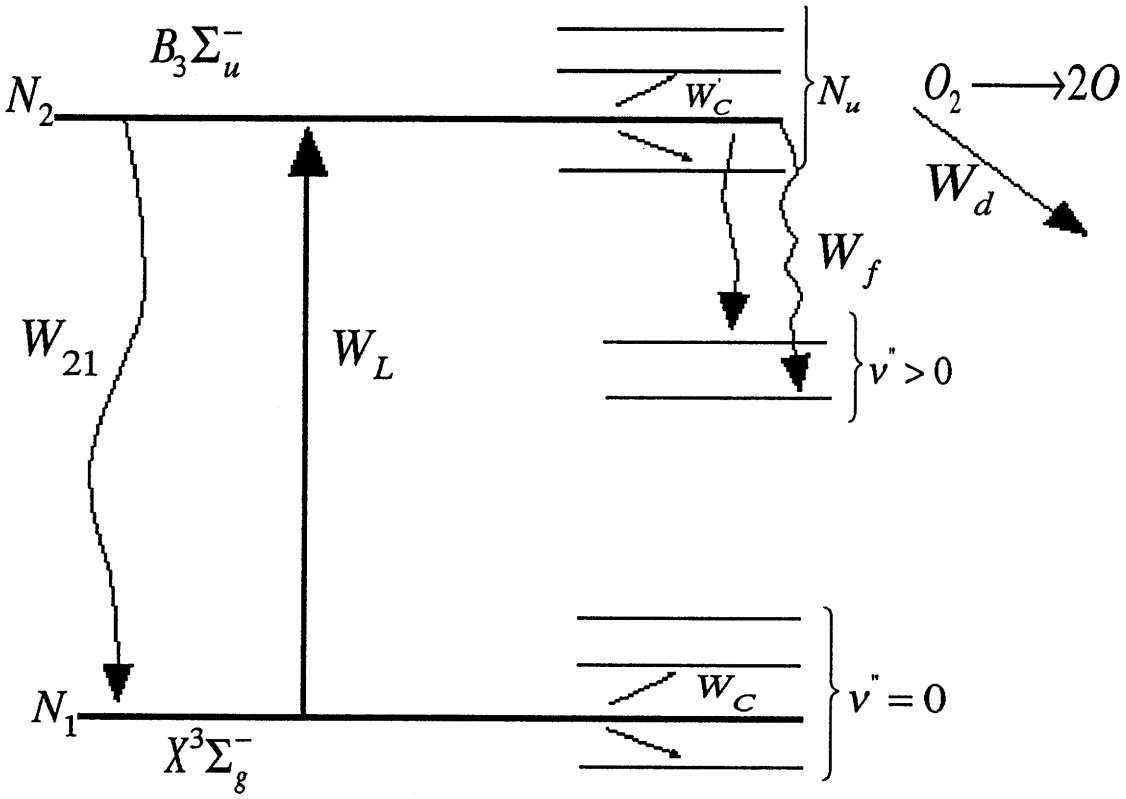

Source : Ref [3]
Laufer, Fletcher and McKenzie, 1990

Figure 2.3 : **Energy level pattern for a rotating for a linear molecule**

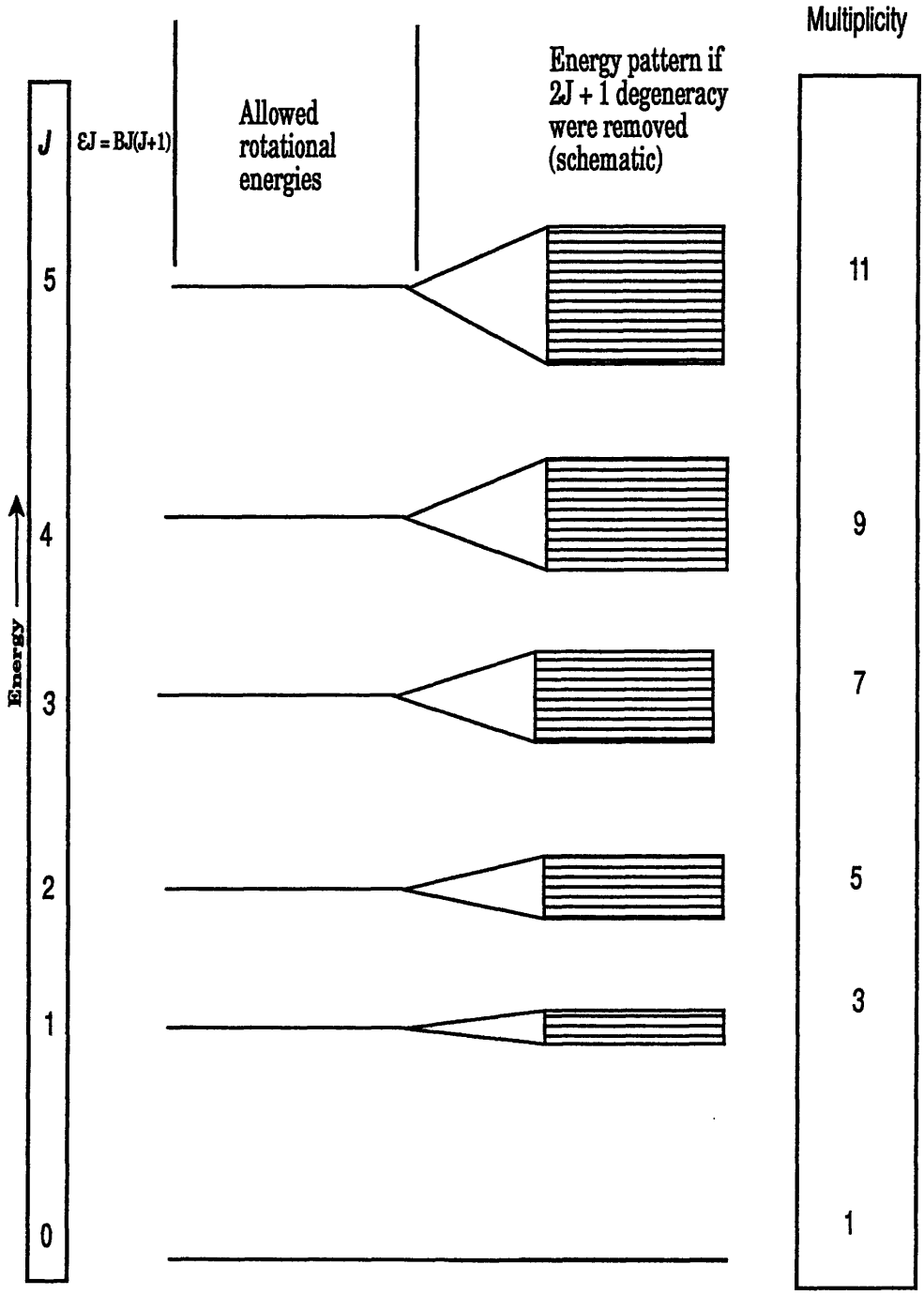

Source : Ref [7]
Barrow G., 1962

Figure 2.4 : Peaks identification Spectrum V72B #3

Conditions : 100 pulses/spectrum
Exposure : 1995 ms
P : NA
Grating 1200 g/mm @ 234 nm

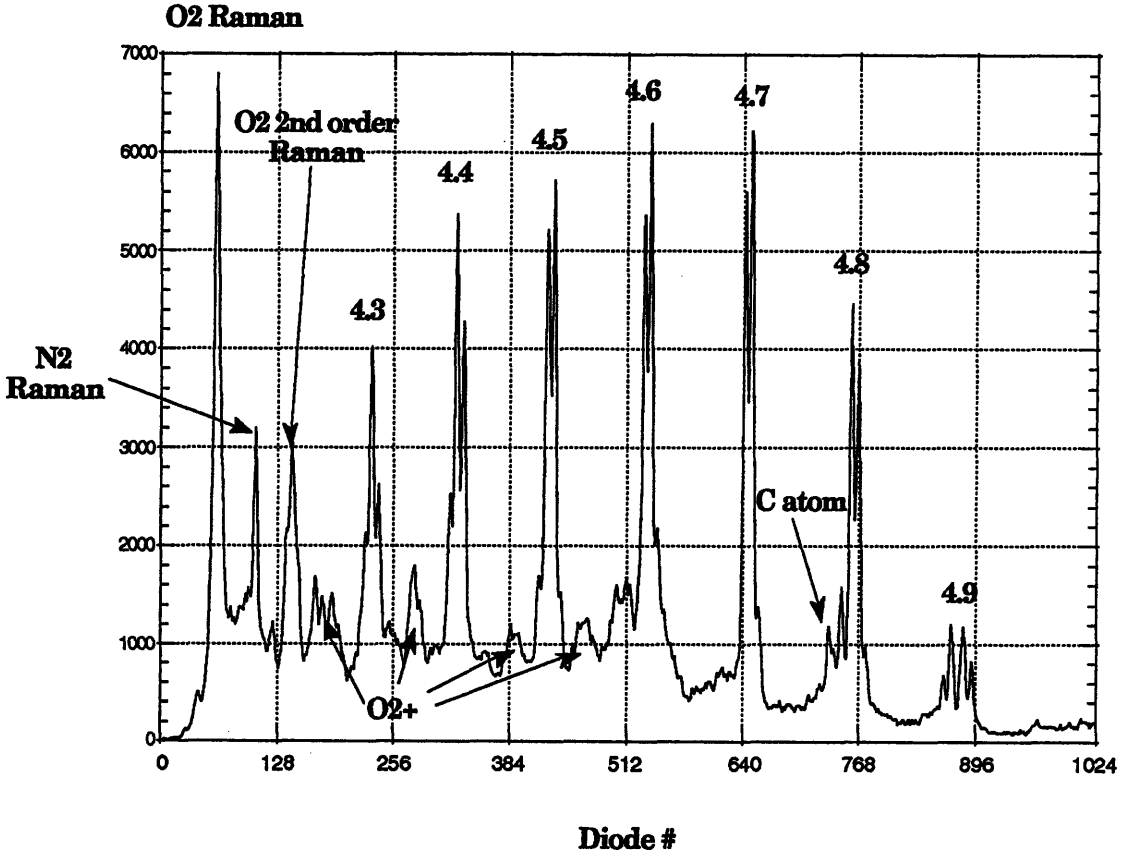

Data file : V72B-Series

Figure 3.1 : **Laser schematic**

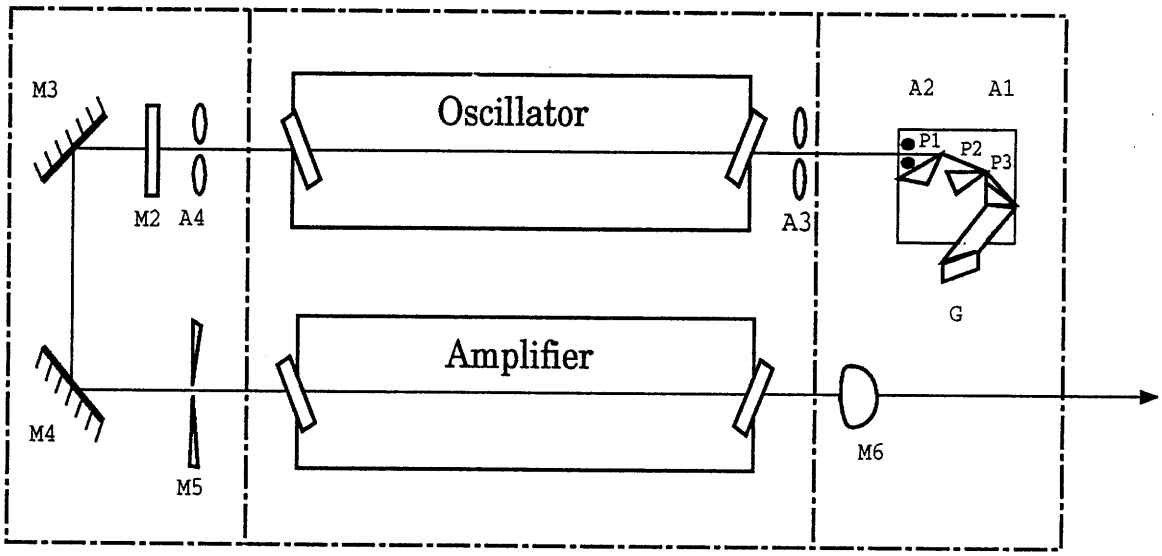

Figure 3.2 : **Gas treatment unit**

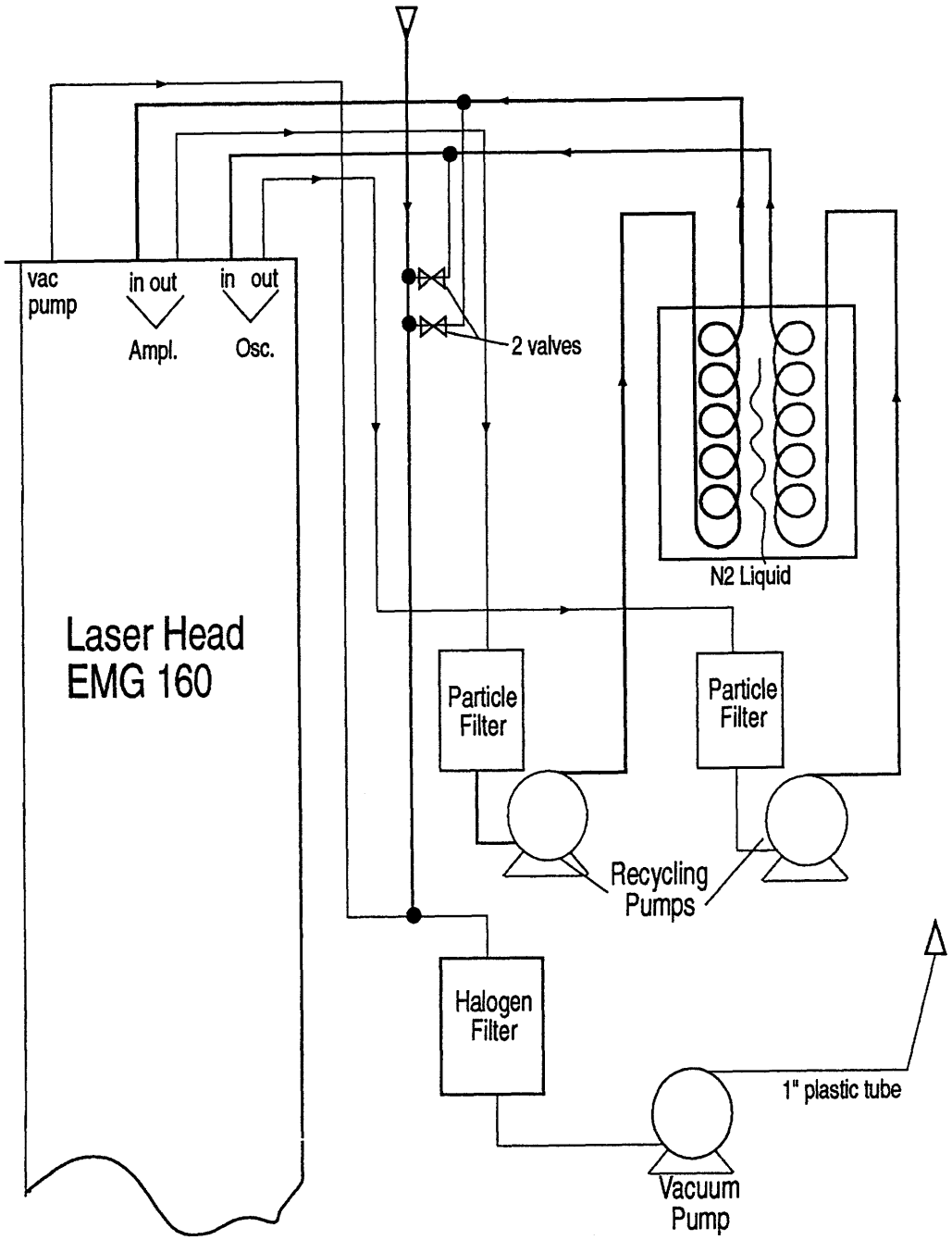

Figure 3.3 : Variation of the laser emission during 10 seconds (1 pulse each second)

Conditions : 1 pulses/spectrum
Exposure : 956 ms
P : unknown
Grating 3600 g/mm @ 386 nm

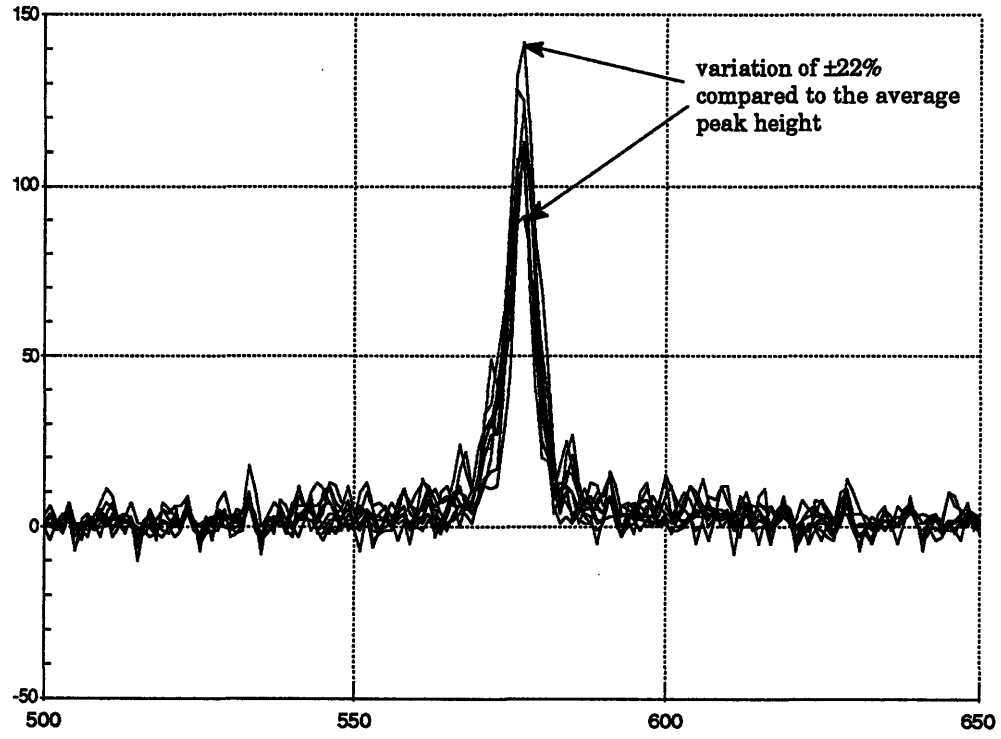

Data file : V75SG2

Figure 3.4 : Variation of the laser emission during 10 seconds (20 pulse each second)

Conditions : 20 pulses/spectrum
Exposure : 1995 ms
P : unknown
Grating 3600 g/mm @ 386 nm

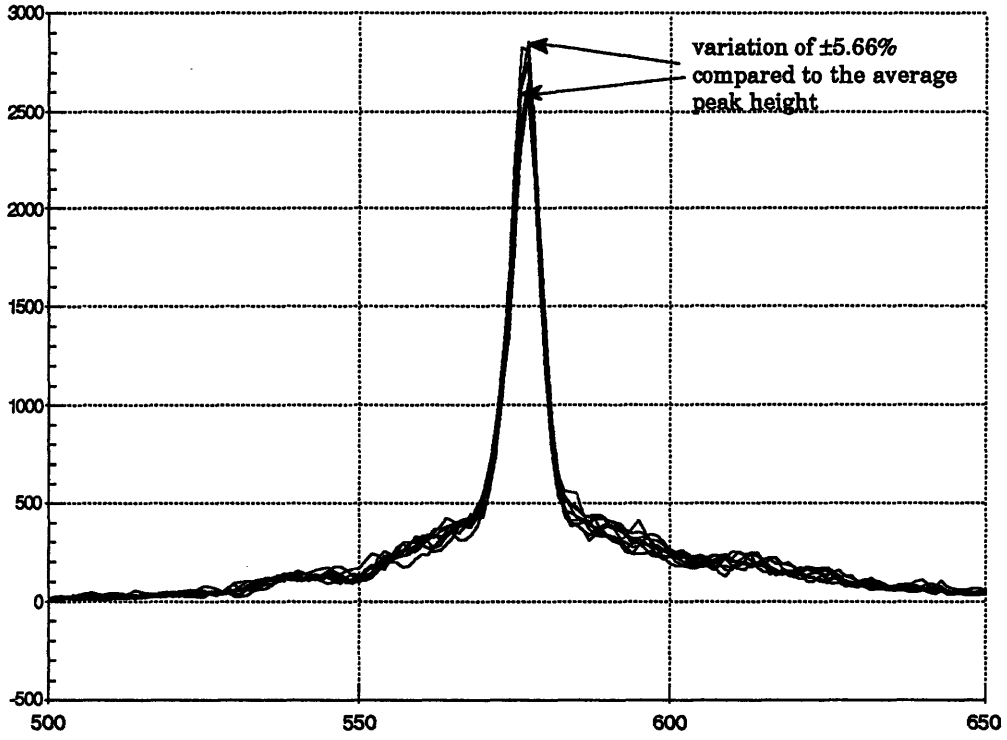

Data file : V72SEE

Figure 3.5 : Dips generated in the gain curve of the laser by oxygen absorption

An experimental curve obtained with the accumulation of 500 shots of the laser is compared to the theoritical curve already shown in Figure 1.1 and coming from Reference # 10 Lee & Hanson

Conditions : 500 pulses/spectrum
Exposure : 10000 ms
P ≈ 1.66 W
Grating 3600 g/mm @ 386 nm

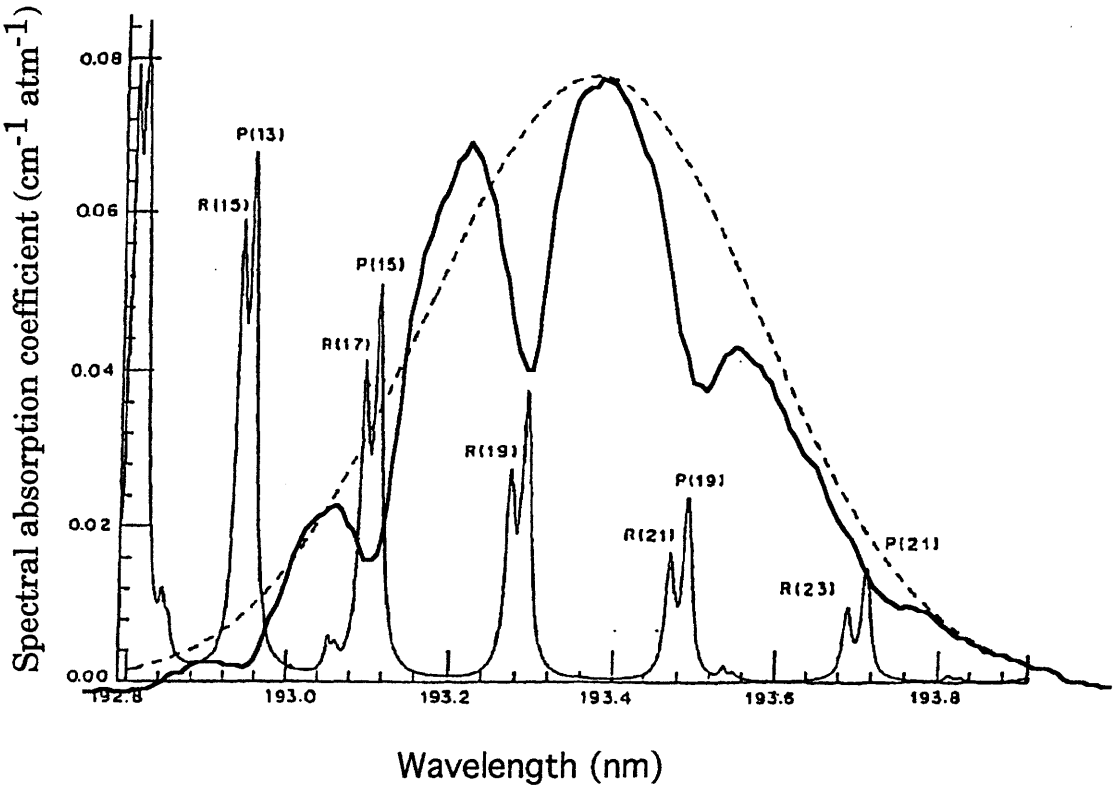

Data file : D72U10

Figure 3.6 : **General experimental set-up**

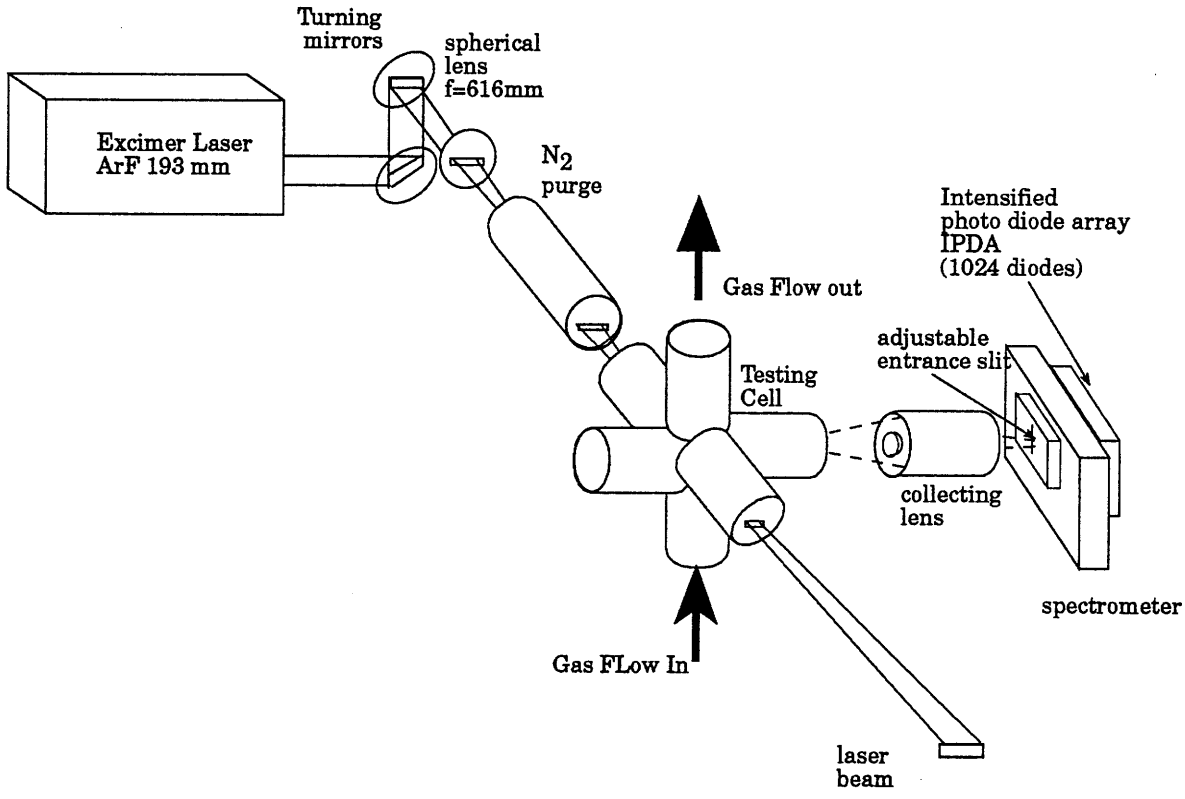

Figure 3.7 : **Spectrometer schematic**

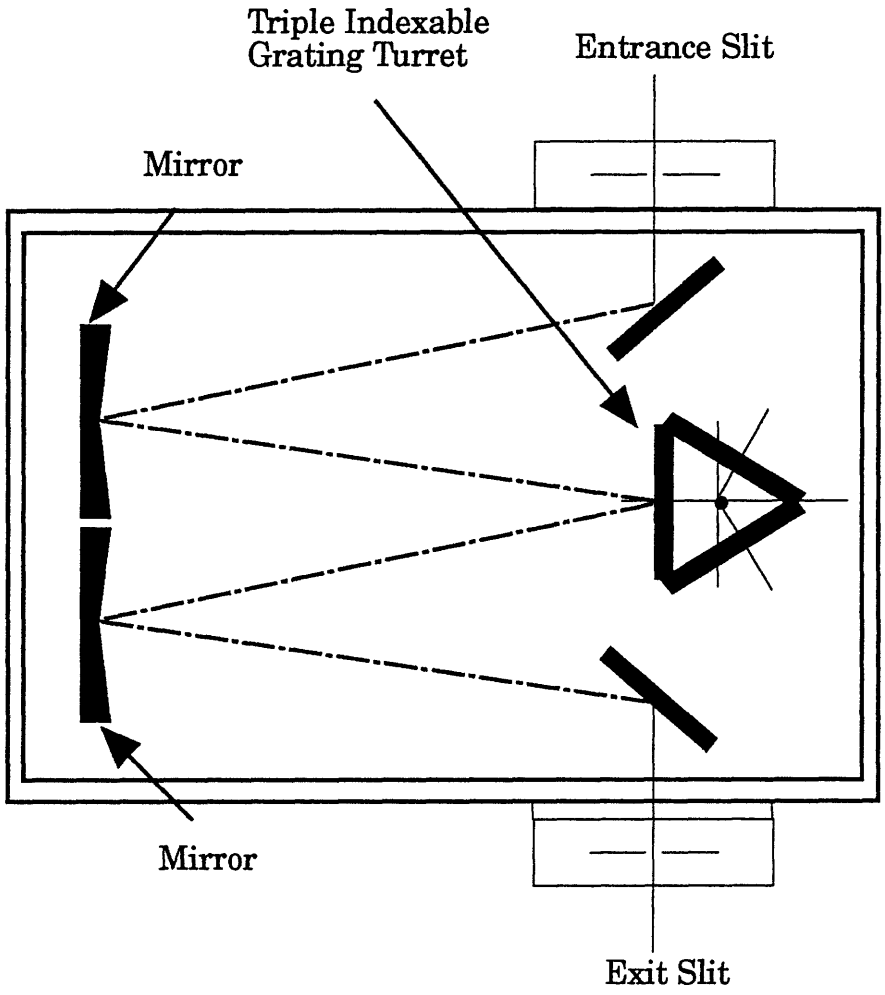

Figure 3.8 : **Imaging Lens**

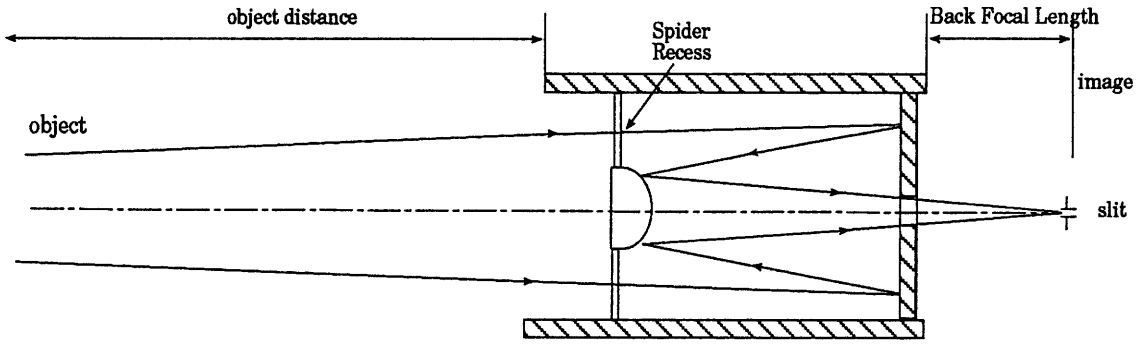

Figure 3.9 : **Testing cell**

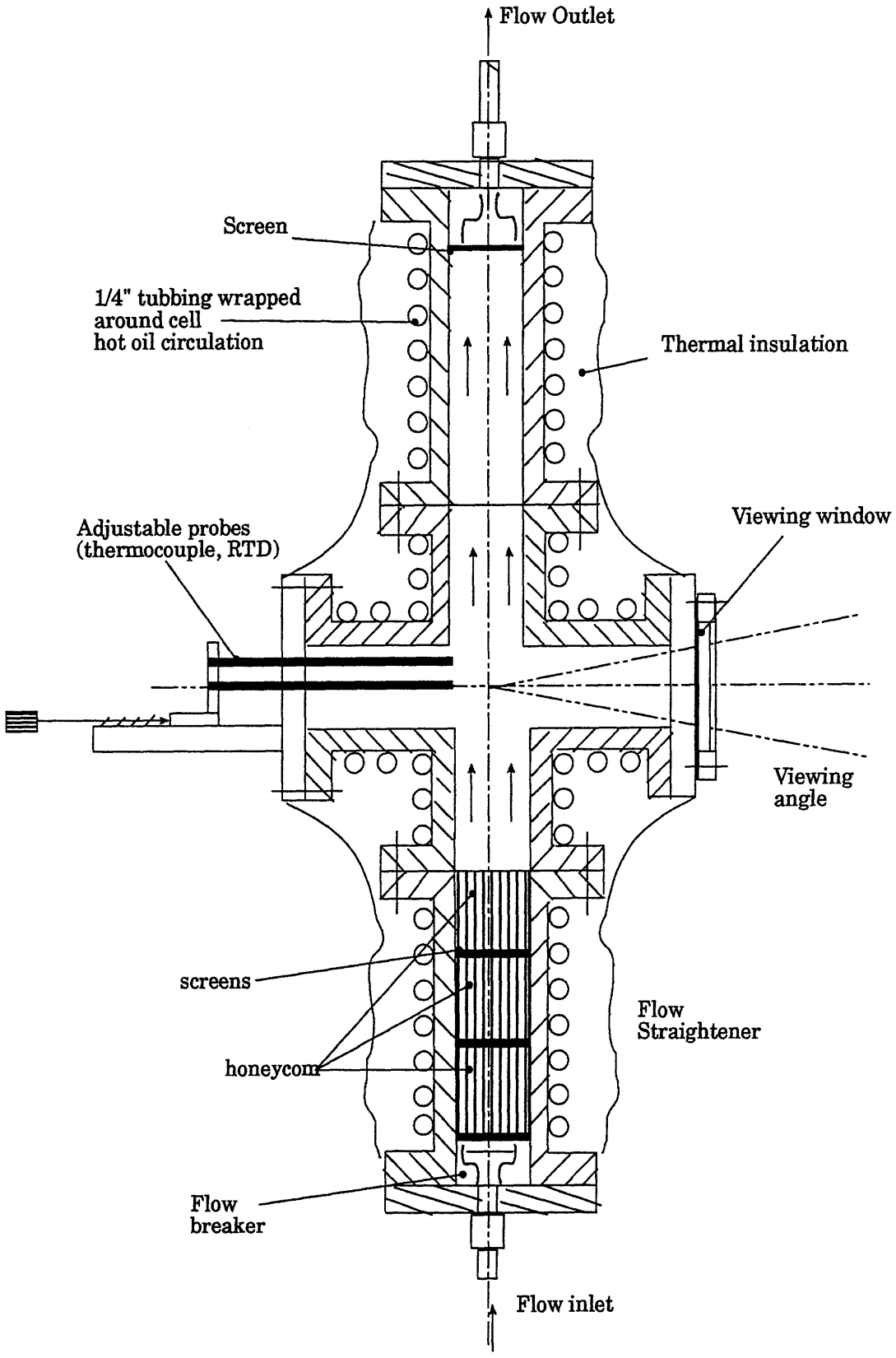

Figure 4.1 : Heat test D42 - general data

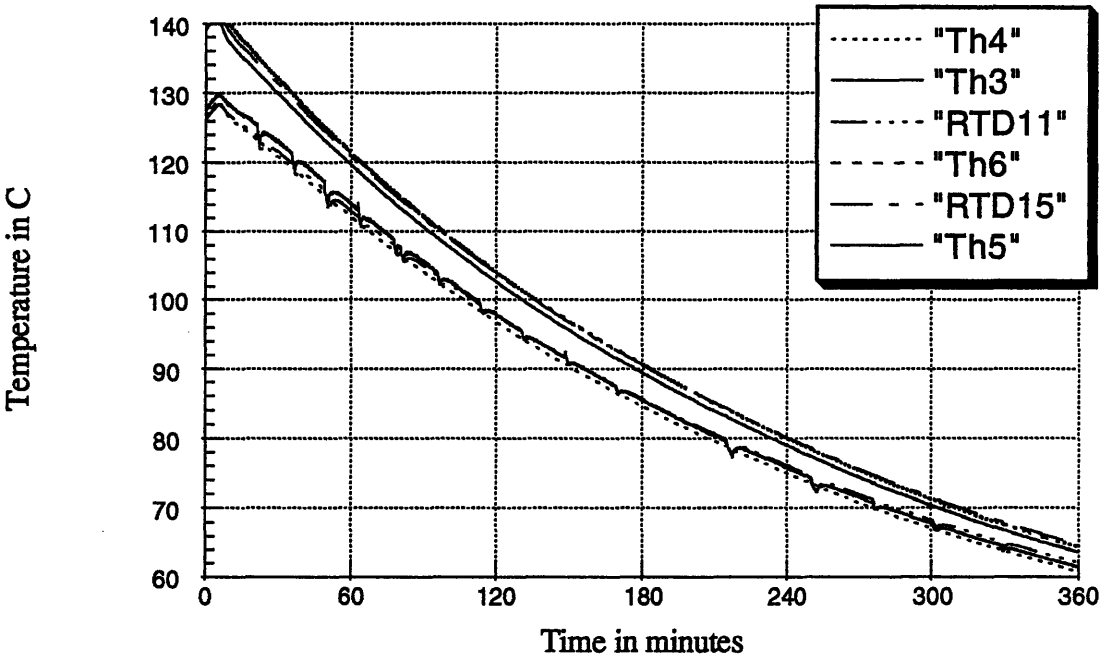

Data File : D42 Temp

Figure 4.2 : **Heat test - calibration curve "raw" data**

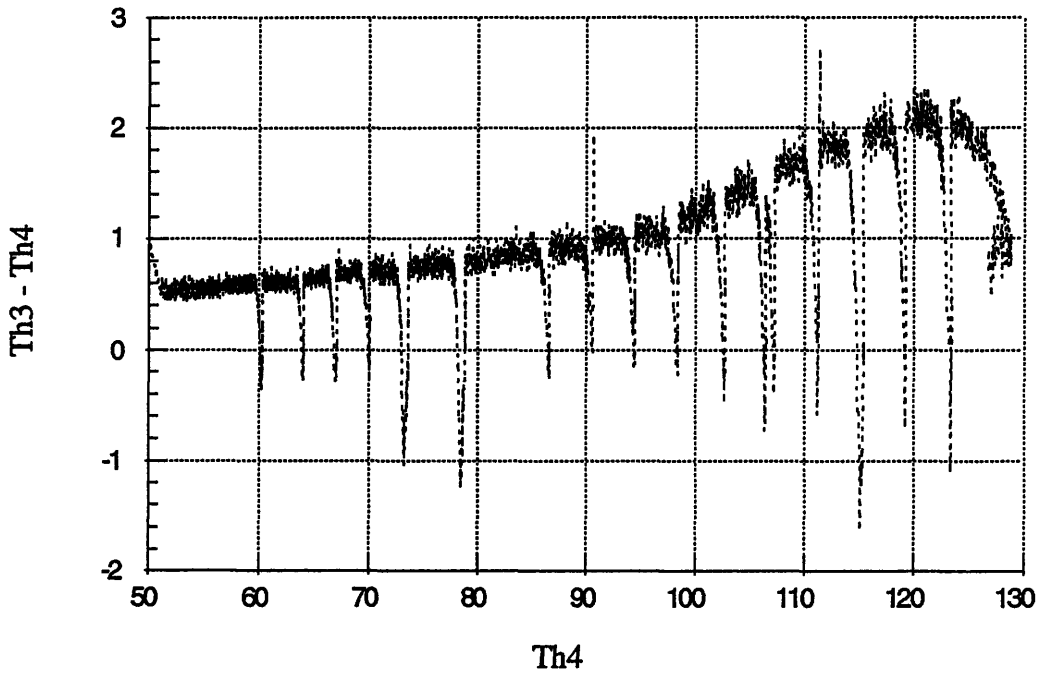

Data File : D42 Temp

Figure 4.3 : **Heat test - calibration curve after smoothing with a window of 10 points**

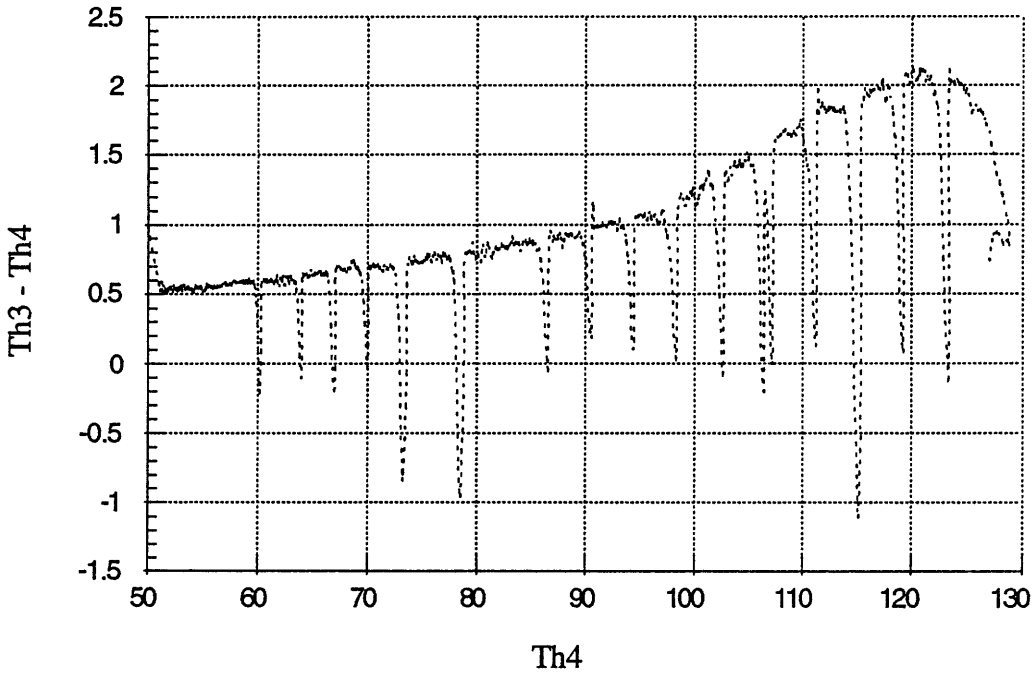

Data File : D42 Temp

Figure 4.4 : **Heat test V72 - general data**

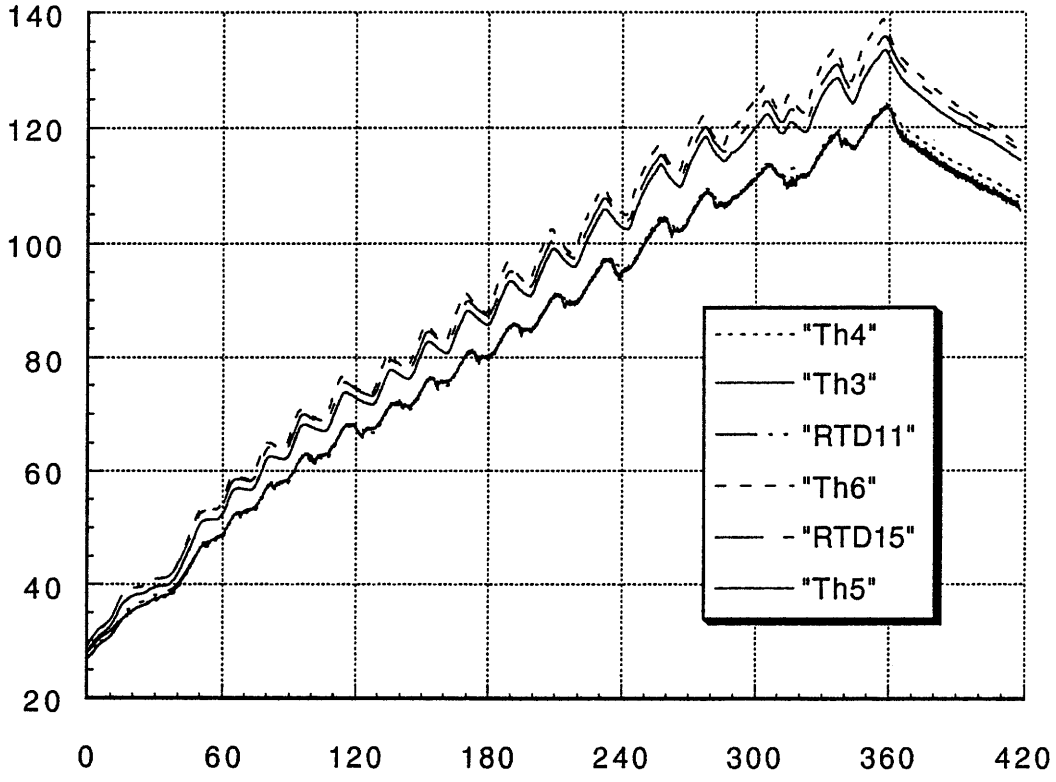

Figure 4.5 : Heat test description of a data acquisition

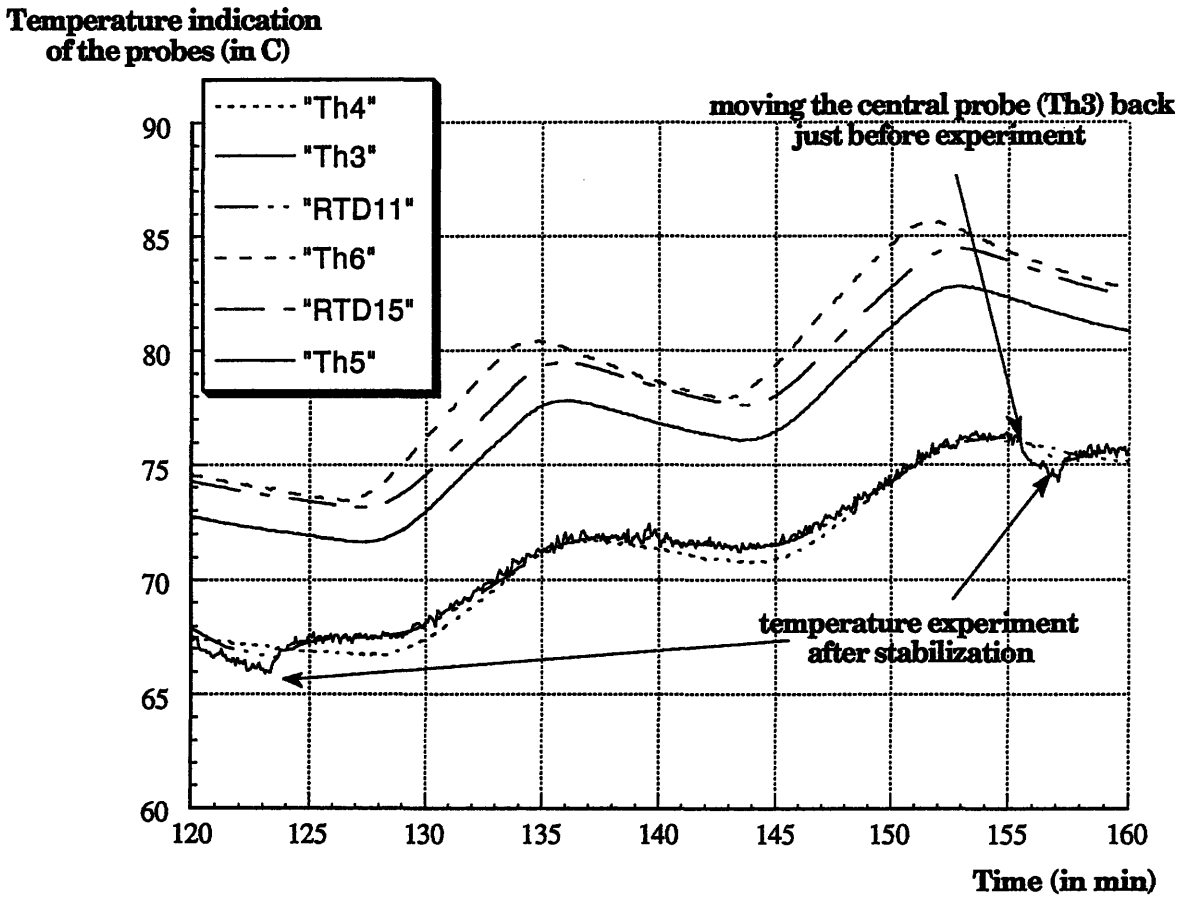

Data File : V72 Temp

Figure 5.1 : Lorentzian curve fitting test V72A Spect #3 - O_2 Raman

Conditions : 100 pulses/spectrum
Exposure : 1995 ms
P : unknown
Grating 1200 g/mm @ 234 nm

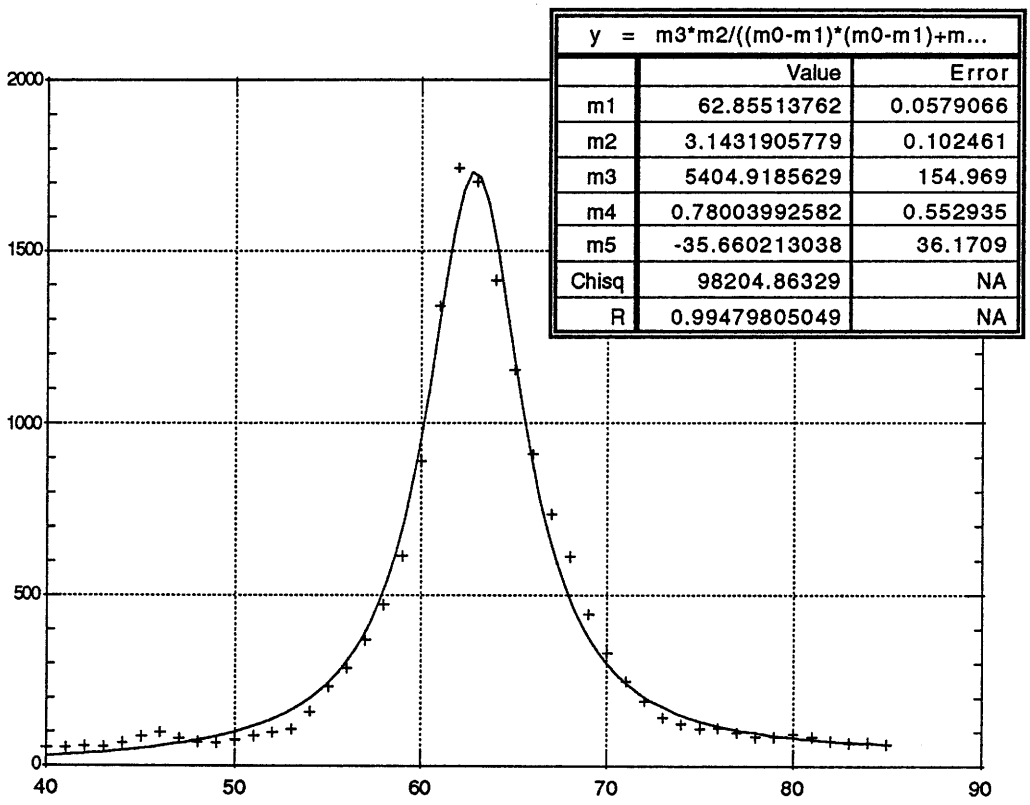

Data file : V72A-Series

Figure 5.2 : Lorentzian curve fitting test V72B#3 - O2 Raman peak

Conditions : 100 pulses/spectrum
Exposure : 1995 ms
P : unknown
Grating 1200 g/mm @ 234 nm

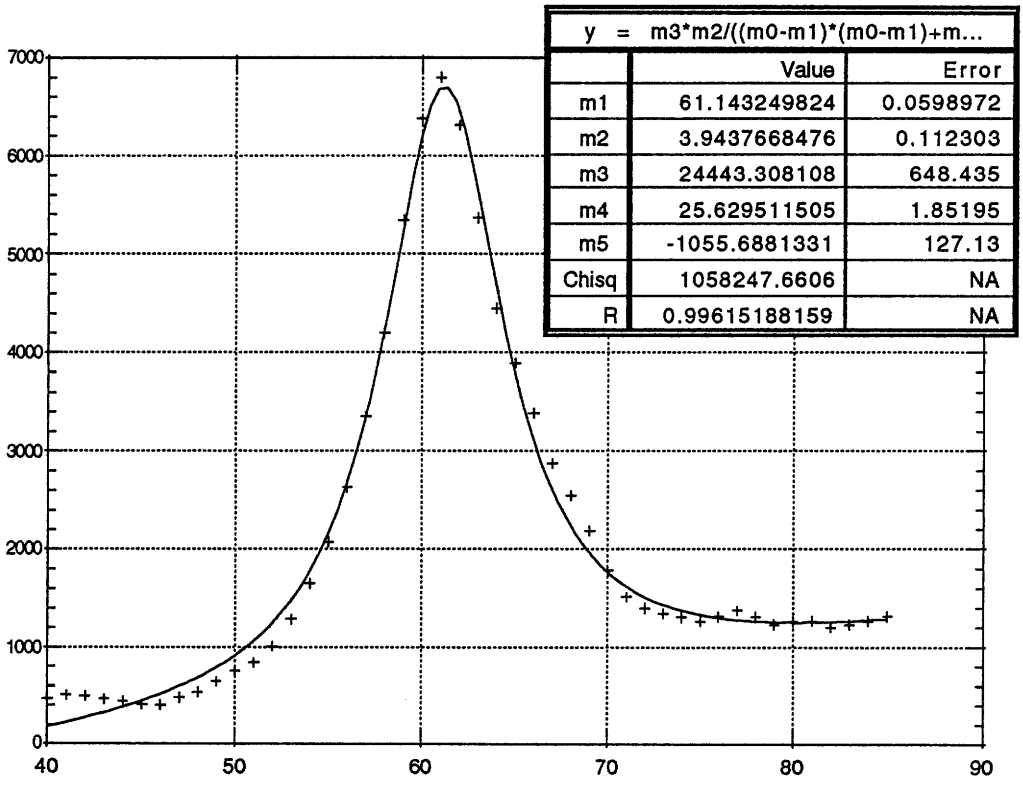

Data file : V72B-Series

Figure 5.3 : Lorentzian curve fitting test V72A #3 - N_2 Raman peak

Conditions : 100 pulses/spectrum
Exposure : 1995 ms
P : unknown
Grating 1200 g/mm @ 234 nm

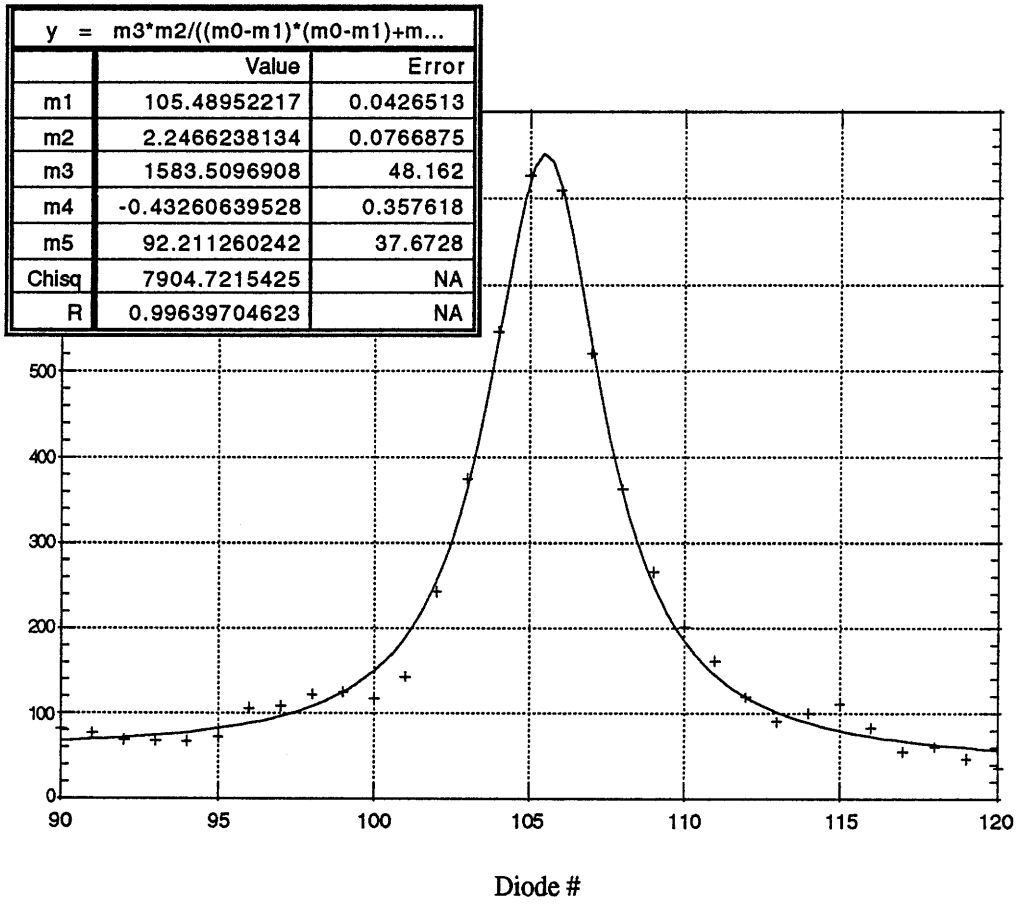

Data file : V72A-Series

Figure 5.4 : Lorentzian curve fitting test V72B #3 - N_2 Raman peak

Conditions : 100 pulses/spectrum
Exposure : 1995 ms
P : unknown
Grating 1200 g/mm @ 234 nm

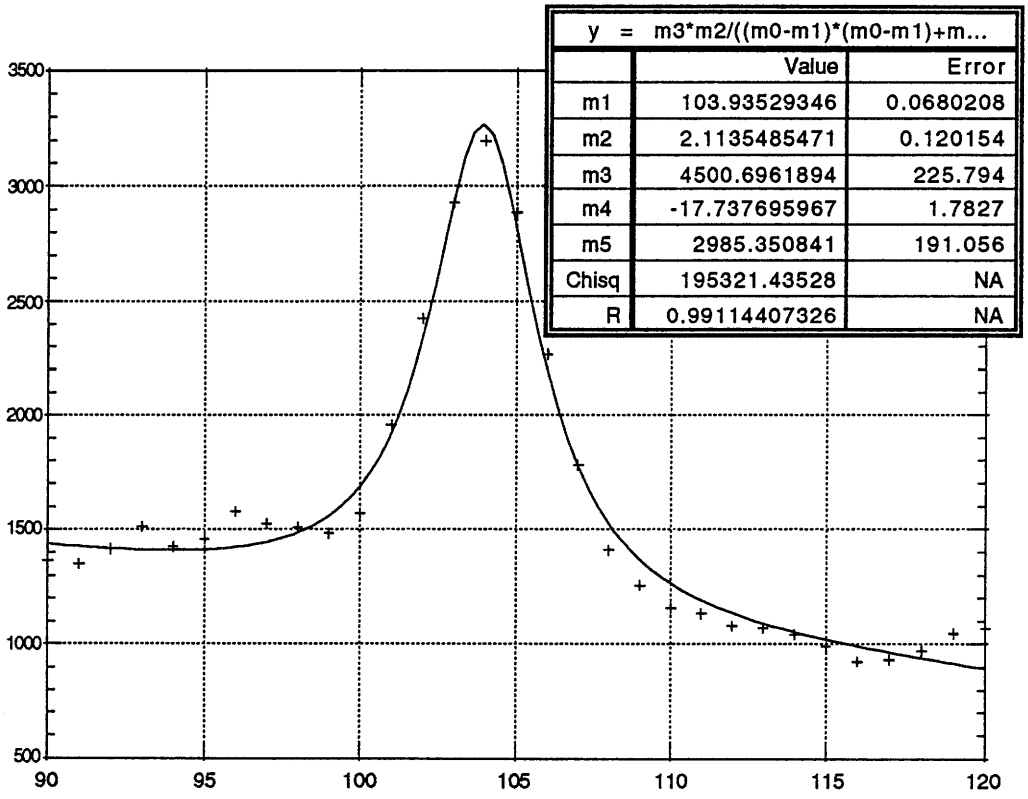

Data file : V72B-Series.

Figure 5.5 : Lorentzian curve fitting test V72A #3 - LIF 4.4 peak

Conditions : 100 pulses/spectrum
Exposure : 1995 ms
P : unknown
Grating 1200 g/mm @ 234 nm

y = m3*m2/((m0-m1)*(m0-m1)+m...		
	Value	Error
m1	327.54108926	0.047984
m2	2.3015714239	0.080944
m3	1420.1371657	44.4579
m4	334.11695732	0.0440731
m5	2.1378582777	0.0754598
m6	1381.0085462	42.867
m7	0.14586641901	0.115318
m8	-25.758051898	38.1052
Chisq	12390.986336	NA
R	0.99752576805	NA

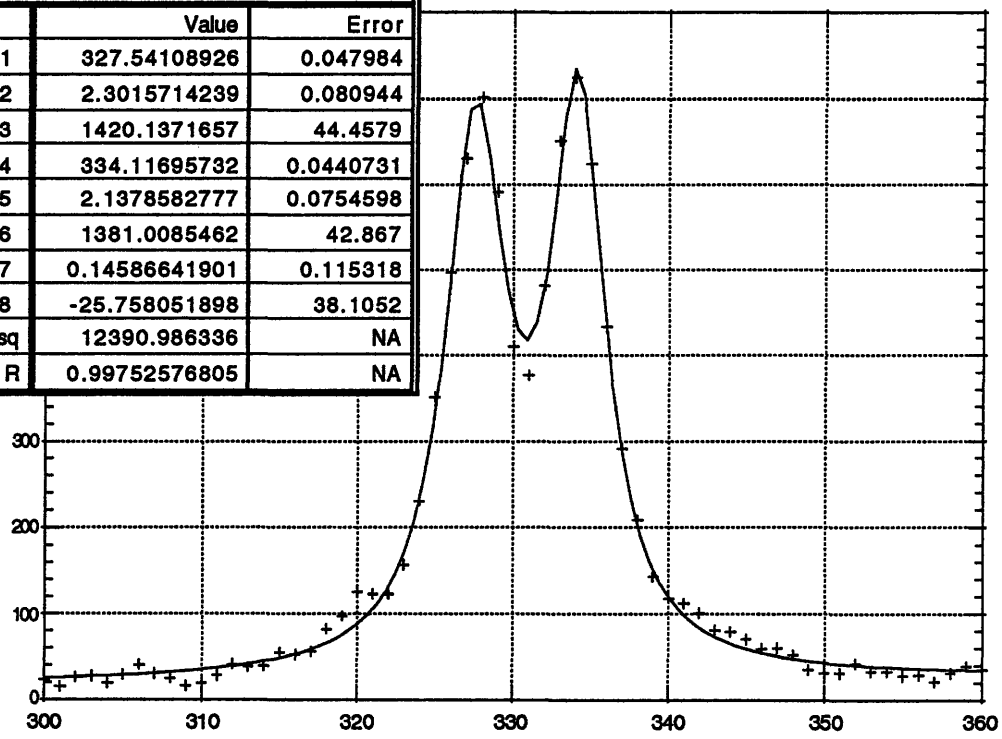

Data file : V72A-Series

Figure 5.6 : Lorentzian curve fitting test V72B #3 - LIF 4.4 peak

Conditions : 100 pulses/spectrum
Exposure : 1995 ms
P : unknown
Grating 1200 g/mm @ 234 nm

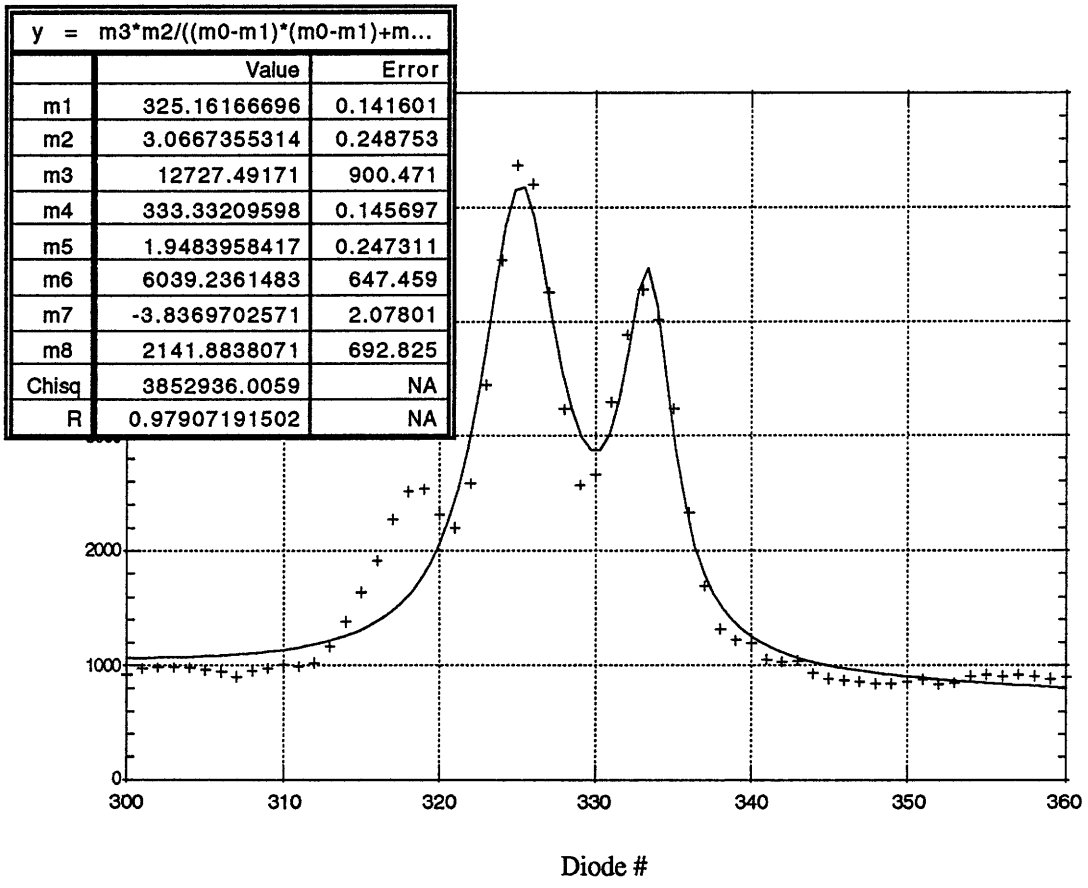

Data file : V72B-Series

Figure 5.7 : Lorentzian curve fitting test V72A #3 - LIF 4.7 peak

Conditions : 100 pulses/spectrum
Exposure : 1995 ms
P : unknown
Grating 1200 g/mm @ 234 nm

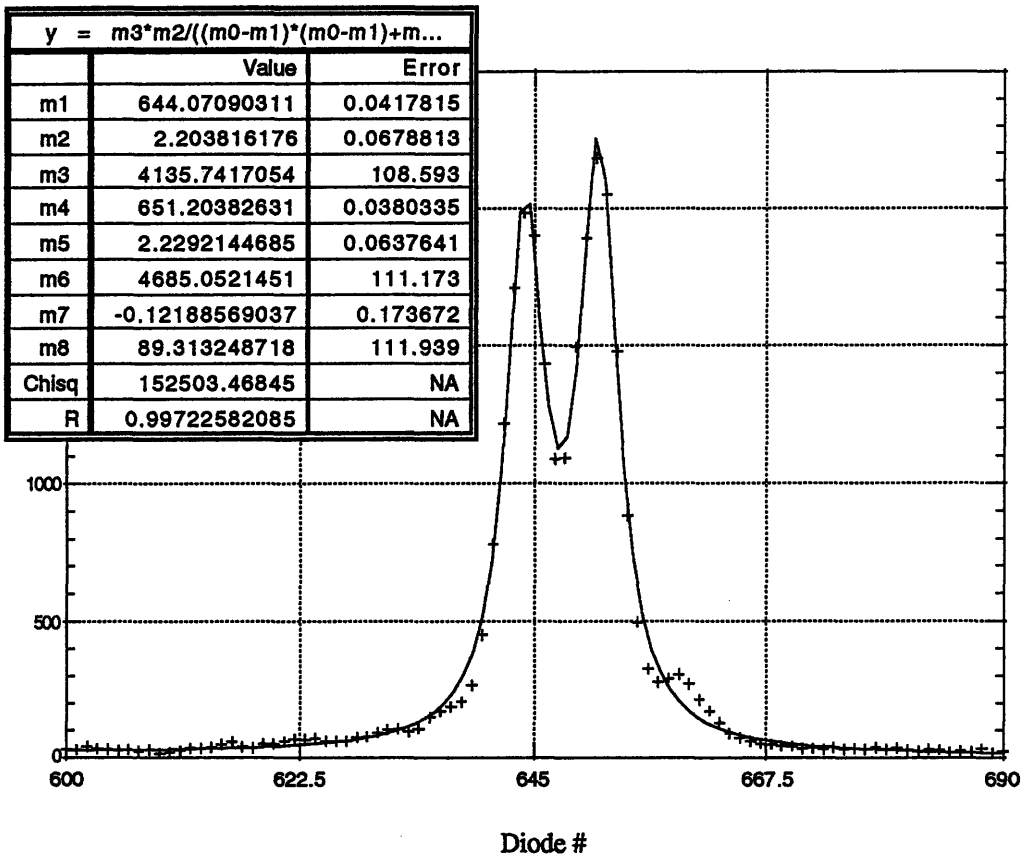

Data file : V72A-Series

Figure 5.8 : Lorentzian curve fitting test V72B #3 - LIF 4.7 peak

Conditions : 100 pulses/spectrum
Exposure : 1995 ms
P : unknown
Grating 1200 g/mm @ 234 nm

y = m3*m2/((m0-m1)*(m0-m1)+m...		
	Value	Error
m1	642.33109866	0.054497
m2	2.1555042841	0.0892028
m3	10649.127421	380.425
m4	649.50653562	0.0516257
m5	2.4196988542	0.0869513
m6	13713.617708	412.212
m7	-3.724593048	0.601815
m8	2839.9378648	388.239
Chisq	1834044.165	NA
R	0.99550324279	NA

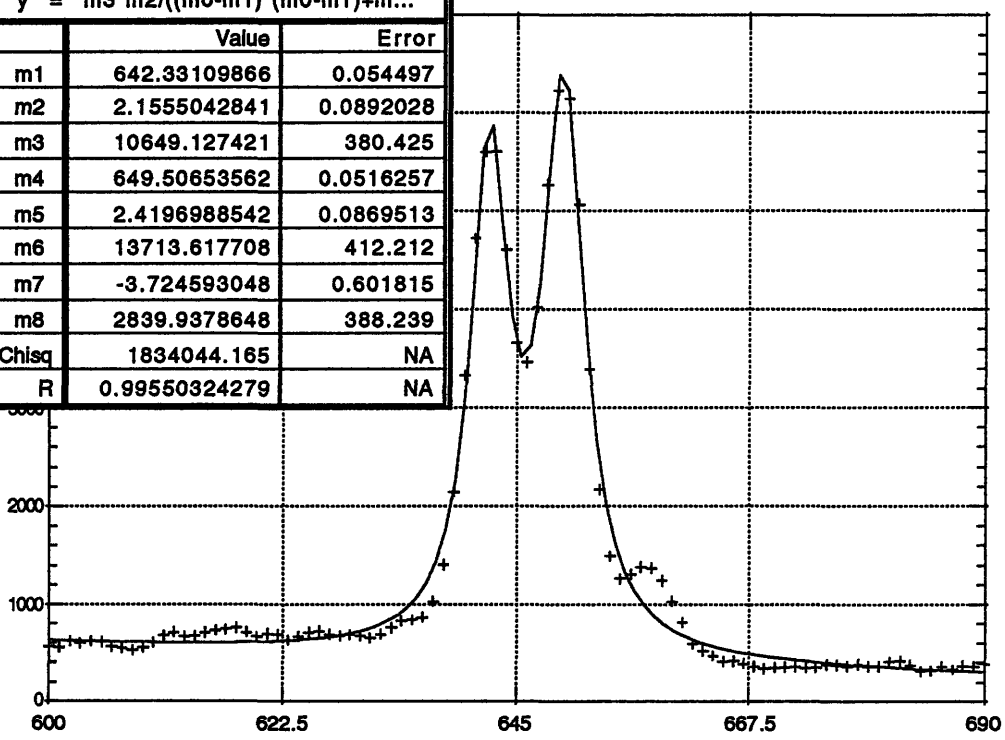

Data file : V72B-Series

Figure 5.9 : Voigt curve fitting test V72A #3 - O2 Raman peak

Conditions : 100 pulses/spectrum
Exposure : 1995 ms
P : unknown
Grating 1200 g/mm @ 234 nm

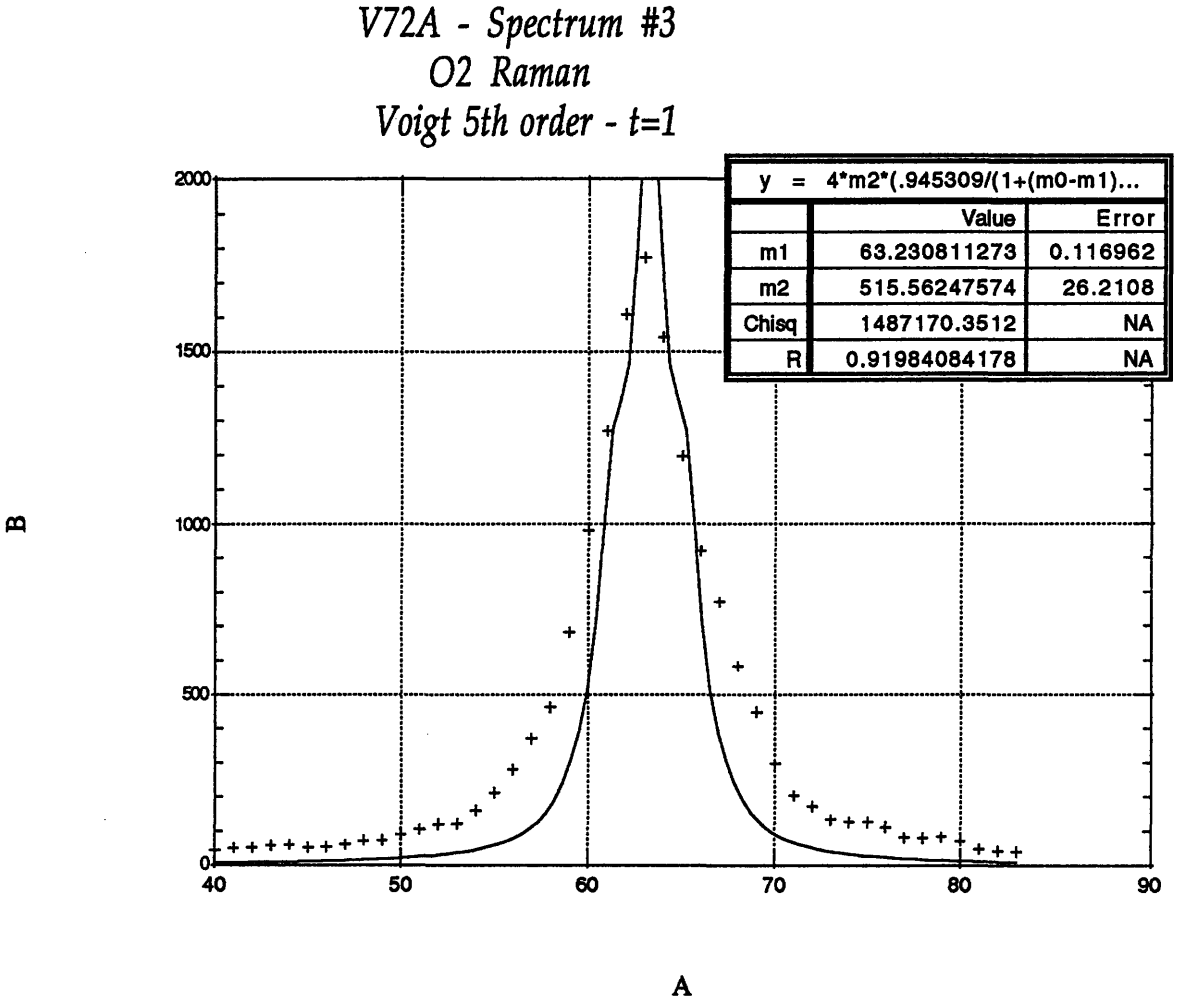

Data file : V72A-Series

Figure 5.10 : Voigt curve fitting test V72A #1 - O_2 Raman peak

Conditions : 100 pulses/spectrum
Exposure : 1995 ms
P : unknown
Grating 1200 g/mm @ 234 nm

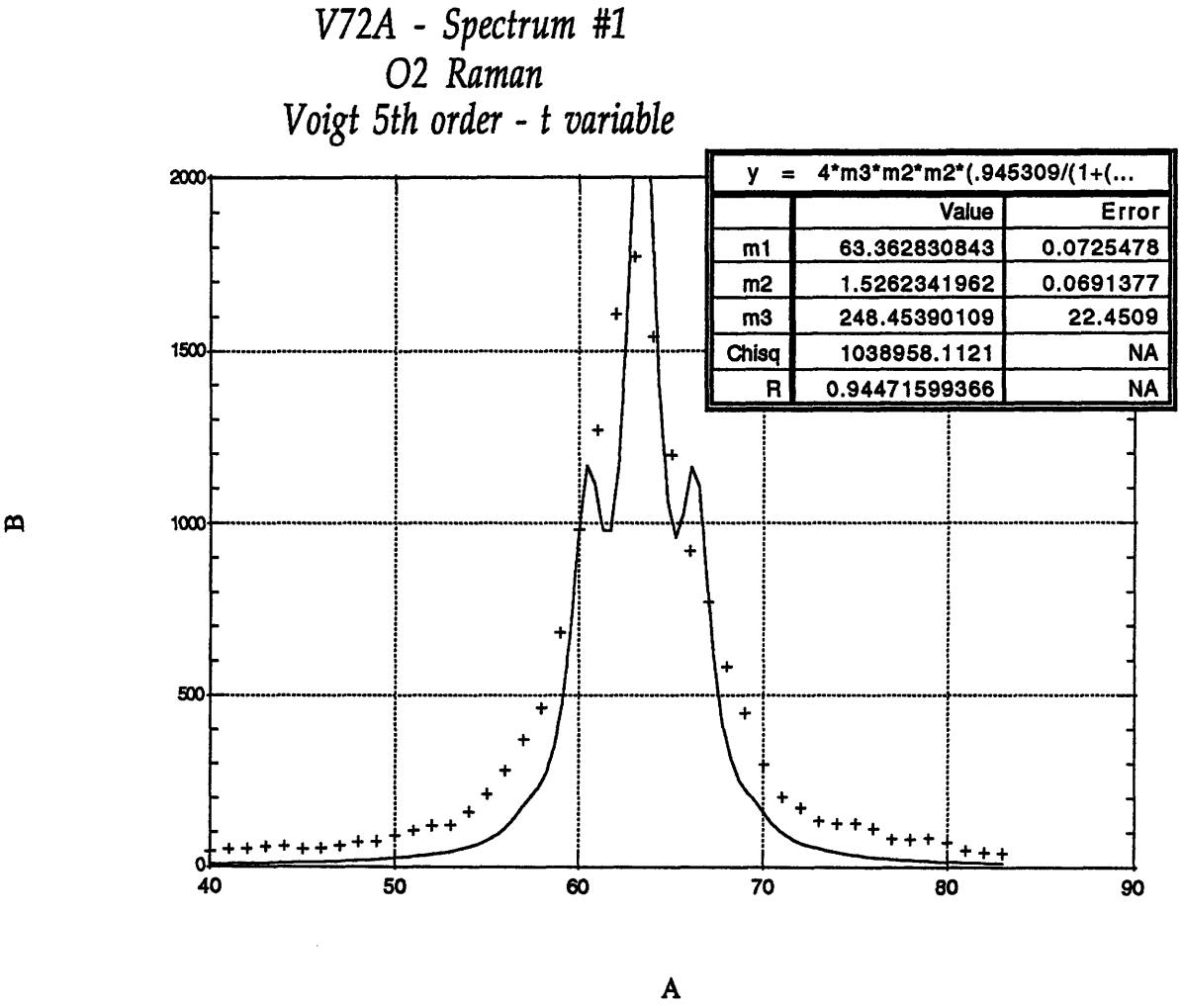

Data file : V72A-Series

Figure 5.11 : Comparison of data reduction procedures
File : V72 Sample
Procedure : curve fitting

Conditions : 100 pulses/spectrum
Exposure : 1995 ms
P : unknown
Grating 1200 g/mm @ 234 nm

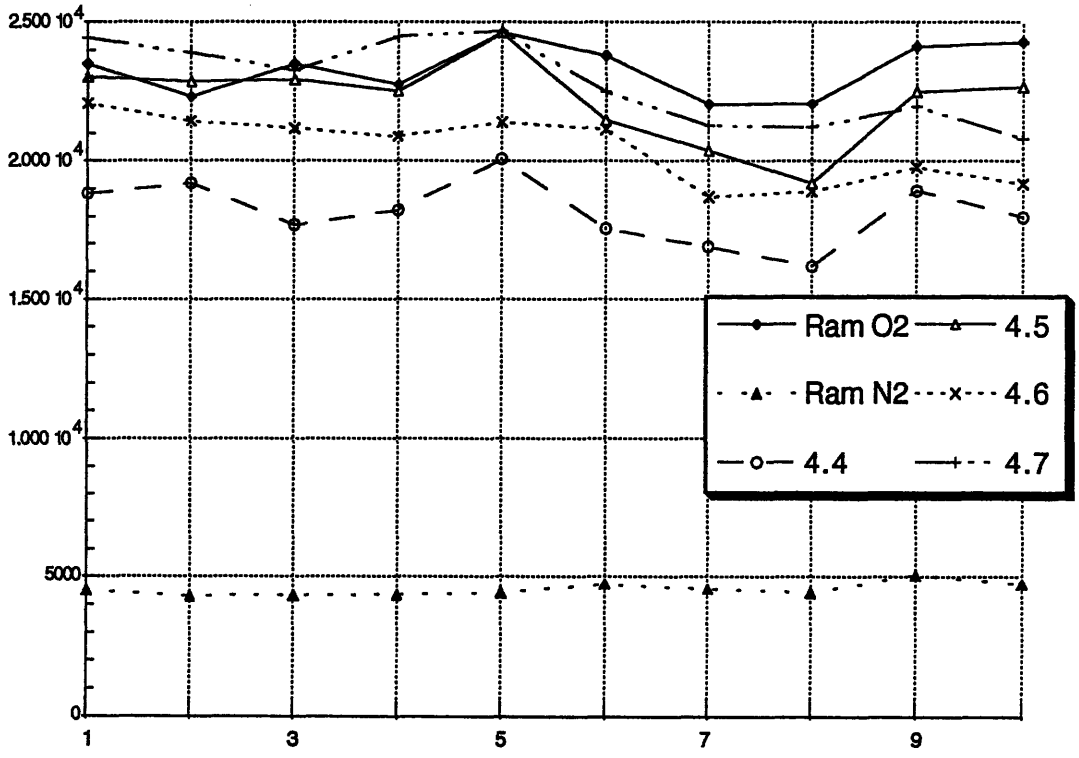

Data file : V72 Sample

Figure 5.12 : Comparison of data reduction procedures
File : V72 Sample
Procedure : empirical approach

Conditions : 100 pulses/spectrum
Exposure : 1995 ms
P : unknown
Grating 1200 g/mm @ 234 nm

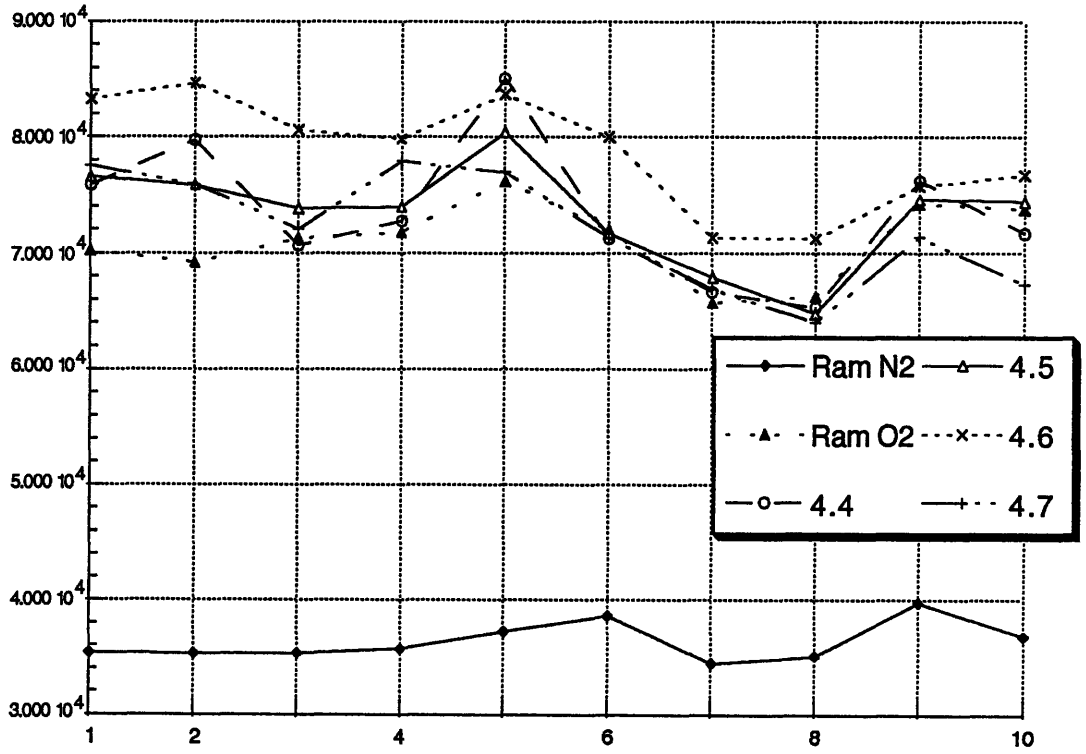

Data file : V72 Sample

Figure 5.13 : Comparison of data reduction procedures
File : V72A
Procedure : curve fitting

Conditions : 100 pulses/spectrum
Exposure : 1995 ms
P : unknown
Grating 1200 g/mm @ 234 nm

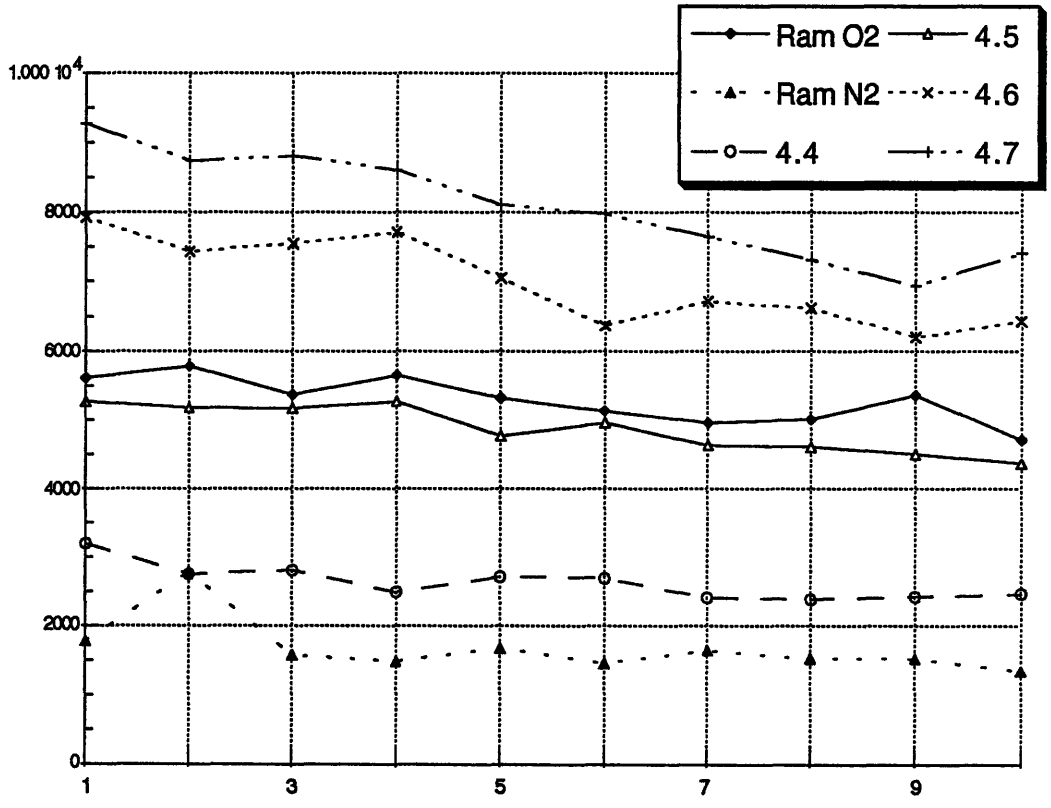

Data file : V72A-Series

Figure 5.14 : Comparison of data reduction procedures
File : V72A
Procedure : empirical approach

Conditions : 100 pulses/spectrum
Exposure : 1995 ms
P : unknown
Grating 1200 g/mm @ 234 nm

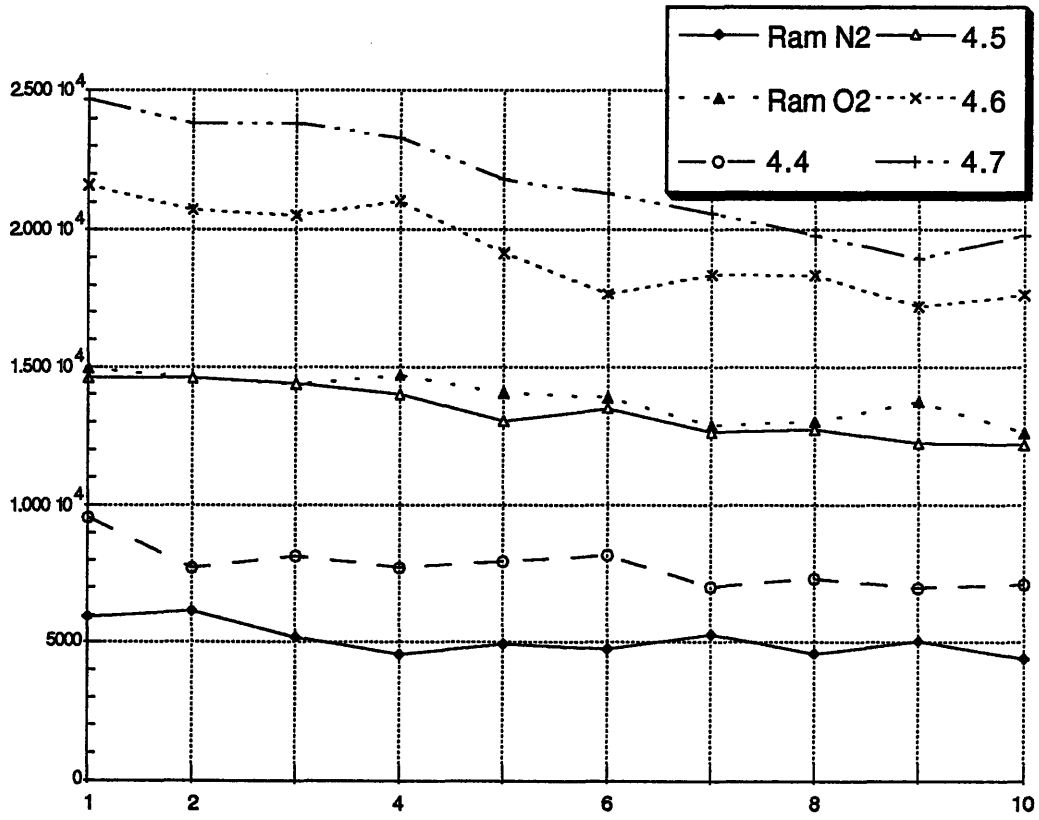

Data file : V72A-Series

Figure 5.15 : Calibration of the tuning position using the broad band emission

Conditions : 500 pulses/spectrum
Exposure : 10000 ms
P : 1.66 W
Grating 3600 g/mm @ 386 nm

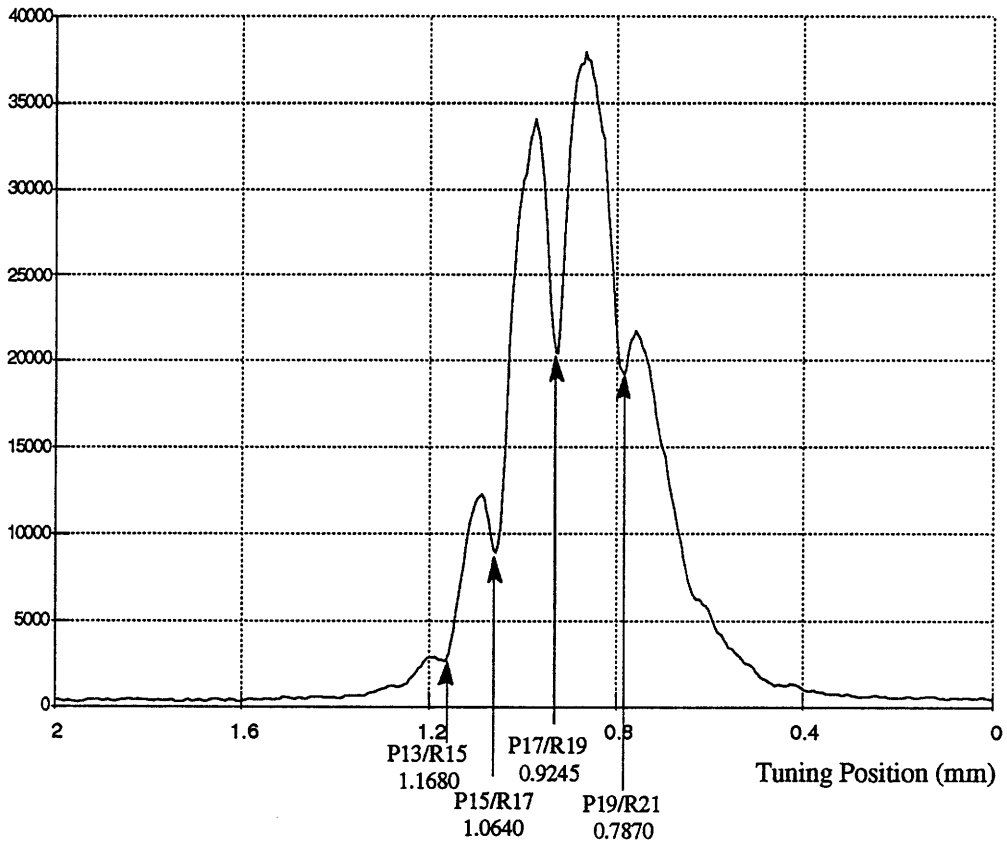

Data file : D72U10

Figure 5.16 : Example of O_2 LIF spectrum for the laser broad band

Conditions : 100 pulses/spectrum
Exposure : 1995 ms
P : unknown
Grating 1200 g/mm @ 234 nm

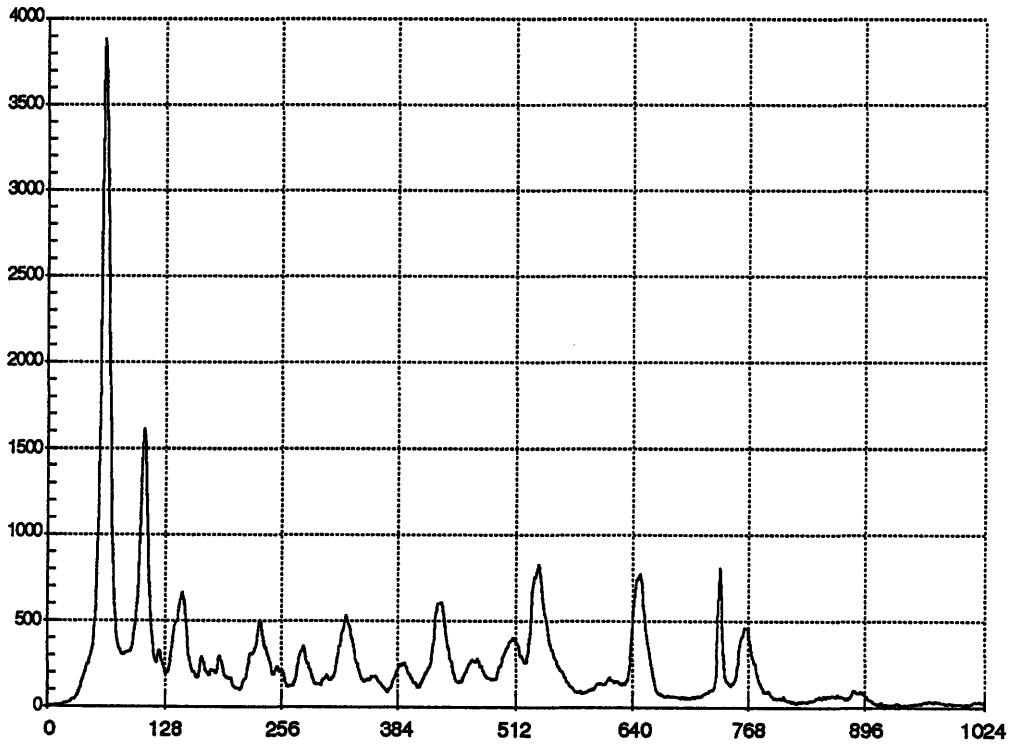

Data file : L73A-Series

Figure 5.17 : Example of O2 LIF spectrum for the laser tuned in the P19 peak

Conditions : 100 pulses/spectrum
Exposure : 1995 ms
P : 0.90 W
Wv : see file name
Grating 1200 g/mm @ 234 nm

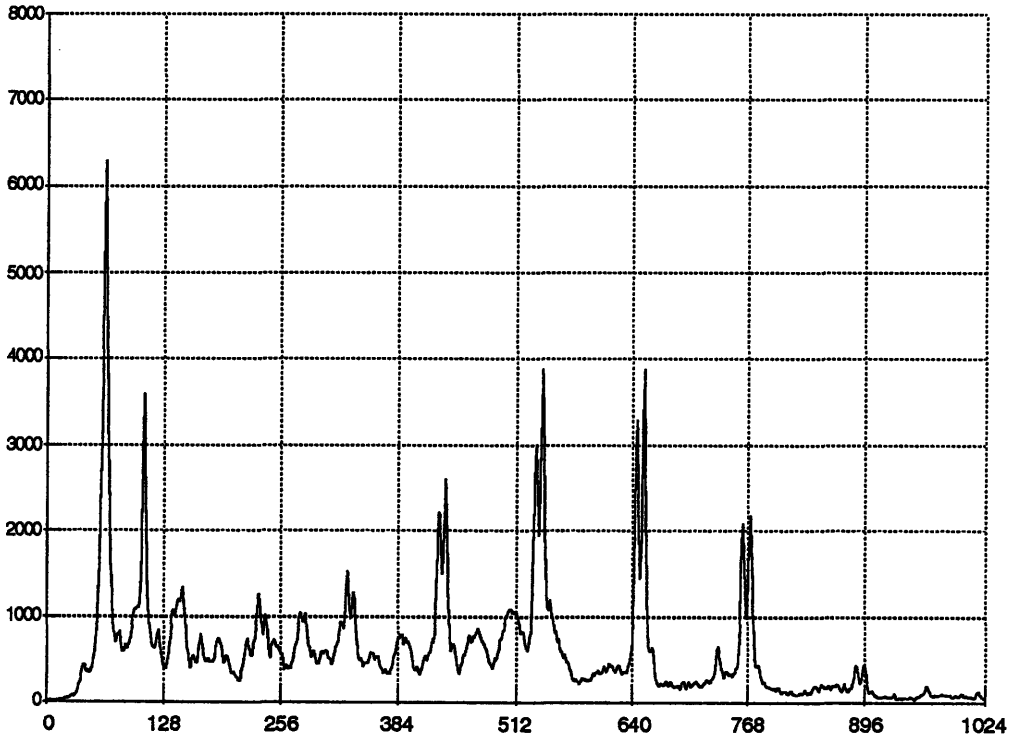

Data file : D72P19 #0.786

Figure 5.18 : Example of O_2 LIF spectrum for the laser tuned in the P13 peak

Conditions : 100 pulses/spectrum
Exposure : 1995 ms
P : 0.90 W
Wv : see file name
Grating 1200 g/mm @ 234 nm

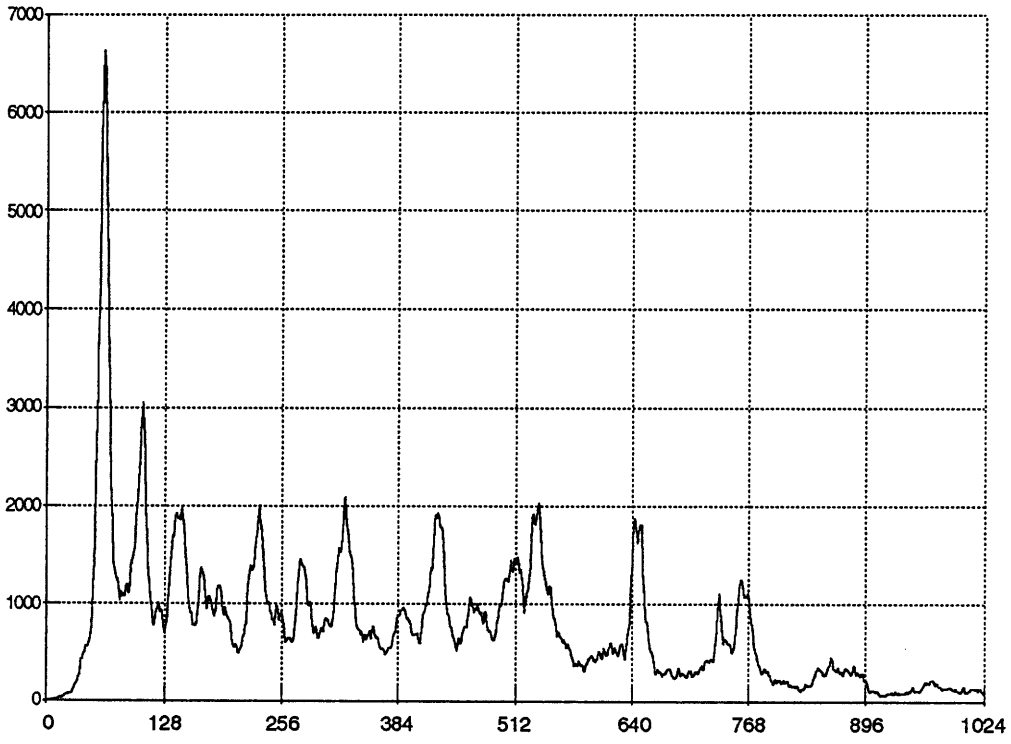

Data file : D72P13 #1.1680

Figure 5.19 : Example #1 of O_2 LIF spectrum for the laser tuned in the P15 peak

Conditions : 100 pulses/spectrum
Exposure : 1995 ms
P : 0.90 W
Wv : see file name
Grating 1200 g/mm @ 234 nm

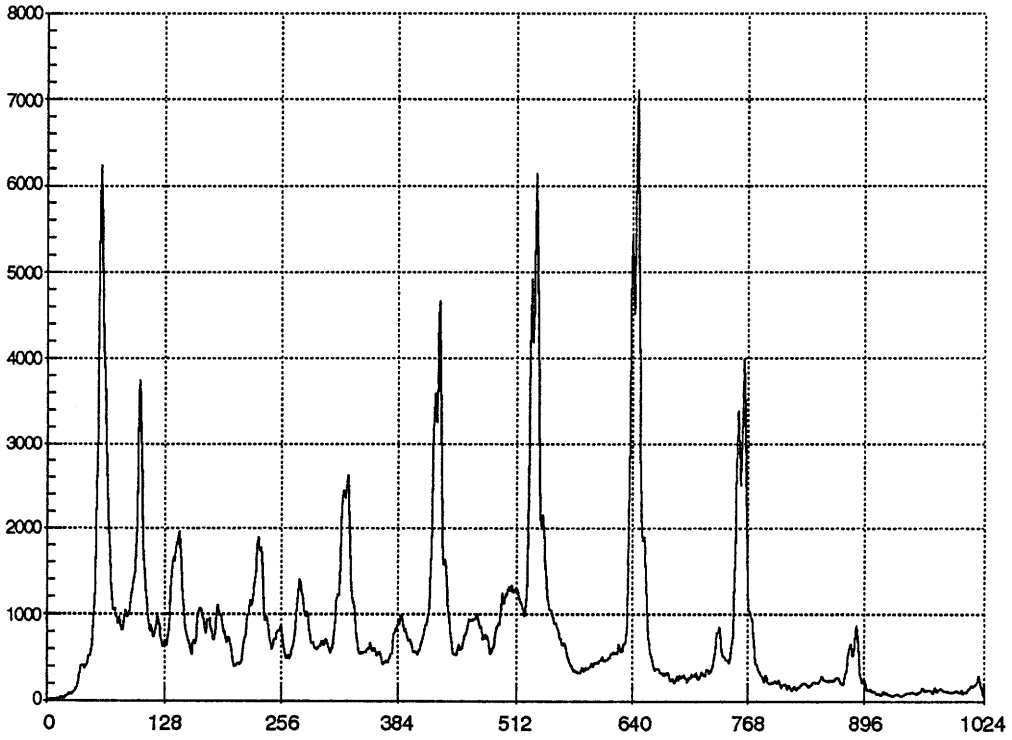

Data file : D72P15 #1.0520

Figure 5.20 : Example #2 of O_2 LIF spectrum for the laser tuned in the P15 peak

Conditions : 100 pulses/spectrum
Exposure : 1995 ms
P : 0.90 W
Wv : see file name
Grating 1200 g/mm @ 234 nm

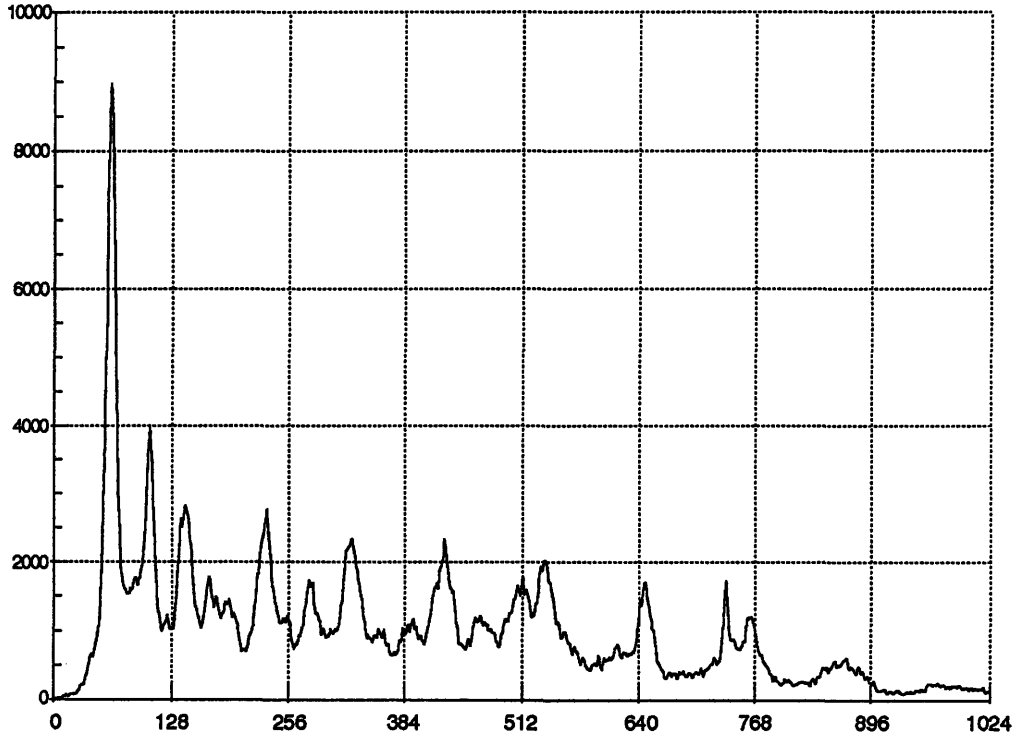

Data file : D72P15 #1.0630

Figure 5.21a : **Example of O2 LIF spectrum for the laser tuned close to the P17 peak**

(same conditions as previous series : P13, P15, P19)

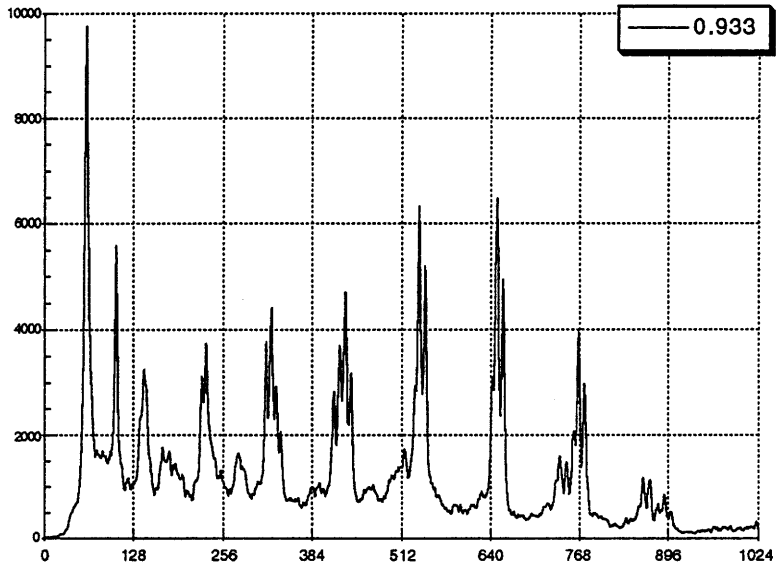

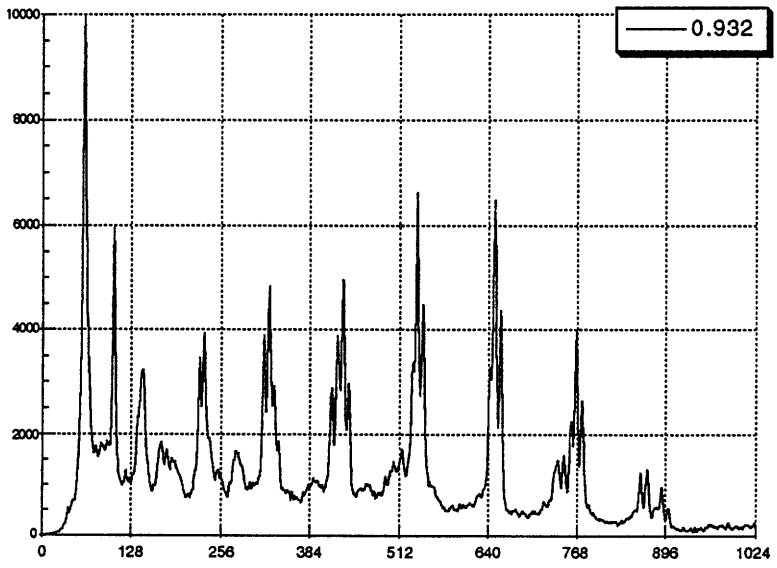

Figure 5.21b : **Example of O2 LIF spectrum for the laser tuned close to the P17 peak**

(same conditions as previous series : P13, P15, P19)

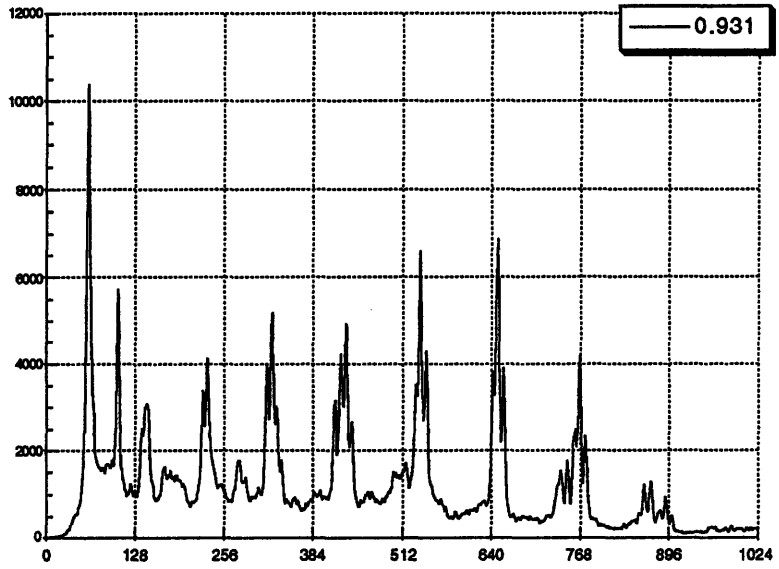

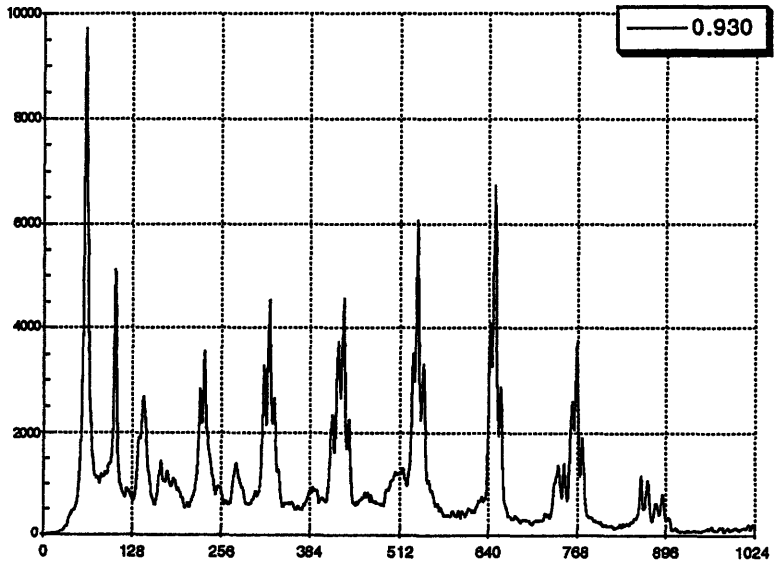

Figure 5.21c : **Example of O2 LIF spectrum for the laser tuned close to the P17 peak**

(same conditions as previous series : P13, P15, P19)

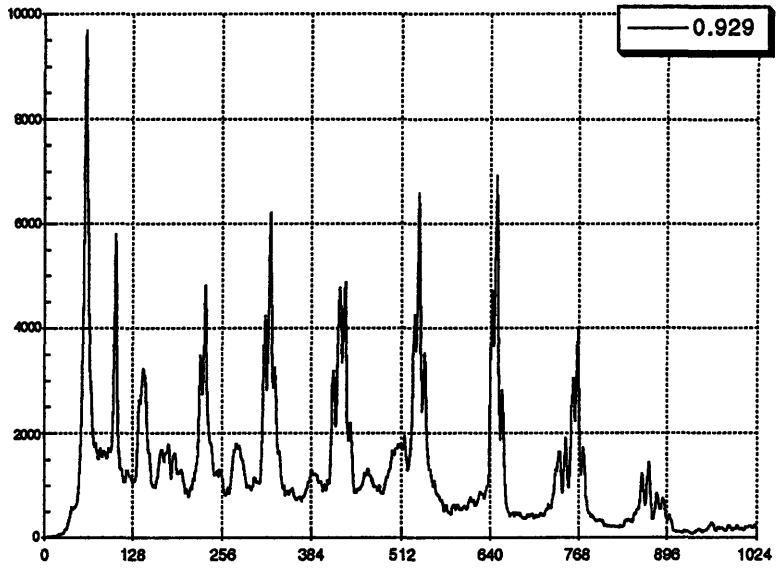

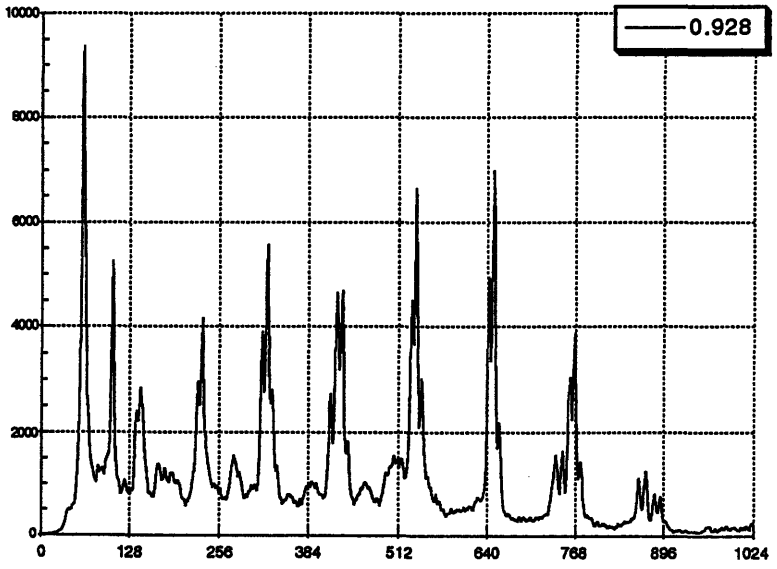

Figure 5.21d : **Example of O2 LIF spectrum for the laser tuned close to the P17 peak**
(same conditions as previous series : P13, P15, P19)

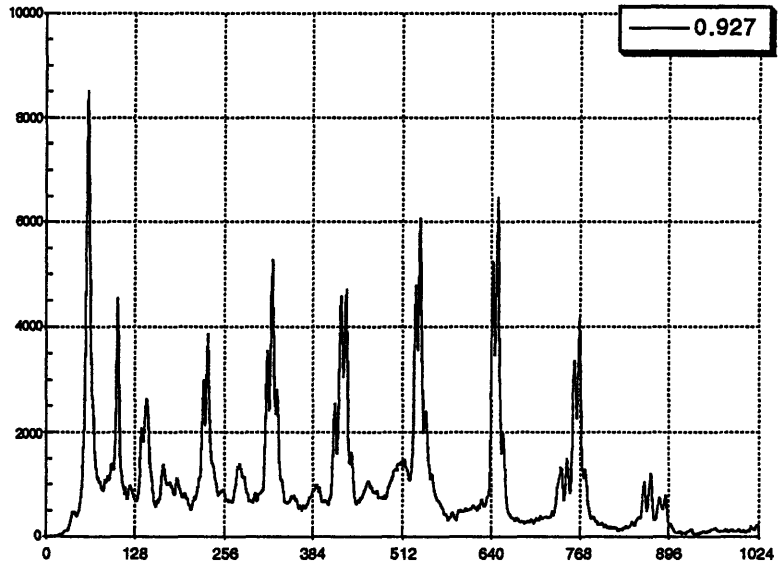

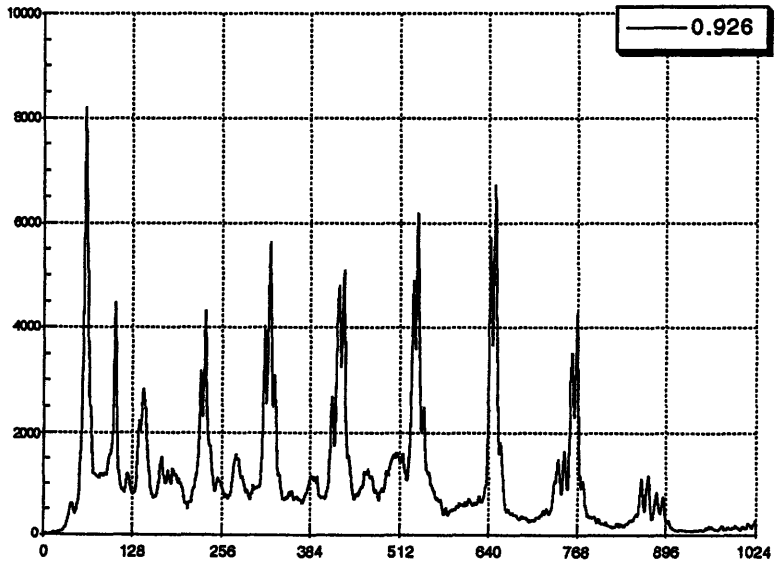

Figure 5.21e : **Example of O2 LIF spectrum for the laser tuned close to the P17 peak**

(same conditions as previous series : P13, P15, P19)

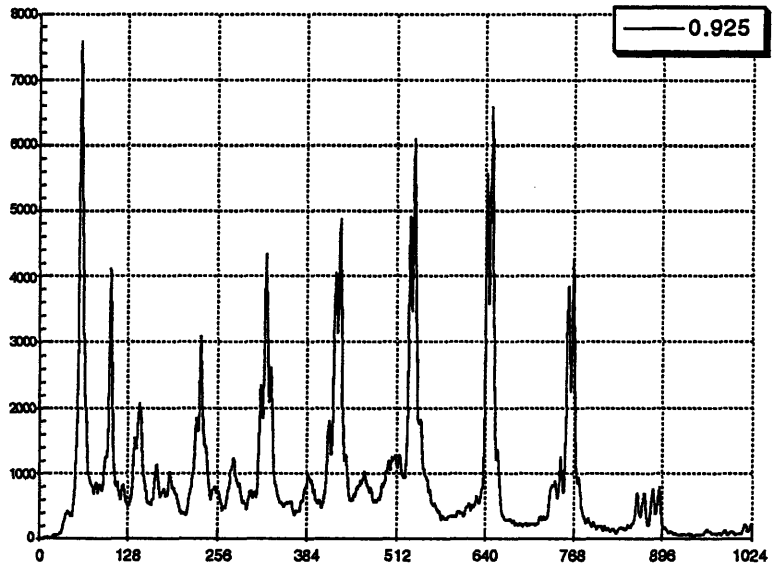

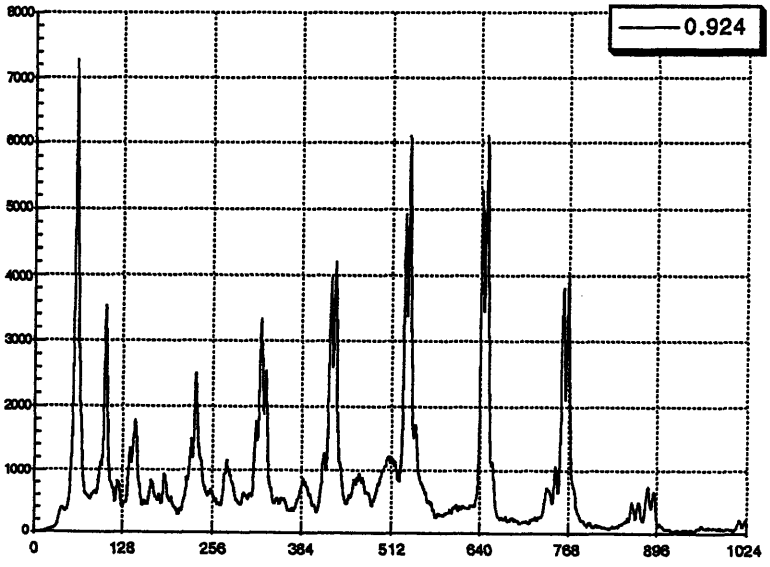

Figure 5.21f : **Example of O2 LIF spectrum for the laser tuned close to the P17 peak**

(same conditions as previous series : P13, P15, P19)

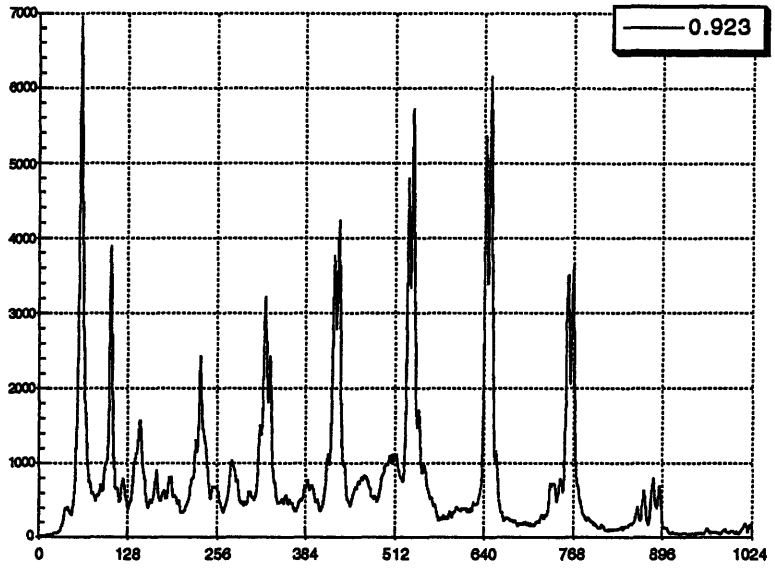

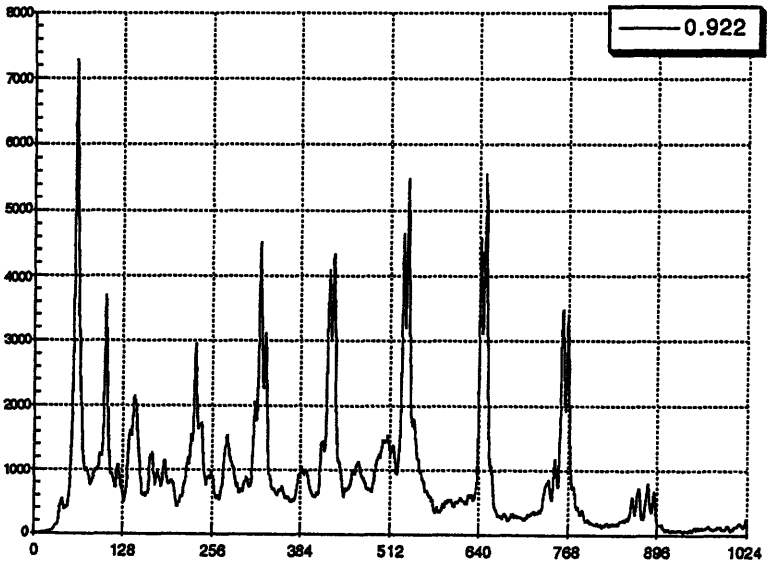

Figure 5.21g : **Example of O2 LIF spectrum for the laser tuned close to the P17 peak**

(same conditions as previous series : P13, P15, P19)

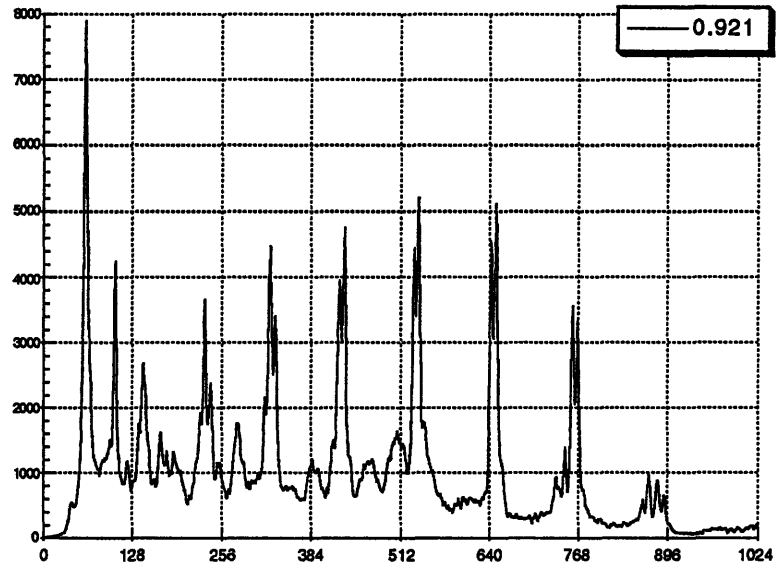

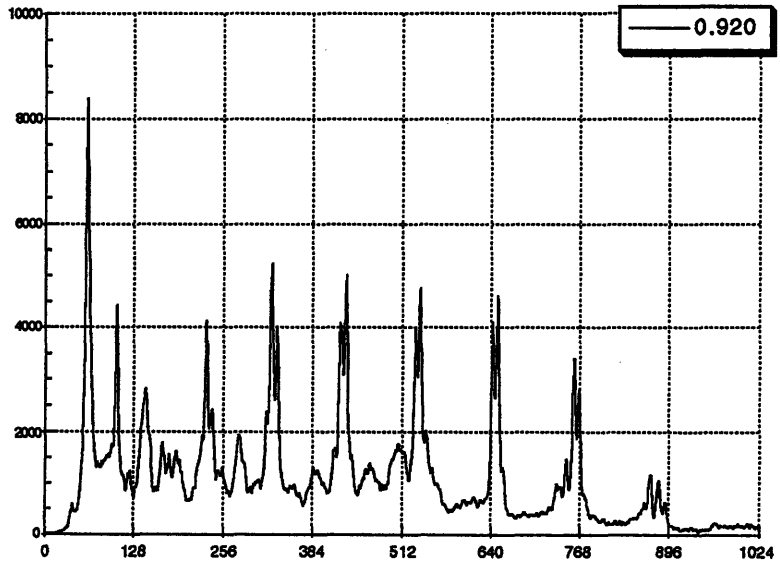

Figure 5.21h : **Example of O2 LIF spectrum for the laser tuned close to the P17 peak**
(same conditions as previous series : P13, P15, P19)

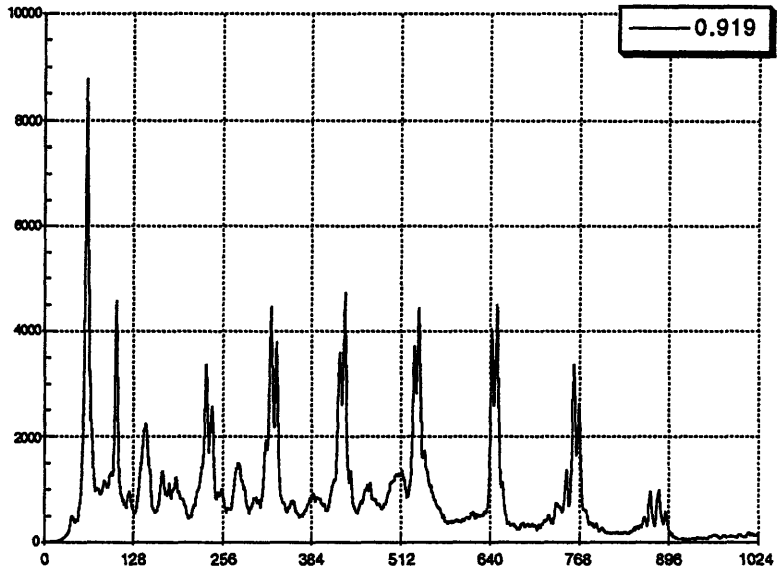

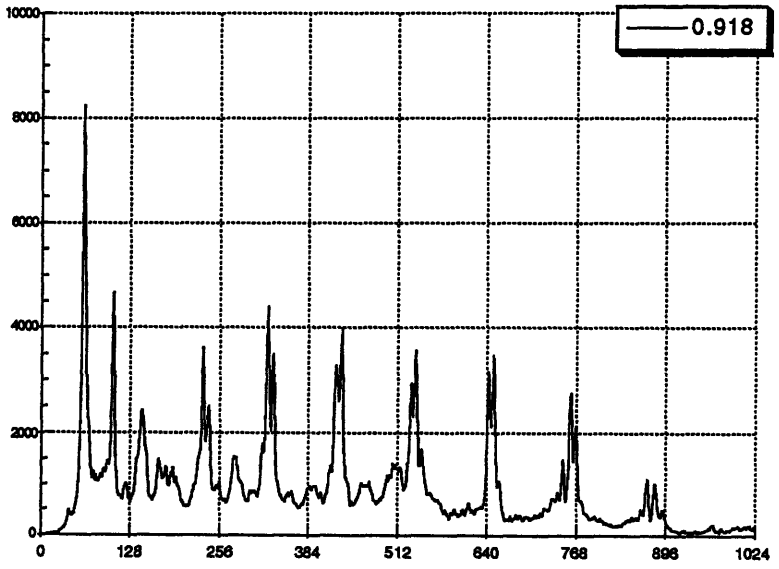

Figure 5.22 : Impact of purging on the broad band emission

Conditions : 500 pulses/spectrum
Exposure : 10000 ms
P : unknown
Grating 3600 g/mm @ 386 nm

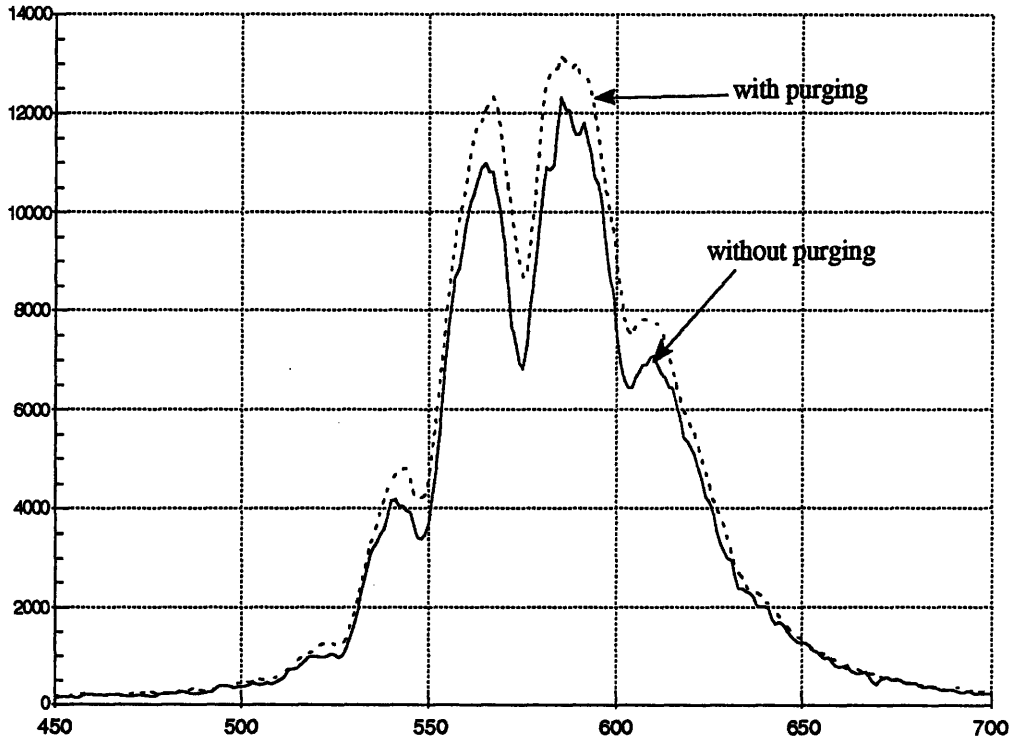

Data file : M72K2 & M72K3

Figure 5.23 : Example of LIF spectrum where the 4 peaks are visible for each rotational line

Conditions : 100 pulses/spectrum
Exposure : 10000 ms
P : 0.21 W
Grating 1200 g/mm @ 234 nm

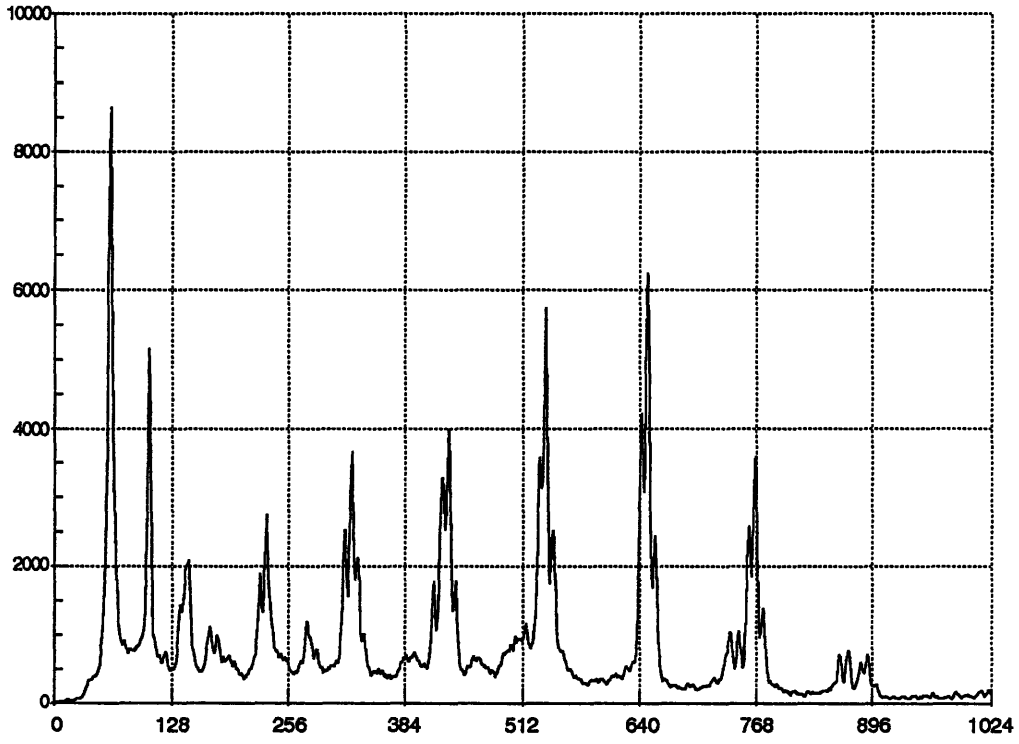

Data file : V71F11

Figure 5.24 : Example of spectrum of O_2^+ with laser tuned at 0.7790 mm

Conditions : 100 pulses/spectrum
Exposure : 10000 ms
P : 0.28 W
Grating 1200 g/mm @ 234 nm

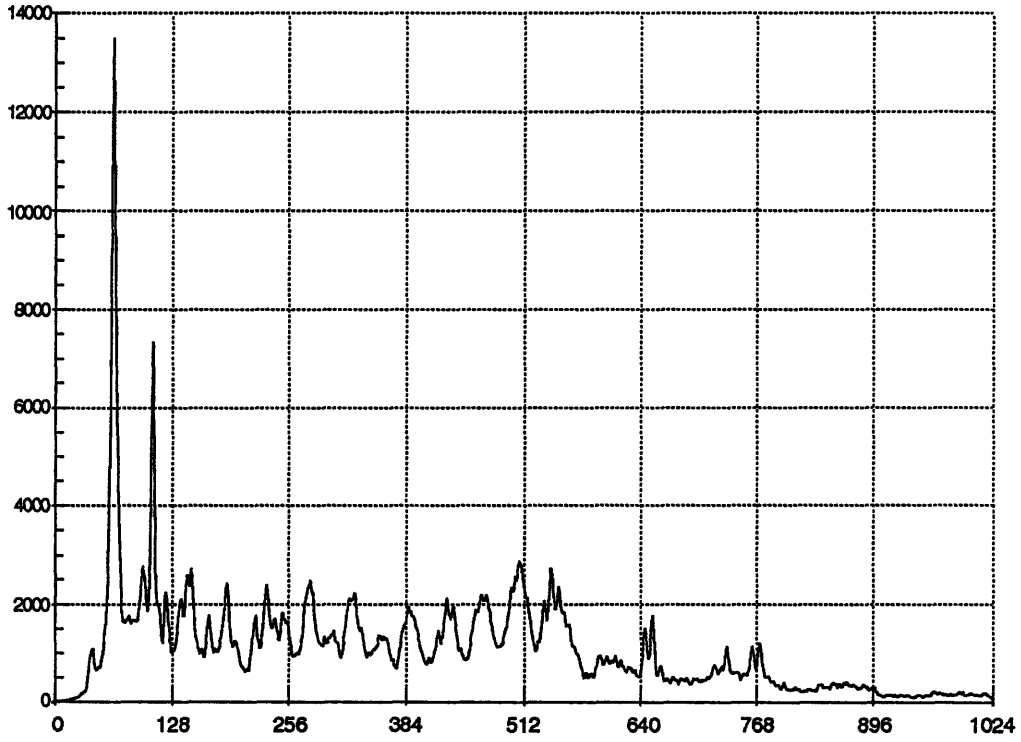

Data file : V71F10

Figure 5.25 : Variation of the gas flow rate in the test chamber (from 0 to 40 scfh) Superposition of 4 spectra(0,10,20 and 40 scfh)

Conditions : 10 pulses/spectrum
Exposure : 956 ms
P : 0.19 W
Grating 1200 g/mm @ 234 nm

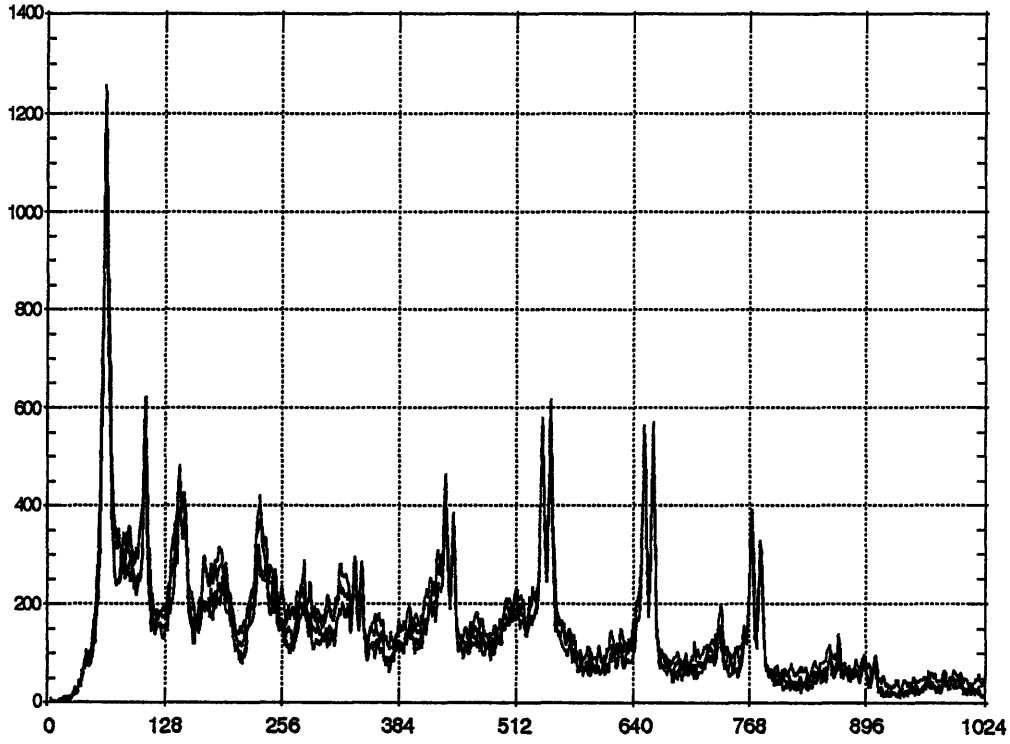

Data file : 165Y Series

Figure 5.26a : Flow rate effect

Flow rate : 0 scfh
Pressure : 2080 mb
Power : 0.19 W - 10 shots/s

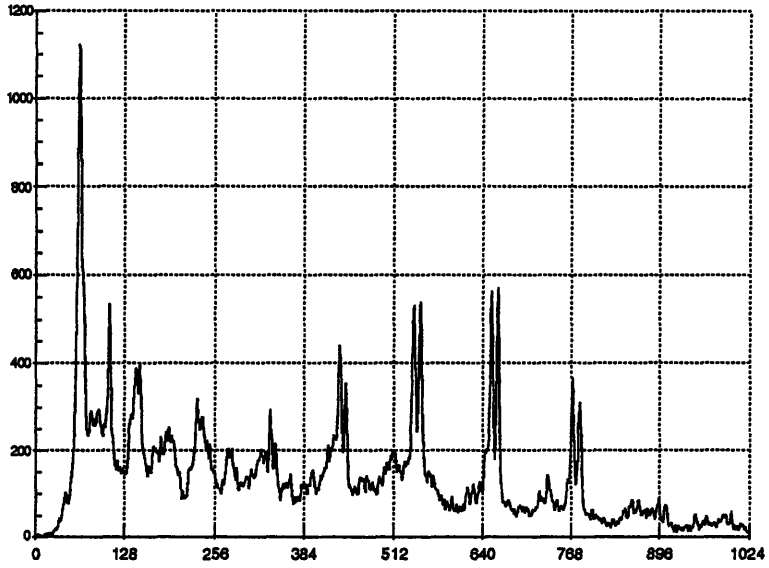

Flow rate : 10 scfh
Pressure : 2080 mb
Power : 0.19 W - 10 shots/s

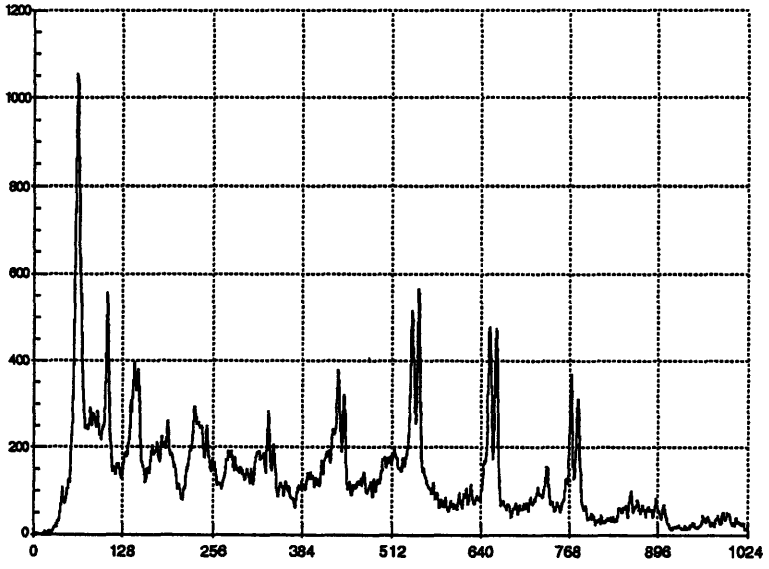

Data file : L65Y-Series

Figure 5.26b : Flow rate effect

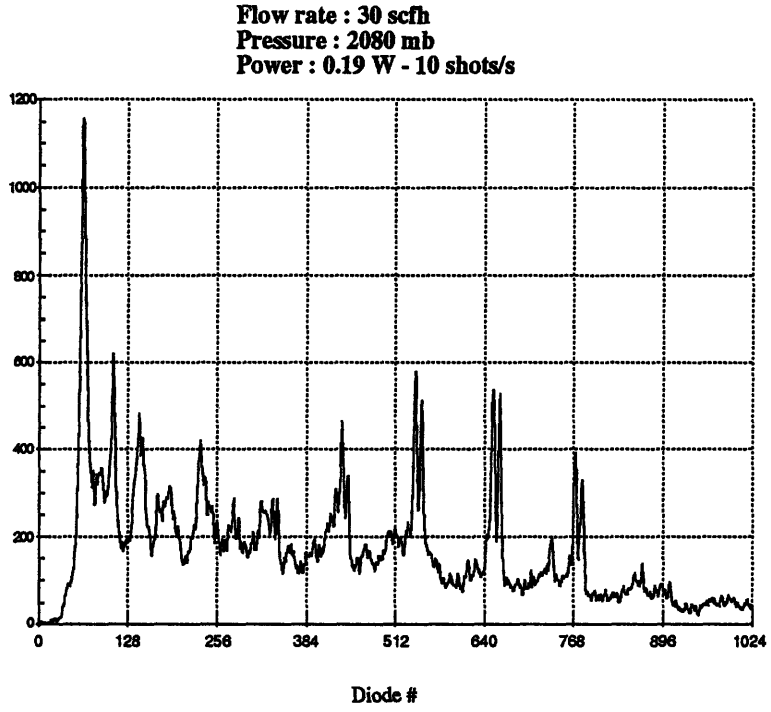

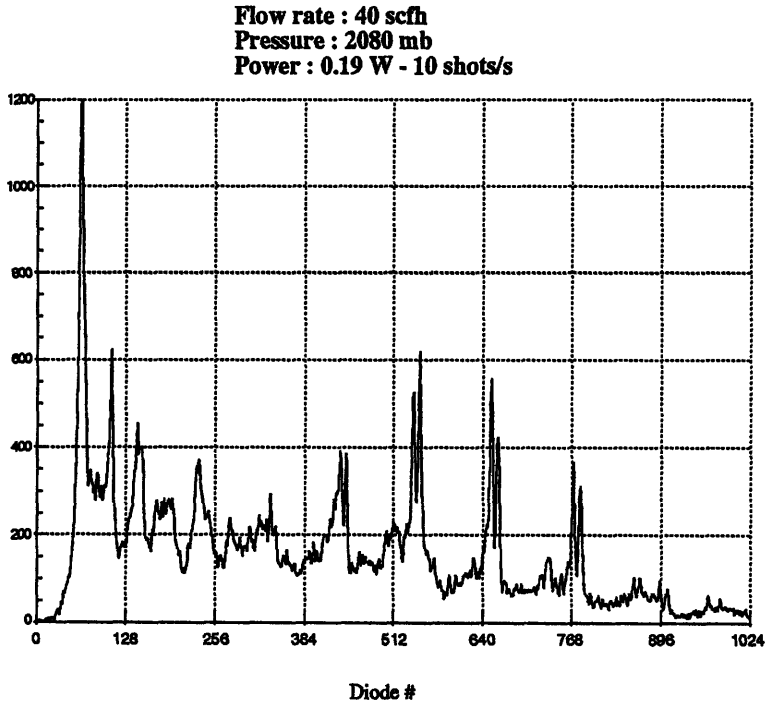

Data file : L65Y-Series

Figure 5.27 : Spectral shape of laser beam for a power variation obtained by inserting windows on the beam path

Conditions : 10 pulses/spectrum
Exposure : 956 ms
P : 0.22 W
Grating 3600 g/mm @ 386 nm

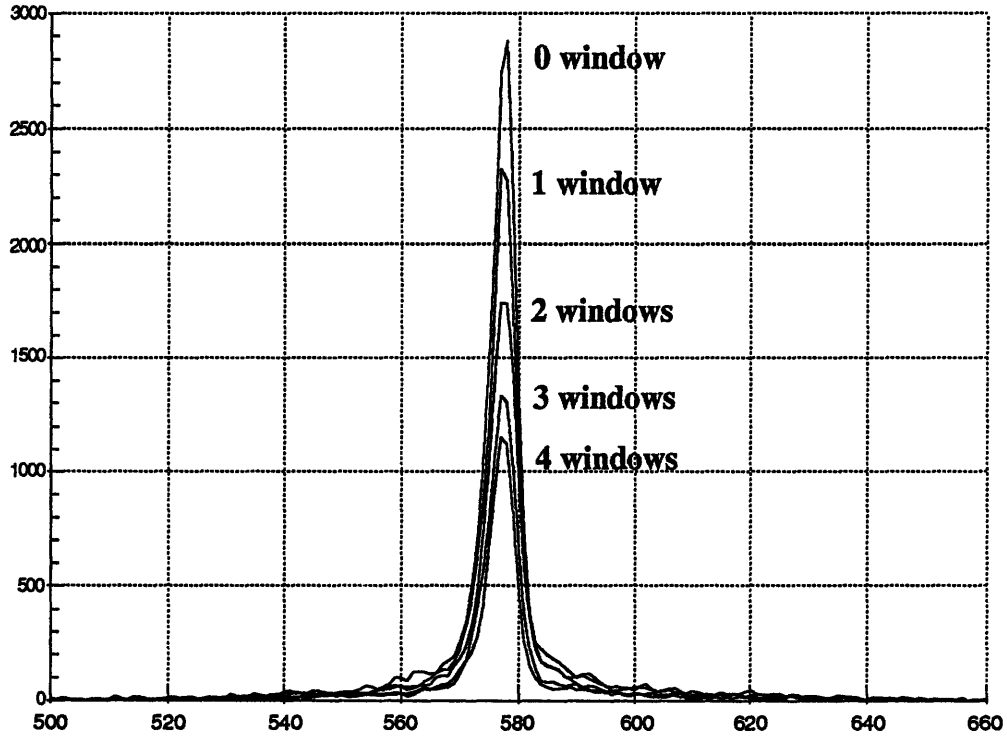

Data file : V75D-Series

Figure 5.28a : Power variation

Conditions : 50 pulses/spectrum
Exposure : 994 ms
P : 1.19 W
Grating 1200 g/mm @ 234 nm

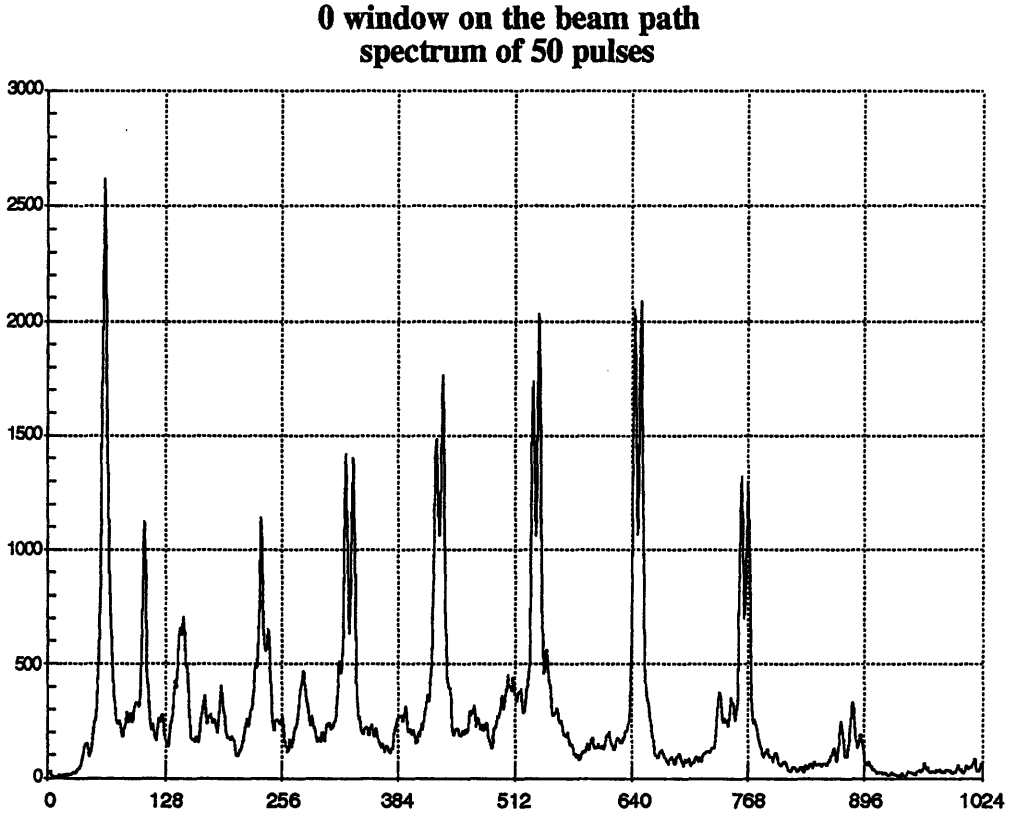

Data file : V75E-Series

Figure 5.28b : Power variation

Conditions : 50 pulses/spectrum
Exposure : 994 ms
P : 1.19 W
Grating 1200 g/mm @ 234 nm

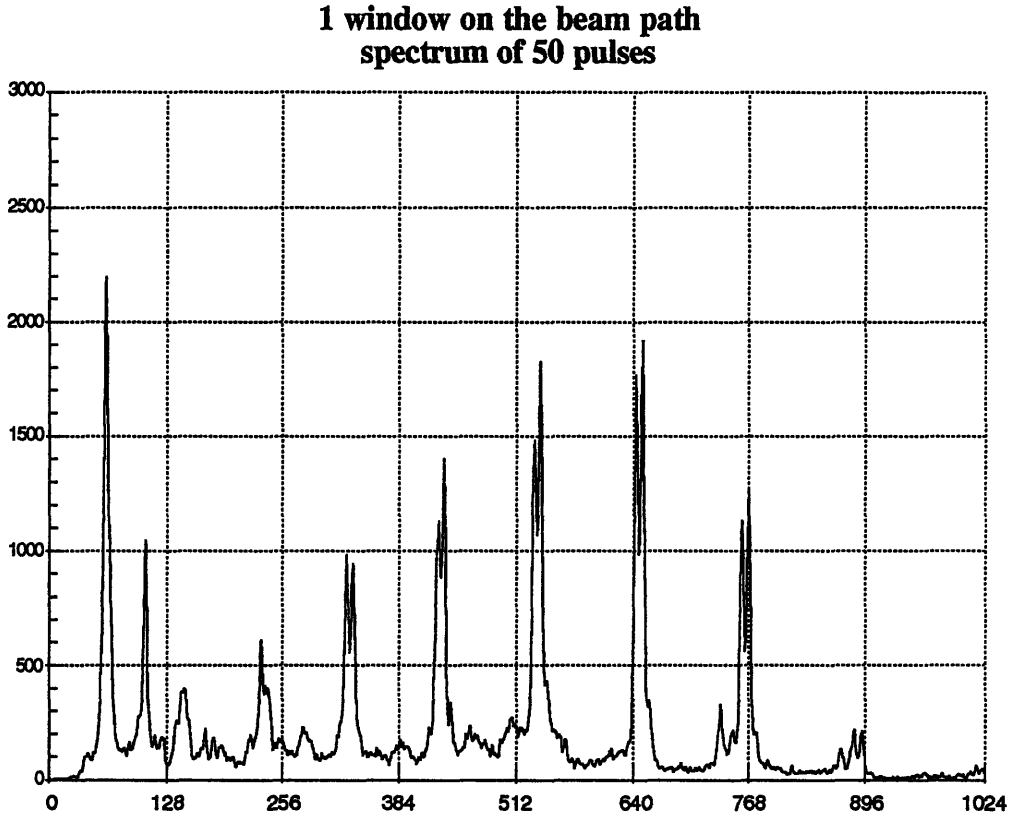

Data file : V75E-Series

Figure 5.28c : Power variation

Conditions : 50 pulses/spectrum
Exposure : 994 ms
P : 1.19 W
Grating 1200 g/mm @ 234 nm

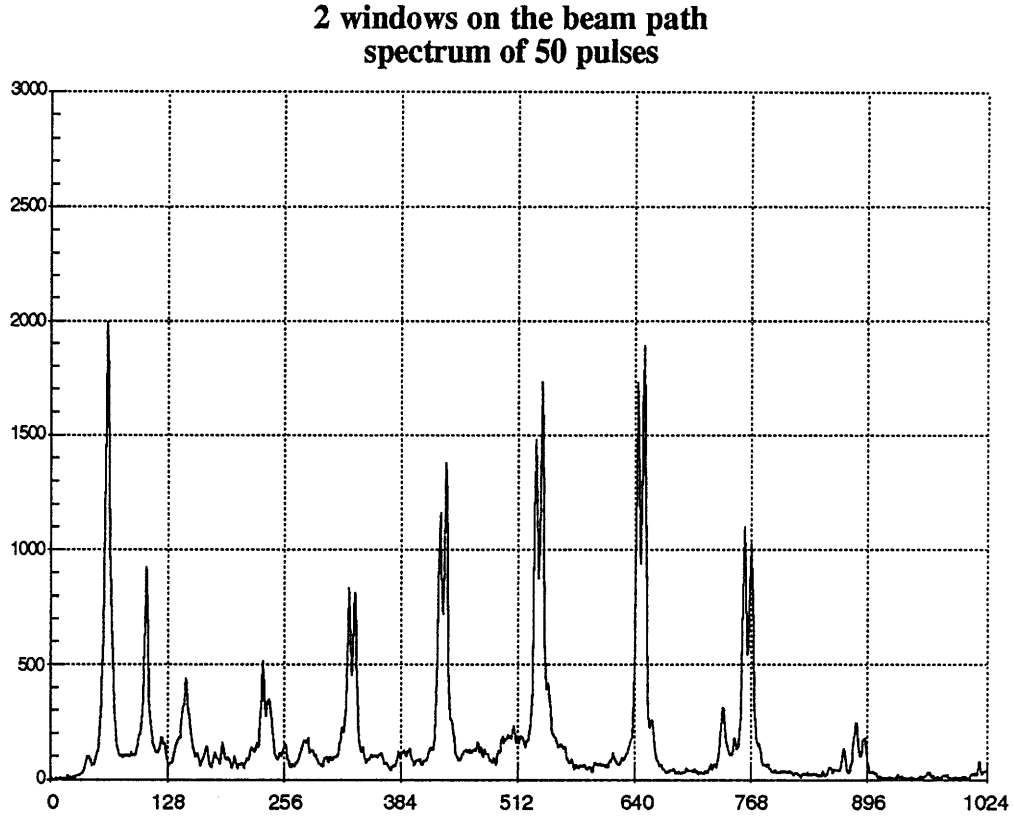

Data file : V715E-Series

Figure 5.28d : Power variation

Conditions : 50 pulses/spectrum
Exposure : 994 ms
P : 1.19 W
Grating 1200 g/mm @ 234 nm

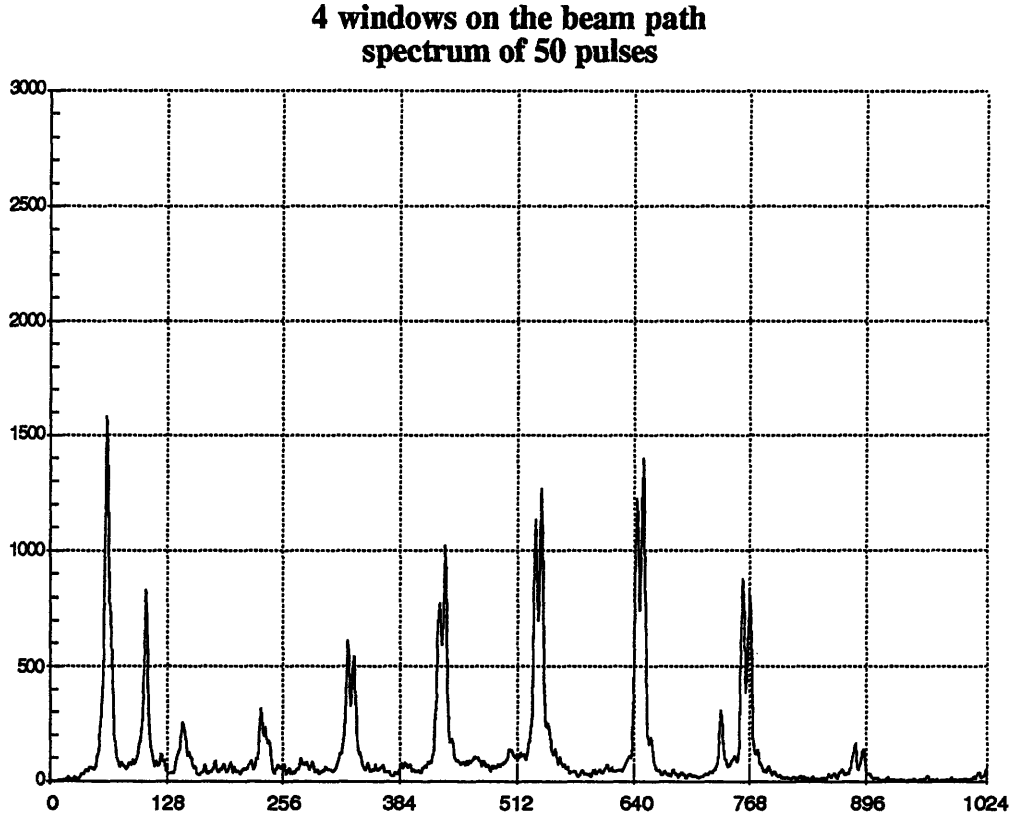

Data file : V75E-Series

Figure 5.28e : Power variation file V75E7

Conditions : 50 pulses/spectrum
Exposure : 994 ms
P : 1.19 W
Grating 1200 g/mm @ 234 nm

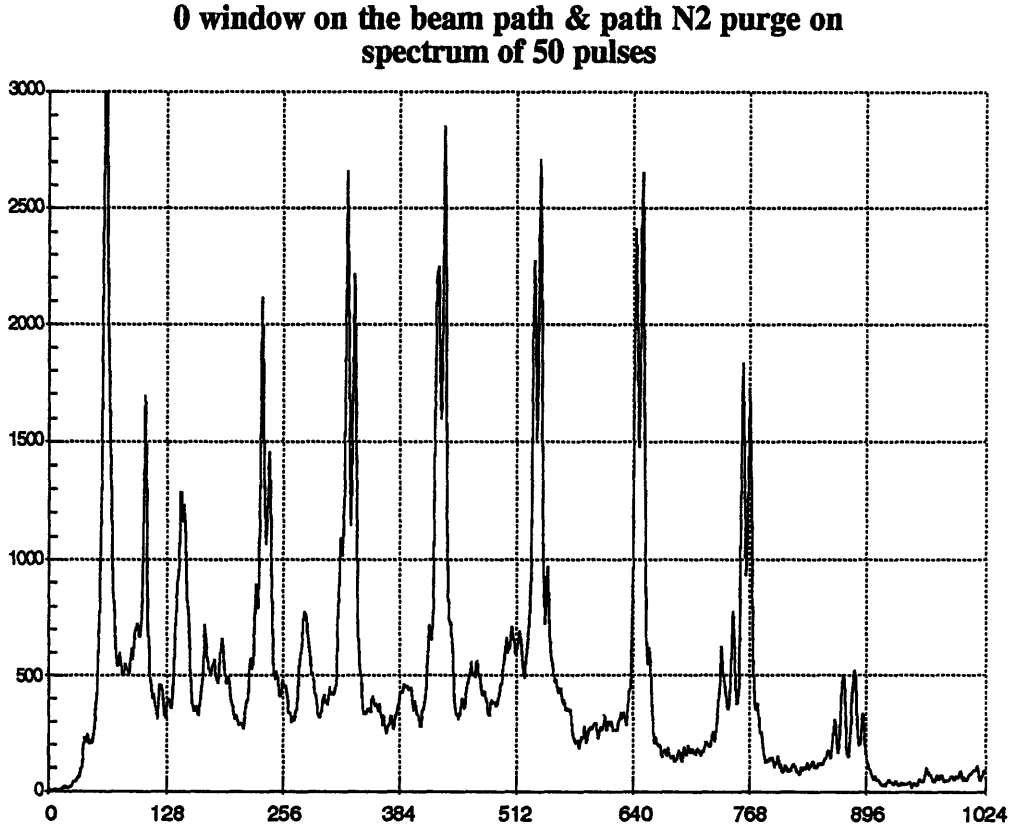

Data file : V75E-Series

Figure 5.29 : Power variation analysis with empirical procedures

Conditions : 50 pulses/spectrum
Exposure : 994 ms
P : 1.19 W
Grating 1200 g/mm @ 234 nm

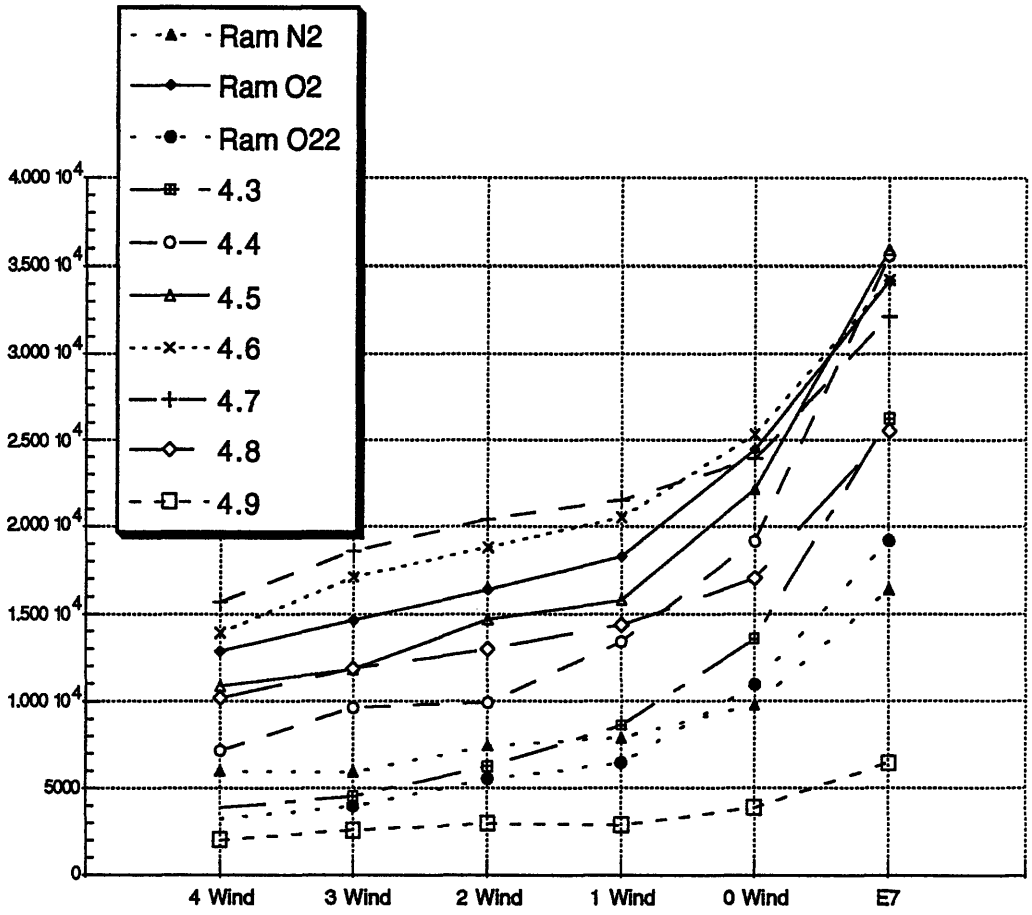

Data file : V75E-Analysis

Figure 5.30 : Power variation analysis variation in % of smaller power case (using empirical procedures data)

Conditions : 50 pulses/spectrum
Exposure : 994 ms
P : 1.19 W
Grating 1200 g/mm @ 234 nm

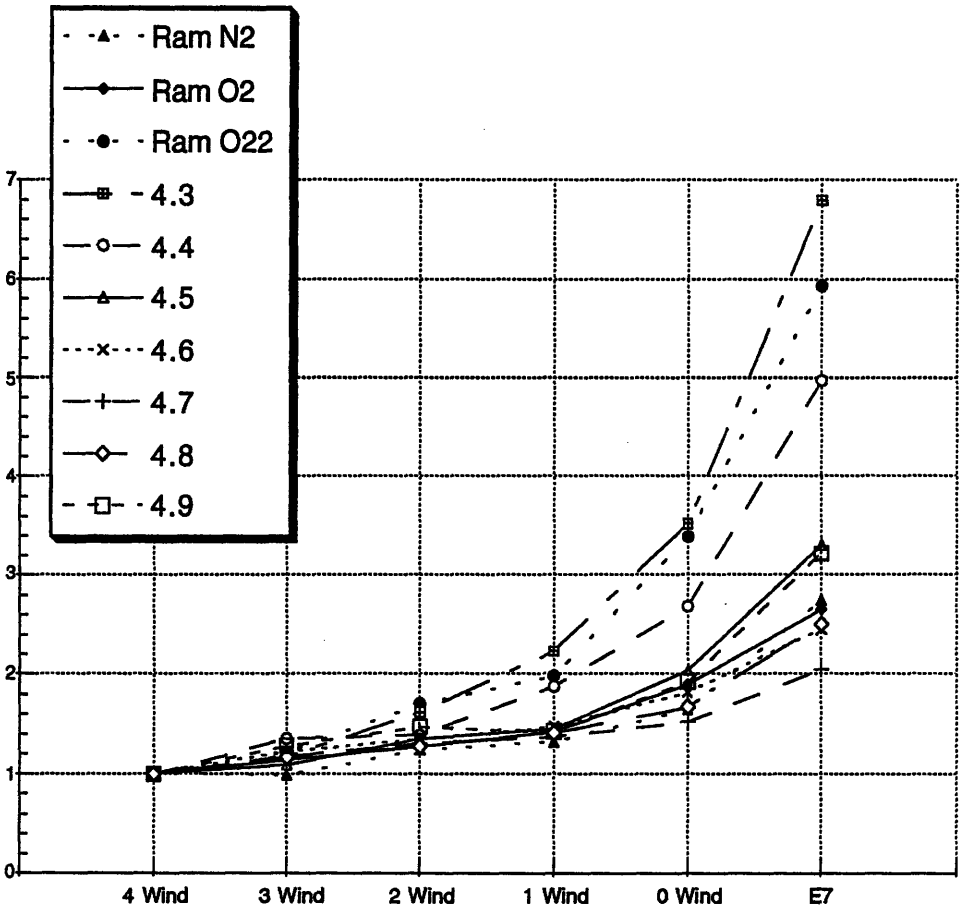

File

Data file : V75E-Series

Figure 5.31 : Power variation purge experiment (empirical proc.)

Conditions : 100 pulses/spectrum
Exposure : 1995 ms
P : unknown
Grating 1200 g/mm @ 234 nm

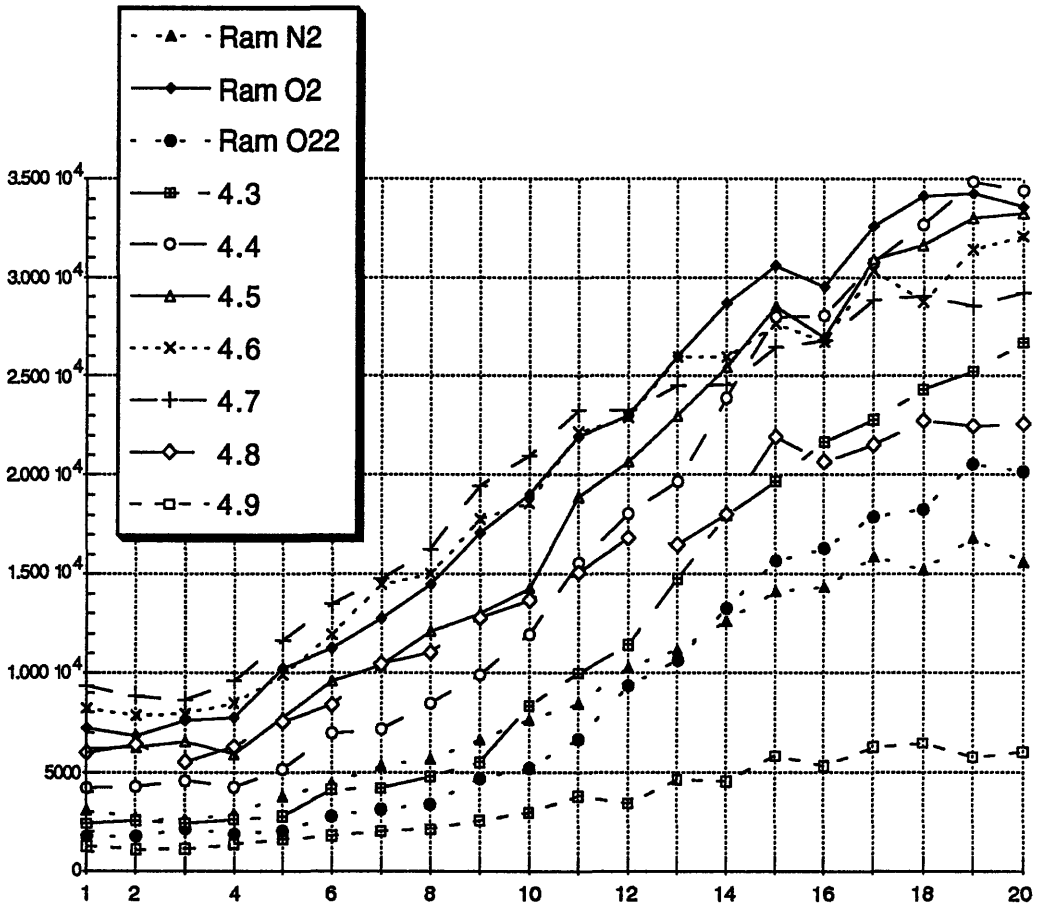

Data file : V75H1-Analysis

Figure 5.32 : Power variation N2 purge experiment variations in % / point #4(empirical proc.)

Conditions : 100 pulses/spectrum
Exposure : 1995 ms
P : 1unknown
Grating 1200 g/mm @ 234 nm

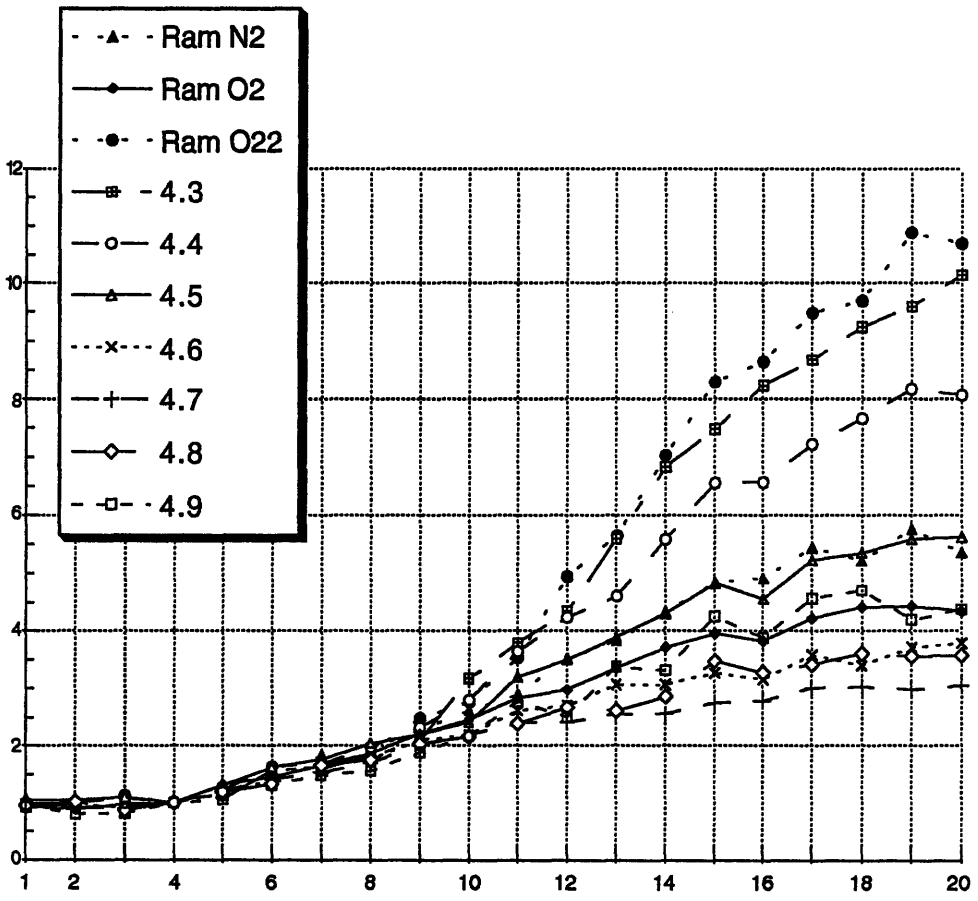

Data file : V75H1-Analysis

Figure 5.33 : Stability test (analysis with empirical procedures)

Conditions : 100 pulses/spectrum
Exposure : 1995 ms
P : unknown
Grating 1200 g/mm @ 234 nm

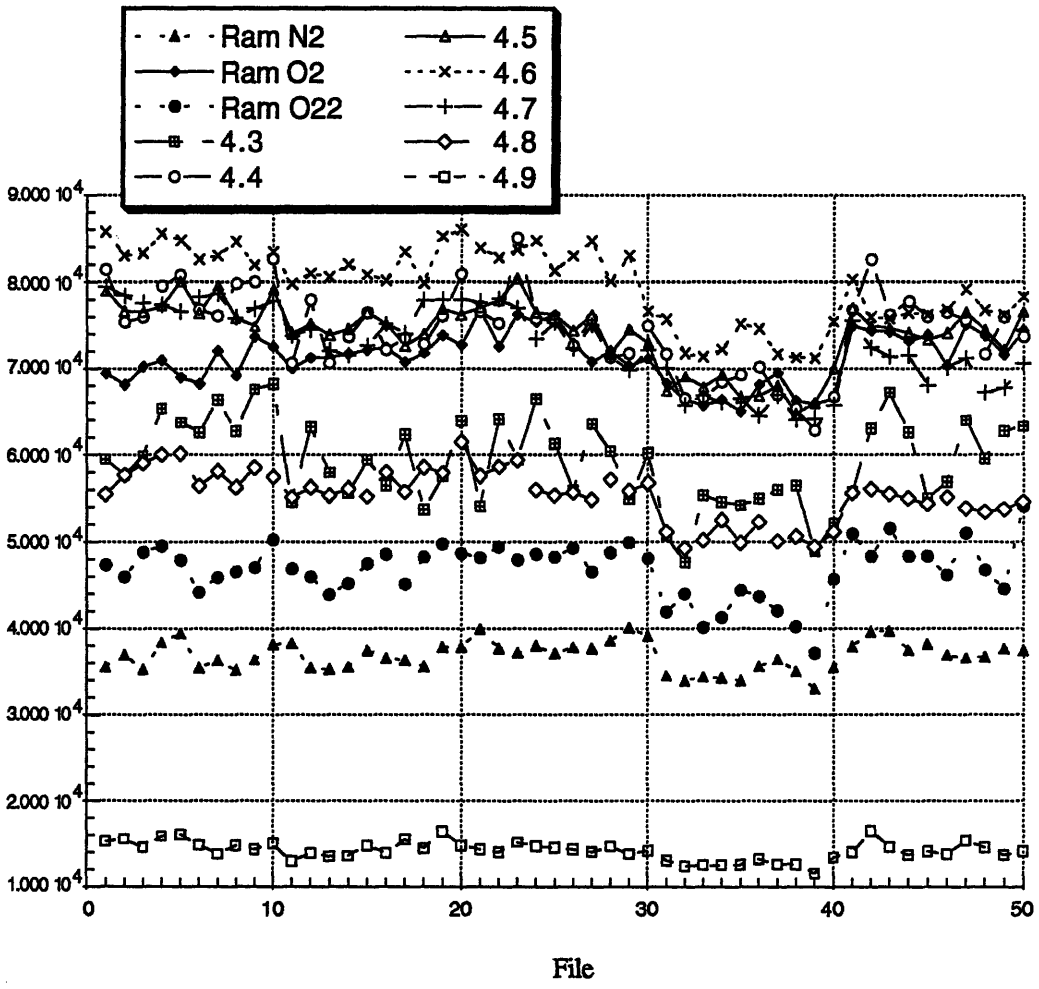

Data file : V72BCDEF-Analysis

Figure 5.34 : Stability test (analysis with empirical procedures)

Conditions : 100 pulses/spectrum
Exposure : 1995 ms
P : unknown
Grating 1200 g/mm @ 234 nm

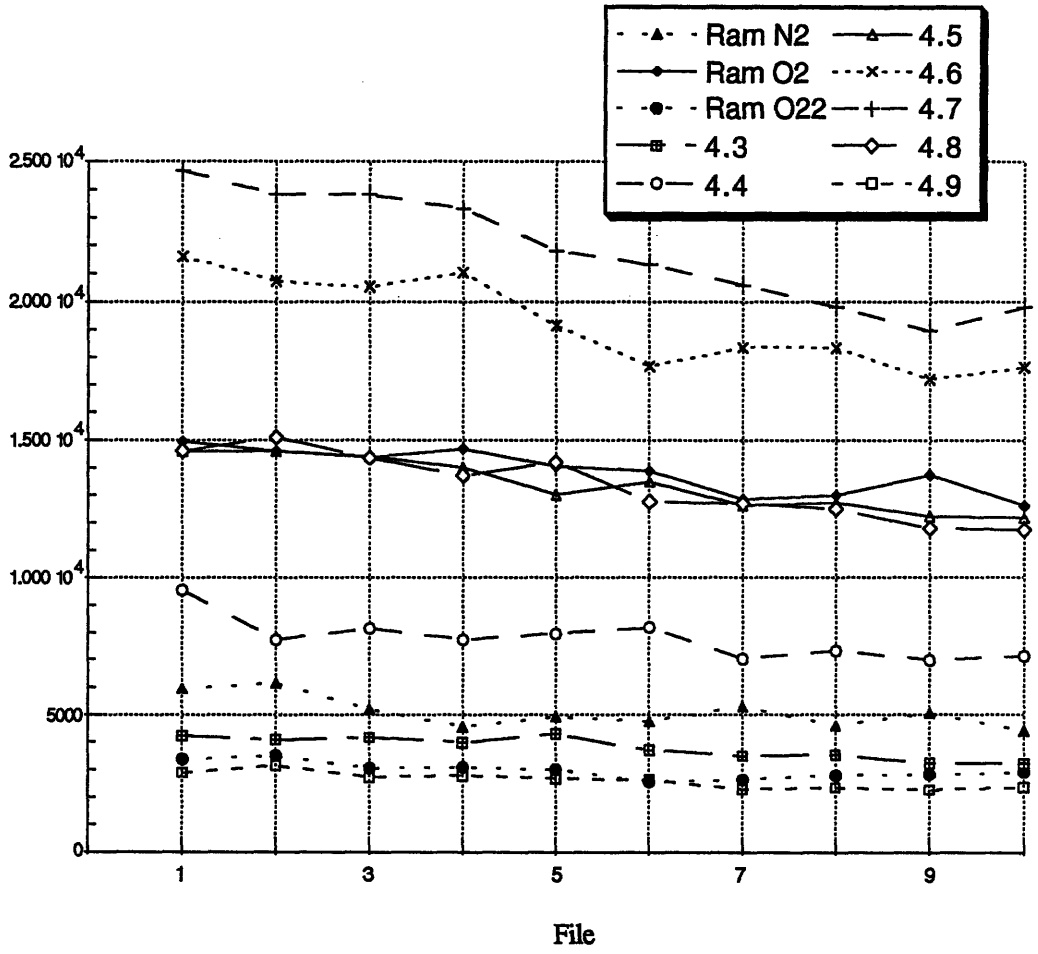

Data file : V72A-Analysis

Figure 5.35 : Stability test (analysis with empirical procedures)

Conditions : 100 pulses/spectrum
Exposure : 1995 ms
P : unknown
Grating 1200 g/mm @ 234 nm

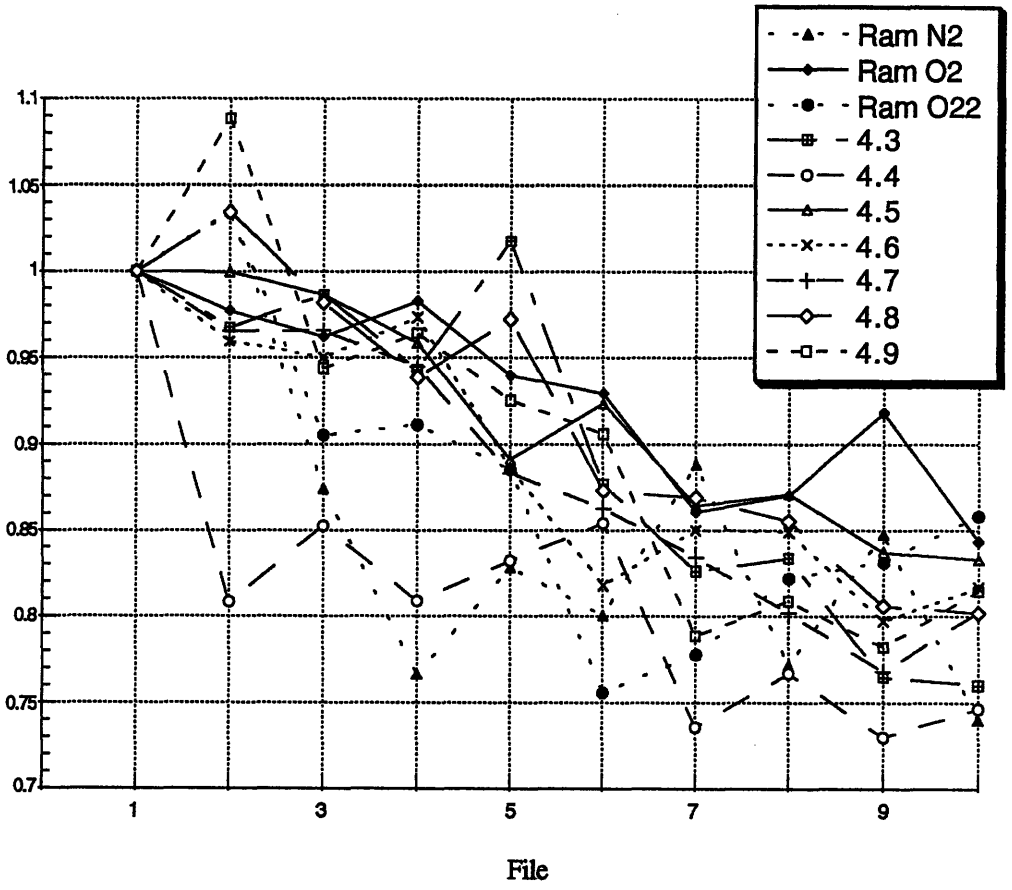

Data file : V72A-Analysis

Figure 5.36 : Pressure sweep (1.3 - 3.0 b) Superposition of 18 spectra

Conditions : 100 pulses/spectrum
Exposure : 1995 ms
P : unknown
Grating 1200 g/mm @ 234 nm

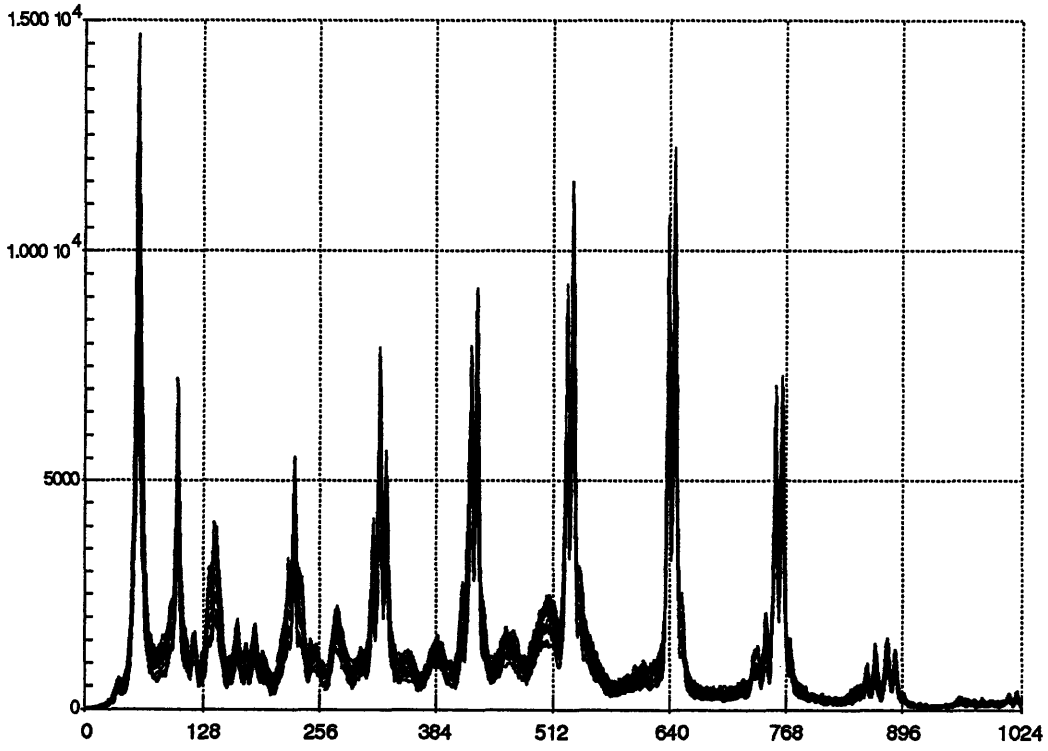

Data file : W72P

Figure 5.37a : Pressure sweep 1.3-3.0 bar (P17 peak)

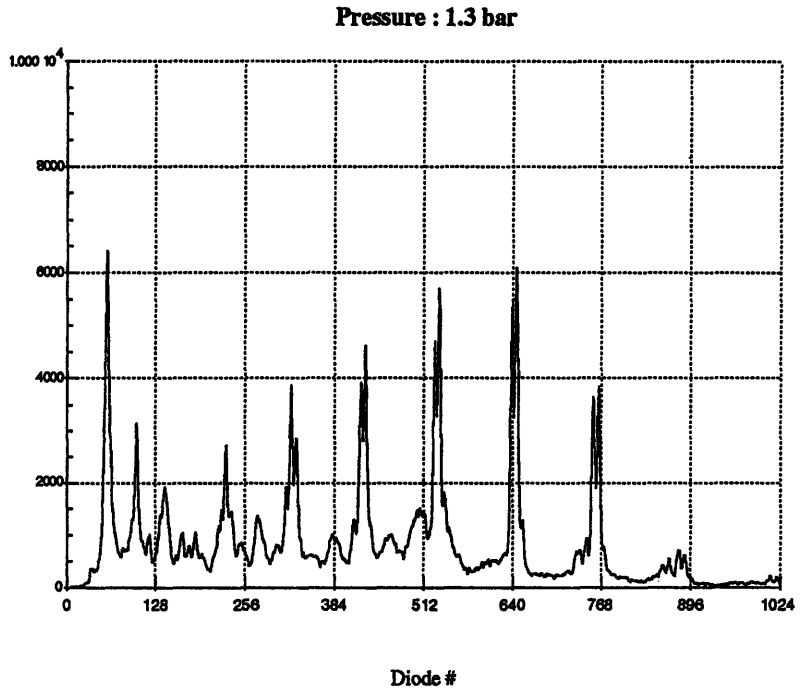

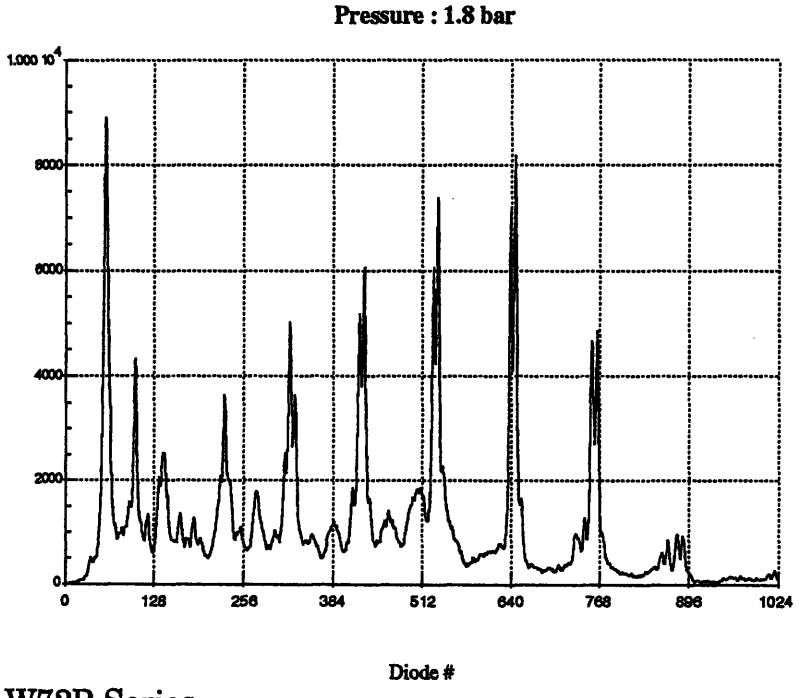

Data file : W72P-Series

Figure 5.37b : Pressure sweep 1.3-3.0 bar (P17 peak)

Conditions see Figure 5.36

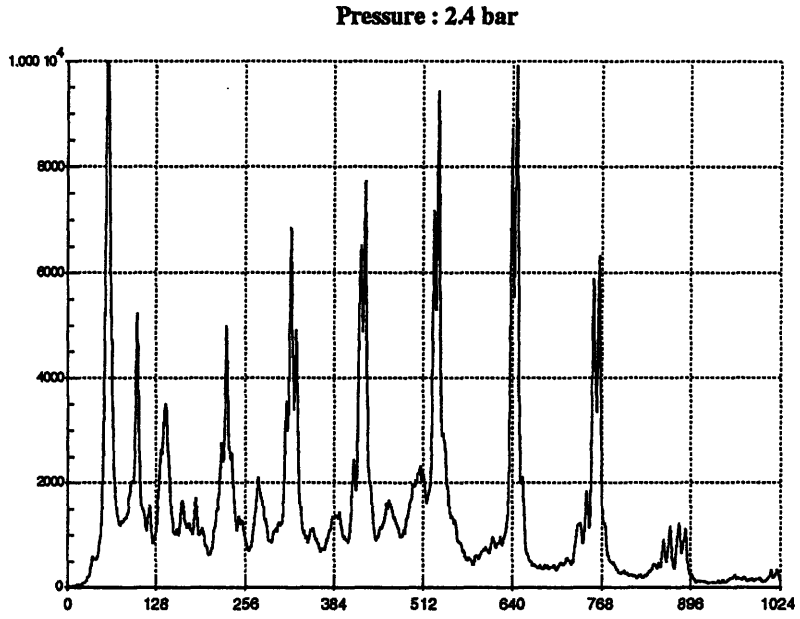

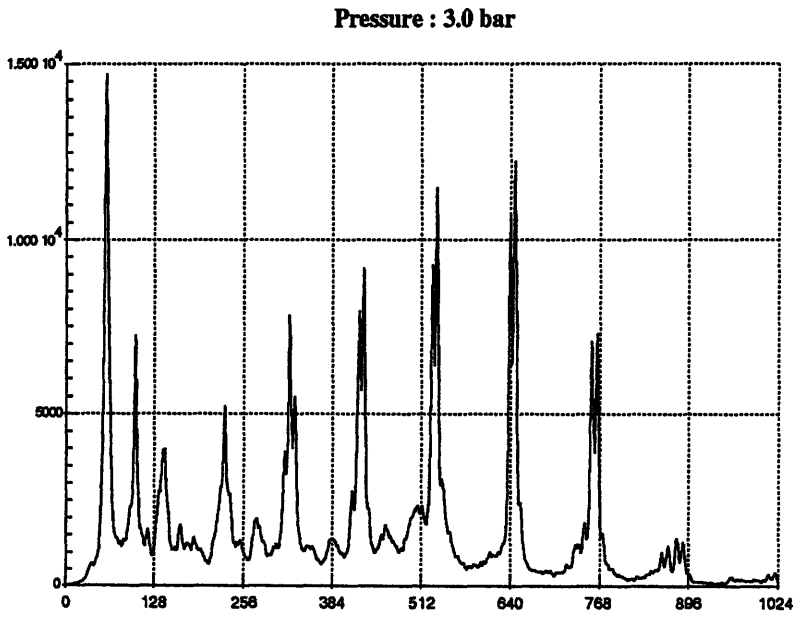

Data file : V71F11

Figure 5.38 : Pressure sweep P17 peak (empirical procedures used)

Conditions : 100 pulses/spectrum
Exposure : 1995 ms
P : unknown
Grating 1200 g/mm @ 234 nm

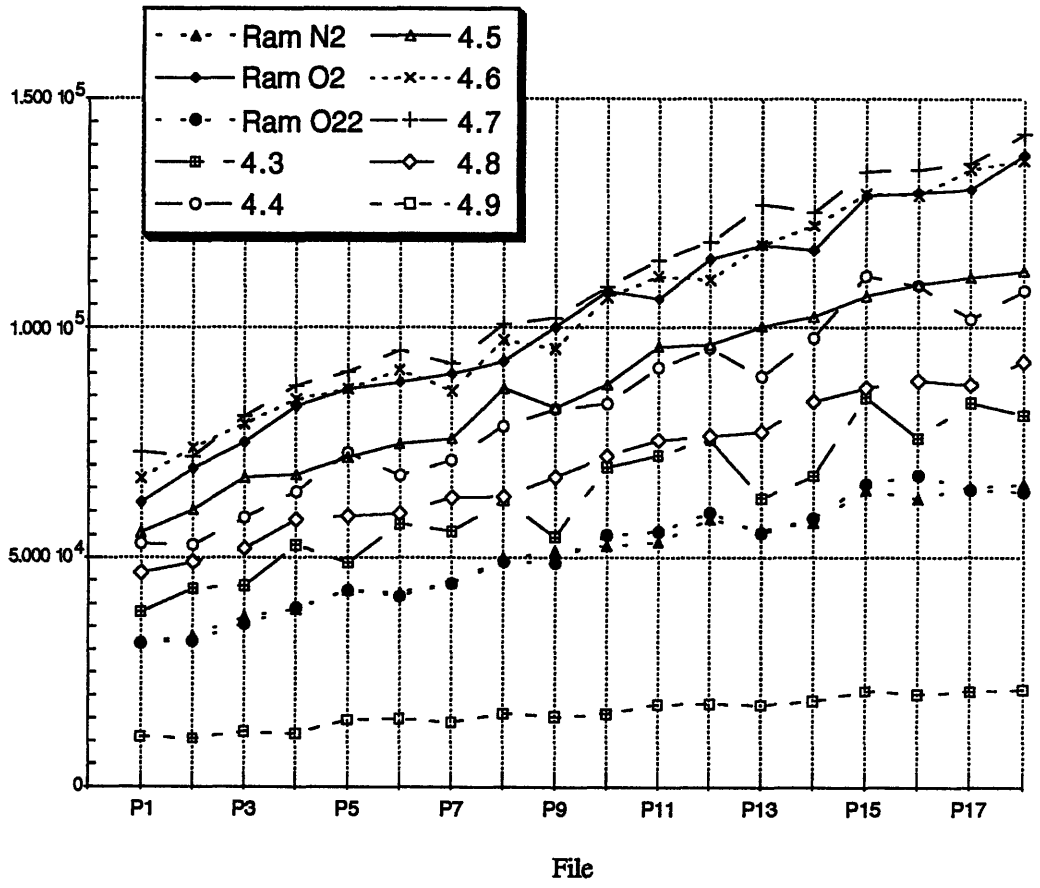

Data file : W72PresP17/res.

Figure 5.39 : Pressure sweep P17 peak % variation (empirical procedures used)

Conditions : 100 pulses/spectrum
Exposure : 1995 ms
P : unknown
Grating 1200 g/mm @ 234 nm

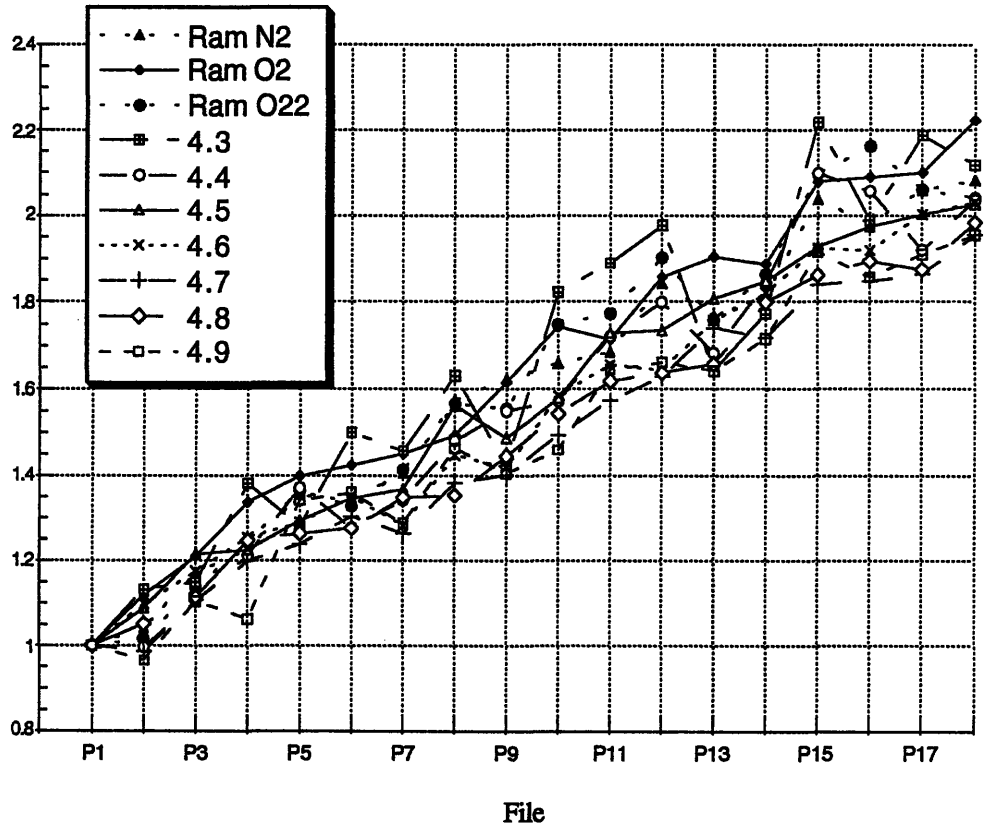

Data file : W72PresP17/res.

Figure 5.40 : Pressure sweep from 1.3 to 3.0 bar / P15 peak (empirical procedures used)

Conditions : 100 pulses/spectrum
Exposure : 1995 ms
P : unknown
Grating 1200 g/mm @ 234 nm

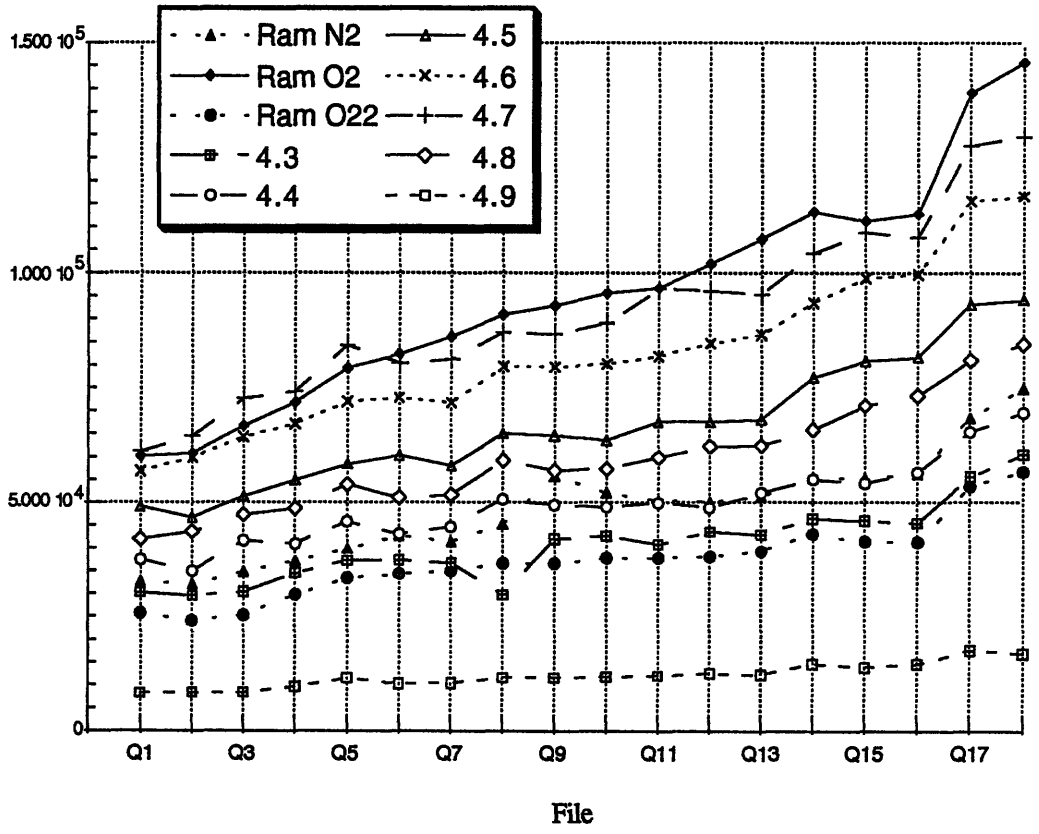

Data file : W72PresP15/res.

Figure 5.41 : Pressure sweep from 1.3 to 3.0 bar / P15 peak % variation (empirical procedures used)

Conditions : 100 pulses/spectrum
Exposure : 1995 ms
P : unknown
Grating 1200 g/mm @ 234 nm

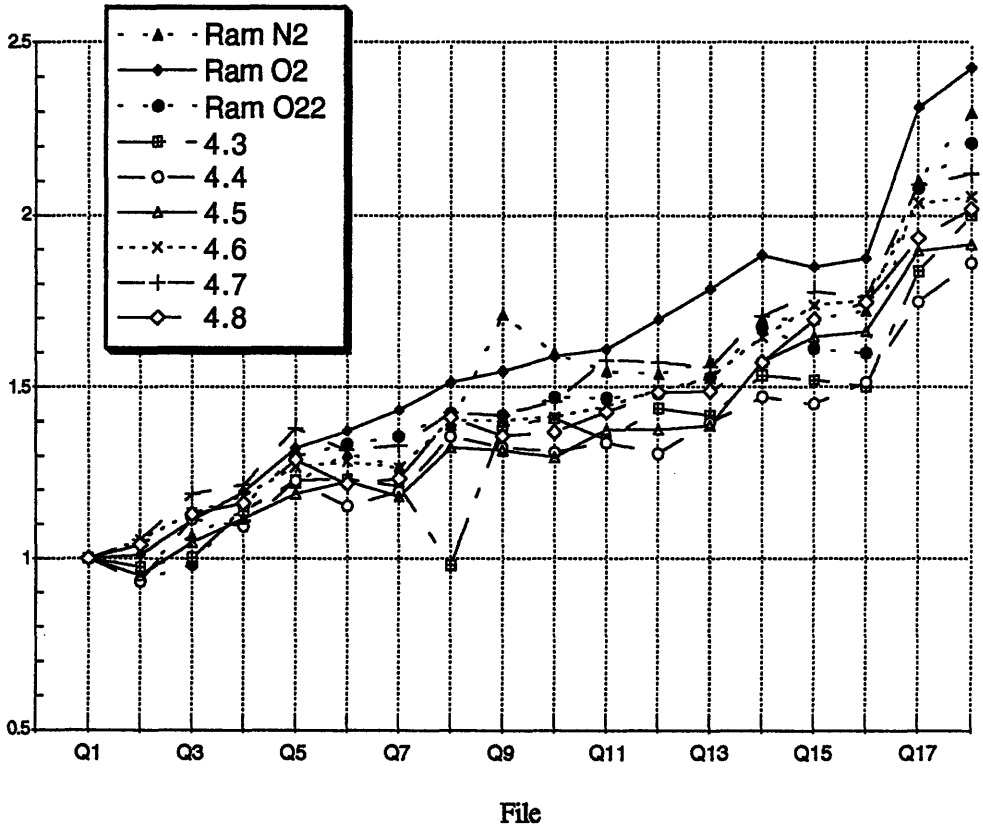

Data file : W72PresP15/res.

Figure 5.42 : Temperature sweep from 28 to 125 C / P17 peak 2 extreme temperature spectra

Conditions : 100 pulses/spectrum
Exposure : 1995 ms
P : unknown
Grating 1200 g/mm @ 234 nm

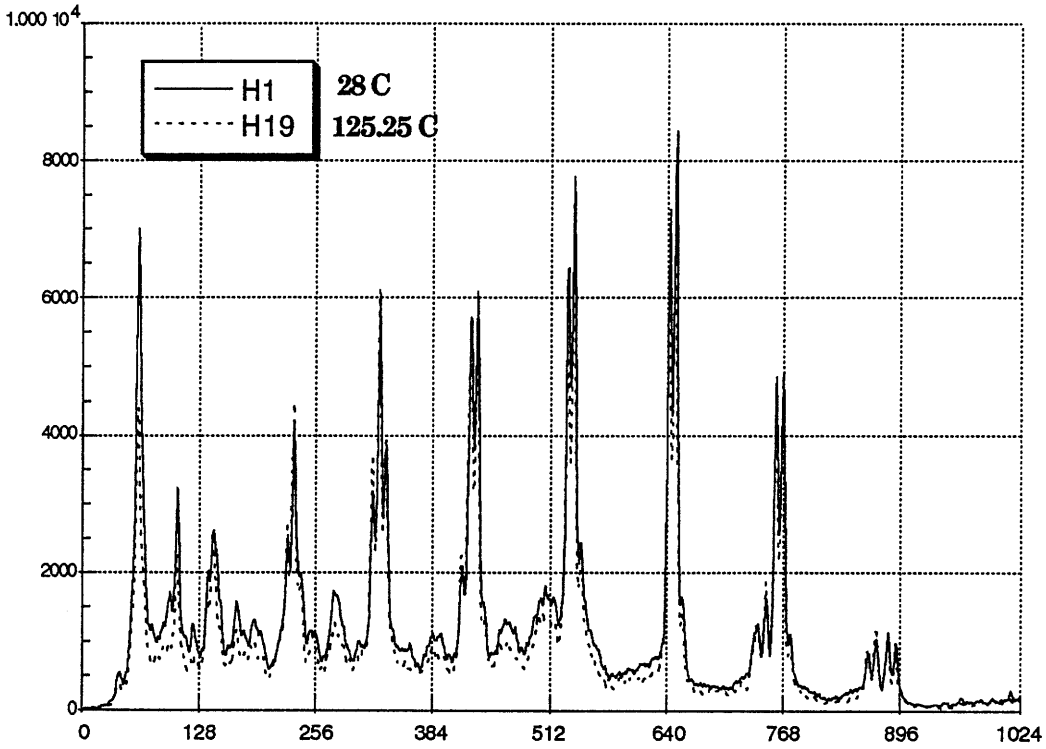

Data file : V72H-Series

Figure 5.43 : Temperature sweep from 28 to 125 C / P17 peak Superposition of 19 spectra

Conditions : 100 pulses/spectrum
Exposure : 1995 ms
P : unknown
Grating 1200 g/mm @ 234 nm

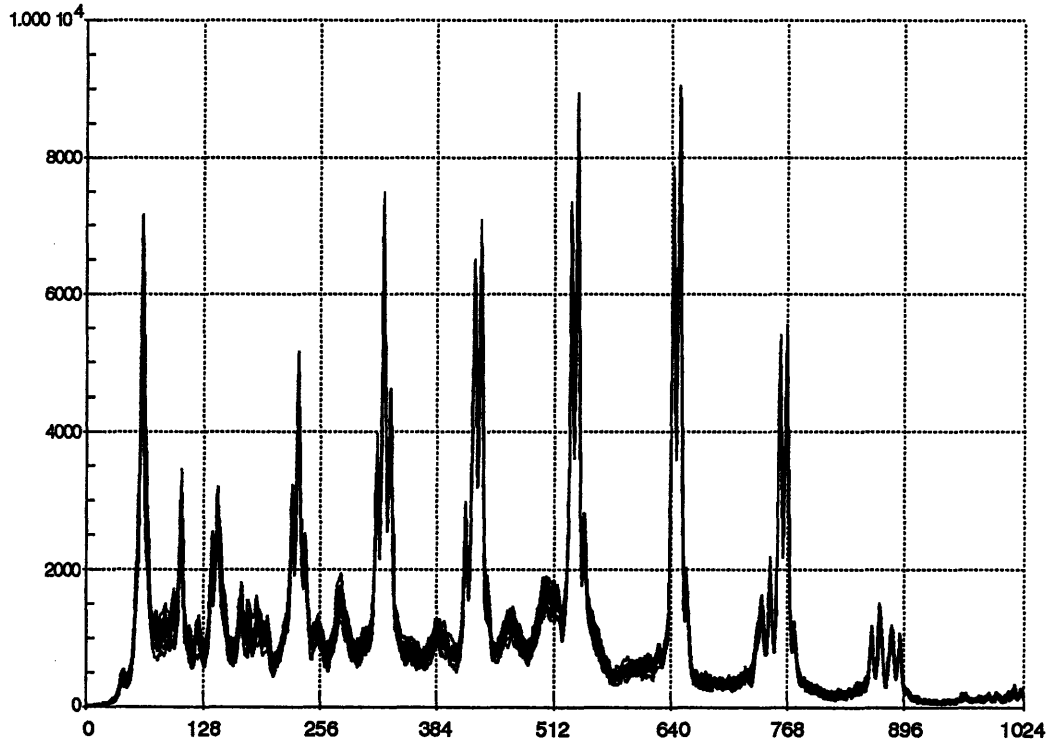

Data file : V72H-Series

Figure 5.44 : Temperature sweep from 28 to 125 C / P17 peak (empirical proc.)

Conditions : 100 pulses/spectrum
Exposure : 1995 ms
P : unknown
Grating 1200 g/mm @ 234 nm

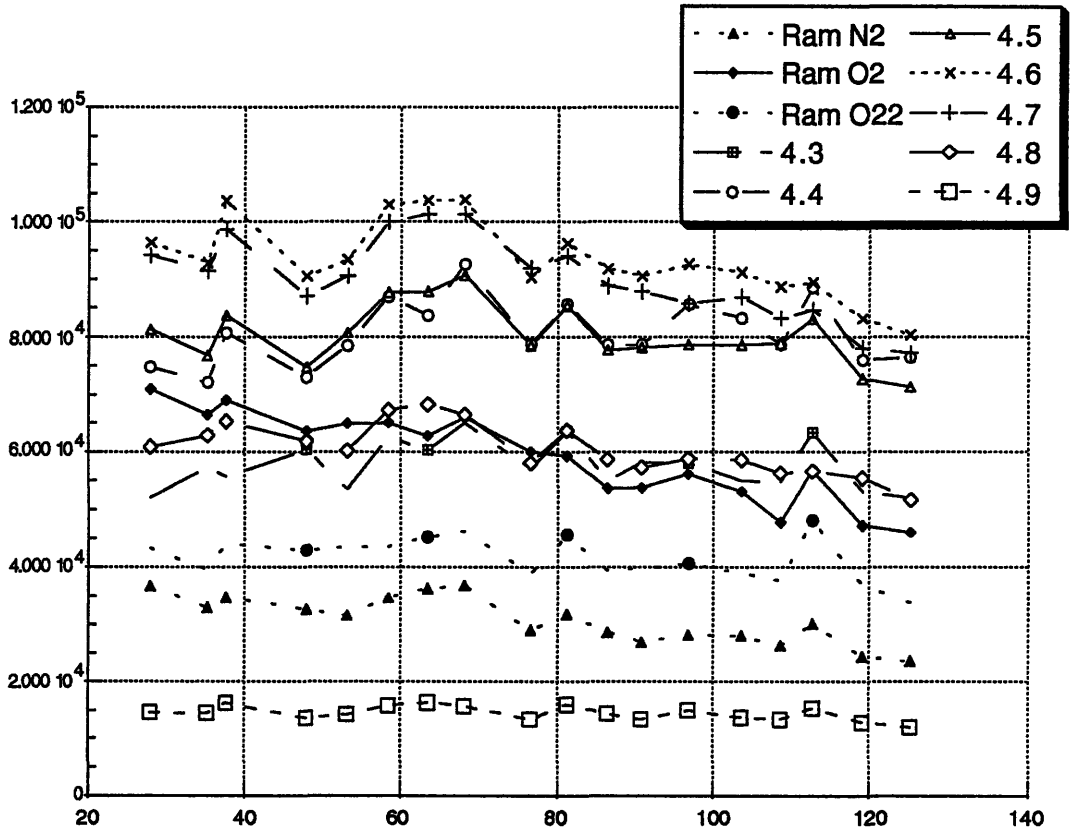

Data file : V72H-Series

Figure 5.45 : Temperature sweep from 28 to 125 C / P17 peak % variations (empirical procedures used)

Conditions : 100 pulses/spectrum
Exposure : 1995 ms
P : unknown
Grating 1200 g/mm @ 234 nm

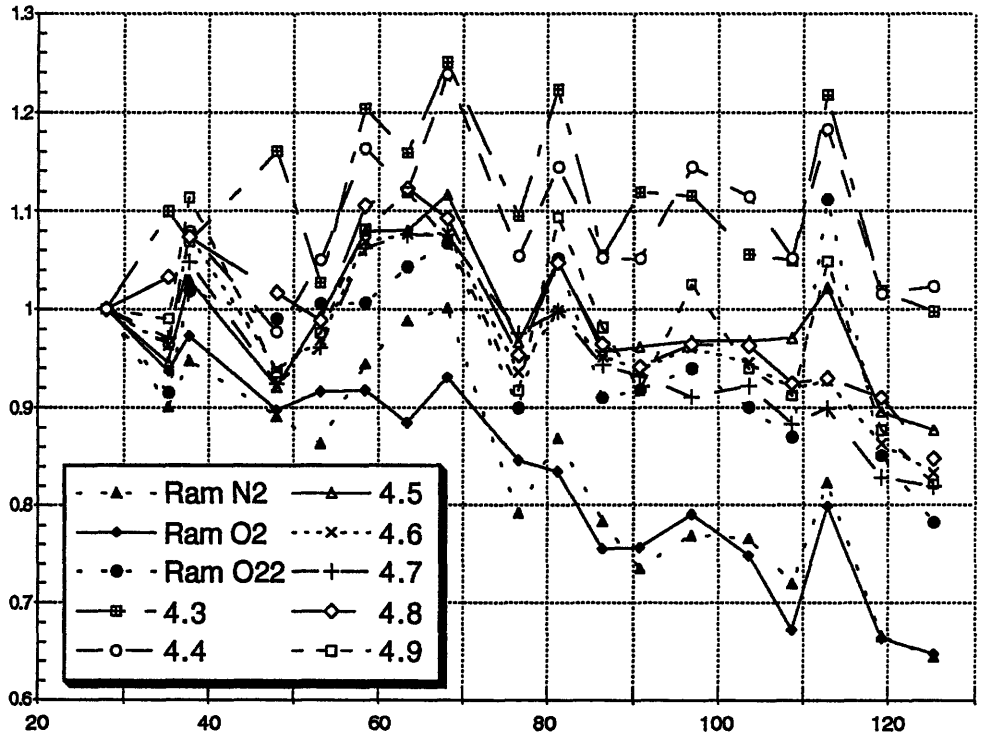

Data file : V72H-Series

Figure 5.46 : Temperature sweep #2 from 27 to 128ºC / P17 peak superposition of 10 spectra

Conditions : 100 pulses/spectrum
Exposure : 1995 ms
P : unknown
Grating 1200 g/mm @ 234 nm

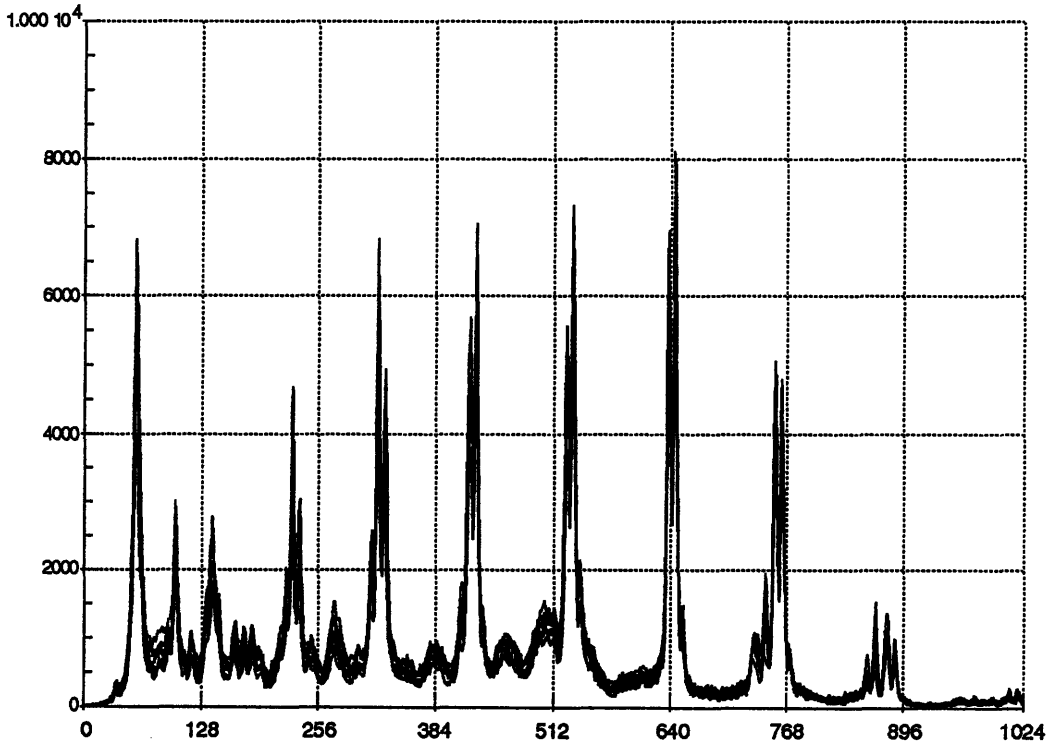

Data file : W72F

Figure 5.47 : Temperature sweep #2 from 27 to 128ºC / P17 peak (empirical procedures used)

Conditions : 100 pulses/spectrum
Exposure : 1995 ms
P : unknown
Grating 1200 g/mm @ 234 nm

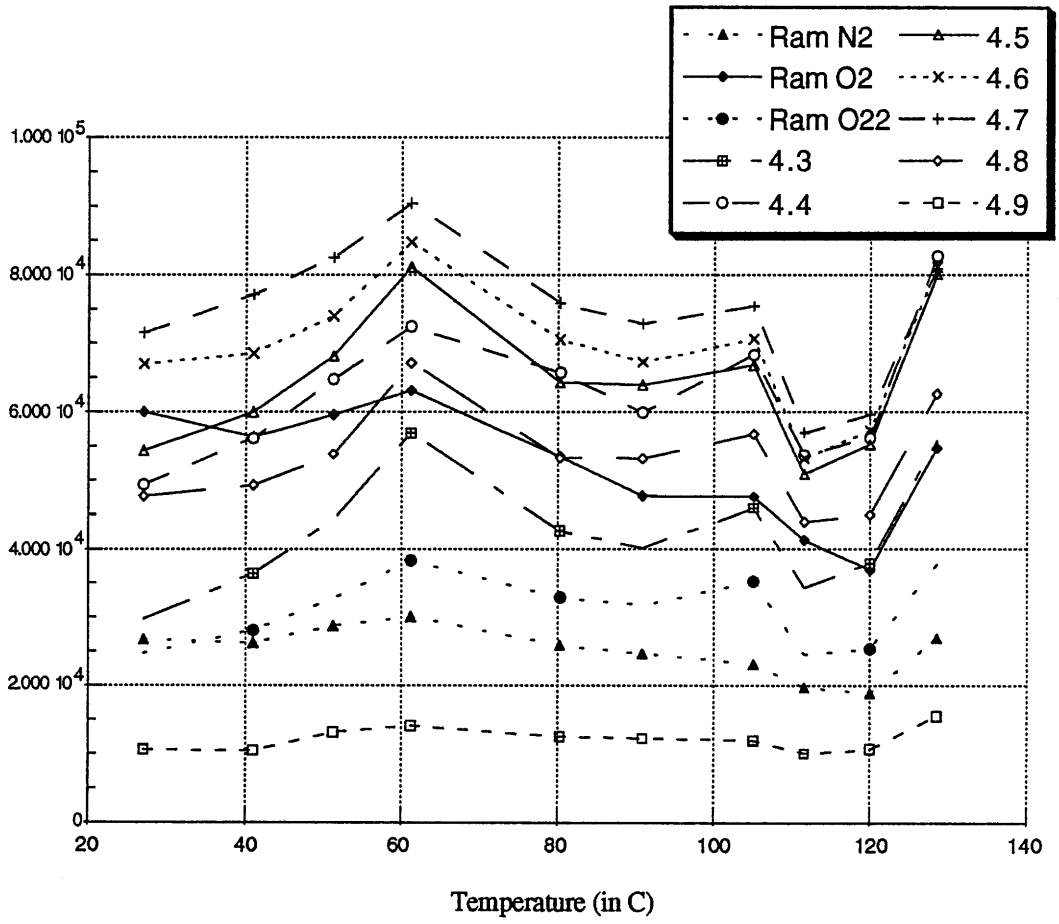

Data file : W72TempP17/res.

Figure 5.48 : Temperature sweep #2 from 27 to 128°C / P17 peak % variation (initial procedures used)

Conditions : 100 pulses/spectrum
Exposure : 1995 ms
P : unknown
Grating 1200 g/mm @ 234 nm

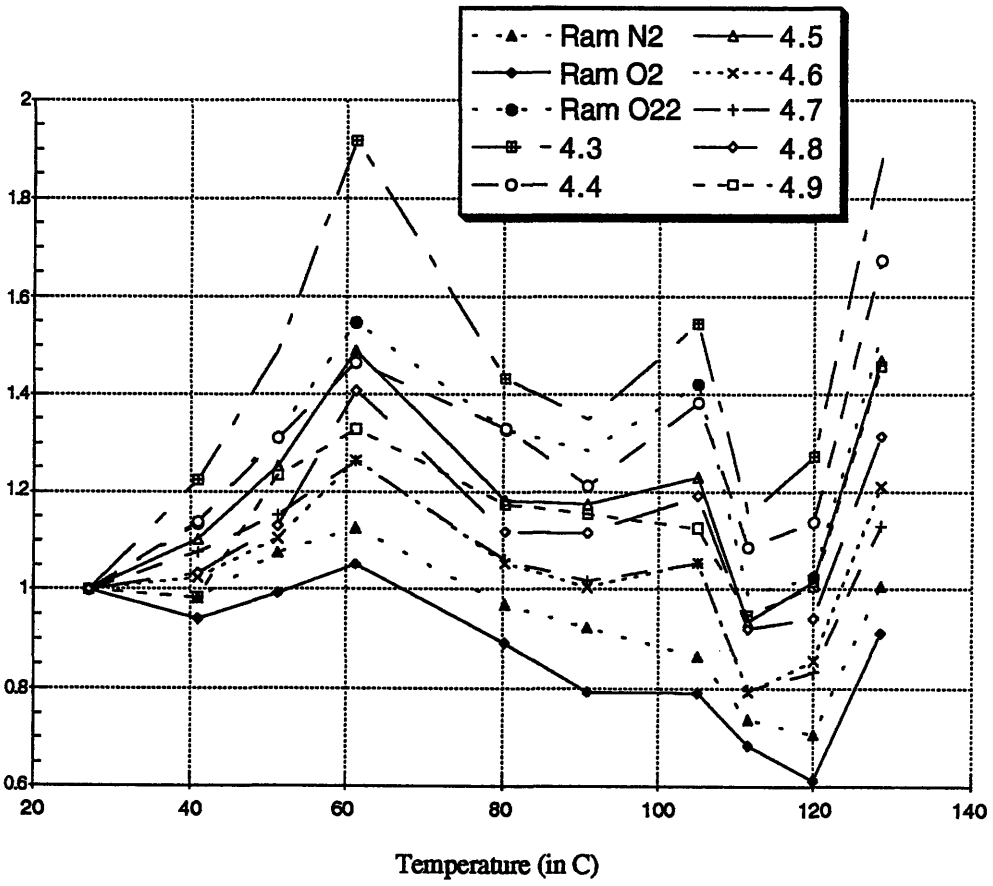

Data file : W72TempP17/res.

Figure 5.49 : Temperature sweep from 27 to 128 ºC/ P15 peak Superposition of 10 spectra

Conditions : 100 pulses/spectrum
Exposure : 1995 ms
P : unknown
Grating 1200 g/mm @ 234 nm

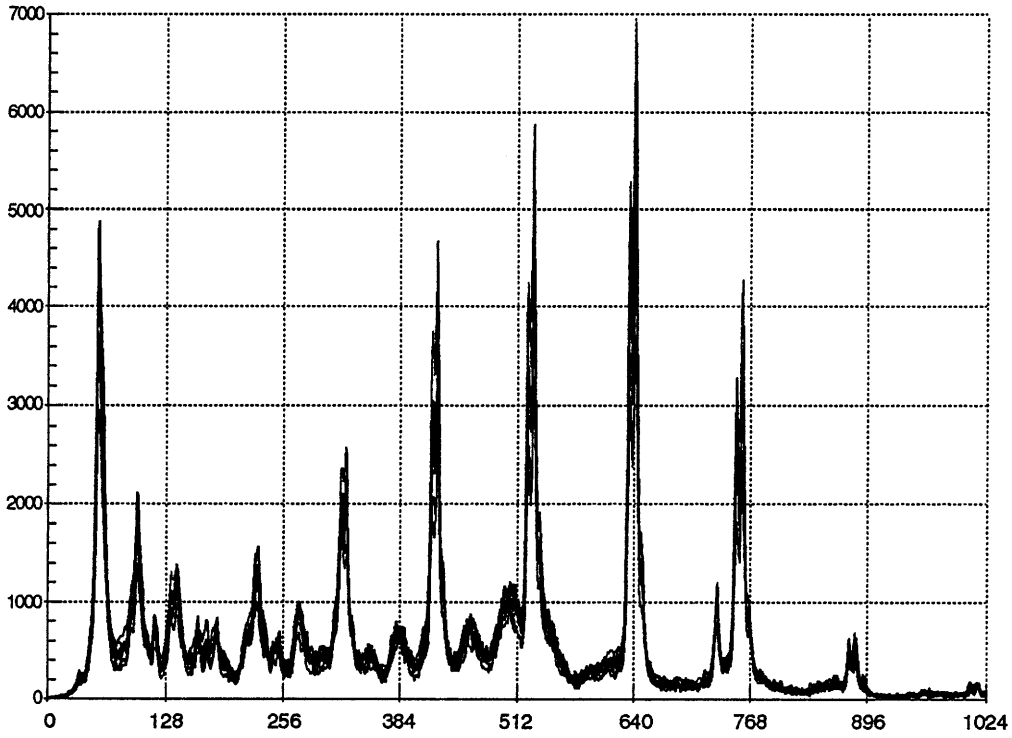

Data file : W72G

Figure 5.50 : Temperature sweep from 27 to 128 °C / P15 peak (empirical procedures used)

Conditions : 100 pulses/spectrum
Exposure : 1995 ms
P : unknown
Grating 1200 g/mm @ 234 nm

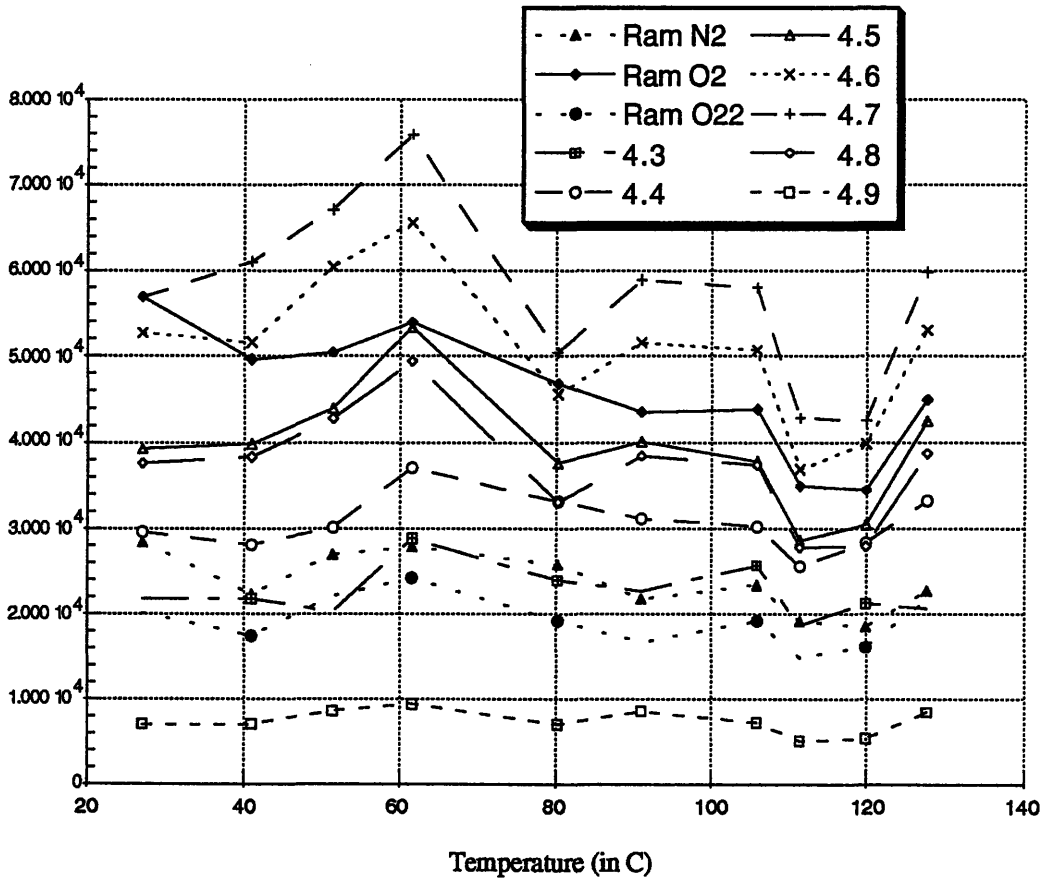

Data file : W72TempP15/res.

Figure 5.51 : Temperature sweep from 27 to 128 °C / P15 peak % variation (empirical procedures used)

Conditions : 100 pulses/spectrum
Exposure : 1995 ms
P : unknown
Grating 1200 g/mm @ 234 nm

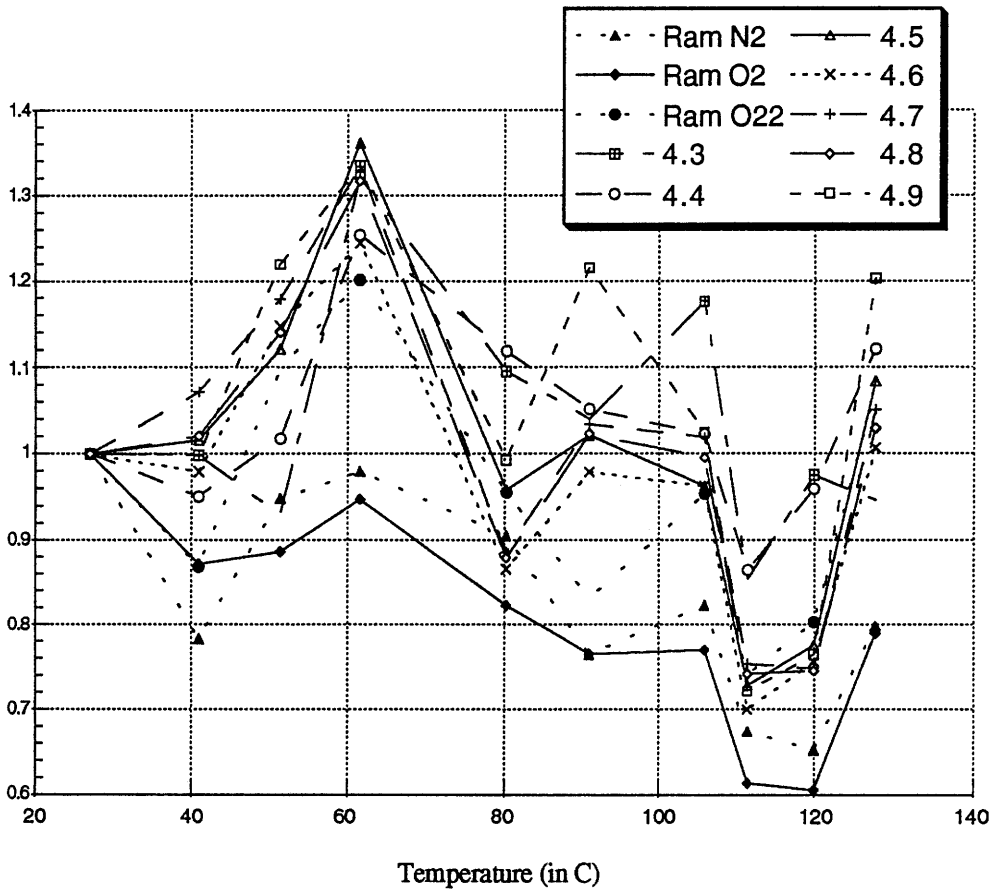

Data file : W72TempP15/res.

Figure 5.52 : **Temperature sweep from 128 to 125C / P17 peak with density correction**

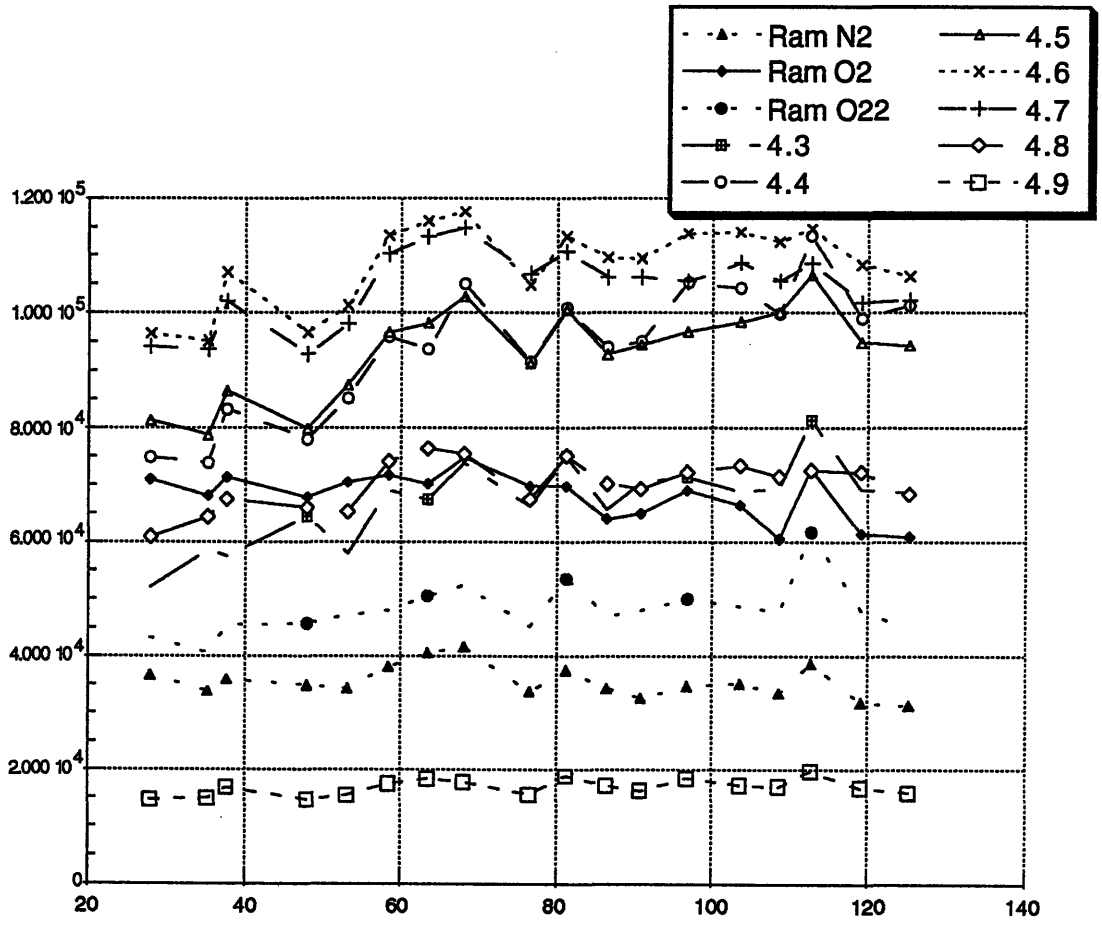

Data file : V72-CorDP17Temp2/res.

Figure 5.53 : Variations of O_2 Raman peak

Temperature variation (Pressure : 1.3 b)

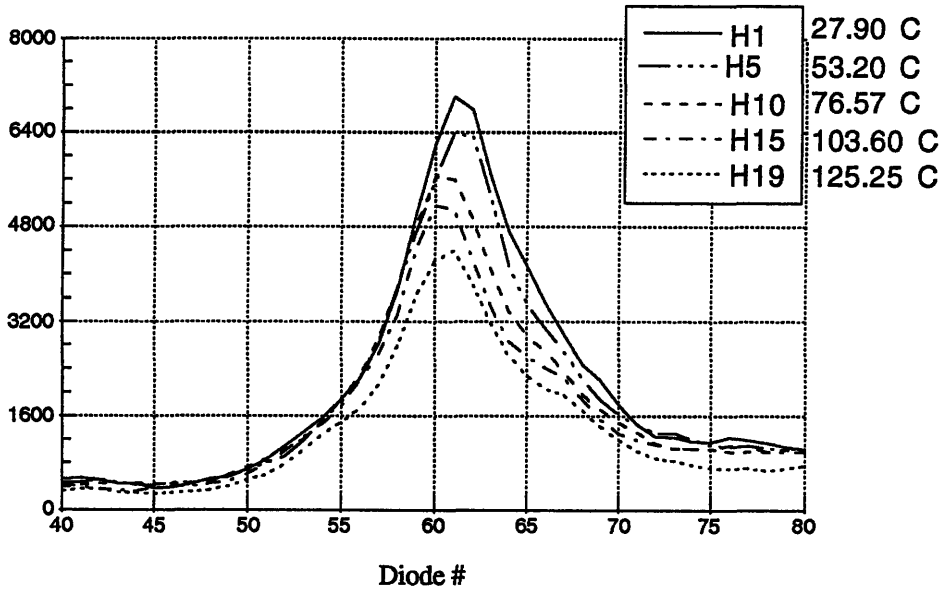

Pressure variation (Temperature : 26 C)

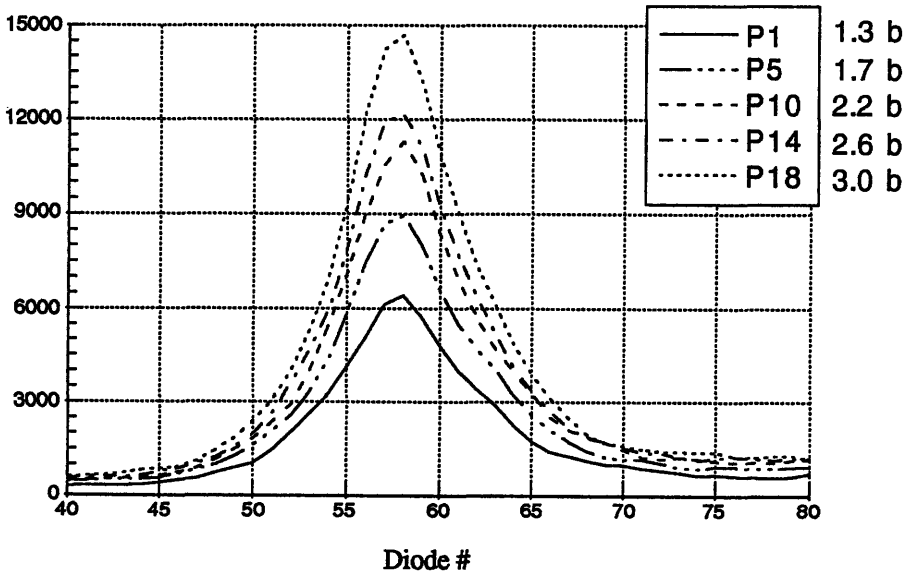

Data file : W72P - V72H

Figure 5.54 : Variations of N_2 Raman peak

Temperature variation (Pressure : 1.3 b)

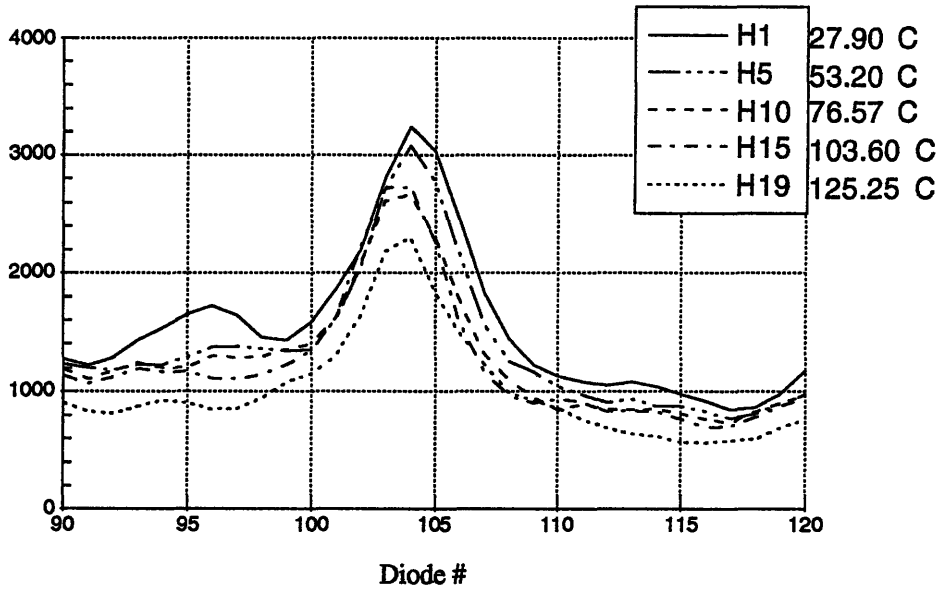

Pressure variation (Temperature : 26 C)

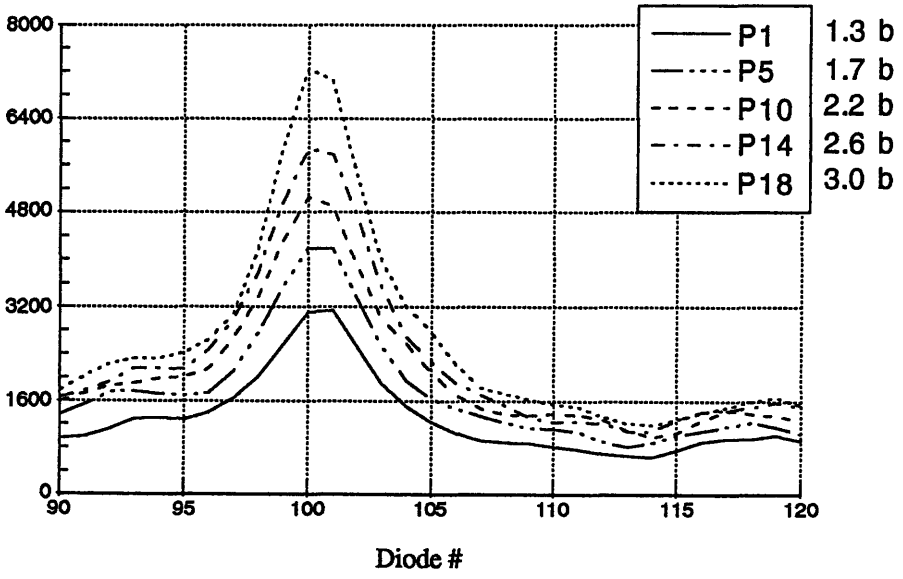

Data file : W72P - V72H

Figure 5.55 : Variations of O2 Raman 2nd order

Temperature variation (Pressure : 1.3 b)

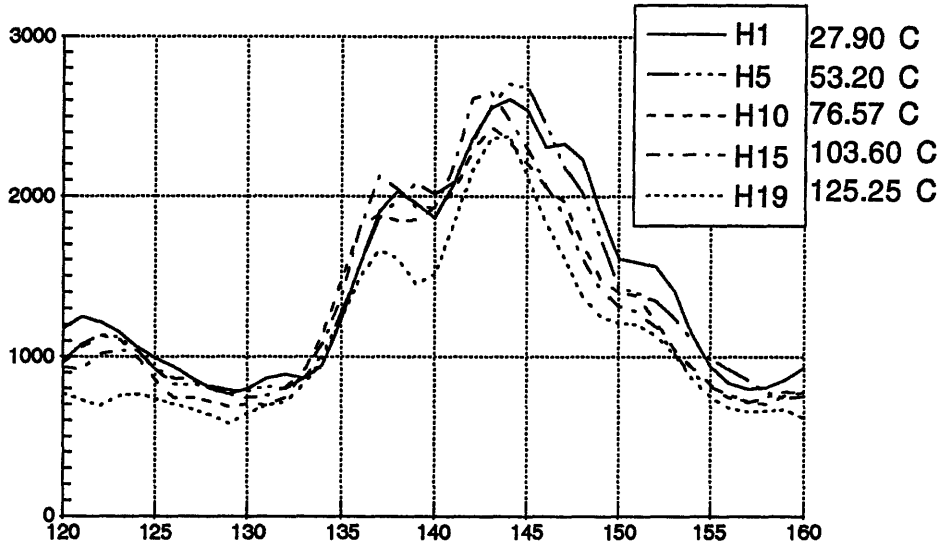

Pressure variation (Temperature : 26 C)

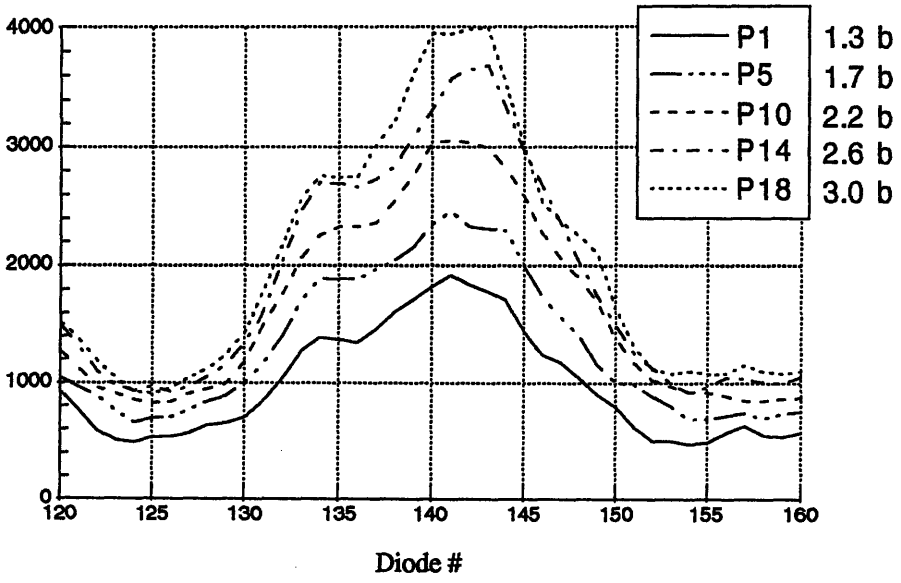

Data file : W72P - V72H

Figure 5.56 : Variations of O2 4.3 LIF peak

Temperature variation (Pressure : 1.3 b)

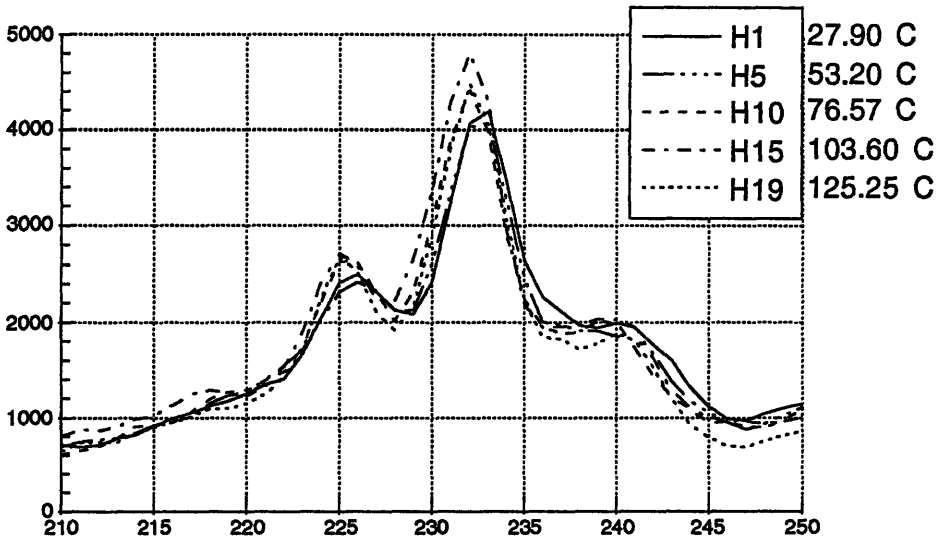

Pressure variation (Temperature : 26 C)

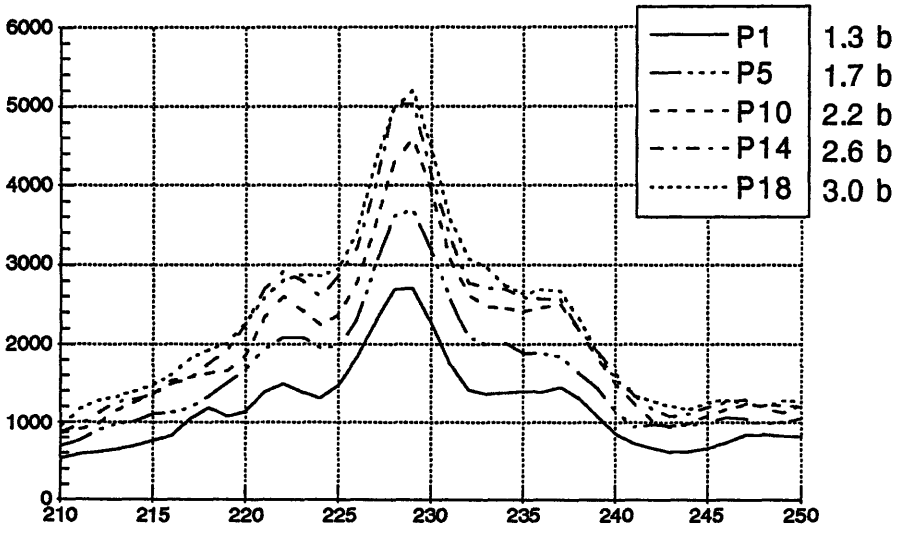

Data file : W72P - V72H

Figure 5.57 : Variations of O2 4.4 LIF peak

Temperature variation (Pressure : 1.3 b)

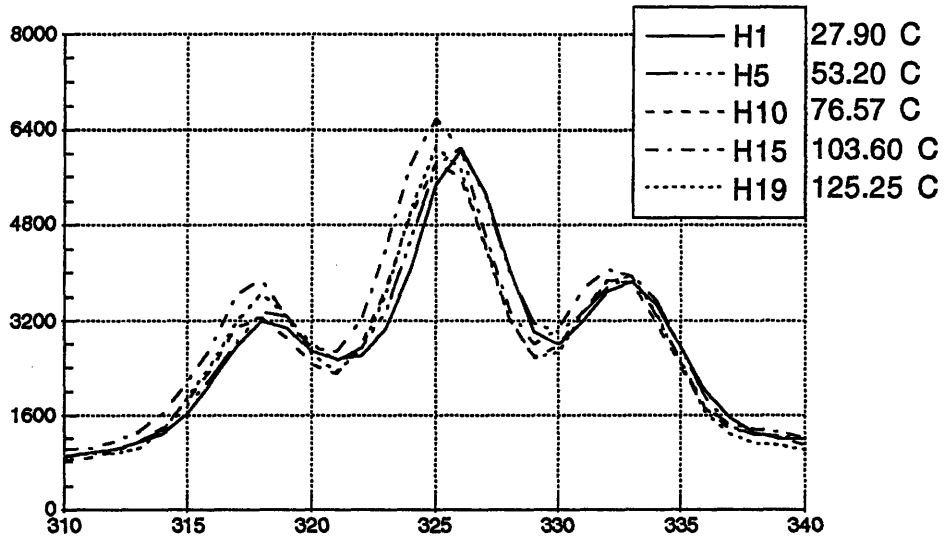

Pressure variation (Temperature : 26 C)

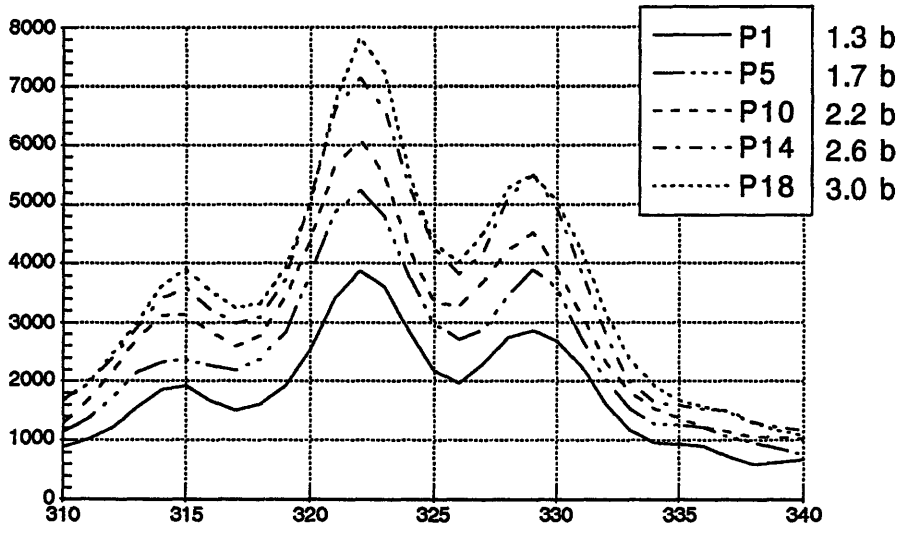

Data file : W72P - V72H

Figure 5.58 : Variations of O2 4.5 LIF peak

Temperature variation (Pressure : 1.3 b)

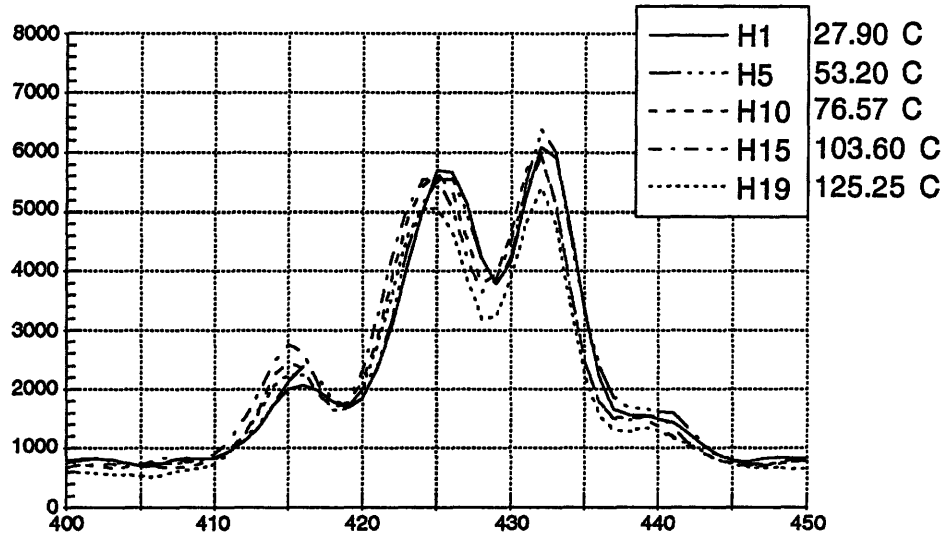

Pressure variation (Temperature : 26 C)

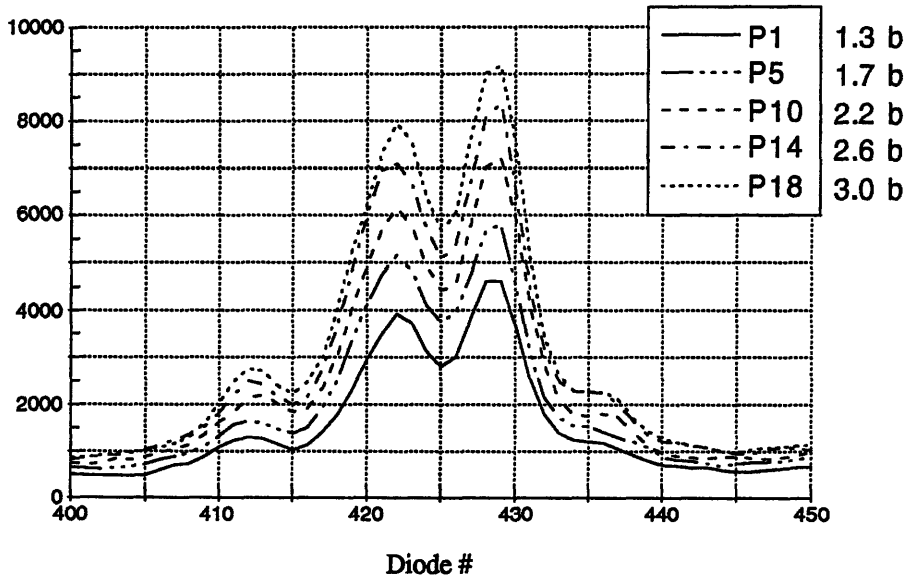

Data file : W72P - V72H

Figure 5.59 : Variations of O2 4.6 LIF peak

Temperature variation (Pressure : 1.3 b)

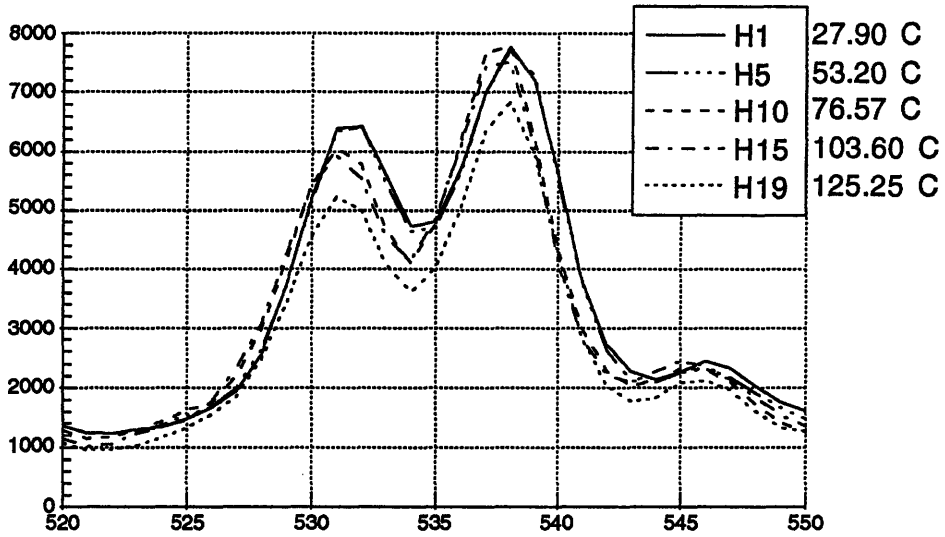

Pressure variation (Temperature : 26 C)

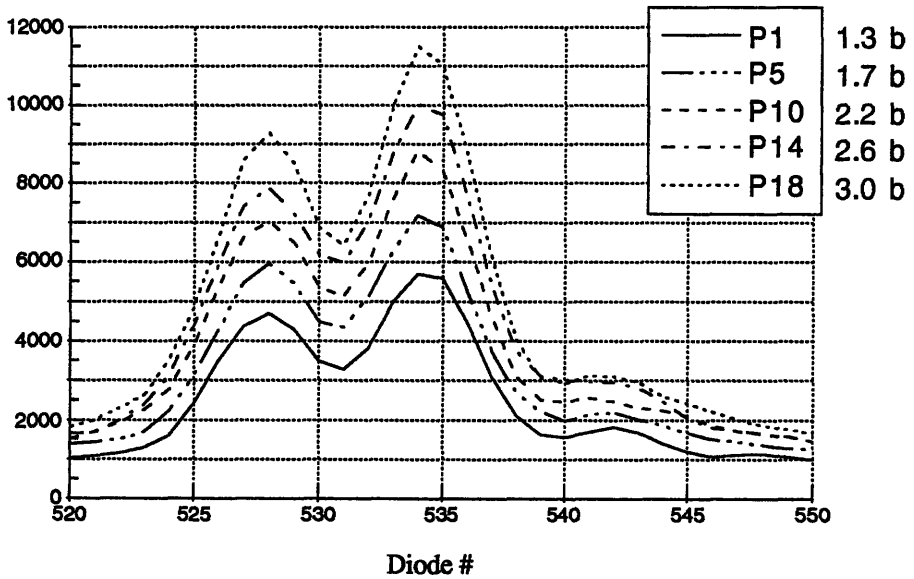

Data file : W72P - V72H

Figure 5.60 : Variations of O2 4.7 LIF peak

Temperature variation (Pressure : 1.3 b)

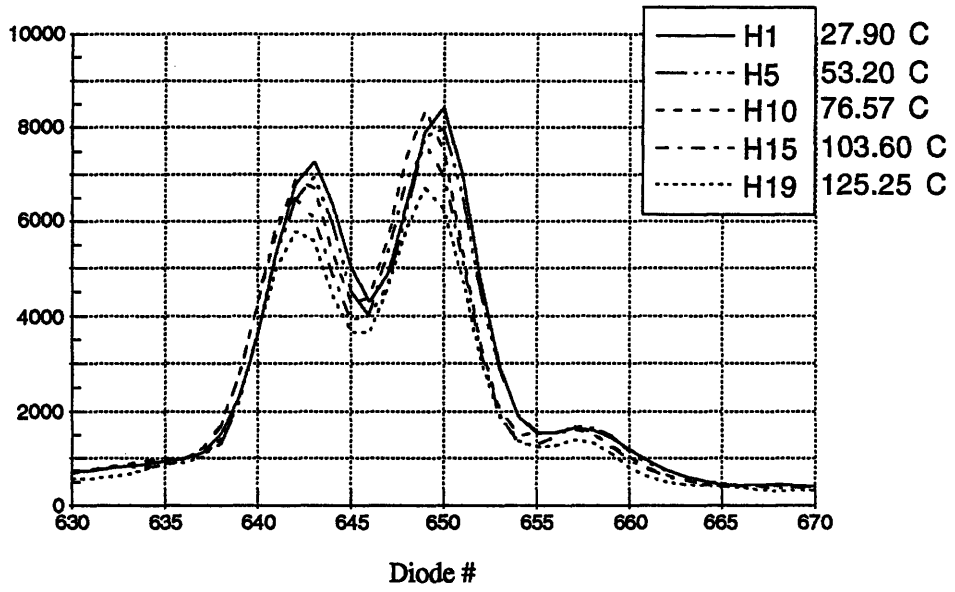

Pressure variation (Temperature : 26 C)

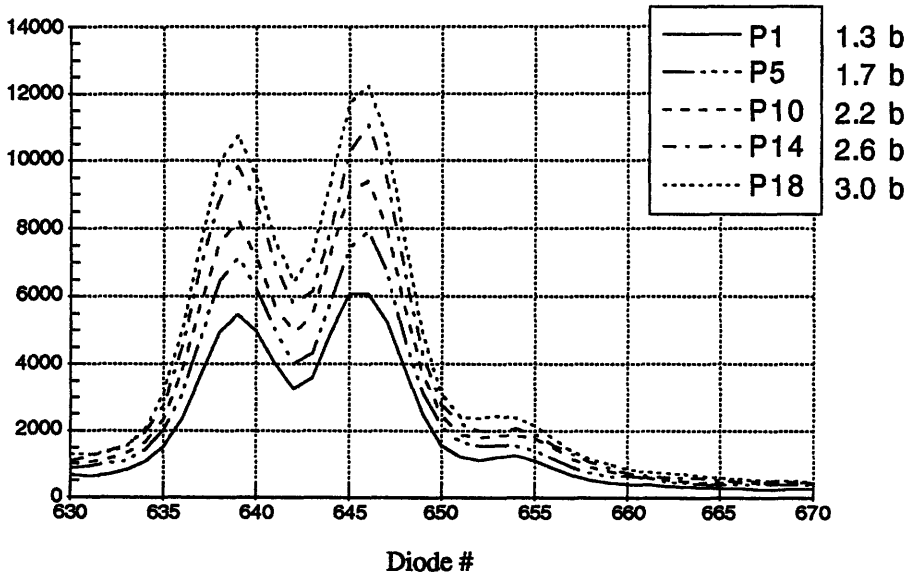

Data file : W72P - V72H

Figure 5.61 : Variations of O2 4.8 LIF peak

Temperature variation (Pressure : 1.3 b)

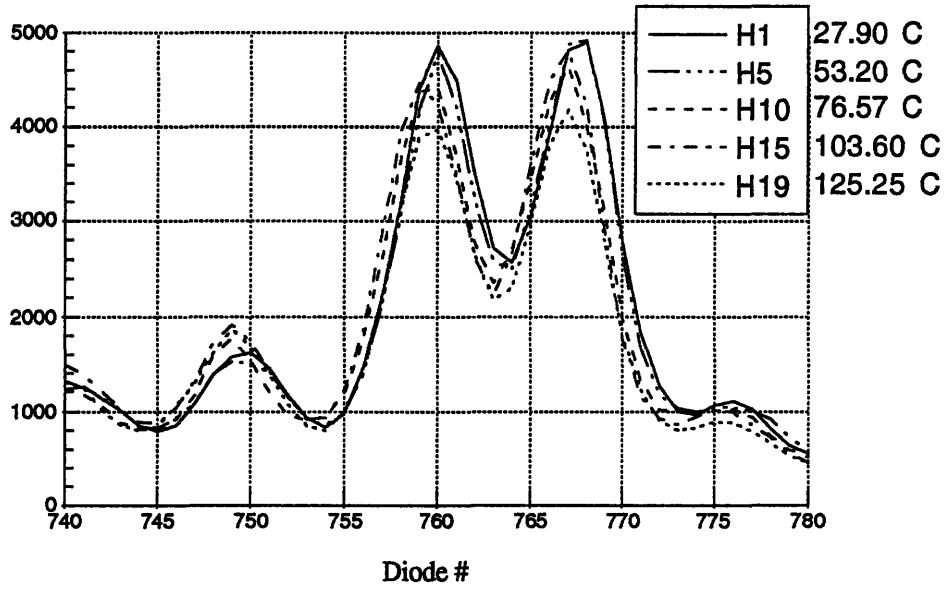

Pressure variation (Temperature : 26 C)

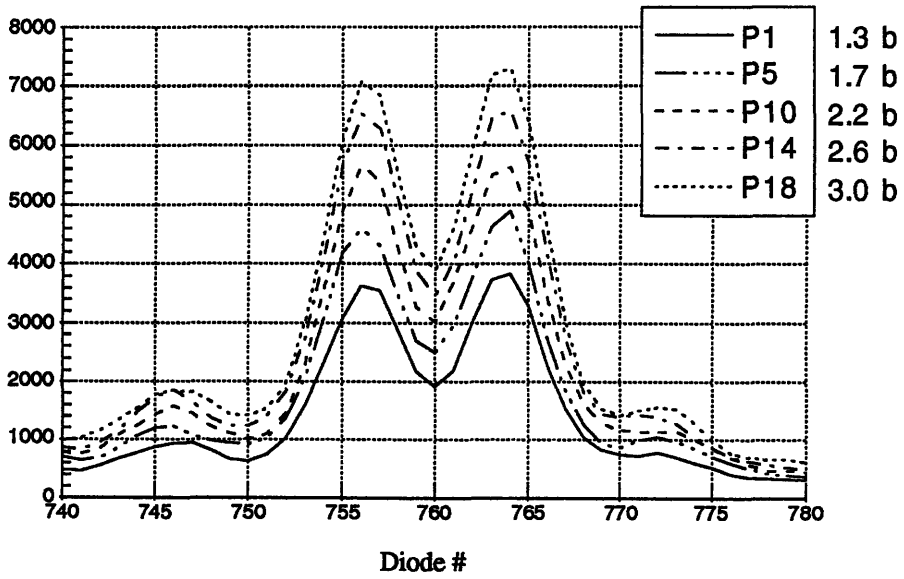

Data file : W72P - V72H

Figure D.1 : **Blades configuration**

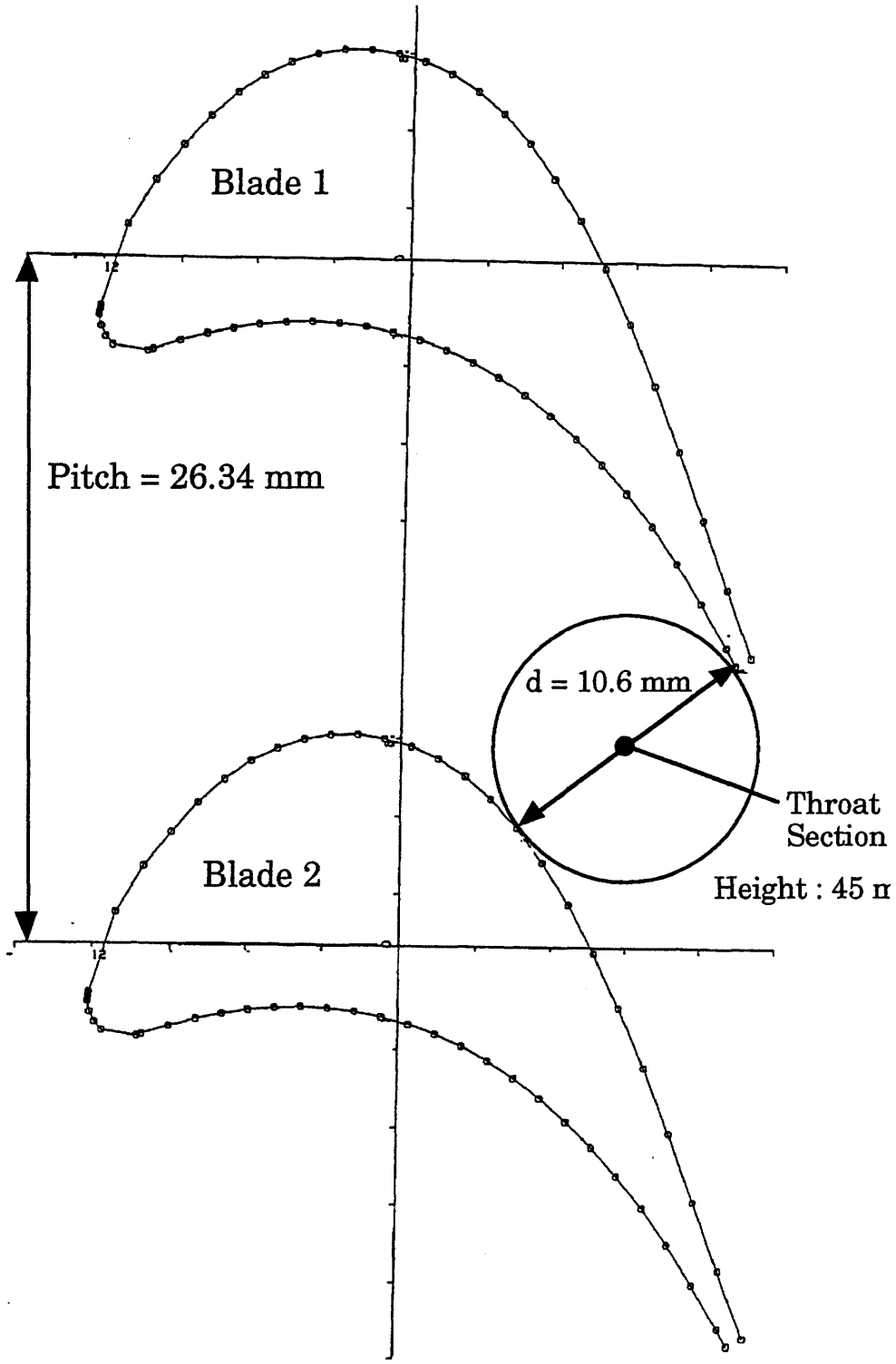

Figure D.2 : **Solid angle considerations**

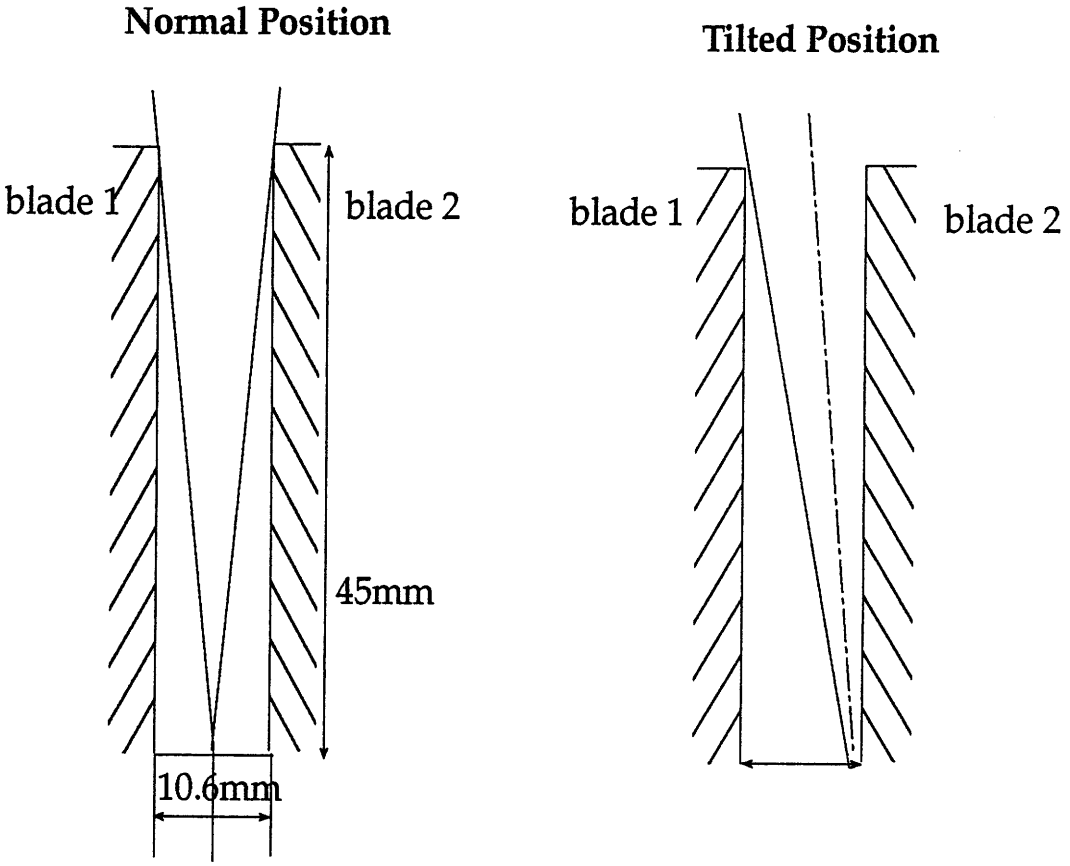

Figure D.3 : **Backscattering set-up**

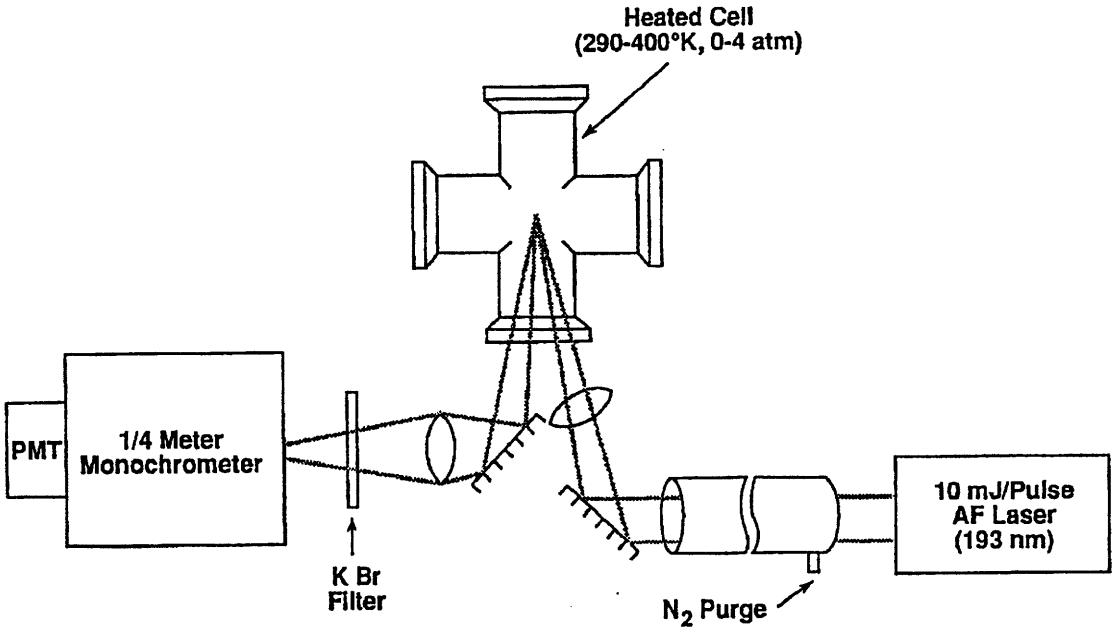

Source : Ref [1]
Annen, 1990

Figure D.4 : **Imaged volume**

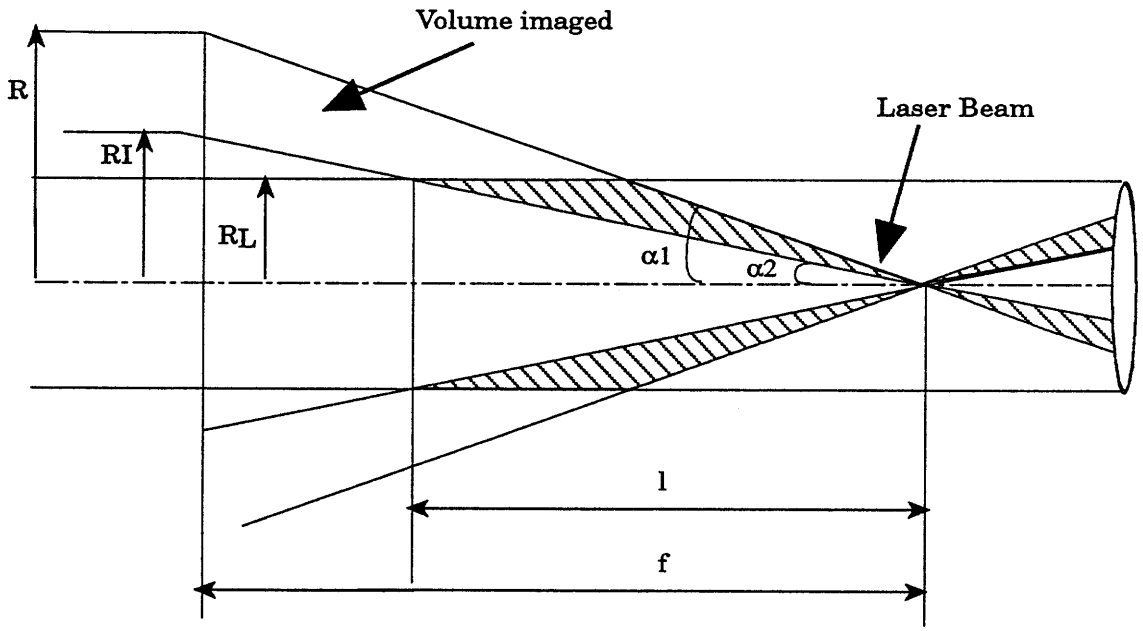

Figure D.5a : **Shape of the section of the focused laser beam**

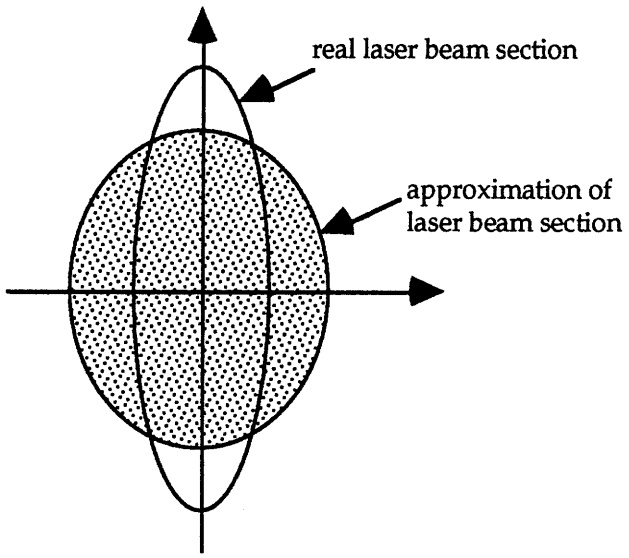

Figure D.5b : **Contour Shape of the laser beam for a short focal length lens**

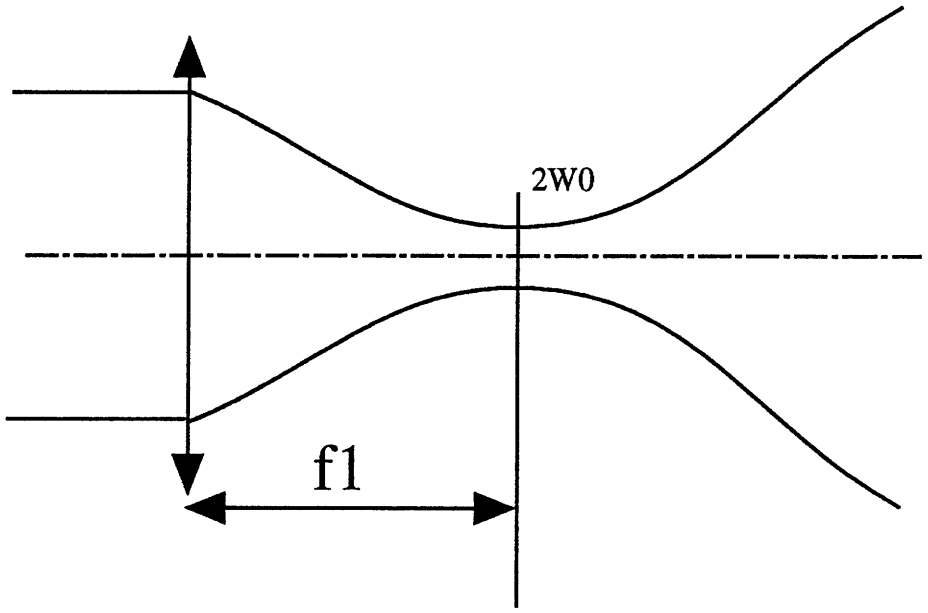

Figure D.5c : **Contour Shape of the laser beam for a long focal length lens**

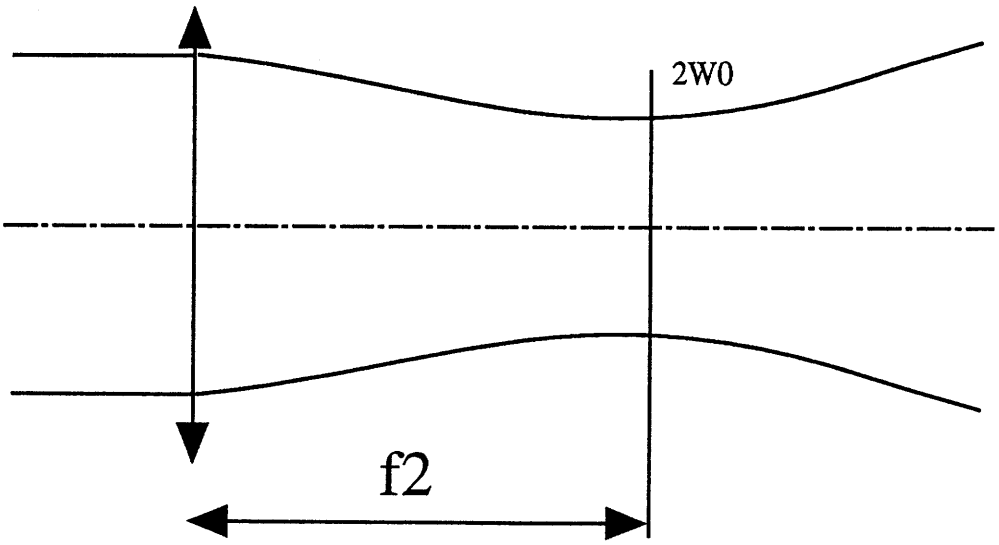

Laser beam shape

Figure D.6a : **General contour shape of laser beam**

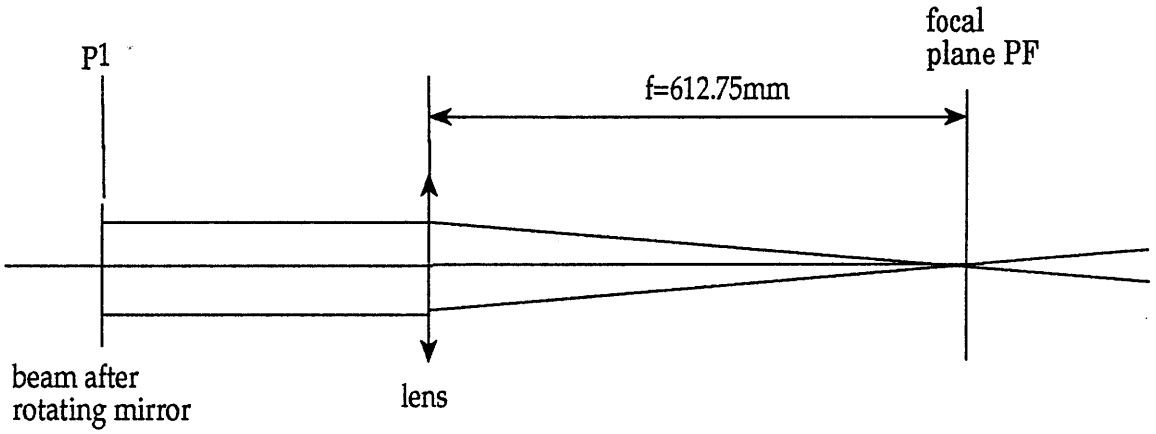

Figure D.6b : **General shape of the laser beam section**

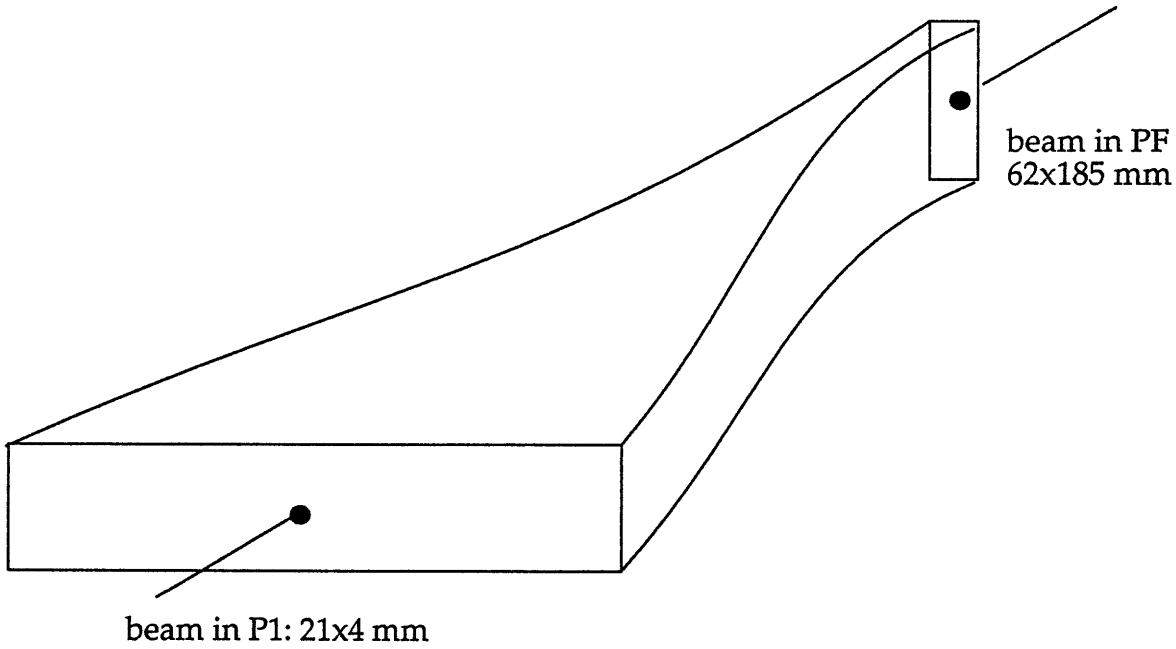

Figure D.7 : **Geometric analysis**

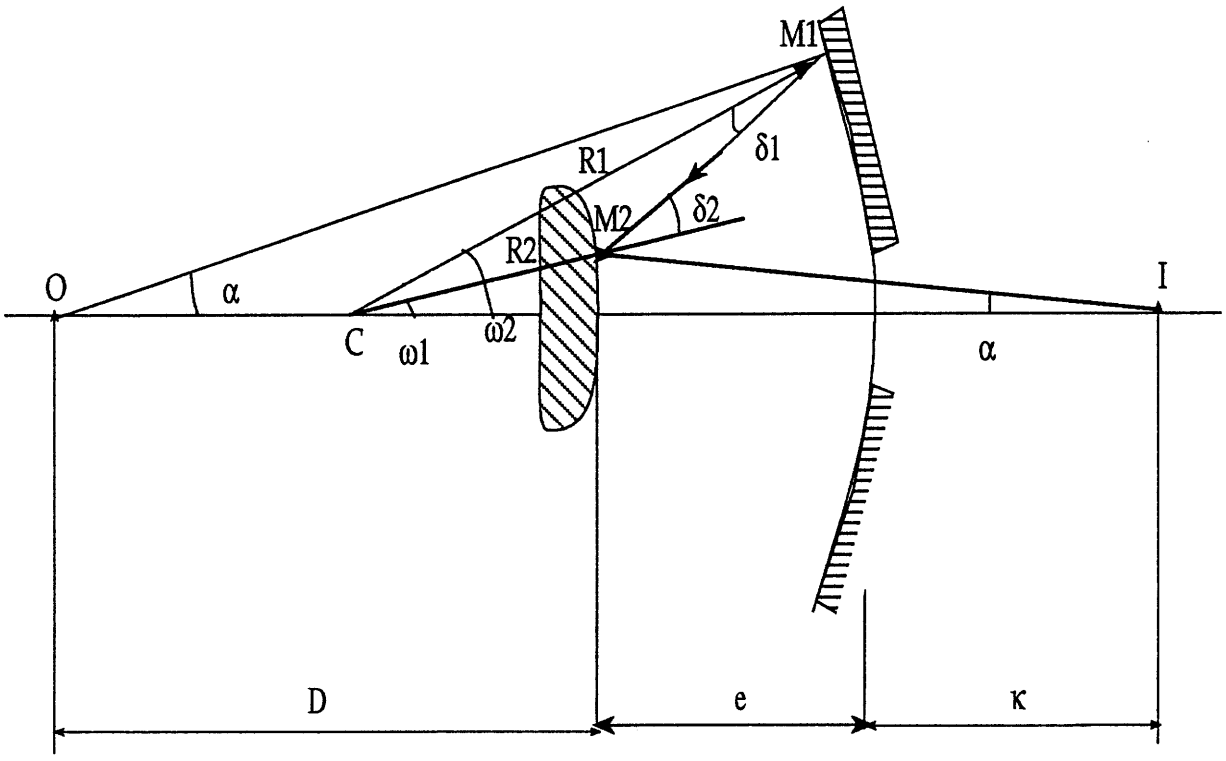

Figure D.8a : **Proposed design dimensions**

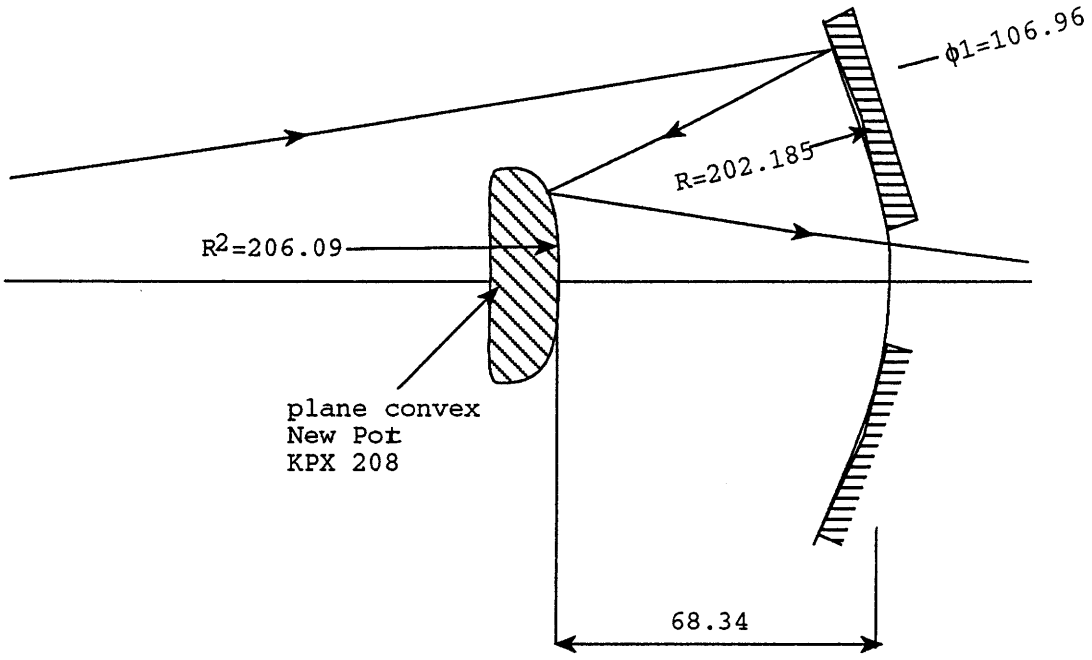

Figure D.8b : **Proposed design set-up**

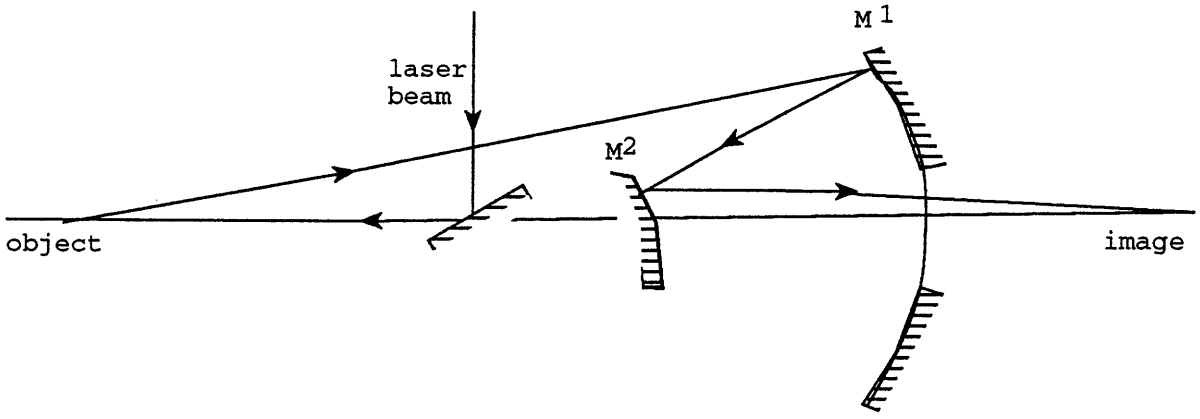

Figure F.1 : Model of Spectrometer

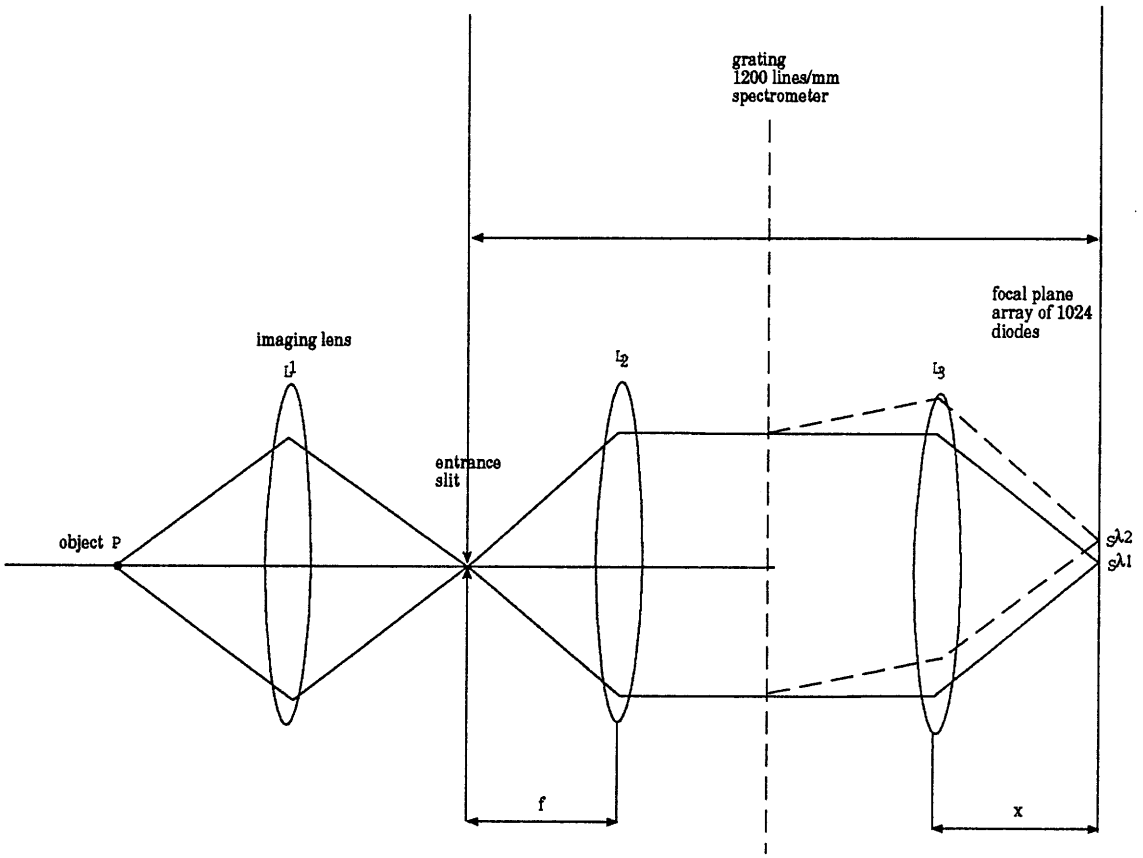

Figure F.2a : **Slit size effects : before grating**

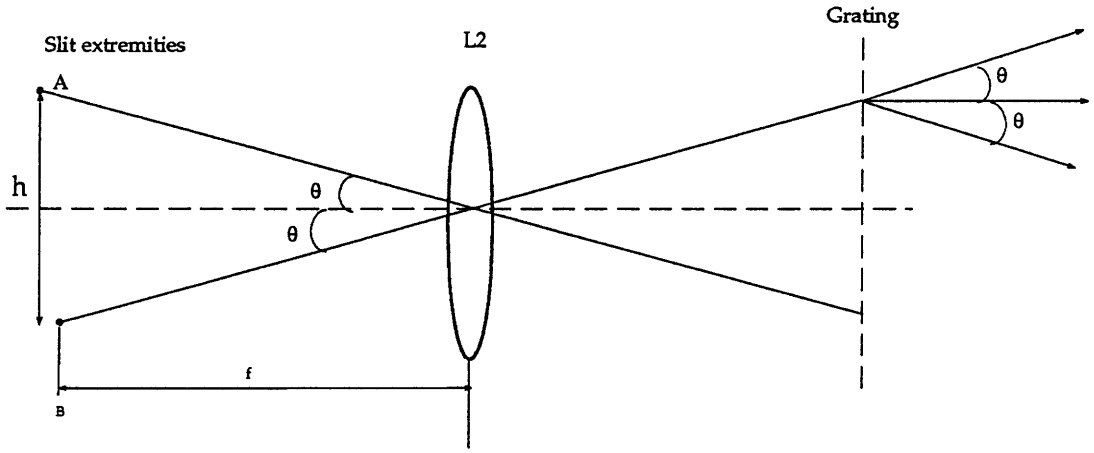

Figure F.2b : **Slit size effects : after grating**

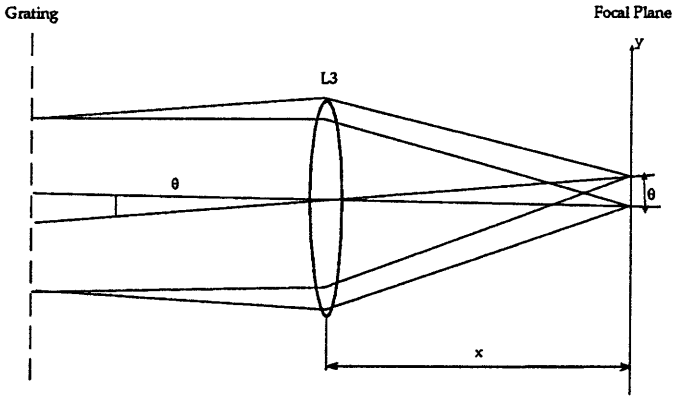

Figure F.3a : **General diffraction pattern**

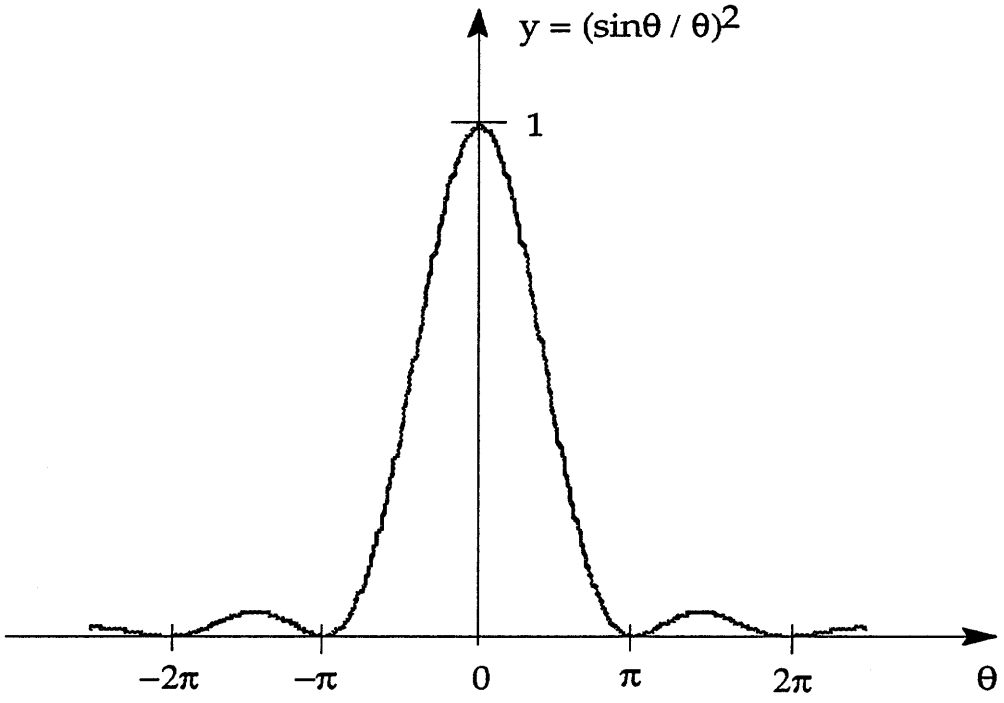

Figure F.3b : **Different configurations possible for the central diode**

Configuration #1
central line on the axis of one diode

Configuration #2
central line between two diodes

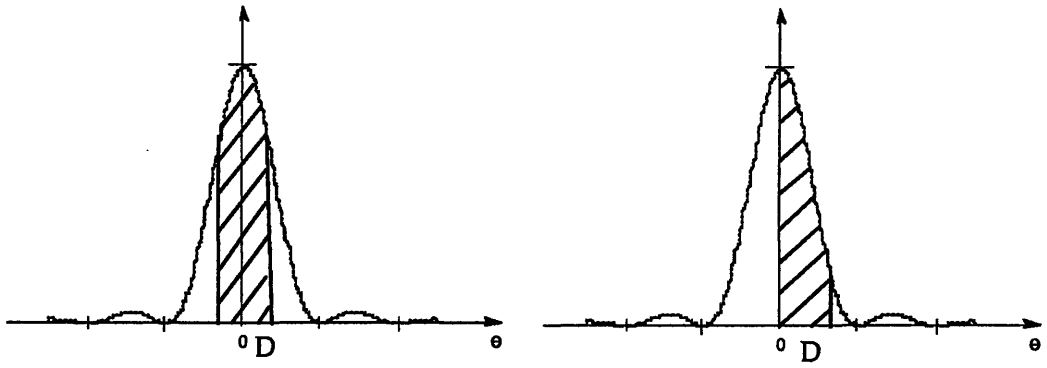

Figure F.3c : **Slit size effect on the central diode signal** (in configuration #1)

small slit size case
(base case : 10μm)

larger slit size case
(for example : 100 μm)

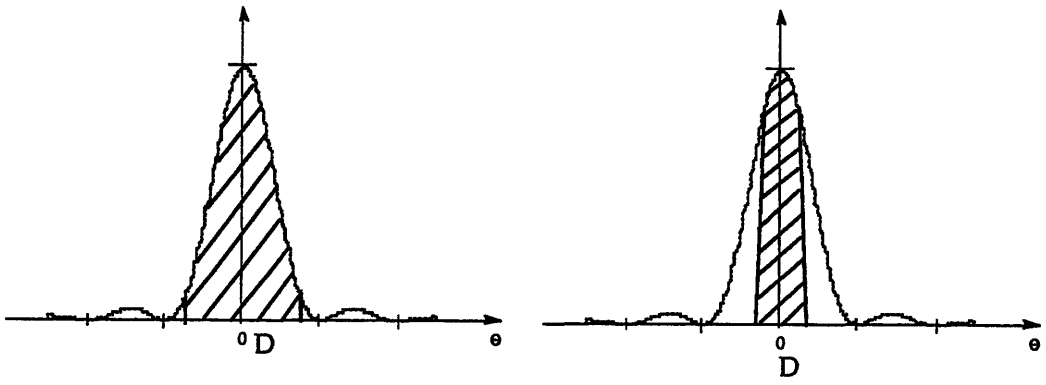

Figure F.4 : Variation of signal received by central diode

Figure F.4a

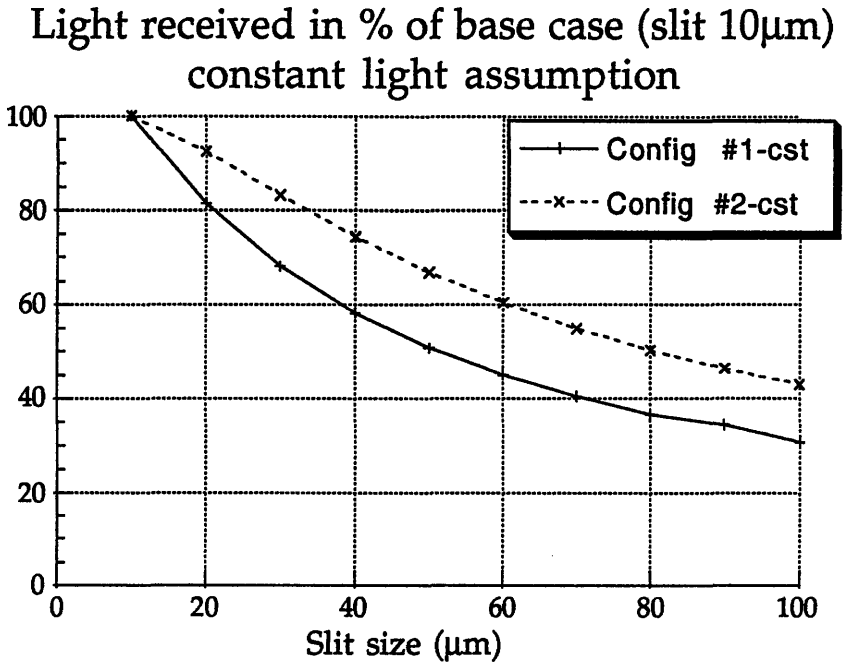

Figure F.4b :